

Quantum Theory of Sensing and Thermoelectricity in Molecular Nanostructures

Qusiy Hibeab Hityhit Al-Galiby

B.Sc, M.Sc.

Department of Physics, Lancaster University, UK

Ph.D. Thesis



This thesis is submitted in partial fulfilment of the requirements
for the degree of Doctor of Philosophy

March 2016

Declaration

Except where stated otherwise, this thesis is a result of the author's original work and has not been submitted in whole or in part for the award of a higher degree elsewhere. This thesis documents work carried out between June 2012 and March 2016 at Lancaster University, UK, under the supervision of Prof. Colin J. Lambert and funded by UK EPSRC grants EP/K001507/1, EP/J014753/1, EP/H035818/1, the European Union Marie-Curie Network MOLESCO 606728, the Ministry of Higher Education and Scientific Research (MOHESR) in Iraq, Al Qadisiyah University and the Ministry of the Presidency of Iraq, Establishment of Martyrs.

Qusiy H. Al-Galiby

March 01, 2016

Abstract

This thesis presents a series of studies into the electronic and thermoelectric properties of molecular junction single organic molecules: They include *perylene Bisimide* (PBIs), *naphthalenediimide* (NDI), *metallo-porphyrins* and a large set of symmetric and asymmetric molecules.

Two main techniques will be included in the theoretical approach, which are Density Functional Theory, which is implemented in the SIESTA code [1], and the Green's function formalism of electron transport (Chapter 2), which is implemented in the GOLLUM code [2], it is a next-generation code, born out of the non-equilibrium transport code SMEAGOL code [3]. Both techniques are used extensively to study a family of *perylene bisimide* molecules (PBIs) (Chapter 3) to understand the potential of these molecules for label-free sensing of organic molecules by investigating a change in the electronic properties of PBI derivatives. Also, these techniques are used to simulate electrochemical gating of a single molecule *naphthalenediimide* (NDI) junction (Chapter 4) using a strategy to control the number of electrons on the molecule by modelling different forms of charge double layers comprising positive and negative ions.

Chapter 5 will deal with the thermoelectric properties of the single organic molecule. I will demonstrate that varying the transition metal-centre of a porphyrin molecule over the family of metallic atoms allows the molecular energy levels to be tuned relative to the Fermi energy of the electrodes and that leads to the ability to tune the thermoelectric properties of metallo-porphyrins.

Chapter 6 will present our new approach to materials discovery for electronic and thermoelectric properties of single-molecule junctions. I will deal with a large set of symmetric and asymmetric molecules to demonstrate a general rule for molecular-scale

quantum transport, which provides a new route to materials design and discovery. The rule of this approach that “the conductance of an asymmetric molecule is the geometric mean of the conductance of the two symmetric molecules derived from it and the thermopower of the asymmetric molecule is the algebraic mean of their thermopowers”.

Acknowledgments

Nothing would have been completed in this thesis without the collaboration, the help and guidance of many people. All my gratitude goes to my supervisor **Prof. Colin J. Lambert** for his continuous guidance and the intensive fruitful discussion over these years. I would like to thank Dr. Steve Baily, Dr. Iain Grace for their continuous support.

I would like also to thank my sponsor, the Ministry of Higher Education and Scientific Research (MOHESR) in Iraq, Al Qadisiyah University and the Ministry of the Presidency of Iraq, Establishment of Martyrs for funding my PhD study.

I would like to thank the collaborating experimental groups, Prof. Thomas Wandlowski and Prof. Wenjing Hong from Bern University for their successful experiments. I would like to thank all my friends and colleagues in Colin's group, especially Hatef Sadeghi, Dr. David Manrique, Dr. Laith Algharagholy, Dr. Thomas Pope, Dr. Amaal Al-Backri, Mohammed Noori, Nasser Almutlaq, Zain Al-Milli, Sara Sangtarash and Elaheh Mostaani.

To the martyrs of Iraq and in particular my brother, the martyr **Saleh Hibeab Al-Galiby**, you are my inspiration in life, eternal bliss to you. My dear father, thank you so much for your great kindness, and my brother Dr. Hayder, thank you for your great efforts, mercy and paradise to you.

Many gratitude and unlimited thanks to my family. My mother, you have done a lot to me, I hope you are proud and satisfied of me and I wish one day I will be able to serve you. My dear wife, many thanks for your support during my study. You were really very kind and without your support, I would not be able to complete the PhD study. My sons Muhammed, Ali, and Yousif, you are my hope in life; I hope to be a good father to you and support you with a good life. Finally, a big thanks to my sisters and brothers for the support and encouragement I received from them.

List of Publications

1. **Al-Galiby, Qusiy**, Iain Grace, Hatef Sadeghi, and Colin J. Lambert. "Exploiting the extended π -system of perylene bisimide for label-free single-molecule sensing." *Journal of Materials Chemistry C* 3, no. 9 (2015): 2101-2106.
2. Li, Yonghai, Masoud Baghernejad, **Al-Galiby Qusiy**, David Zsolt Manrique, Guanxin Zhang, Joseph Hamill, Yongchun Fu et al. "Three-State Single-Molecule Naphthalenediimide Switch: Integration of a Pendant Redox Unit for Conductance Tuning." *Angewandte Chemie International Edition* 54, no. 46 (2015): 13586-13589.
3. **Al-Galiby, Qusiy H.**, Hatef Sadeghi, Laith A. Algharagholy, Iain Grace, and Colin Lambert. "Tuning the thermoelectric properties of metallo-porphyrins." *Nanoscale* 8, no. 4 (2016): 2428-2433.
4. Manrique, D. Z., **Al-Galiby, Q. H.**, Hong, W., & Lambert, C. J. (2016). A new approach to materials discovery for electronic and thermoelectric properties of single-molecule junctions. *Nano letters*.

Contents

1. Introduction	4
1.1 Molecular Electronics (ME)	4
1.1.1 Perylene Bisimide (PBIs)	6
1.1.2 Naphthalenediimide (NDI)	7
1.1.3 Porphyrin	8
2. Theory of Quantum Transport	9
2.1 The Landauer formula	10
2.2 Thermoelectric coefficients	13
2.2.1 Generalized formula for the thermoelectric coefficients	15
2.3 Scattering Theory	20
2.3.1 One dimensional (1-D) linear crystalline lattice	20
2.3.2 One dimensional (1-D) scattering	24
2.4 Generalization of the Scattering Formalism	28
2.4.1 A doubly infinite Hamiltonian and Green's function of the electrodes	29
2.4.2 Effective Hamiltonian of the Scattering Region	36
2.4.3 Scattering Matrix	38
2.5 Calculation in Practice	40
2.6 Features of the Transport Curve	40
2.6.1 Breit-Wigner Resonance	40
2.6.2 Fano Resonances	42
2.6.3 Anti-Resonances	44

2.7 Hamiltonian used in the thesis	46
3. Single-Molecule Sensing of Perylene Bisimide	48
3.1 Single-Molecule Conductance of Perylene Bisimide (PBIs)	48
3.1.1 Motivation	48
3.1.2 Computational Methods	49
3.1.2.1 Molecular junction and the conductance	51
3.1.3 Results and discussion	53
3.1.3.1 Locating the optimal value of E_F	54
3.2 Exploiting the Extended π -System of Perylene Bisimide for Label-free Single-Molecule Sensing	56
3.2.1 Motivation	56
3.2.2 Molecular Complexes	59
3.2.3 Molecular junction and the conductance	63
3.2.4 Evaluating of error in the currents for a distribution of geometries.	70
3.2.5 Fluctuation positions of the analytes above the PBIs backbone...	70
3.2.6 Quantifying the sensitivity of the PBIs for discriminating sensing.	78
3.3 Summary	80
4. Three States Single-Molecule Naphthalenediimide Switch: Integration of Pendant Redox Unit for Conductance Tuning	81
4.1 Introduction	81
4.2 Experimental work	83
4.2.1 Single-molecule break junction experiments	83
4.2.2 Further analysis of NDI-D conductance measurement.....	88
4.3 Theoretical Method	88
4.3.1 The junction and Charge double layer geometries	89

4.4 Results and discussion	92
4.5 Summary	97
5. Tuning the thermoelectric properties of metallo-porphyrins	98
5.1 Motivation	98
5.2 Introduction	100
5.3 Methods	101
5.4 Results and Discussion	103
5.4.1 Plots of frontier orbitals and spin-dependent transmission coefficients	110
5.4.2 Thermoelectric properties of Fe(III)-porphyrin in presence of a Cl counter anion	118
5.4.3 The calculation of Mn-porphyrin in presence of (Cl)	121
5.5 Summary	124
6. A New Approach to Materials Discovery for Electronic and Thermoelectric Properties of Single-Molecule Junctions	125
6.1 Introduction	126
6.2 Methods	129
6.3 Results and discussion	132
6.4 Associated Content	143
6.5 Summary	164
7. Conclusion	165
Bibliography	171

Chapter 1

Introduction

1.1 Molecular Electronics

In recent decades technological advances have accelerated at a rapid pace, partially due to the ever increasing need for the miniaturization of electronic devices. Whether the progress of research and development will be able to help this need in the future depends on how much we can further extend our computational capabilities through nanotechnology.

In the mid-1960s, Gordon Moore observed that the number of transistors per unit area on a chip was doubling approximately once every two years [1]. The size of the current silicon based transistors are now down to only tens of *nanometers*, where he expected that this trend could continue for only a 10-year long period, nearly half a century later, the exponential growth continues. However, if Moore's law is to continue, the transistors will have to shrink to the atomic scale within twenty years and enter the field of sub-10 nm *nanoelectronics*. One important branch of this field, that this thesis is focused on, is *molecular electronics* (ME), a bottom up approach where electronic circuits are constructed, with specifically designed molecules taking the roles of both the active components and connecting wires. Not only are these circuits attractive for their minute size, but also for their potential to be

fast and cheap, with lower power consumption. Therefore, single molecule devices are very appealing candidates for future applications.

So far, theoretical and experimental studies have focused on electrode-molecule-electrode (EME) junctions, which will be discussed in this thesis. The main experiment techniques to study these systems are Scanning Tunnelling Microscopy Break Junctions (STM-BJ) [2, 3] and Mechanically Controllable Break Junctions MCBJ [4, 5]. Using such break junctions, a third electrode can be also introduced by chemical gating [6, 7].

A simplistic picture of the physics of such the molecules in EME contacts is that they are a kind of quantum dot, because they are small finite sized objects and have discrete electronic spectra and single-electron charging energies reaching the electron-volt range. However, molecules are more than “just” quantum dots. The word “dot” carries with it the impression of a relatively structureless, even quasi-zero-dimensional object. Yet, the long-term goal of molecular electronic (ME) is precisely to take the advantages of the endless variability of chemical compounds to design molecules having just the right properties for use as single-molecule electronic components. Furthermore molecules can have multiple conformations and they could be used as rectifiers [8]. Indeed Aviram and Ratner proposed theoretically the first molecular rectifier and their suggestion was the starting point for the development of this field. Molecular electronics also could be used in a wide range of applications such as switches [9] and sensors [10, 11].

As a part of the development of molecular electronic devices, the ability to control electron transport through a single molecule is considered to be a crucial task in this field [8, 12, 13]. Most studies in molecular electronics have focused on two-electrodes devices [14-17]. A molecular junction with a gate electrode in a transistor configuration gives the possibility to tune the transport characteristics [18], as will be discussed in this thesis.

The ability to manage waste heat is a major challenge, which currently limits the performance of information technologies. To meet this challenge, there is a need to develop novel materials and device concepts, innovative device architectures, and smart integration schemes, coupled with new strategies for managing and scavenging on-chip waste heat. The development of new high-efficiency and low-cost thermoelectric materials and devices is a major target of current research. Thermoelectric materials, which allow highly-efficient heat-to-electrical-energy conversion from otherwise wasted low-level heat sources, would have enormous impact on global energy consumption.

Nanoscale systems and especially nanoscale structures are very promising in this respect, due to the fact that transport takes place through discrete energy levels. The ability to measure thermopower in nanoscale junctions opens the way to developing fundamentally-new strategies for enhancing the conversion of heat into electric energy [19]. The thermoelectric properties of materials will be discussed in this thesis.

Therefore one aim of this thesis is to provide rules for the discovery of new materials by predicting electronic [20] and thermoelectric properties of molecules. This is particularly important, because theoretical methods such as density functional theory and GW many body theory do not usually provide quantitative predictions of such properties.

1.1.1 Perylene bisimide (PBIs)

Partly in response to predictions that silicon technology might soon reach the limits of its evolution [21, 22], there is increasing interest in controlling charge transport across nanometer-scale metal-molecule-metal junctions [8, 23-26]. In this thesis, I address the properties of functions formed from three classes of molecules. The first class involves the perylene bisimide (PBIs) (also called perylene diimides) [27-30], which have emerged as one of the most investigated families of organic molecules, both for their fundamental

electronic properties and their industrial applications as dyes and pigments [8, 23]. Their unique properties are primarily derived from their large extended π -systems, which in π -stacked arrays lead to a variety of intermolecular π -orbital overlaps for the different derivatives [31]. Furthermore their high electron affinities, large electron mobilities, chemical and thermal stabilities, and variety of functional forms with different bay-area substituents has led to their widespread use in organic solar cells [32-35], organic field-effect transistors (OFETs) [36, 37] particularly as n-type materials [38, 39], and organic sensors [40-47].

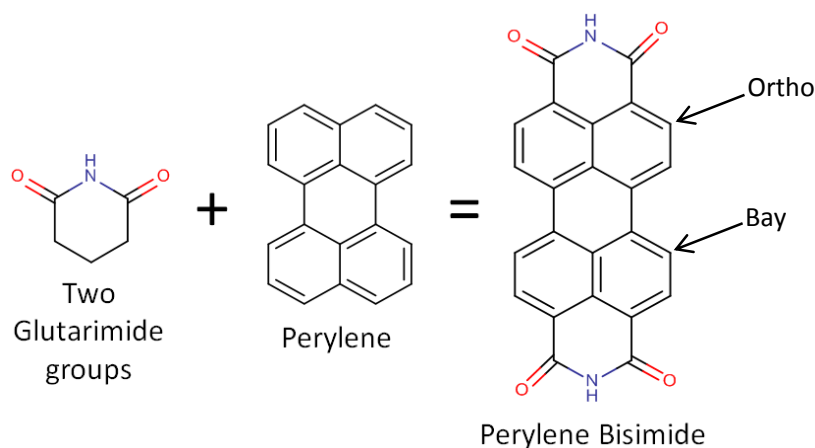


Figure 1.1: shows the chemical structure of Perylene Bisimide (PBIs) molecule.

The chemical structure of *perylene bisimide* (Figure 1.1) involves two *glutarimide* groups with two *naphthalenes* (which is called perylene). The core of *perylene bisimide* can be functionalized in different ways by varying both the *bay* and *ortho* positions [23].

1.1.2 Naphthalenediimide (NDI)

The second class of molecular function are formed from naphthalene diimide (NDI), which has attracted much attention in organic electronics [48-50] and the supramolecular chemistry [51] community acting as an electron acceptor with n-type semiconductor characteristics. This molecule is studied in chapter 4 and comprises of a pyrene core with two alkyl chains

in the bay-area position and benzothiophenes (DBT) as anchor groups as shown in Figure 1.2.

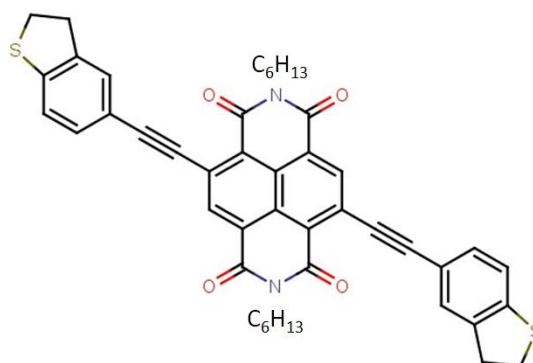


Figure 1.2: shows the chemical structure of naphthalenediimide (NDI) molecule.

1.1.3 Porphyrin

Finally I investigate functions formed from porphyrins, which are attractive as building blocks for molecular-scale devices, because they are conjugated, rigid, chemically stable and form metalloporphyrins by coordinating a variety of metallic ions [52-60]. The porphyrin molecule comprises of a four pyrrole cores (the inner ring π -system), whereas the metalloporphyrin involves a four pyrrols cores with a metallic atom χ in the centre of the molecule as shown in Figure 1.3 (a and b). Typical example of χ are zinc, copper, nickel and various others.

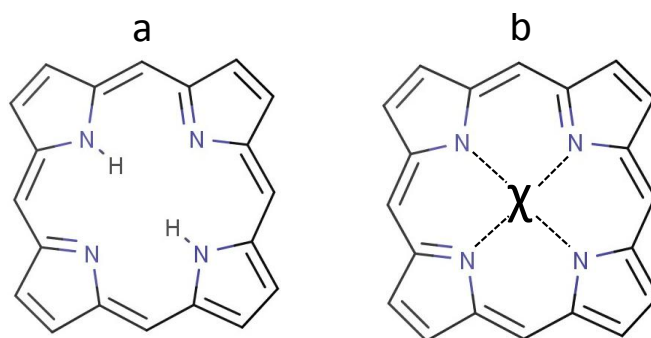


Figure 1.3: (a and b) illustrate the chemical structure of porphyrin and metallo-porphyrin molecules, respectively.

Chapter 2

Theory of Quantum Transport

One of the important challenges in molecular electronic how to connect the molecule to metallic or any other electrodes to probe its electronic properties. For the molecular system, the contacts between the molecule and the electrodes are usually a significant part which determines the electronic properties in addition to the molecular properties. This contact involves scattering processes from the electrode to the molecule and from the molecule to the electrode. A system like this is not periodic, so a band structure is no longer sufficient to describe its electronic properties. For this reason a general approach is required to understand and calculate the scattering processes between the electrodes that are interconnected with a molecule.

Our aim in this section is to understand the Landauer formalism in a general form, and the discussion will start with a brief derivation of the Landauer formula. I will introduce an example of a one dimensional structure to present the general methodology used to describe transport in mesoscopic conductors of arbitrarily complex geometry. This method assumes that the interaction between carriers and inelastic processes are negligible, which is known to be a reasonable room-temperature assumption at least for molecule less than ~ 3 nm in length.

2.1 The Landauer formula

The standard way to describe transport phenomena in phase-coherent mesoscopic systems is by evaluating the Landauer formula [61, 62]. The applicability of the method holds for phase-coherent systems, in other words where a single wave function of fixed energy is sufficient to describe the electronic flow. For a mesoscopic sample the relation between the electrical conductance and the transmission properties of electrons passing through this sample can be described by the Landauer formula, which is the key formula that translates the theoretical electron transmission probability calculations obtained from the scattering formalism to the experimental quantities, such as the conductivity or the current.

Our starting point begins by considering a mesoscopic scatterer connected to two electron reservoirs (or contacts) by means of two ideal ballistic leads as shown in Figure 2.1. All inelastic relaxation processes are limited to the reservoirs [63]. The reservoirs have slightly different chemical potentials $\mu_L - \mu_R > 0$, which will drive electrons from the left to the right reservoir. Initially, I will discuss the solution for one open channel (i.e. where only one electron is allowed to travel in a given direction).

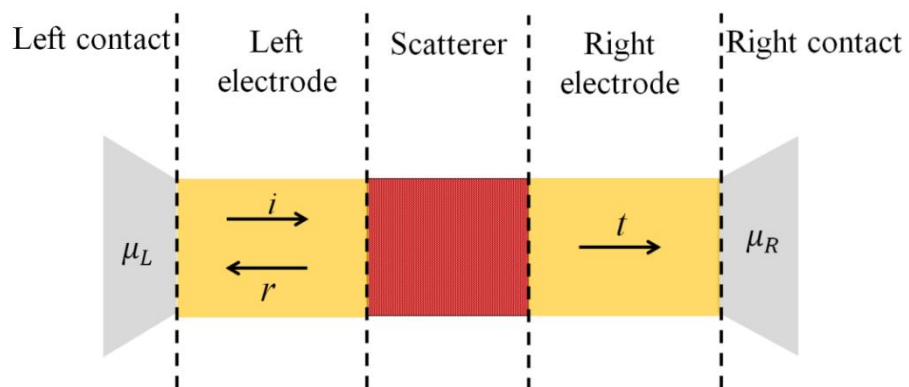


Figure 2.1: illustrates a mesoscopic scatterer connected to contacts by ballistic leads. The μ_L and μ_R represent the chemical potential in the contacts. When an incident wave packet hits the scatterer from the left then it will be transmitted with probability $T = tt^*$ and reflected with probability $R = rr^*$ where, t , t^* , r and r^* represent the transmission and the reflection amplitudes from the left to the right and vice versa. Charge conservation requires $T + R = 1$.

To calculate the current in such a system we start by analyzing the incident electric current, δI , generated by the chemical potential gradient:

$$\delta I = ev \frac{\partial n}{\partial E} (\mu_L - \mu_R) \quad (2.1.1)$$

where e is the electronic charge, v in the group velocity and $\partial n / \partial E$ is the density of states per unit length in the lead in the energy window defined by the chemical potentials of the contacts:

$$\frac{\partial n}{\partial E} = \frac{\partial n}{\partial k} \frac{\partial k}{\partial E} = \frac{\partial n}{\partial k} \frac{1}{v\hbar} \quad (2.1.2)$$

In one dimension, after including a factor of 2 for spin dependency, $\partial n / \partial k = 1 / \pi$. By substituting this into Eq. 2.1.2 we find that $\partial n / \partial E = 1 / v\hbar$. This simplifies Eq. 2.1.1 to:

$$\delta I = \frac{2e}{h} (\mu_L - \mu_R) = \frac{2e^2}{h} \delta V \quad (2.1.3)$$

where δV is the voltage generated by the potential mismatch. From Eq. 2.1.3, it is clear that in the absence of a scattering region, the conductance of a quantum wire with one open channel is $2e^2 / h$, which is approximately $77.5 \mu S$ (or in other words, a resistance of $12.9 K\Omega$). This is reasonable quantity; it typically appears on the circuit boards of everyday electrical appliances.

Now if we consider a scattering region, the current collected in the right contacts will be:

$$\delta I = \frac{2e}{h} \tau \delta V \Rightarrow \frac{\delta I}{\delta V} = G = \frac{2e^2}{h} \tau \quad (2.1.4)$$

This is widely-known Landauer formula, relating the conductance, G , of a mesoscopic scatterer to the transmission probability, τ of the electrons traveling through it. It describes the linear response conductance, hence it only holds for small bias voltages, $\delta V \approx 0$.

For the case of more than one open channel, the Landauer formula has been generalized by Büttiker [62], where the transmission coefficient is replaced by the sum of all the transmission amplitudes describing electrons incoming from the left contact and arriving to the right contact. The Landauer formula Eq. (2.1.3) for many open channels hence becomes:

$$\frac{\delta I}{\delta V} = G = \frac{2e^2}{h} \sum_{i,j} |t_{i,j}|^2 = \frac{2e^2}{h} \text{Tr}(tt^\dagger) \quad (2.1.5)$$

Where $t_{i,j}$ is the transmission amplitude describing scattering from j th channel of the left electrode to the i th channel of the right electrode. Similarly, the reflection amplitudes $r_{i,j}$ which describe scattering processes where the particle is scattered from the j th channel of the left electrode to the i th channel of the same electrode. By combining the reflection and transmission amplitudes, one obtaining the matrix which connects states coming from the left lead and vice versa, this object is called the S matrix:

$$S = \begin{pmatrix} r & t' \\ t & r' \end{pmatrix} \quad (2.1.6)$$

where r and t describe electrons coming of the left and r' and t' describe electrons coming from the right. Eq. 2.1.5 shows that r , t , r' and t' are matrices for more than one channel (Multichannel), and could be complex (in the presence of a magnetic field for example). On the other hand charge conservation demands the S matrix be unitary: $SS^\dagger = I$. The S matrix is a central object of scattering theory. It is useful not only in describing transport in the linear response regime, but also in other problems, such as adiabatic pumping [64].

2.2 Thermoelectric coefficients

In the linear-response regime, the electric current I and heat current \dot{Q} passing through a device is related to the voltage difference ΔV and temperature difference ΔT by Buttiker, Imry, Landauer, et al. [62, 65-67]. Therefore both currents are related to the temperature and potential differences through the thermoelectric coefficients G , L , M , and K [68, 69]

$$\begin{pmatrix} I \\ \dot{Q} \end{pmatrix} = \begin{pmatrix} G & L \\ M & K \end{pmatrix} \begin{pmatrix} \Delta V \\ \Delta T \end{pmatrix} \quad (2.2.1)$$

The thermoelectric coefficients L and M , in the absence of a magnetic field, are related by an Onsager relation

$$M = -LT.$$

where T is temperature. By rearranging these equations, the current relations in terms of the measurable thermoelectric coefficients: electrical resistance $R = 1/G$, thermopower $S = -\Delta V/\Delta T$, Peltier coefficients Π and the thermal conductance k can be expressed

$$\begin{pmatrix} \Delta V \\ \dot{Q} \end{pmatrix} = \begin{pmatrix} \frac{1}{G} & -\frac{L}{G} \\ \frac{M}{G} & K - \frac{LM}{G} \end{pmatrix} \begin{pmatrix} I \\ \Delta T \end{pmatrix} = \begin{pmatrix} R & S \\ \Pi & -k \end{pmatrix} \begin{pmatrix} I \\ \Delta T \end{pmatrix} \quad (2.2.2)$$

The thermopower S is defined as the potential drop due to a temperature difference in the absence of an electrical current

$$S \equiv -\left(\frac{\Delta V}{\Delta T}\right)_{I=0} = \frac{L}{G}, \quad (2.2.3)$$

the Peltier coefficient Π is defined as the heat transferred purely due to the charge current in the absence of a temperature difference

$$\Pi \equiv \left(\frac{\dot{Q}}{I}\right)_{\Delta T=0} = \frac{M}{G} = -ST, \quad (2.2.4)$$

and the thermal conductance k is defined as the heat current due to the temperature drop in the absence of an electric current

$$k \equiv -\left(\frac{\dot{Q}}{\Delta T}\right)_{I=0} = -K\left(1 + \frac{S^2 GT}{K}\right), \quad (2.2.5)$$

Therefore the evaluation of S or Π gives an idea of how well the device will act as a heat driven current generator or a current driven cooling device.

An additional quantity, the thermoelectric figure of merit, ZT [70, 71] can also be defined in terms of these measurable thermoelectric coefficients

$$ZT = \frac{S^2 GT}{k}. \quad (2.2.6)$$

From classical electronics, ZT is derived by finding the maximum induced temperature difference produced by an applied electrical current in the presence of Joule heating. Let's consider a current carrying conductor placed between two heat baths with temperatures T_L and T_R , and electrical potentials V_L and V_R respectively. The thermoelectric figure of merit can be defined by finding the maximum induced temperature difference of the conductor due to an electrical current. Defining \dot{Q} as the gain in heat from bath L to R , then from Eq. (2.2.2) that's

$$\dot{Q} = \Pi I - k \Delta T.$$

This heat transfer will cause the left bath to cool and the right bath to heat, with a result that ΔT increases. The amount of Joule heating can be expressed as $\dot{Q}_J = RI^2$, which is proportional to the electrical resistance and the square of the current. This Joule heating will also affect the temperature difference induced by the heat transfer, and therefore in the steady state case

$$\Pi I - k \Delta T = \frac{RI^2}{2}. \quad (2.2.7)$$

where, $R/2$ is the sum of two parallel resistances (internal and external resistances). After rearranging this, the temperature difference is

$$\Delta T = \frac{1}{k} \left(\Pi I - \frac{RI^2}{2} \right) \quad (2.2.8)$$

This expression shows how the temperature difference depends on the current. To find the maximum temperature difference a differentiation Eq. (2.2.8) with respect to the electric current is made

$$\frac{\partial \Delta T}{\partial I} = \frac{\Pi - IR}{k} = 0.$$

Finally by writing back $I = \Pi/R$ and substituting Eq. (2.2.4) into Eq. (2.2.8), for the maximum of the temperature different we get

$$(\Delta T)_{max} = \frac{\Pi^2}{2kR} = \frac{S^2 T^2 G}{2k}.$$

$$\frac{(\Delta T)_{max}}{T} = \frac{S^2 T^2 G}{2k} = \frac{1}{2} ZT,$$

yielding a dimensionless number that can be used to characterize the 'efficiency' of a molecular device.

2.2.1 Generalized formula for the thermoelectric coefficients

To be able to calculate all thermoelectric coefficients we still need to know \dot{Q} . Following [69] one can write a formula for the total heat current on one of the leads as the difference of the left- and right-going heat currents on the same lead. The heat current on the left lead is, where the Fermi distribution function on the left is $f_L(E)$ and on the right is $f_R(E)$ and $f_L(E) f_R(E)$ cancelled out during the derivation, yielding

$$\dot{Q}_L = \dot{Q}_L^+ - \dot{Q}_L^- = \frac{2}{h} \int_{-\infty}^{\infty} dE \tau(E) ((E - \mu_L)f_L(E) - (E - \mu_R)f_R(E)), \quad (2.2.9)$$

where \dot{Q}_L^+ (\dot{Q}_L^-) is the total heat current moving to the right (left) on the left lead. For simplicity I will define the general current I^p , which will represent the charge current if $p = 0$ or the heat current if $p = 1$

$$I^p = \begin{cases} \frac{I}{e} & p = 0 \\ \dot{Q} & p = 1 \end{cases}.$$

With this the general formula for the current is

$$\begin{aligned} I^p &= \frac{2}{h} \int_{-\infty}^{\infty} dE \tau(E) ((E - \mu_L)^p f_L(E) - (E - \mu_R)^p f_R(E)) \\ &= \frac{2}{h} \int_{-\infty}^{\infty} dE \tau(E) A(E). \end{aligned} \quad (2.2.10)$$

We now define the following quantities

$$\mu = \frac{\mu_R + \mu_L}{2}, \quad T = \frac{T_R + T_L}{2},$$

and rewrite the left and right reservoir's Fermi distributions in terms of these with

$\Delta\mu = \mu_L - \mu_R$ and $\Delta T = T_L - T_R$, yielding

$$\mu_L = \mu + \frac{\Delta\mu}{2}, \quad T_L = T + \frac{\Delta T}{2},$$

$$\mu_R = \mu - \frac{\Delta\mu}{2}, \quad T_R = T - \frac{\Delta T}{2}.$$

Therefore, the left and right Fermi distributions become

$$f_L(E) = \left(1 + e^{\frac{E - \mu - \frac{\Delta\mu}{2}}{k_B(T + \frac{\Delta T}{2})}} \right)^{-1},$$

$$f_R(E) = \left(1 + e^{\frac{E - \mu + \frac{\Delta\mu}{2}}{k_B(T - \frac{\Delta T}{2})}} \right)^{-1}.$$

Expanding Eq. (2.2.10) in a Taylor series to linear order in ΔV and ΔT yields

$$\begin{aligned} I^p &= I^p \Big|_{\substack{\Delta T=0 \\ \Delta\mu=0}} + \frac{\partial I^p}{\partial \Delta\mu} \Big|_{\substack{\Delta T=0 \\ \Delta\mu=0}} \Delta\mu + \frac{\partial I^p}{\partial \Delta T} \Big|_{\substack{\Delta T=0 \\ \Delta\mu=0}} \Delta T \\ &= \frac{2}{h} \int_{-\infty}^{\infty} dE \tau(E) \left[A(E) \Big|_{\substack{\Delta T=0 \\ \Delta\mu=0}} + \frac{\partial A(E)}{\partial \Delta\mu} \Big|_{\substack{\Delta T=0 \\ \Delta\mu=0}} \Delta\mu + \frac{\partial A(E)}{\partial \Delta T} \Big|_{\substack{\Delta T=0 \\ \Delta\mu=0}} \Delta T \right]. \end{aligned} \quad (2.2.11)$$

The first term in the Taylor expansion is zero, and the two remaining terms reduce down to the derivatives of the two Fermi distribution functions

$$\frac{\partial A(E)}{\partial \Delta\mu} \Big|_{\substack{\Delta T=0 \\ \Delta\mu=0}} = -(E - \mu)^p \frac{\partial f(E)}{\partial(E)},$$

$$\frac{\partial A(E)}{\partial \Delta T} \Big|_{\substack{\Delta T=0 \\ \Delta\mu=0}} = \frac{(E - \mu)^{p+1}}{T} \frac{\partial f(E)}{\partial(E)},$$

where $f(E) = \left(1 + e^{\frac{E - \mu}{k_B T}} \right)^{-1}$ is the Fermi distribution function. Substituting these terms into the Taylor expansion (2.2.11) and writing the chemical potential in terms of the applied electrical bias $\Delta\mu = e\Delta V$, the currents in the linear regime can be expressed as

$$\begin{aligned} I^p &= \frac{2e}{h} \int_{-\infty}^{\infty} dE \tau(E) (E - \mu_L)^p (-1) \frac{\partial f(E)}{\partial(E)} \Delta V \\ &\quad + \frac{2}{h} \int_{-\infty}^{\infty} dE \tau(E) \frac{(E - \mu)^{p+1}}{T} (-1) \frac{\partial f(E)}{\partial(E)} \Delta T \end{aligned} \quad (2.2.12)$$

From Eq. (2.2.12) the thermoelectric coefficients G , L , M and K are

$$G = \frac{2e^2}{h} \int_{-\infty}^{\infty} dE \tau(E) (-1) \frac{\partial f(E)}{\partial(E)}, \quad (2.2.13)$$

$$L = \frac{2e}{h} \int_{-\infty}^{\infty} dE \tau(E) \frac{(E - \mu)}{T} (-1) \frac{\partial f(E)}{\partial(E)}, \quad (2.2.14)$$

$$M = \frac{2e}{h} \int_{-\infty}^{\infty} dE \tau(E) (E - \mu) (-1) \frac{\partial f(E)}{\partial(E)}, \quad (2.2.15)$$

$$K = \frac{2}{h} \int_{-\infty}^{\infty} dE \tau(E) \frac{(E - \mu)^2}{T} (-1) \frac{\partial f(E)}{\partial(E)}, \quad (2.2.16)$$

An interesting point that the integrals in Eqs. (2.2.13)-(2.2.16) look like the n^{th} central moments L_n of a probability function $P(E)$ defined by

$$P(E) = -\tau(E) \frac{\partial f(E)}{\partial(E)}, \quad (2.2.17)$$

but note that $P(E)$ is not a real probability distribution function, since

$$\int_{-\infty}^{\infty} dE P(E) \neq 1.$$

Let's define the following quantity

$$L_n = \int_{-\infty}^{\infty} dE (E - \mu)^n P(E) = \langle (E - \mu)^n \rangle. \quad (2.2.18)$$

Substituting Eq. (2.2.18) into Eqs. (2.2.13)-(2.2.16), the measurable thermoelectric coefficients can be expressed as

$$G = \frac{2e^2}{h} L_0, \quad (2.2.19)$$

$$S = -\frac{1}{eT} \frac{L_1}{L_0}, \quad (2.2.20)$$

$$\Pi = -\frac{1}{e} \frac{L_1}{L_0}, \quad (2.2.21)$$

$$k = -\frac{2}{hT} \left(L_2 - \frac{L_1^2}{L_0} \right), \quad (2.2.22)$$

and then Eq. (2.2.1) can be written as

$$\begin{pmatrix} I \\ \dot{Q} \end{pmatrix} = \frac{1}{h} \begin{pmatrix} e^2 L_0 & \frac{e}{T} L_1 \\ e L_1 & \frac{1}{T} L_2 \end{pmatrix} \begin{pmatrix} \Delta V \\ \Delta T \end{pmatrix} \quad (2.2.23)$$

where T is the reference temperature.

For the spin-dependent thermoelectric coefficients, since transport through a system is assumed to be phase-coherent, even at room temperature, the coefficients L_n are given by

$$L_n = L_n^\uparrow + L_n^\downarrow \quad (n = 0, 1, 2), \text{ where [72]}$$

$$L_n^\sigma = \int_{-\infty}^{\infty} (E - E_F)^n \tau^\sigma(E) \left(-\frac{\partial f(E, T)}{\partial E} \right) dE \quad (2.2.24)$$

In the expression in Eq. (2.2.24), $\tau^\sigma(E)$ is the transmission coefficient for electrons of energy E , spin of $\sigma = [\uparrow, \downarrow]$ passing through the molecule from one electrode to the other [68] and $f(E, T)$ is Fermi distribution function defined as $f(E, T) = [e^{(E-E_F)/k_B T} + 1]^{-1}$ where k_B is Boltzmann's constant. Eq. (2.2.23) can be rewritten in terms of the electrical conductance (G), thermopower (S), Peltier coefficient (Π), and the electronic contribution to the thermal conductance (κ_e):

$$\begin{pmatrix} \Delta V \\ \dot{Q} \end{pmatrix} = \begin{pmatrix} 1/G & S \\ \Pi & \kappa_e \end{pmatrix} \begin{pmatrix} I \\ \Delta T \end{pmatrix} \quad (2.2.25)$$

where κ_e represents the electronic contribution to the thermal conductance which is given by

$$\kappa_e = \frac{1}{hT} \left(L_2 - \frac{(L_1)^2}{L_0} \right) \quad (2.2.26)$$

From the above expressions, the electronic thermoelectric figure $ZT_e = S^2 GT / \kappa_e$ is given by

$$ZT_e = \frac{(L_1)^2}{L_0 L_2 - (L_1)^2} \quad (2.2.27)$$

For E close to E_F , if $\tau(E)$ varies approximately linearly with E on the scale of $k_B T$ then these formulae take the form [73]

$$G(T) \approx \left(\frac{2e^2}{h}\right) \tau(E_F), \quad (2.2.28)$$

$$S(T) \approx -\alpha eT \left(\frac{d \ln \tau(E)}{dE}\right)_{E=E_F}, \quad (2.2.29)$$

$$\kappa_e \approx L_0^g T G, \quad (2.2.30)$$

where $\alpha = \left(\frac{k_B}{e}\right)^2 \frac{\pi^2}{3}$ is the Lorentz number = $2.44 \times 10^{-8} \text{ W}\Omega\text{K}^{-2}$. Eq. (2.2.29) demonstrates that S is enhanced by increasing the slope of $\ln \tau(E)$ near $E=E_F$ and hence it is of interest to explore systems on the nanoscale where the gradient of $\tau(E)$ changes close to Fermi energy E_F which in the case of molecular transport involves moving resonances close to the Fermi energy.

2.3 Scattering Theory

2.3.1 One dimensional (1-D) linear crystalline lattice

To give a clear outline of the methodology used to simulate a complicated scattering matrix; it is useful to analyze a simple one-dimension system. The following discussions in this section will be about the form of the Green's function. I am going to consider a simple tight-binding approach to get a qualitative understanding of electronic structure calculation in periodic systems, as shown in Figure (2.3.1).

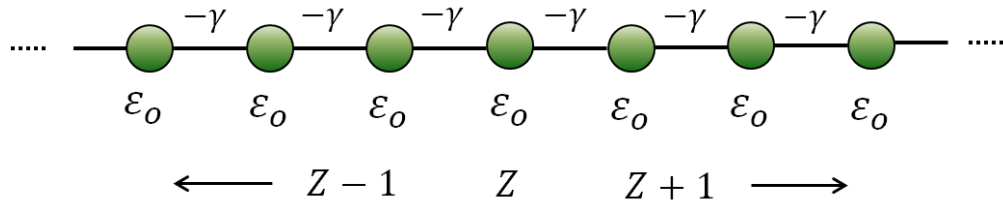


Figure 2.3.1: illustrates tight-binding model of a one-dimensional perfect lattice with on-site ε_0 and hopping γ energies, respectively, where Z is the label of the orbital.

The matrix form of the Hamiltonian is written simply:

$$H = \begin{pmatrix} \ddots & -\gamma & & & \\ -\gamma & \varepsilon_o & -\gamma & & \\ & -\gamma & \varepsilon_o & -\gamma & \\ & & -\gamma & \varepsilon_o & -\gamma \\ & & & -\gamma & \ddots \end{pmatrix} \quad (2.3.1)$$

where ε_o is on-site energies and γ is real hopping parameters.

According to the time independent Schrödinger equation (Eq. 2.3.2) which can be expanded at a lattice site Z in terms of the energy and wavefunction Ψ_Z (Eq. 2.3.3).

$$(EI - H)\Psi = 0 \quad (2.3.2)$$

Taking a single row:

$$\varepsilon_o \Psi_Z - \gamma \Psi_{Z+1} - \gamma \Psi_{Z-1} = E \Psi_Z \quad (2.3.3)$$

For this periodic lattice, the wave function takes the form of a propagating Bloch state Eq. (2.2.4)

$$\Psi_Z = \frac{1}{\sqrt{v}} e^{ikz} \quad (2.3.4)$$

$$E = \varepsilon_o - 2\gamma \cos k \quad (2.3.5)$$

here we introduce the quantum number, k , which is commonly referred to as the wavenumber. Another useful quantity, group velocity, can be given by differentiating the dispersion relation $E(k)$:

$$v = \frac{1}{\hbar} \frac{\partial E}{\partial k}. \quad (2.3.6)$$

In the z direction the retarded Green's function can be written as $g(z, z')$ which is closely related to the wavefunction and is in the fact the solution to a second order differential equation, similar to that of the Schrödinger equation.

$$(E - H)g(z, z') = \delta_{z, z'} \quad (2.3.7)$$

From a physical view point, the retarded Green's function $g(z, z')$ describes the response of a system at a point z due to an excitation (a source) at a point z' . Intuitively, we expect such a source to give rise to two waves, propagating outwards from the point of excitation, with the amplitudes A^+ and A^- as shown in Figure 2.3.2.

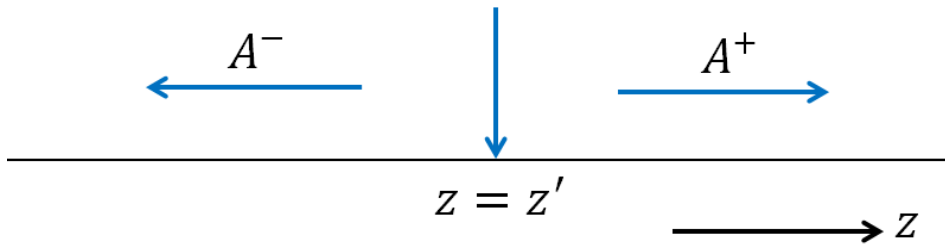


Figure 2.3.2: shows the retarded Green's function of an infinite one-dimensional lattice. The source (excitation point) at $z = z'$ causes the wave to propagate left and right with amplitudes A^- and A^+ respectively.

These propagating waves can be expressed simply as:

$$\begin{aligned} g(z, z') &= A^+ e^{ikz} & z \geq z' \\ g(z, z') &= A^- e^{-ikz} & z \leq z' \end{aligned} \quad (2.3.8)$$

The solution satisfies Eq. 2.3.7 at every point but $z = z'$. To overcome this, the Green's function must be continuous, so we equate the two at $z = z'$:

$$|g(z, z')|_{z=z'^-} = |g(z, z')|_{z=z'^+} \quad (2.3.9)$$

$$A^+ e^{ikz'} = A^- e^{-ikz'} \quad (2.3.10)$$

To find the solution, we guess

$$A^+ = \beta e^{-ikz'} \quad (2.3.11)$$

$$A^- = \beta e^{ikz'} \quad (2.3.12)$$

From Eqs (2.3.8) and (2.3.10) we get

$$g(z, z') = \beta e^{ik|z-z'|} \quad (2.3.13)$$

To obtain the constant β , we use Eq. (2.3.7) which for $z = z'$ gives

$$\begin{aligned} (\varepsilon_0 - E)\beta - \gamma\beta e^{ik} - \gamma\beta e^{-ik} &= -1 \\ \gamma\beta(2 \cos k - 2e^{ik}) &= -1 \end{aligned}$$

$$\beta = \frac{1}{2i\gamma \sin k} = \frac{1}{i\hbar v}$$

where $\hbar v = \frac{\partial E}{\partial k} = 2i\gamma \sin k$.

$$A^+ e^{ikz'} \frac{\hbar v}{2k} 2ik = 1 \rightarrow A^+ e^{ikz'} = \frac{1}{i\hbar v} \quad (2.3.14)$$

And also, the retarded Green's function can be written

$$g^R(z, z') = \frac{1}{i\hbar v} e^{ik|z-z'|} \quad (2.3.15)$$

where the group velocity, found from the dispersion relation, is:

$$v = \frac{1}{\hbar} \frac{\partial E(k)}{\partial k} = 2\gamma \sin k \quad (2.3.16)$$

A more thorough derivation can be found in the literature [63, 74, 75]. It is also worth noting that another solution can be found to this problem. Above, I have shown the retarded Green's function, $g^R(z, z')$. The advanced Green's function, $g^A(z, z')$, is an equally valid solution:

$$g^A(z, z') = \frac{i}{\hbar v} e^{-ik|z-z'|} \quad (2.3.17)$$

Rather than describing outgoing waves from the source point, $z = z'$, as the retarded Green's function does, the advanced Green's function describes two incoming waves that disappear

at sink, $z = z'$. In this thesis, I will use the retarded Green's function and for the sake of simplicity, drop the R from its representation. So $g(z, z') = g^R(z, z')$.

Since the probability of an electron to propagate between two points on this perfect lattice will be unity if its energy is within $\varepsilon_0 - 2\gamma$ and $\varepsilon_0 + 2\gamma$, this system is of little use to us. However, if some defect is created within the lattice, this will act as a scatterer and the transmission coefficient will be modified.

2.3.2 One dimensional (1-D) scattering

To understand the generalized methodology, it is useful to describe the scattering matrix of a simple system. In this section I will introduce two pieces of one dimensional tight binding semi-infinite leads connected by a coupling element β . Both leads are equal with ε_0 on-site potential and $-\gamma$ hopping elements between the sites as shown below, in Figure 2.3.3. To make our solution in the simplest way, I will derive the transmission and reflection coefficients for a particle traveling from the left lead towards the scattering region, however, it turns out that all scattering processes can be reduced back to this topology of one-dimensional setups.

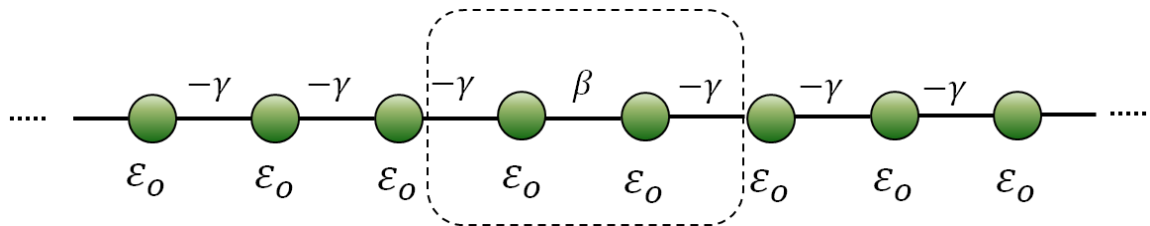


Figure 2.3.3: illustrates a simple tight-binding model of a one-dimensional scatterer attached to one dimensional leads, where ε_0 is on-site energy, $-\gamma$ is hopping elements between the sites and β is a coupling element between two pieces of semi-infinite chains.

The corresponding Hamiltonian is an infinite matrix of the form:

$$H = \begin{pmatrix} \ddots & -\gamma & & & & & \\ -\gamma & \varepsilon_0 & -\gamma & & & & \\ & -\gamma & \varepsilon_0 & \beta & & & \\ & & -\beta & \varepsilon_0 & -\gamma & & \\ & & & -\gamma & \varepsilon_0 & -\gamma & \\ & & & & -\gamma & \ddots & \end{pmatrix} = \begin{pmatrix} H_L & V_c \\ V_c^\dagger & H_R \end{pmatrix} \quad (2.3.18)$$

Here, H_L and H_R denote Hamiltonians for the leads which are the semi-infinite equivalent of the Hamiltonians shown in Eq. (2.3.18). V_c denotes the coupling parameter.

For real γ , the dispersion relation corresponding to the leads introduced above was given in Eq. (2.3.5) and group velocity was given in Eq. (2.3.16):

$$E(k) = \varepsilon_0 - 2\gamma \cos k \quad (2.3.19)$$

$$v = \frac{1}{\hbar} \frac{\partial E(k)}{\partial k} \quad (2.3.20)$$

In order to obtain the scattering amplitudes we need to calculate the Green's function of the system. The Green's function for a system obeying the Schrödinger's equation

$$(E - H)\psi = 0, \quad (2.3.21)$$

is defined via Green's function which is satisfied the following equation

$$(EI - H)G = I, \quad (2.3.22)$$

where G, H are matrices and I represents the unit matrix. The equation 2.3.22 produced two matrices which are $[(EI - H)G]$ and $[I]$ and these end up with the formal solution can be written as

$$G = (E - H)^{-1}, \quad (2.3.23)$$

This formal solution Eq. (2.3.23) possesses the singularity behaviour (sometimes it is called a pole) as shown in figure (2.3.4) when the energy E is equal to an eigenvalue of the Hamiltonian H . To get rid of this singularity one considers in practice the limit

$$G_{\pm} = \lim_{\eta \rightarrow 0} (E - H \pm i\eta)^{-1}, \quad (2.3.24)$$

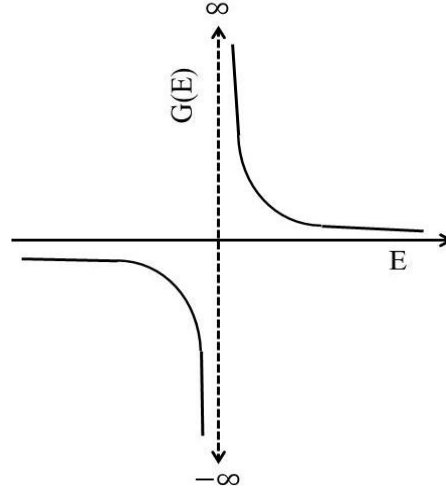


Figure 2.3.4: shows the singularity behaviour of function (Eq 2.3.24).

to make the solution of (Eq 2.3.22). Here η is a positive number, and G_+ (G_-) is the retarded (advanced) Green's function, respectively. In this thesis I will only use retarded Green's functions and hence choose the $-$ sign.

The retarded Green's function for an infinite, one dimensional chain with the same parameters is defined in Eq.(2.3.15):

$$g_{jl} = \frac{1}{i\hbar v} e^{ik|j-l|} \quad (2.3.25)$$

where j, l are the label of the sites in the chain. In order to obtain the Green's function of a semi-infinite lead we need to introduce the appropriate boundary conditions. In this case, the lattice is semi-infinite, so the chain must terminate at a given point, i_0 , so that all points for which $i \geq i_0$ are missing. This is achieved by adding a wave function to the Green's function to mathematically represent this condition. The wavefunction in this case is:

$$\psi_{jl}^{i_0} = -\frac{e^{ik(j+l-2i_0)}}{i\hbar v} \quad (2.3.26)$$

The Green's function $g_{jl} = g_{jl}^{\infty} + \psi_{jl}^{i_0}$ will have the following simple form at the boundary $j = l = i_0$:

$$g_{i_0, i_0} = -\frac{e^{ik}}{\gamma} \quad (2.3.27)$$

If we consider the case of decoupled leads, $\beta = 0$, the total Green's function of the system will simply be given by the decoupled Green's function:

$$g = \begin{pmatrix} -\frac{e^{ik}}{\gamma} & 0 \\ 0 & -\frac{e^{ik}}{\gamma} \end{pmatrix} = \begin{pmatrix} g_L & 0 \\ 0 & g_R \end{pmatrix} \quad (2.3.28)$$

If we now switch on the interaction, then in order to get the Green's function of the coupled system, \hat{G} , we need to use Dyson's equation:

$$\hat{G}^{-1} = (g^{-1} - V) \quad (2.3.29)$$

Here the operator V describing the interaction connecting the two leads will have the form:

$$V = \begin{pmatrix} 0 & V_c \\ V_c^\dagger & 0 \end{pmatrix} = \begin{pmatrix} 0 & \beta \\ \beta^* & 0 \end{pmatrix} \quad (2.3.30)$$

The solution to Dyson's equation, Eq.(3.3.29) reads:

$$\hat{G} = \frac{1}{\beta^2 - \gamma^2 e^{-2ik}} \begin{pmatrix} \gamma e^{-ik} & \beta \\ \beta^* & \gamma e^{-ik} \end{pmatrix} \quad (2.3.31)$$

The only remaining step is to calculate the transmission, t , and reflection, r , amplitudes from the Green's function Eq.(2.3.31). This is done by making use of the Fisher-Lee relation [62, 76] which relates the scattering amplitudes of a scattering problem to the Green's function of the problem. The Fisher-Lee relations in this case read:

$$r = \hat{G}_{1,1} i\hbar v - 1 \quad (2.3.32)$$

$$t = \hat{G}_{1,2} i\hbar v e^{ik} \quad (2.3.33)$$

These amplitudes correspond to particles incident from the left. If one would consider particles coming from the right than similar expressions could be recovered for the transmission, t' , and reflection, r' , amplitudes.

Since we are now in the possession of the full scattering matrix we can use the Landauer formula Eq.(2.1.4) to calculate the zero bias conductance. The procedure by which this analytical solution for the conductance of a one-dimensional scatterer was found can be generalized for more complex geometries. So to briefly summarize the steps:

1. The first step was to calculate the Green's function describing the surface sites of the leads.
2. The total Green's function in the presence of a scatterer is obtained by Dyson's equation.
3. The Fisher-Lee relation gives us the scattering matrix from the Green's function.
4. Using the Landauer formula, we can then find the zero-bias conductance.

Later on we will see that the setup considered in this section, despite the fact that it looks simple, is quite general.

2.4 Generalization of the above scattering formalism

A generalized approach to transport calculations will be shown in this section. This approach follows the derivation of Lambert, presented in [77-79]. This is similar to the previous approach. First the surface Green's function of crystalline leads is computed, then the technique of decimation is introduced to reduce the dimensionality of the scattering region and finally the scattering amplitudes are recovered by means of a generalization of the Fisher-Lee relation.

2.4.1 A doubly infinite Hamiltonian and Green's function of the electrodes.

To obtain a qualitative understanding of the electronic structure in periodic systems, we study a general doubly-infinite crystalline electrode; this system can be described within the tight-binding approximation in terms of two Hamiltonians. If we consider that the direction of electron transport is along the z axes, then the system could include a periodic sequence of slices, given by an intra-slice matrix H_0 which represents the structure of each slice and the inter-slice nearest-neighbour matrix H_1 which represents the hopping elements between all orbitals within the slices. The system described in this way could be a single atom in an atomic chain, an atomic plane or a more complex cell.

In general, the spectrum of an infinite Hamiltonian is continuous because the electrodes are crystalline. We first introduce the structure of a doubly-infinite one-dimensional (1-D) lead in Figure 2.4.1

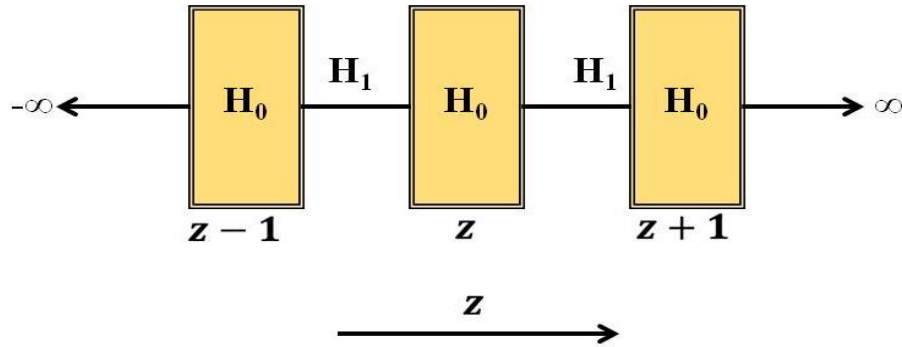


Figure 2.4.1: Illustrates an example of doubly-infinite generalized electrodes with one dimensional (1-D) structure. It shows that H_0 and H_1 are the Hamiltonians and hopping energies respectively. The direction z is defined the periodicity along one direction.

We start with a total Hamiltonian operator \hat{H} whose structure can be written as an infinite block tri-diagonal matrix of the form

$$H = \begin{pmatrix} \ddots & H_1 & 0 & 0 \\ H_1^\dagger & H_0 & H_1 & 0 \\ 0 & H_1^\dagger & H_0 & H_1 \\ 0 & 0 & H_1^\dagger & \ddots \end{pmatrix}, \quad (2.4.1)$$

where H_0 and H_1 are in general complex matrices and the only restriction is that the full Hamiltonian, H , should be Hermitian. Our first goal in this section is to calculate the Green's function of such a lead for general H_l and H_0 . In order to calculate the Green's function, one has to calculate the spectrum of the Hamiltonian by solving the Schrödinger equation of the lead.

$$H_0\psi_z - H_1\psi_{z+1} - H_1^\dagger\psi_{z-1} = E\psi_z \quad (2.4.2)$$

where ψ_z is a column vector whose elements specify the amplitude of the wave function on each degree of freedom within a slice located at point z along the z axis. That means equation (2.4.2) is satisfied for all z to $\pm\infty$, and the on-site wave function can be represented in Bloch form consisting of a product of a propagating plane wave and a wavefunction, ϕ_k , which is perpendicular to the transport direction, z . If the intra-layer Hamiltonian, H_0 , has dimensions $M \times M$ (or in other words consists of M site energies and their respective hopping elements), then the perpendicular wavefunction, ϕ_k , will have M degrees of freedom and take the form of a $1 \times M$ dimensional vector. So the wave function, ψ_z , takes the form:

$$\psi_z = \sqrt{n_k} e^{ikz} \phi_k \quad (2.4.3)$$

where, n_k is an arbitrary normalization parameter. Substituting this into the Schrödinger equation Eq.(2.4.2) gives:

$$(H_0 + e^{ikz}H_1 + e^{-ikz}H_1^\dagger - E) \phi_k = 0 \quad (2.4.4)$$

Typically, to find the band structure for such a problem, one would select values of k and calculate the eigenvalues at that point, $E = E_l(k)$, where $l = 1, \dots, M$. Here, l denotes the

band index. For each value of k , there will be M solutions to the eigenproblem, and so M energy values. In this way, by selecting multiple values for k , it is relatively simple to build up a band structure. In a scattering problem, the problem is approached from the opposite direction; instead of finding the values of E at a given k , we find the values of k at a given E . In order to accomplish this, a root-finding method might have been used, but this would have required an enormous numerical effort, since the wave numbers are in general complex. Instead, we can write down an alternative eigenvalue problem in which the energy is the input and the wave numbers are the result by introducing the function:

$$\vartheta_k = e^{ikz} \phi_k \quad (2.4.5)$$

and combining it with

$$\begin{pmatrix} H_1^{-1}(H_0 - E) & -H_1^{-1}H_1^\dagger \\ I & 0 \end{pmatrix} \begin{pmatrix} \phi_k \\ \vartheta_k \end{pmatrix} = e^{ikz} \begin{pmatrix} \phi_k \\ \vartheta_k \end{pmatrix} \quad (2.4.6)$$

For a layer Hamiltonian, H_0 , of size $M \times M$, Eq(2.4.6) will yield $2M$ eigenvalues, e^{ikz} and eigenvectors, ϕ_k , of size M . We can sort these states into four categories according to whether they are propagating or decaying and whether they are left going or right going. A state is propagating if it has a real wave number, k_l , and is decaying if it has an imaginary part. If the imaginary part of the wave number is positive then we say it is a left decaying state, if it has a negative imaginary part it is a right decaying state. The propagating states are sorted according to the group velocity of the state defined by

$$v_{k_l} = \frac{1}{\hbar} \frac{\partial E_{k,l}}{\partial k} \quad (2.4.7)$$

If the group velocity, v_{k_l} , of the state is positive than it is a right propagating state if it is negative than it is a left propagating state. To summarize

	Left	Right
Decaying	$Im(k_l) > 0$	$Im(k_l) < 0$
Propagating	$Im(k_l) = 0, v_{k_l} < 0$	$Im(k_l) = 0, v_{k_l} > 0$

Table 2.4.1: Sorting the eigenstates into left and right propagating or decaying states according to the wave number and group velocity.

For convenience, from now on I will denote the k_l wave numbers which belong to the left propagating/decaying set of wave numbers by \bar{k}_l and the right propagating/decaying wave numbers will remain plainly k_l . Thus, ϕ_k is a wave function associated to a "right" state and $\bar{\phi}_k$ is associated to a "left" state. If H_l is invertible, there must be exactly the same number, M , of left and right going states. It is clear that if H_l is singular, the matrix in Eq.(2.4.6) cannot be constructed, since it relies of the inversion of H_l . However, any one of several methods can be used to overcome this problem. The first [78] uses the decimation technique to create an effective, non-singular H_l . Another solution might be to populate a singular H_l with small random numbers, hence introducing an explicit numerical error. This method is reasonable as the introduced numerical error can be as small as the numerical error introduced by decimation. Another solution is to re-write Eq.(2.4.6) such that H_l need not be inverted:

$$\begin{pmatrix} (H_0 - E) & -H_1^\dagger \\ I & 0 \end{pmatrix} \begin{pmatrix} \phi_k \\ \vartheta_k \end{pmatrix} = e^{ikz} \begin{pmatrix} H_1 & 0 \\ 0 & I \end{pmatrix} \begin{pmatrix} \phi_k \\ \vartheta_k \end{pmatrix} \quad (2.4.8)$$

However, solving this generalized eigenproblem is more computationally expensive. Any of the aforementioned methods work reasonably in tackling the problem of a singular H_1 matrix, and so can the condition that there must be exactly the same number, M , of left and right going states, whether H_1 is singular or not.

The solutions to the eigenproblem Eq.(2.4.4) at a given energy, E , will not generally form an orthogonal set of states. This is crucial, since we will have to deal with the nonorthogonality

when constructing the Green's function. It is, therefore, necessary to introduce the duals to ϕ_{k_l} and $\phi_{\bar{k}_l}$ in such a way that they obey:

$$\tilde{\phi}_{k_j} \phi_{k_j} = \tilde{\phi}_{\bar{k}_l} \phi_{\bar{k}_l} = \delta_{ij} \quad (2.4.9)$$

This yields the generalized completeness relation:

$$\sum_{l=1}^M \tilde{\phi}_{k_l} \phi_{k_l} = \sum_{l=1}^M \tilde{\phi}_{\bar{k}_l} \phi_{\bar{k}_l} = I \quad (2.4.10)$$

Once we are in possession of the whole set of eigenstates at a given energy we can calculate the Green's function first for the infinite system and then, by satisfying the appropriate boundary conditions, for the semi-infinite leads at their surface. Since the Green's function satisfies the Schrödinger equation when $z \neq z'$ we can build up the Green's function from the mixture of the eigenstates ϕ_{k_l} and $\phi_{\bar{k}_l}$

$$g(z, z') = \begin{cases} \sum_{l=1}^M \phi_{k_l} e^{ik_l(z-z')} \omega_{k_l} & z \geq z' \\ \sum_{l=1}^M \phi_{\bar{k}_l} e^{i\bar{k}_l(z-z')} \omega_{\bar{k}_l} & z \leq z' \end{cases} \quad (2.4.11)$$

where the M -component vectors ω_{k_l} and $\omega_{\bar{k}_l}$ are to be determined, and the vectors ϕ_k and ω_{k_l} contain the degrees of freedom in the transverse direction.

The task now is to obtain the ω vectors. As in section (2.4.1), we know that Eq. (2.4.11) must be continuous at $z = z'$ and should fulfil the Green's Eq. (2.3.6). The first condition is expressed as:

$$\sum_{l=1}^M \phi_{k_l} \omega_{k_l} = \sum_l \phi_{\bar{k}_l} \omega_{\bar{k}_l} \quad (2.4.12)$$

and the second:

$$\sum_{l=1}^M [(E - H_0) \phi_{k_l} \omega_{k_l} + H_1 \phi_{k_l} e^{ik_l} \omega_{k_l} + H_1^\dagger \phi_{\bar{k}_l} e^{i\bar{k}_l} \omega_{\bar{k}_l}] = I$$

These two conditions imply the following equation:

$$\begin{aligned} \sum_{l=1}^M [(E - H_0) \phi_{k_l} \omega_{k_l} + H_1 \phi_{k_l} e^{ik_l} \omega_{k_l} + H_1^\dagger \phi_{\bar{k}_l} e^{i\bar{k}_l} \omega_{\bar{k}_l} + H_1^\dagger \phi_{k_l} e^{ik_l} \omega_{k_l} - H_1^\dagger \phi_{k_l} e^{ik_l} \omega_{k_l}] &= I \\ \sum_{l=1}^M [H_1^\dagger \phi_{\bar{k}_l} e^{i\bar{k}_l} \omega_{k_l} - H_1^\dagger \phi_{k_l} e^{ik_l} \omega_{k_l}] + \sum_{l=1}^M [(E - H_0) + H_1 e^{ik_l} + H_1^\dagger e^{i\bar{k}_l}] \phi_{k_l} \omega_{k_l} &= I \end{aligned}$$

and since, from the Schrödinger equation Eq.(2.4.4), we know that:

$$\sum_{l=1}^M [(E - H_0) + H_1 e^{ik_l} + H_1^\dagger e^{i\bar{k}_l}] \phi_{k_l} = 0 \quad (2.4.13)$$

this yields:

$$\sum_{l=1}^M H_1^\dagger (\phi_{\bar{k}_l} e^{-i\bar{k}_l} \omega_{\bar{k}_l} - \phi_{k_l} e^{-ik_l} \omega_{k_l}) = I \quad (2.4.14)$$

Now let us make use of the dual vectors defined in Eq.(2.4.9). Multiplying Eq.(3.4.14) by

$\tilde{\phi}_{k_p}$ we get:

$$\sum_{l=1}^M \tilde{\phi}_{k_p} \phi_{\bar{k}_l} \omega_{\bar{k}_l} = \omega_{k_p} \quad (2.4.15)$$

and similarly multiplying by $\tilde{\phi}_{\bar{k}_p}$ gives:

$$\sum_{l=1}^M \tilde{\phi}_{\bar{k}_p} \phi_{k_l} \omega_{k_l} = \omega_{\bar{k}_p} \quad (2.4.16)$$

Using the continuity equation Eq.(2.4.12), Eq.(2.4.15), Eq.(2.4.16), then the Green's equation Eq.(2.4.13) becomes:

$$\sum_{l=1}^M \sum_{p=1}^M H_1^\dagger (\phi_{k_l} e^{-ik_l} \tilde{\phi}_{k_l} - \phi_{\bar{k}_l} e^{-i\bar{k}_l} \tilde{\phi}_{\bar{k}_l}) \phi_{\bar{k}_p} \omega_{\bar{k}_p} = I \quad (2.4.17)$$

From which follows:

$$\sum_{l=1}^M [H_1^\dagger (\phi_{k_l} e^{-ik_l} \tilde{\phi}_{k_l} - \phi_{\bar{k}_l} e^{-i\bar{k}_l} \tilde{\phi}_{\bar{k}_l})]^{-1} = \sum_{p=1}^M \phi_{\bar{k}_p} \omega_{\bar{k}_p} = \sum_{p=1}^M \phi_{k_p} \omega_{k_p} \quad (2.4.18)$$

This immediately gives us an expression for ω_k :

$$\omega_k = \tilde{\phi}_{k_l} \nu^{-1} \quad (2.4.19)$$

Where ν is defined as:

$$\nu = \sum_{l=1}^M H_1^\dagger (\phi_{k_l} e^{-ik_l} \tilde{\phi}_{k_l} - \phi_{\bar{k}_l} e^{-i\bar{k}_l} \tilde{\phi}_{\bar{k}_l}) \quad (2.4.20)$$

The wave vector, k , in Eq.(2.4.19) refers to both left and right type of states. Substituting Eq.(2.4.19) into Eq.(2.4.11) we get the Green's function of an infinite system:

$$g(z, z') = \begin{cases} \sum_{l=1}^M \phi_{k_l} e^{ik_l(z-z')} \tilde{\phi}_{k_l} \nu^{-1} & z \geq z' \\ \sum_{l=1}^M \phi_{\bar{k}_l} e^{i\bar{k}_l(z-z')} \tilde{\phi}_{\bar{k}_l} \nu^{-1} & z \leq z' \end{cases} \quad (2.4.21)$$

In order to get the Green's function for a semi-infinite lead we have to add a wave function to the Green's function in order to satisfy the boundary conditions at the edge of the lead, as with the one dimensional case. The boundary condition here is that the Green's function must vanish at a given place, $z = z'$. In order to achieve this we simply add:

$$\Delta = \sum_{l,p=1}^M \phi_{\bar{k}_l} e^{i\bar{k}_l(z-z_0)} \tilde{\phi}_{\bar{k}_l} \phi_{k_p} e^{ik_p(z-z_0)} \tilde{\phi}_{k_p} \nu^{-1} \quad (2.4.22)$$

to the Green's function, Eq.(2.4.21), $g = g^\infty + \Delta$. This yields the surface Green's function for a semi-infinite lead going left:

$$g_L = \left(I - \sum_{l,p} \phi_{\bar{k}_l} e^{-i\bar{k}_l} \tilde{\phi}_{\bar{k}_l} \phi_{k_p} e^{ik_p} \tilde{\phi}_{k_p} \right) v^{-1} \quad (2.4.23)$$

and going right;

$$g_R = \left(I - \sum_{l,p} \phi_{\bar{k}_l} e^{i\bar{k}_l} \tilde{\phi}_{\bar{k}_l} \phi_{k_p} e^{-ik_p} \tilde{\phi}_{k_p} \right) v^{-1} \quad (2.4.24)$$

So now we have a versatile method for calculating the surface Green's functions Eqs.(2.4.23) and (2.4.24) for a semi-infinite crystalline electrode using the numerical approach in Eq (2.4.6). The next step is to apply this to a scattering problem.

2.4.2 Effective Hamiltonian of the Scattering Region

In section (2.3.2) I have discussed that, given a coupling matrix between the surfaces of the semi-infinite leads, the Dyson Equation (2.3.31) can be used to calculate the Green's function of the scatterer. However, the scattering region is not generally described simply as a coupling matrix between the surfaces. Therefore, it is useful to use the decimation method to reduce the Hamiltonian down to such a structure. Other methods have been developed [80, 81], but in this thesis I will use the decimation method.

Consider again the Schrödinger equation

$$\sum_j H_{ij} \Psi_j = E \Psi_i \quad (2.4.25)$$

If we separate the l th degree of freedom in the system:

$$H_{il} \Psi_l + \sum_{j \neq l} H_{ij} \Psi_j = E \Psi_i \quad i \neq l \quad (2.4.26)$$

$$H_{ll} \Psi_l + \sum_{j \neq l} H_{lj} \Psi_j = E \Psi_l \quad i = l \quad (2.4.27)$$

From Eq. (2.4.27) we can express Ψ_l as:

$$\Psi_l = \sum_{j \neq l} \frac{H_{lj} \Psi_j}{E - H_{ll}} \quad (2.4.28)$$

If we then substitute Eq. (2.4.28) into Eq. (3.4.26) we get:

$$\sum_{j \neq l} \left[H_{ij} \Psi_j + \frac{H_{il} H_{lj} \Psi_j}{E - H_{ll}} \right] = E \Psi_i \quad i \neq l \quad (2.4.29)$$

So we can think of Eq. (2.4.29) as an effective Schrödinger equation where the number of degrees of freedom is decreased by one compared to Eq. (2.4.25). Hence we can introduce a new effective Hamiltonian, H' , as:

$$H'_{ij} = H_{ij} + \frac{H_{il} H_{lj}}{E - H_{ll}} \quad (2.4.30)$$

This Hamiltonian is the decimated Hamiltonian produced by simple Gaussian elimination. A notable feature of the decimated Hamiltonian is that it is energy dependent, which suits the method presented in the previous section very well. Without the decimation method, the hamiltonian describing the system in general would take the form:

$$H = \begin{pmatrix} H_L & V_L & 0 \\ V_L^\dagger & H_{scatt} & V_R \\ 0 & V_R^\dagger & H_R \end{pmatrix} \quad (2.4.31)$$

Here, H_L and H_R denote the semi-infinite leads, H_{scatt} denotes the Hamiltonian of the scatterer and V_L and V_R are the coupling Hamiltonians, which couple the original scattering region to the leads. After decimation, we produce an effectively equivalent Hamiltonian:

$$H = \begin{pmatrix} H_L & V_c \\ V_c^\dagger & H_R \end{pmatrix} \quad (2.4.32)$$

Here, V_c denotes an effective coupling Hamiltonian, which now describes the whole scattering process.

Now we can apply the same steps as with the one-dimensional case; using the Dyson Eq. Eq. (2.3.31). Hence, the Green's function for the whole system is described by the surface Green's functions Eqs. (2.4.23) and (2.4.24) and the effective coupling Hamiltonian from Eq. (2.4.32).

$$G = \begin{pmatrix} g_L^{-1} & V_c \\ V_c^\dagger & g_R^{-1} \end{pmatrix}^{-1} = \begin{pmatrix} G_{00} & G_{01} \\ G_{10} & G_{11} \end{pmatrix} \quad (2.4.33)$$

2.4.3 Scattering Matrix

Now, we can move on to the calculation of the scattering amplitudes. A generalization of the Fisher-Lee relation [76, 78, 82], assuming that states are normalized to carry unit flux, will give the transmission amplitude from the left lead to the right lead as:

$$t_{hl} = \tilde{\Phi}_{k_h} G_{01} v_L \Phi_{k_l} \sqrt{\left| \frac{v_h}{v_l} \right|} \quad (2.4.34)$$

where Φ_{k_h} is a right moving state vector in the right lead and Φ_{k_l} is a right moving state vector in the left lead. The corresponding group velocities are denoted v_h and v_l respectively.

The reflection amplitudes in the left lead similarly read:

$$r_{hl} = \tilde{\Phi}_{\bar{k}_h} (G_{00} v_L - I) \Phi_{k_l} \sqrt{\left| \frac{v_h}{v_l} \right|} \quad (2.4.35)$$

Here $\Phi_{\bar{k}_h}$ is a left moving state vector in the left lead and Φ_{k_l} is a right moving state vector in the left lead. In both cases v_L is the v operator defined by Eq. (2.4.20) for the left lead.

Similarly we can define the scattering amplitudes for particles coming from the right:

$$t'_{hl} = \tilde{\Phi}_{\bar{k}_h} G_{10} \nu_R \Phi_{\bar{k}_l} \sqrt{\frac{|v_h|}{|v_l|}} \quad (2.4.36)$$

$$r'_{hl} = \tilde{\Phi}_{\bar{k}_h} (G_{11} \nu_R - I) \Phi_{\bar{k}_l} \sqrt{\frac{|v_h|}{|v_l|}} \quad (2.4.37)$$

Here the definitions are identical, but for the obvious note that what was left in the previous case is now right and vice versa.

So now we can build a scattering matrix and, using the Landauer formula Eq. (2.1.5) presented in section 2.1, we can calculate the conductance. And since this method is valid for any choice of the Hamiltonians H_0 , H_I and H_{scatt} it is remarkably general.

Below, in figure (2.4.2) I explain briefly the transport mechanism by physical and mathematical structures.

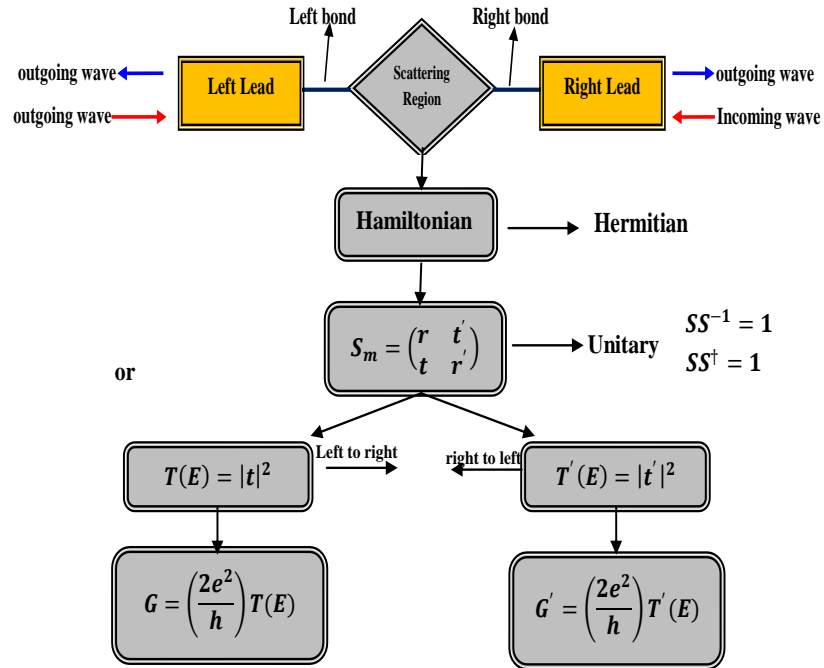


Figure 2.4.2: shows the diagram of transport mechanism by physical and mathematical structures.

2.5 Calculation in Practice

In recent years, the method presented has been used in many areas of mesoscopic transport. It has been successfully applied to molecular electronics [79, 83, 84], spintronics [78, 85] and mesoscopic superconductivity [86, 87]. The method has also been extended for finite bias employing the non-equilibrium Green's function technique [88].

A Hamiltonian, which describes our system, can be created manually or can be an output of a numerical calculation, such as HF, DFT code or density functional tight-binding method.

The three following features will be studied below the Breit-Wigner resonances [89], Fano Resonances [90, 91] and more general antiresonances due to quantum interference [92, 93].

2.6 Features of the Transport Curve

To have an idea for the most important features of the transport curves, it would be useful to briefly study, with the use of simple models, a few key features we might expect to see in the more complicated transport curves of real systems. I will use the decimation method Eq. (2.4.30) to reduce the discussed systems down to an effective Hamiltonian with the topology which is shown in Figure (2.3.2). From there, it is simply a matter of using the Green's function Eq. (2.3.31) to calculate the transmission amplitude using Eq. (2.3.33) and then the transmission probability.

2.6.1 Breit-Wigner Resonance

To study the behaviour of resonances for transmission function $T(E)$ we should know about Breit-Wigner distribution [94]. The simplest feature to understand is the Breit-Wigner resonance. This is a Lorentzian peak in the transmission probability which occurs when the energy of the incident wave resonates with an energy level within the scatterer. Therefore, Figure (2.6.1) shows a one dimensional crystalline linear chain with a single impurity is

placed in the middle of the chain as a defect ε_1 which is coupled to the left and right of semi-infinite crystalline chains by hopping elements β . Using the formula in Eq. (2.6.1), I calculated the transmission probabilities.

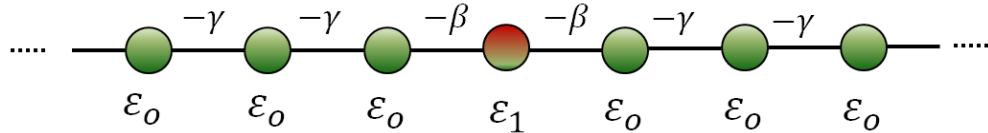


Figure 2.6.1. Simple model to study the behaviour of resonances. The dot ε_1 is coupled by $-\beta$ to two one-dimensional semi-infinite crystalline chains.

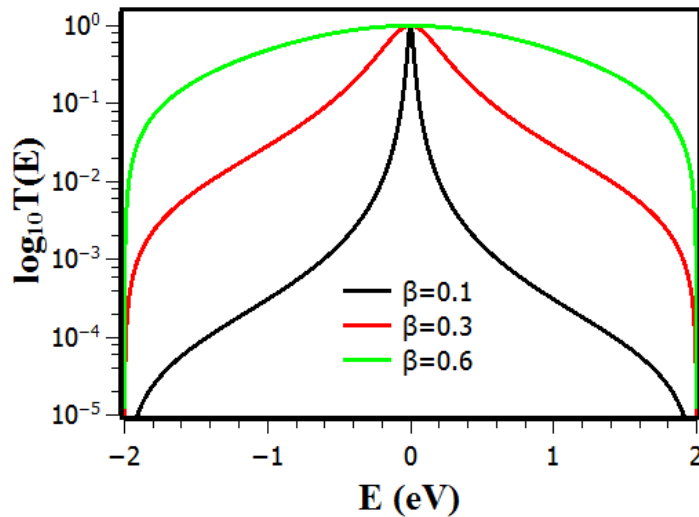


Figure 2.6.2 Transmission curves for tight-binding model in Figure 2.5.1 containing the scatterer $N=1$, where, $\varepsilon_o = \varepsilon_1 = 0, \gamma = 1$, coupled by β , 0.1 (black), 0.3 (red) and 0.6 (green).

$$T(E) = \frac{4 \beta^2}{(E - \varepsilon_1)^2 + 4 \beta^2} \quad (2.6.1)$$

For the model in Figure 2.6.1, Figure (2.6.2) shows the transmission coefficients $T(E)$ as a function of energy E pass through the left semi-infinite chain to the right. The black, red, and green lines show the transmission probabilities for this system when $\varepsilon_o = \varepsilon_1 = 0, \gamma = 1$, coupled by $\beta= 0.1$ (black), 0.3 (red) and 0.6 (green). The calculations show that the width

of the resonance is defined by the coupling component β and its location by the site energy ε_1 . Typically, the scatterer has many energy levels, but in a sufficiently weakly coupled system, they are easy to identify. Resonances corresponding to the HOMO and LUMO levels of the system are most notable because the Fermi Energy, and therefore the conductance of the scatterer, is between these two peaks. In general, if the coupling element, β , is large, the resonances are wider and the conductance is larger.

2.6.2 Fano Resonances

Fano resonances occur when two scattering amplitudes, one due to scattering within a continuum of states (the background process) and the second due to an excitation of a discrete state (the resonant process) interfere. For example, a molecule with a side group produces a Fano resonance when the energy, E , of the incident electron is close to an energy level in the side group. A Fano resonance is usually denoted by a resonance showing the typical Fano line shape, which is a resonance followed by an anti-resonance, example of which can be seen in Figure 2.6.3.

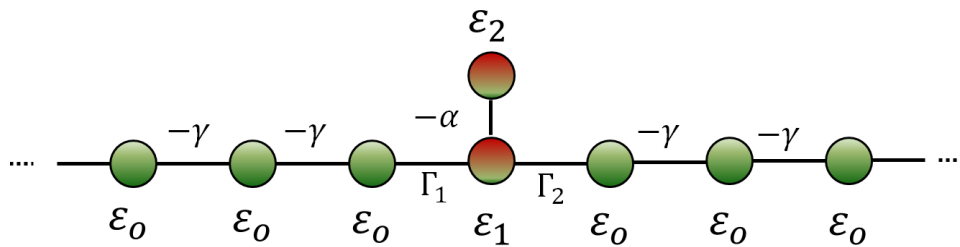


Figure 2.6.3. Simple model to study Fano resonances. Two one-dimensional semi-infinite crystalline chains coupled to a scattering region of site energy ε_1 by hopping elements Γ_1 and Γ_2 . An extra energy level, ε_2 , is coupled to the scattering level by hopping element $-\alpha$.

To illustrate the origin of Fano resonances, consider the model showing two one dimensional semi-infinite crystalline chains with site energies ε_0 and hopping elements $-\gamma$ coupled to a scattering region with two site energies ε_1 (a backbone state) and ε_2 (a bound state). A bound state of energy ε_2 , is coupled to an extended backbone state of energy ε_1 by

a coupling matrix element α . The site energy ε_1 is coupled to the leads with hopping elements Γ_1 and Γ_2 .

Using the formula in Eq. (2.6.2), I calculated the transmission probabilities. Figure 2.6.4 shows the transmission probabilities for this system when $\varepsilon_1 = -1.5$, $\varepsilon_2 = 0.5$, $\varepsilon_0 = 0$, $\gamma = 1$, and α is varied to be 0.24 (blue line), 0.14 (red line) and 0.04 (green line). The width of Fano resonances become narrow by varying the α coupling and the Fano resonances occur at $E = \varepsilon_2$.

$$T(E) = \frac{4 \Gamma_1 \Gamma_2}{\left(E - \varepsilon_1 - \frac{\alpha \alpha^*}{E - \varepsilon_2}\right)^2 + (\Gamma_1 + \Gamma_2)^2} \quad (2.6.2)$$

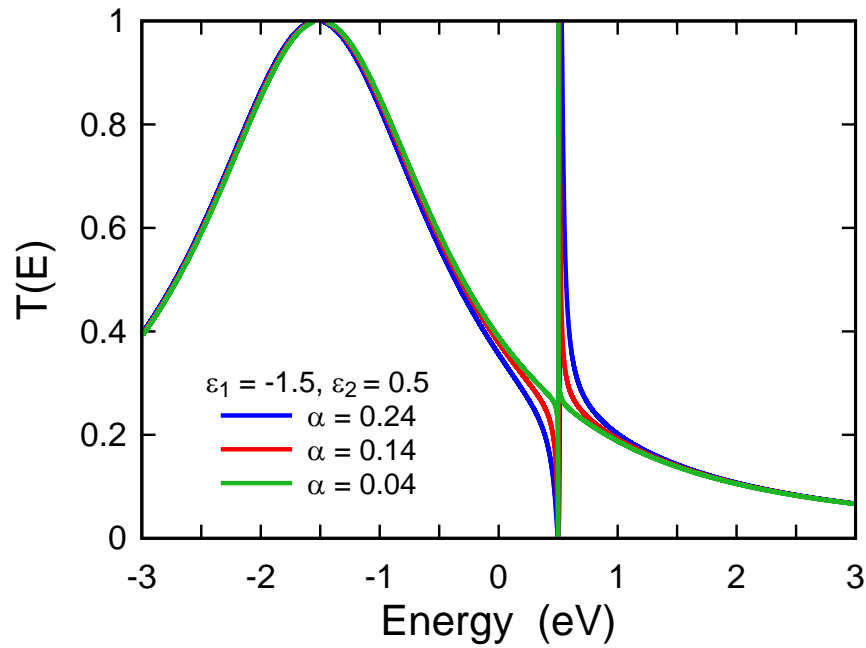


Figure 2.6.4 shows the transmission coefficients for the systems described in Figure 2.6.3

Fano resonances have shown to be tuneable via the molecular side groups [91] or gate voltages [95] and have been shown to give the molecules interesting thermoelectric properties [96, 97].

2.6.3 Anti-Resonances

One important feature in the transmission probability curve is an anti-resonance which appears when the system is multi-branched and destructive interference occurs between propagating waves at the nodal point.

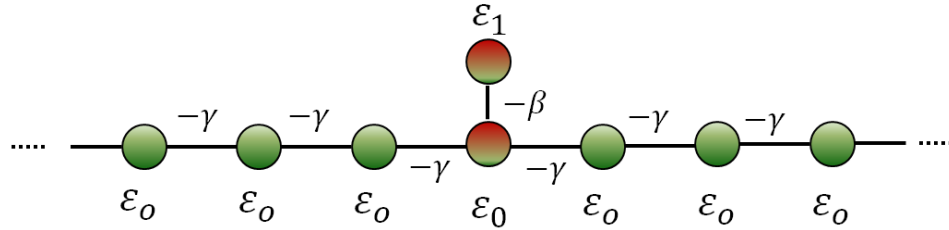


Figure 2.6.5 illustrates a simple model to study anti-resonances. One atomic site with energy ϵ_1 is attached to the 1-D crystalline chain with a coupling β .

We use the tight binding model to study the single electron transport properties of a one dimensional (1-D) chain with a dangling bond. A numerical decimation (which is described in chapter 2) of the dangling bond is described in Figure 2.6.5, where one atomic site with energy ϵ_1 is attached to the 1-D crystalline chain with a coupling β .

For the model in Figure 2.6.5, the algorithm of numerical decimation method is given by

$$\tilde{\epsilon}_1 = \epsilon_0 + \frac{\beta^2}{(E - \epsilon_1)} \quad (2.6.2)$$

where $\tilde{\epsilon}_1$ is the decimated on-site energy, ϵ_0 is the on-site energy of the 1-D chain, ϵ_1 is the dangling site energy, β the dangling bond energy and E the system energy. We calculated the transmission coefficient from the formula that described a single scattering level between two semi-infinite chains:

$$T(E) = \frac{1}{1 + \alpha^2} \quad (2.6.3)$$

where $\alpha = \frac{\tilde{\epsilon}_1 - \epsilon_0}{2\gamma \sin k}$ and $k = \cos^{-1} \left(\frac{\epsilon_0 - E}{2\gamma} \right)$, and by substituting Eq. (2.6.2) into Eq.

(2.6.3) we get:

$$\alpha = \frac{\beta^2}{(E - \varepsilon_1)2\gamma \sin k} \quad (2.6.4)$$

When we send an electron through the lattice shown in figure (2.6.5) with energy $E = \varepsilon_1$ or equal to diagonal energy, then α will be infinite and then $T(E) = 0$. That means the transmission coefficient completely destroys when the energy level lies exactly in the site of chain. This is called destructive interference and results in anti-resonance in the transmission spectrum.

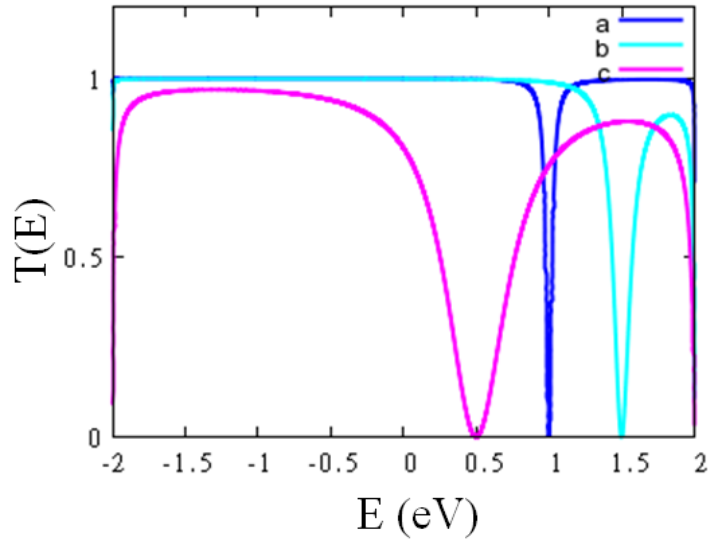


Figure 2.6.6. shows the transmission coefficients for the systems described in Figure 2.6.5. This system is modelled using the following parameters: in the leads, $\varepsilon_0 = 0$ and $\gamma = 1$, for the contact with cases: (a) $\tilde{\varepsilon}_1 = 1$, $\varepsilon_1 = 1$, $\beta = 0.2$, (b) $\tilde{\varepsilon}_1 = 1$, $\varepsilon_1 = 1.5$, $\beta = 0.3$, (c) $\tilde{\varepsilon}_1 = 1$, $\varepsilon_1 = 0.5$, $\beta = 0.7$.

Figures (2.6.5 and 2.6.6) demonstrate the impact of the β value on the width of the peaks. when β and is quite small, then we get a sharp anti-resonance and $T(E)$ goes to zero, this is called an anti-resonance. The position of the anti-resonance is determined by the nature of the energy sites in the scattering region.

2.7 Hamiltonian used in the thesis

Now, we want to describe the molecules and the question is where do we get the Hamiltonian of the molecules from? A Hamiltonian, which describes our system, can be created manually or can be an output of a numerical calculation, such as HF, DFT code SIESTA or density functional tight-binding method. To understand the behaviour of molecular electronics devices it is important to have a reliable source of the structural and electronic behaviour of the isolated molecule and that will lead to the starting point with theory of quantum transport. Density functional theory (DFT) and the numerical implementation, SIESTA (Spanish Initiative for Electronic Simulations with Thousands of Atoms) [98], which I have used during my PhD study as a theoretical tool. It can be considered as a “theoretical laboratory” to investigate the structures of the isolated molecules, and most electrical properties such as charge densities, band structures, binding energies (bond length) and potential surfaces. SIESTA is a set of methods and a complete software package that can be used to perform DFT calculations on a massive number of atoms (~1000) within a lifetime.

The basic idea of DFT is that any physical properties of a complicated system, including of many interacting particles, can be expressed as a functional of the ground-state density of the system. The first proof of this functional was introduced by Hohenberg and Kohn in 1964 [99]. The simplicity of this proof does not indicate the actual form of the functional. In spite of this, the assumption about the form of the functional (an ansatz) was suggested by Kohn and Sham [100] lighted up the way to applications for realistic physical systems. Density functional theory has since become a standard tool in theoretical physics and molecular chemistry.

There are many text books present of the foundations and numerical applications of DFT. Wide literatures with the subject with considerably more details have presented this subject [101-104]. After obtaining the main-field DFT Hamiltonian of system which involves a metallic- molecule-metallic, I use the theory of quantum transport which is shown in this chapter to probe its electronic properties.

Chapter 3

Single-Molecule Sensing of Perylene Bisimide

In this chapter I will present theoretical work motivated by experiments in the group of the late Prof. Thomas Wandlowski of the University of Bern [105]. This work focuses on the electronic properties of perylene bisimide molecules. Here we, theoretically, demonstrate the potential of perylene bisimide (PBI) for label-free sensing of organic molecules and the results presented here were published in the following paper [106]:

“Exploiting the extended p-system of perylene bisimide for label-free single-molecule sensing” *Journal of Materials Chemistry C*, 3(9), 2101-2106, 2015

3.1 Single-Molecule Conductance of Perylene Bisimide (PBIs).

3.1.1 Motivation

Based on the discussion in the introduction (chapter 1), it has been experimentally demonstrated that single PBI-based molecules can be attached to gold electrodes and their electrical conductance can be measured [105]. In the present chapter the aim is to demonstrate that the extended π systems of PBIs make them candidates for the single-

molecule, label-free sensing of a variety of analytes. In this section, I will investigate the electronic properties at a single-molecule level by varying the bay-area substituents of the five PBI derivatives shown in Figure 3.1, which possess the same PBI core, but with the following bay-area substituents: *pyrrolidinyl* (aPy-PBI, Py-PBI), *tert-butyl-phenoxy* (P-PBI), *thiobutyl* (S-PBI), and *chlorine* (Cl-PBI). Four molecules (Py-PBI, P-PBI, Cl-PBI, S-PBI) possess pyridyl anchor groups at opposite ends and are therefore symmetric. The fifth molecule (aPy-PBI) has a *pyridyl* anchor group on the top and a *cyclohexyl* anchor group on the bottom[105] and is asymmetric.

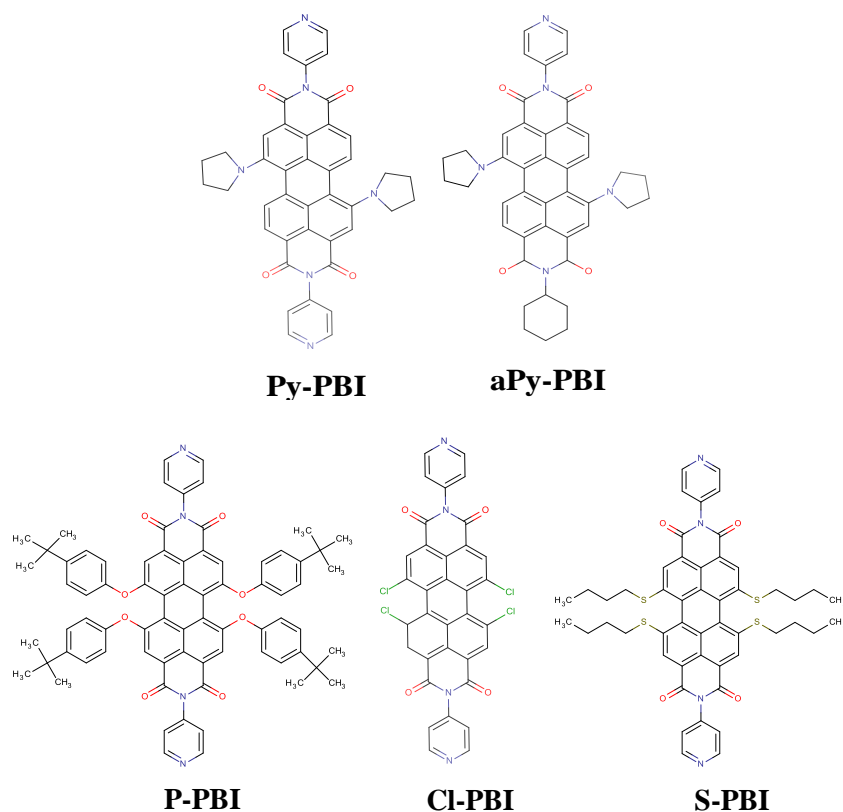


Figure 3.1. PBI-based molecular structures: Py-PBI, (aPy-PBI), P-PBI, Cl-PBI and S-PBI.

3.1.2 Computational Methods

To calculate electrical properties of the molecules in Figure 3.1, the relaxed geometry of each molecule was found using the density functional (DFT) code SIESTA [107] which

employs Troullier-Martins pseudopotentials to represent the potentials of the atomic cores [108] and a local atomic-orbital basis set. We used a double-zeta polarized basis set for all atoms and the generalized gradient approximation (GGA-PBE) for the exchange and correlation functionals [109, 110]. The Hamiltonian and overlap matrices are calculated on a real-space grid defined by a plane-wave cutoff of 150 Ry. Each molecule was relaxed to the optimum geometry until the forces on the atoms are smaller than 0.02 eV/\AA and in case of the isolated molecules, a sufficiently-large unit cell was used, for steric and electrostatic reasons. All PBI molecules with anchor groups and bay-area substituents were found to be twisted after relaxation. Figure 3.2 shows that the frontier molecular orbitals of all five PBI derivatives are delocalized across their central backbones, where the density of states for both the HOMO and the LUMO have large amplitudes around the central carbon backbone atoms of the molecule, with little density on the anchor groups. This means the contacting groups act as tunnelling barriers between the central region and the electrodes.

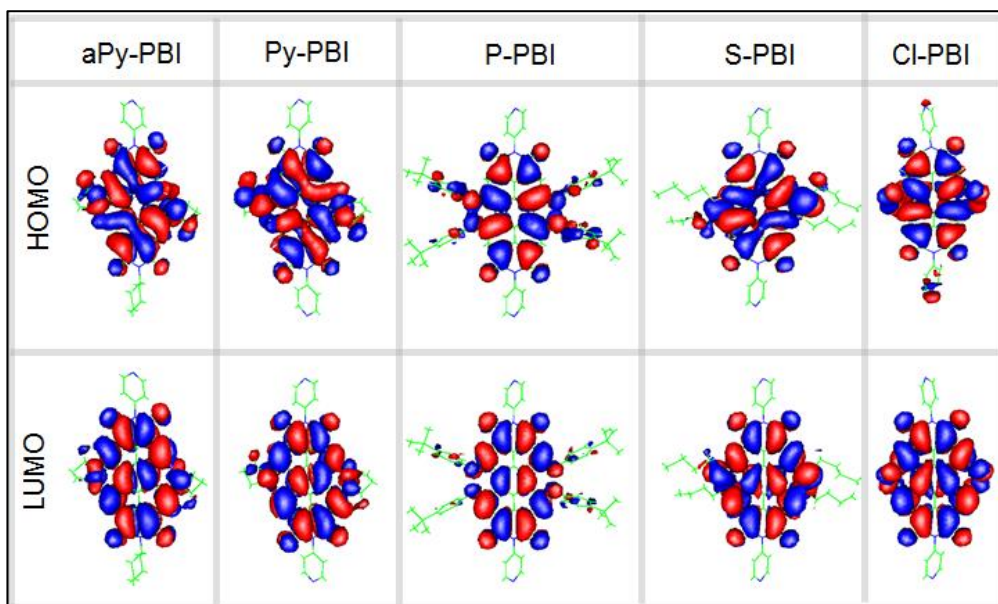


Figure 3.2. Iso-surfaces of frontier molecular orbitals of the all perylene bisimide derivatives obtained using the DFT code SIESTA. Red corresponds to positive and blue to negative regions of the wave functions.

3.1.2.1 Molecular junction and the conductance

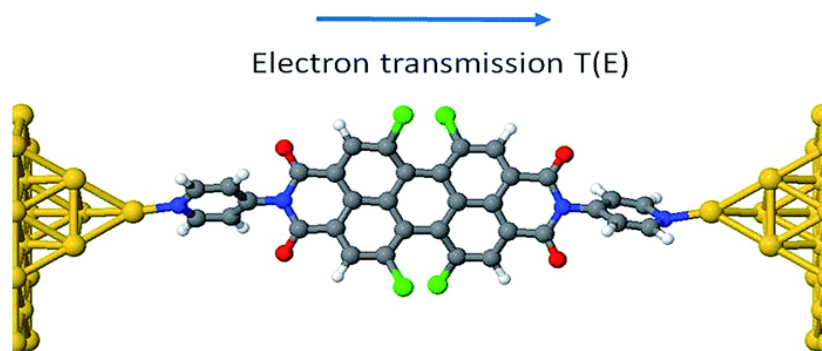


Figure 3.4. An example of an optimized configuration of the system containing a single molecule (Cl-PBI) attached to two metallic leads. Further details for the rest optimized configurations of PBIs with the gold leads are in Figure (3.5).

After obtaining the relaxed geometry of each isolated molecule, the molecules were then placed between gold electrodes, as shown in Figure 3.4. For structures such as that shown in Figure 3.4, the central region of the junction is composed of a single molecule attached to two gold (111) leads. The equilibrium distance between the N atom of each pyridyl anchor group and the centre of the apex atom of each gold pyramid was initially 1.9 Å. After geometry optimization the distance changed slightly from the initial value to a final value of 2.05 Å. Similarly, the distance between the cyclohexyl group of asymmetric molecule (aPy-PBI) and the centre of the apex atom of gold was found to be 2.89 Å.

For each relaxed structure, such as Figure 3.4, we use the GOLLUM method [111] to compute the transmission coefficient $T(E)$ for electrons of energy E passing from the left gold electrode to the right electrode. GOLLUM is a next-generation code, born out of the non-equilibrium transport code SMEAGOL code [112] and is optimised for computing scattering properties of a range of quantum systems such as molecular junctions. Once $T(E)$ is computed, we calculate the zero-bias electrical conductance G using the Landauer formula:

$$G = \frac{I}{V} = G_0 \int_{-\infty}^{\infty} dE T(E) \left(-\frac{df(E)}{dE} \right) \quad (3.1.2)$$

where $G_0 = \left(\frac{2e^2}{h}\right)$ is the quantum of conductance, and $f(E)$ is Fermi distribution function defined as $f(E) = [e^{(E-E_F)/k_B T} + 1]^{-1}$ where k_B is the Boltzmann constant $k_B = 8.62 \times 10^{-5} eV/k$ and T is the temperature. Since $f(E)$ is a function of the Fermi energy E_F , the conductance G is a function of the energetic locations of the molecular orbitals of the PBI-analyte complexes relative to E_F . Since the quantity $(-df(E)/dE)$ is a normalised probability distribution of width approximately equal to $k_B T$, the above integral represents a thermal average of the transmission function $T(E)$ over an energy window of the width $k_B T$ ($= 25\text{meV}$ at room temperature). In what follows, we shall demonstrate that either the zero-bias conductances or the current-voltage (I-V) relations of each bare PBIs molecule to investigate the effect of bay-area substituents or each complex can be used to discriminate between the different analytes (it will be shown in section 3.2). To compute the electrical current I at finite voltage V we use the expression:

$$I = \left(\frac{2e}{h}\right) \int_{-\infty}^{\infty} dE T(E) [f_{left}(E) - f_{right}(E)] \quad (3.1.3)$$

where $f_{left}(E) = [e^{(1/k_B T)(E-E_F^{left})} + 1]^{-1}$ and $f_{right}(E) = [e^{(1/k_B T)(E-E_F^{right})} + 1]^{-1}$, with $E_F^{left} = E_F + \frac{eV}{2}$ and $E_F^{right} = E_F - \frac{eV}{2}$.

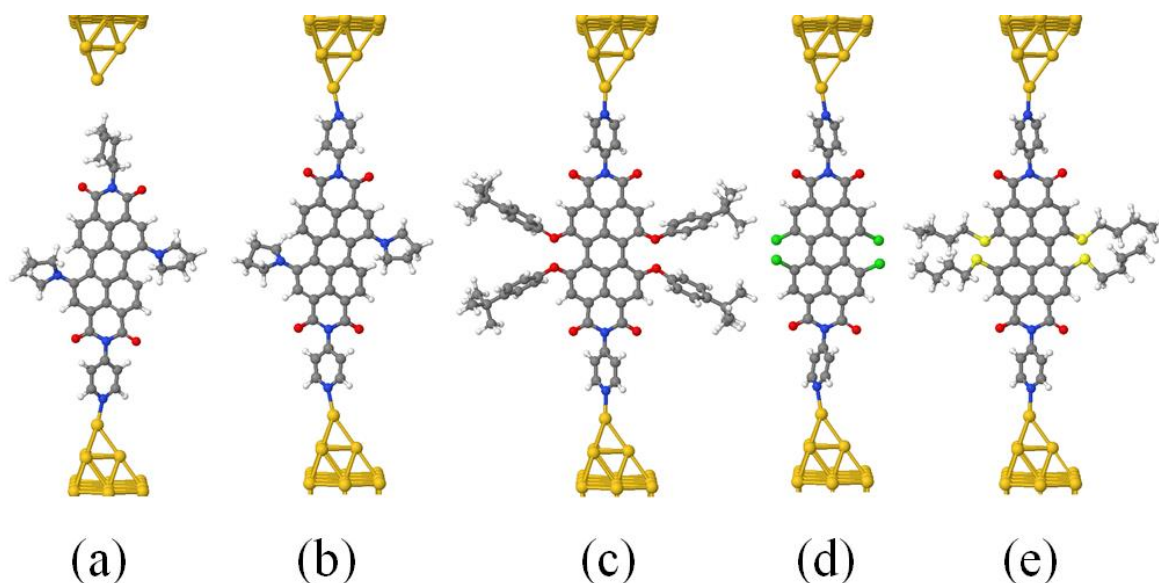


Figure 3.5. Optimized configurations of the single molecules (a) aPy-PBI, (b) Py-PBI, (c) P-PBI, (d) Cl-PBI, and (e) S-PBI attached to two metallic leads.

3.1.3 Results and discussion

We first compare our theoretical predictions with experimental measurements of ref. [29], where it was found that the electrical conductances of the bare PBIs are ordered as follows: Cl-PBI < PBI < S-PBI < aPy-PBI < Py-PBI. For each of these molecules, Figure 3.6a shows the transmission coefficients $T(E)$ as a function of energy E , relative to the DFT-predicted Fermi energy E_F^{DFT} (0 eV). Figure 3.6a shows that the effect of the bay substituent atoms is to shift the position of the HOMO resonances of the bare PBIs, while the LUMOs remain pinned close to the Fermi energy. The corresponding room-temperature conductances as a function of E_F are shown in Figure 3.6b. Furthermore, the corresponding results for the room-temperature current as a function of the voltage for the five perylene bisimides in the bare case are shown in Figure 3.6c.

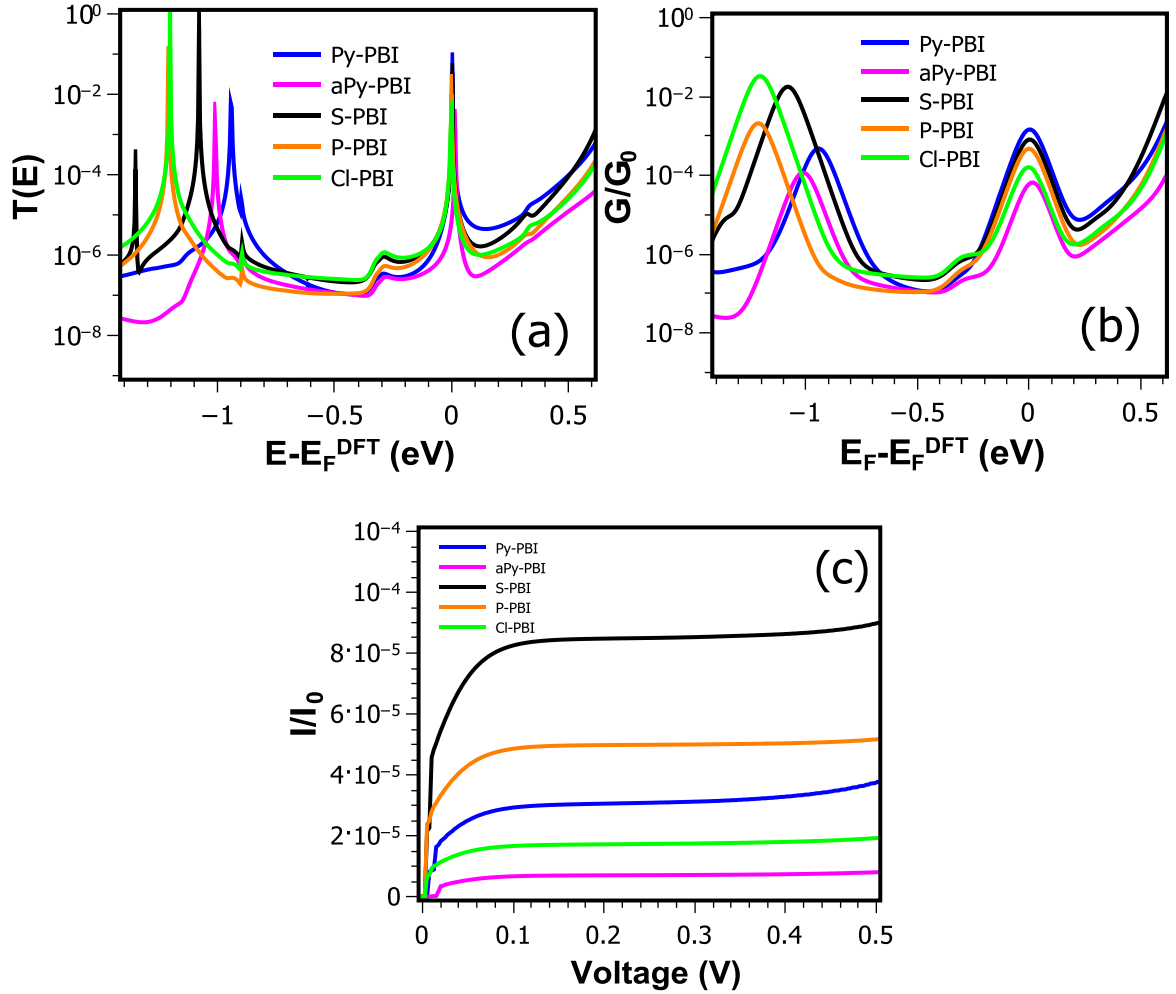


Figure 3.6. (a) Transmission coefficients as a function of energy for the five perylene bisimides. (b) Room-temperature conductance as a function of the Fermi energy. (c) DFT calculations for the corresponding results for the room-temperature current as a function of the voltage for the five perylene bisimides in bare case.

3.1.3.1 Locating the optimal value of E_F

It is well-known that DFT can give an incorrect value for the Fermi energy and therefore I use Eq. (3.1.2) to evaluate the room-temperature conductance for a range of values of E_F in the vicinity of E_F^{DFT} and then choose the value of E_F which yields the closest agreement with experiment. The optimal value of E_F was chosen by minimising the quantity

$$Y^2(E_F) = \sum_{i=1}^5 (\text{Log}(G_i^{theo}) - \text{Log}(G_i^{exp}))^2 \quad (3.1.4)$$

Where G_i^{theo} is the theoretical conductance for a given E_F and G_i^{exp} is the experimental conductance reported in ref [105], where i labels the PBIs. This mean-square deviation between theory and experiment is plotted in Figure 3.7 and shows a minimum at $E_F = 0.08\text{eV}$, which is the values chosen throughout this paper.

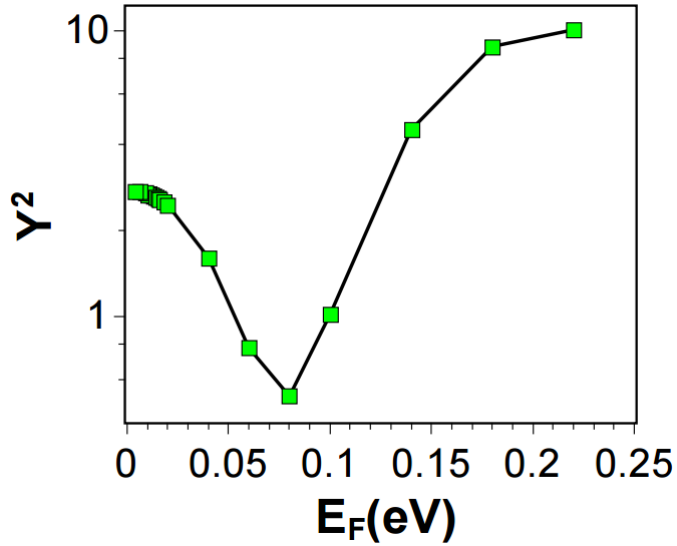


Figure 3.7. The mean square deviation of theory from the experiment as a function of Fermi energy.

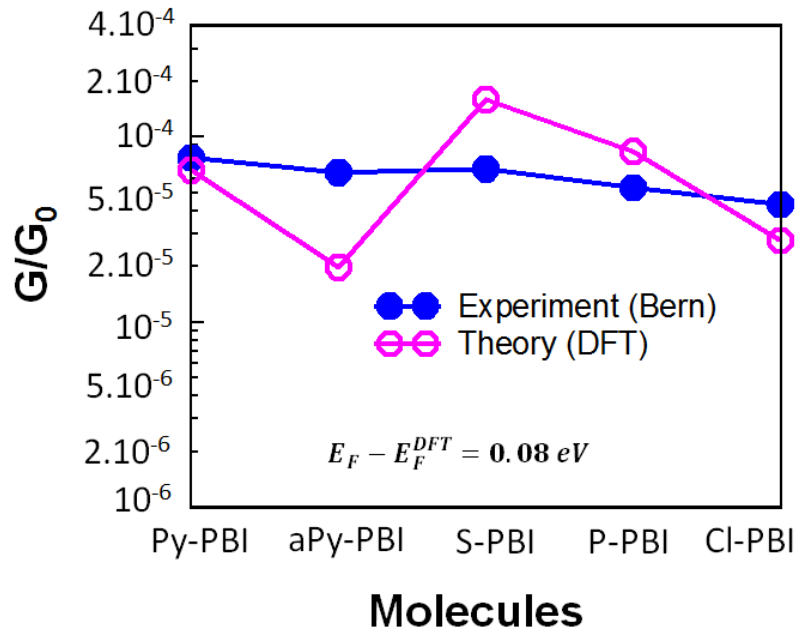


Figure 3.8. Comparison between the experimental [105] and theoretical conductances of the bare PBIs, obtained with E_F shifted by 0.08 eV relative to the bare DFT value.

For a given value of E_F , the five theoretical conductances obtained from Figure 3.6b were compared with the experimentally-measured conductances [105] and a value of $E_F = E_F^{DFT} + 0.08 \text{ eV}$ was chosen to yield the closest fit to experiment, which is shown in Figure 3.7. Figure 3.8 shows the resulting comparison between experiment and theory.

In general, through the experiment measurements only change over a very small range. Therefore it is the pinning of the LUMO resonance close to the Fermi energy which accounts for the similar conductance values for all molecules.

3.2 Exploiting the Extended π -System of Perylene Bisimide for Label-free Single-Molecule Sensing

3.2.1 Motivation

Molecular recognition is the basis of fundamental biological processes such as transcription and translation of genetic information. Considerable effort has been devoted to the design of receptors or sensors that recognise and sense target analytes. Typically this involves designing a receptor, which selectively binds most strongly to a particular analyte. PBI has been used as a reporter dye in a number of such studies, including fluoride fluorescent chemosensors based on perylene derivatives linked by urea [46] and spermine-alanine functionalized PBI [47], which binds to DNA/RNA via non-covalent interactions. In all such studies, the binding of an analyte is signalled by a change in the spectroscopic properties of the PBI. Furthermore, the ability of the PBI derivative to discriminate between analytes is limited, because the PBI derivative is tailored to the analyte of interest.

Label-free methods for detecting small molecules are a desirable target technology, because they avoid the need for chemical modification or separation of the analytes, potentially leading to lower costs. Examples of label-free detection include micelle-based bacterial quorum sensing [42] aptamer-based sensing platforms [40], label-free, sequence specific DNA sensing based on fluorescence resonant energy transfer (FRET) [41] and nuclear magnetic resonance [43], nanoplasmonics [44], and surface enhanced Raman spectroscopy (SERS) [45]. However all of these require expensive detectors and are not shrinkable to sub-micron-scale devices and therefore the cost-lowering advantages of label-free sensing are not yet fully realised.

In this section, we demonstrate a completely different strategy for molecular recognition based on single-molecule electrical junctions. Each junction contains a single PBI-derivative molecule attached to nanogap electrodes, whose electrical conductance changes when an analyte binds to the extended π system of the PBI. The crucial point is that the response of each derivative to analyte binding is different and the collection of responses from a collection of PBI-derivatives constitutes a unique fingerprint that discriminates between different analytes.

The rewards for realising cheap and versatile discriminating sensors cannot be overstated. During the next three years, the size of the MEMS market in cell phones and tablets is predicted to grow to \$500 per annum. The market for chemical sensing with applications to personal health, mood sensing, context-aware computing and the deployment of sensory swarms is equally large, provided low-power, low-cost discriminating molecular sensors can be developed.

This work will be of interest to the molecular electronics and nano electronics communities, as well as chemists and physicist working on the fundamental aspects of functionalised

surfaces, smart functional packaging, enhanced dyes, pigments and fluorophores for applications from display devices to solar cells.

In the present section, my aim is to demonstrate the potential of perylene bisimide (PBI) for label-free sensing of organic molecules by investigating the change in electronic properties of five symmetric and asymmetric PBI derivatives shown in Figure 3.1, which share a common backbone, but are functionalised with various bay-area substituents. Density functional theory was combined with a Green's function scattering approach to compute the electrical conductance of each molecule attached to two gold electrodes by pyridyl anchor groups. We studied the change in their conductance in response to the binding of three analytes, namely *Trinitrotoluene* (TNT) and *Tetracyanoethylene* (TCNE) which are well known electron acceptors [113, 114] and the donor *Bis(ethylenedithia)tetrathiafulvalene* (BEDT-TTF) [115-117] whose π -donor capability is weaker than that of TTF [118], and found that the five different responses provided a unique fingerprint for the discriminating sensing of each analyte.

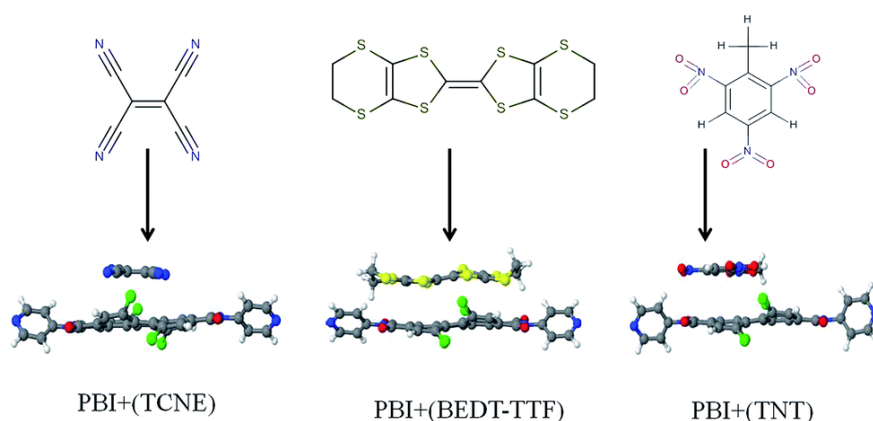


Figure 3.9. The DFT calculated optimum geometries for molecular complexes of TCNE, BEDT-TTF, and TNT with the PBI molecule.

This ability to sense and discriminate was a direct consequence of the extended π system of the PBI backbone, which strongly binds the analytes, combined with the different charge

distribution of the five PBI derivatives, which leads to a unique electrical response to analyte binding.

3.2.2 Molecular Complexes

The sufficiently extended conjugation of perylene bisimide PBIs facilitate the charge transfer complex formation, and recently it is reported that the PBIs molecules exhibit interesting structural features, in particular a twisted π -system which results in a conformational chirality [119]. The twisting of π -system attributed to repulsive interactions between the sterically encumbered bay-substituents and this dependency can be varied on the size of the bay-substituents [24]. Therefore in this chapter, it is important to gain deeper understanding for the effect of substituents in the bay position of the backbone of PBIs, particularly when one says the PBIs based-the extended π -system can sense and discriminate between the organic analyte molecules.

In what follow, for complexation of organic molecules, to calculate the charge-transfer ΔQ and binding energy ΔE between the backbone of each PBIs molecule and three analytes which are TCNE, TNT and BEDT-TTF, we used a double-zeta polarized basis set for all atoms and the generalized gradient approximation (GGA-PBE) for the exchange and correlation functionals [109] but we also made these calculations with the local density approximation (LDA-CA) [120] and van der Waals interactions [121]. The Hamiltonian and overlap matrices are calculated on a real-space grid defined by a plane-wave cutoff of 150 Ry. Each PBI molecule with three analytes are relaxed into the optimum geometry until the forces on the atoms are smaller than $0.02 \text{ eV}/\text{\AA}$. The tolerance of Density Matrix is 10^{-4} , and in case of the isolated molecules a sufficiently-large unit cell was used, for steric and electrostatic reasons.

For binding energy calculations E^B , the basis set superposition errors were avoided by retaining ‘ghost states’ as prescribed in the counterpoise method [122, 123], using the formula

$$E^B = E_{AB} - (E_{aB} + E_{Ab}) \quad (3.2.1)$$

In this expression the total energy of entity A bound to B is E_{AB} , the total energy of B in the presence of the ghost states a is E_{aB} and the total energy of A in the presence of the ghost states b is E_{Ab} . For the five PBI molecules in Figure 3.1, the formation of molecular complexes with each of the three different analytes TCNE, BEDT-TTF and TNT was investigated using DFT.

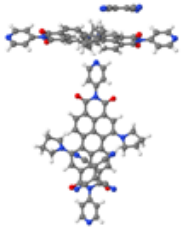
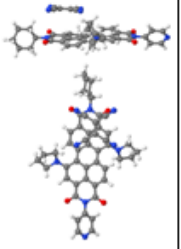
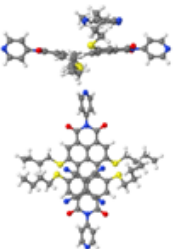
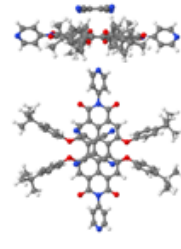
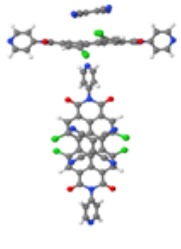
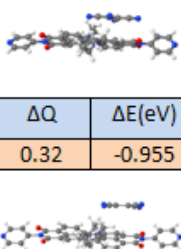
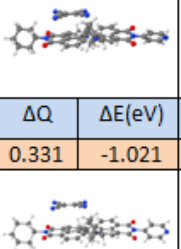
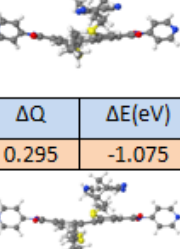
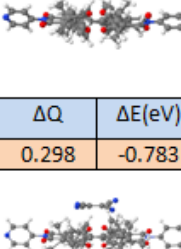
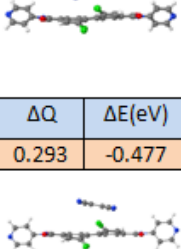
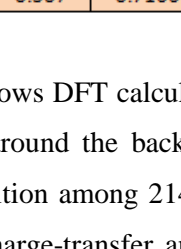
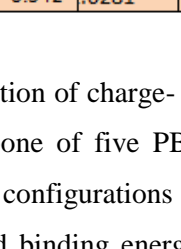
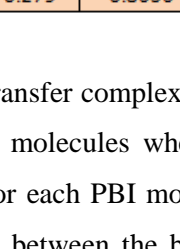
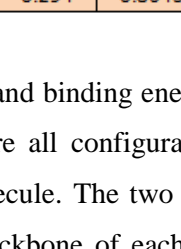
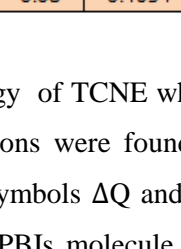
	Py+TCNE		aPy+TCNE		S+TCNE		P+TCNE		Cl+TCNE	
GGA										
	ΔQ	$\Delta E(\text{eV})$	ΔQ	$\Delta E(\text{eV})$	ΔQ	$\Delta E(\text{eV})$	ΔQ	$\Delta E(\text{eV})$	ΔQ	$\Delta E(\text{eV})$
	0.311	-0.301	0.317	-0.293	0.279	-0.294	0.292	-0.245	0.289	-0.027
LDA										
	ΔQ	$\Delta E(\text{eV})$	ΔQ	$\Delta E(\text{eV})$	ΔQ	$\Delta E(\text{eV})$	ΔQ	$\Delta E(\text{eV})$	ΔQ	$\Delta E(\text{eV})$
	0.32	-0.955	0.331	-1.021	0.295	-1.075	0.298	-0.783	0.293	-0.477
Vdw										
	ΔQ	$\Delta E(\text{eV})$	ΔQ	$\Delta E(\text{eV})$	ΔQ	$\Delta E(\text{eV})$	ΔQ	$\Delta E(\text{eV})$	ΔQ	$\Delta E(\text{eV})$
	0.307	-0.7166	0.342	.0281	0.279	-0.8636	0.294	-0.8643	0.08	-0.4054

Table 3.1. shows DFT calculation of charge- transfer complex and binding energy of TCNE which is analyzed around the backbone of five PBI molecules where all configurations were found in optimum position among 214 configurations for each PBI molecule. The two symbols ΔQ and ΔE denote the charge-transfer and binding energy between the backbone of each PBIs molecule and three analytes, respectively.

In each case, after geometry relaxation, the charge transferred between the two molecules and the binding energy was computed (This data is shown in tables 3.1- 3.3). The calculations show that TCNE and TNT gain electrons from the backbone of PBI, but the BEDT-TTF donates electrons to the backbone. These tables show also the binding energies for the three analytes, obtained using three different density functionals (GGA, LDA and van der Waals), all of which show that the analytes form stable complexes to the PBI. The most accurate of these includes van der Waals interactions and predicts binding energies which vary between 0.4 eV and 1.2 eV, depending on the combination of analyte and backbone. As an example, Figure 3.9 shows the optimised TCNE, TNT and BEDT-TTF-(Py-PBI) complex, in which each analyte pi-stacks a distance $Y=0.37$ nm above the perylene. The details of all optimised PBI-adsorbate complexes are shown in Tables 3.1, 3.2, and 3.3.

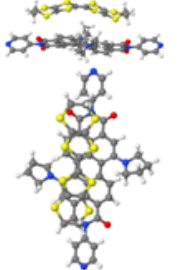
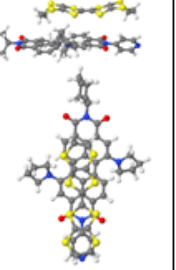
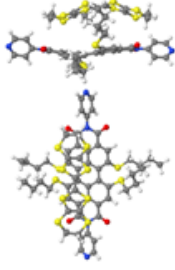
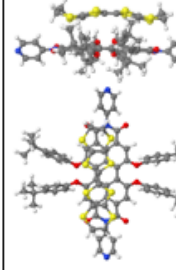
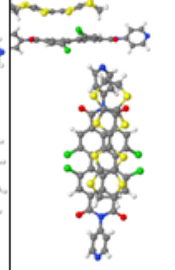
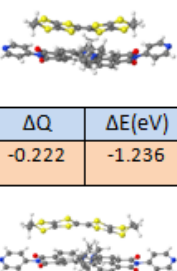
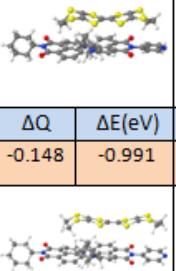
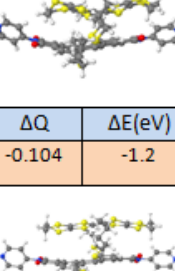
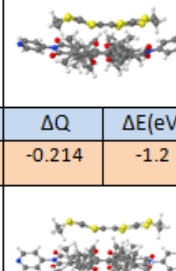
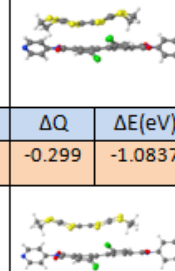
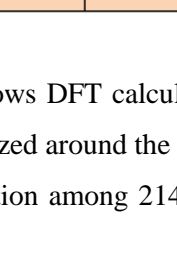
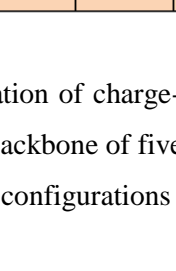
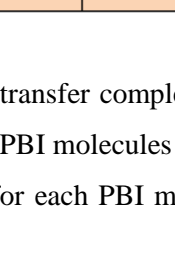
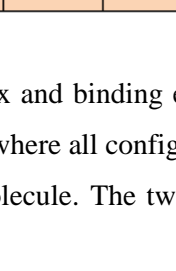
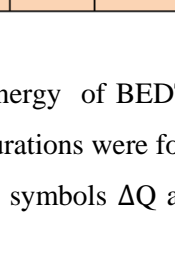
	Py+BEDT-TTF		aPy+ BEDT-TTF		S+ BEDT-TTF		P+ BEDT-TTF		Cl+ BEDT-TTF	
GGA										
	ΔQ	$\Delta E(\text{eV})$	ΔQ	$\Delta E(\text{eV})$	ΔQ	$\Delta E(\text{eV})$	ΔQ	$\Delta E(\text{eV})$	ΔQ	$\Delta E(\text{eV})$
	-0.043	-0.284	-0.053	-0.199	-0.007	-0.225	-0.179	-0.151	-0.239	-0.1820
LDA										
	ΔQ	$\Delta E(\text{eV})$	ΔQ	$\Delta E(\text{eV})$	ΔQ	$\Delta E(\text{eV})$	ΔQ	$\Delta E(\text{eV})$	ΔQ	$\Delta E(\text{eV})$
	-0.222	-1.236	-0.148	-0.991	-0.104	-1.2	-0.214	-1.2	-0.299	-1.0837
vdW										
	ΔQ	$\Delta E(\text{eV})$	ΔQ	$\Delta E(\text{eV})$	ΔQ	$\Delta E(\text{eV})$	ΔQ	$\Delta E(\text{eV})$	ΔQ	$\Delta E(\text{eV})$
	-0.166	-1.184	-0.079	-1.0064	-0.064	-1.1611	-0.133	-1.1837	-0.224	-1.0432

Table 3.2. shows DFT calculation of charge- transfer complex and binding energy of BEDT-TTF which is analyzed around the backbone of five PBI molecules where all configurations were found in optimum position among 214 configurations for each PBI molecule. The two symbols ΔQ and ΔE

denote the charge-transfer and binding energy between the backbone of each PBI molecule and three analytes, respectively.

Tables 3.1-3.3 demonstrate that the sufficiently extended conjugation of PBIs facilitate the charge transfer complex formation. Therefore, for five PBI molecules in the presence of each of the three different analytes: TCNE and TNT gain electrons from the backbone as shown in Table 3.1 and 3.3, whereas the BEDT-TTF denotes electrons into the backbone which is shown in Table 3.2. However, the values of transferred electrons are different from backbone to other because each backbone possesses different bay- position substitutes. The inset optimal geometries in Table 3.1-3.3 show that it is difficult to obtain the stable position of each analyte complexed with the backbone of PBIs due to the bay-substitutes.

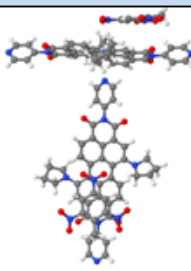
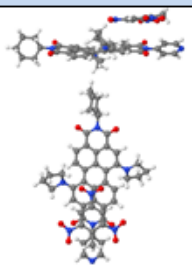
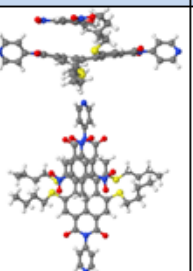
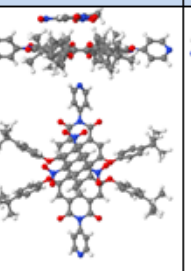
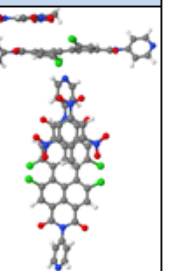
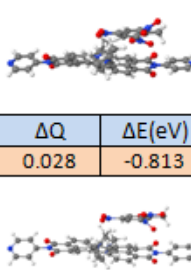
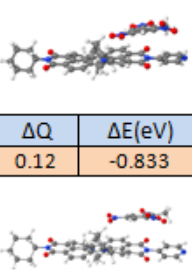
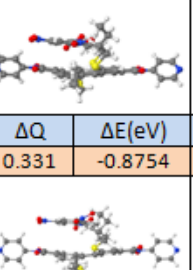
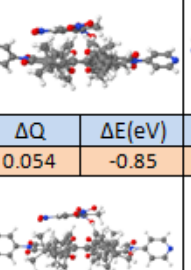
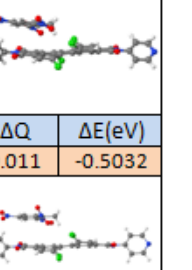
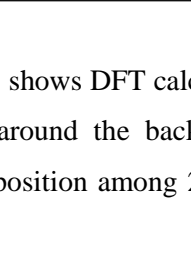
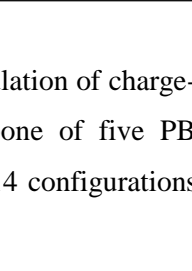
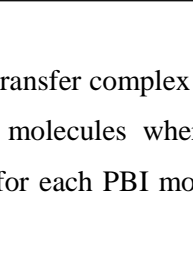
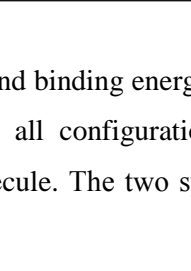
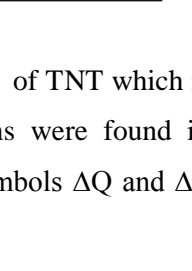
	Py+TNT		aPy+TNT		S+TNT		P+TNT		Cl+TNT	
GGA										
	ΔQ	$\Delta E(\text{eV})$	ΔQ	$\Delta E(\text{eV})$	ΔQ	$\Delta E(\text{eV})$	ΔQ	$\Delta E(\text{eV})$	ΔQ	$\Delta E(\text{eV})$
	0.023	-0.141	0.11	-0.097	0.132	-0.102	0.049	-0.0921	0.011	-0.015
LDA										
	ΔQ	$\Delta E(\text{eV})$	ΔQ	$\Delta E(\text{eV})$	ΔQ	$\Delta E(\text{eV})$	ΔQ	$\Delta E(\text{eV})$	ΔQ	$\Delta E(\text{eV})$
	0.028	-0.813	0.12	-0.833	0.331	-0.8754	0.054	-0.85	0.011	-0.5032
Vdw										
	ΔQ	$\Delta E(\text{eV})$	ΔQ	$\Delta E(\text{eV})$	ΔQ	$\Delta E(\text{eV})$	ΔQ	$\Delta E(\text{eV})$	ΔQ	$\Delta E(\text{eV})$
	0.023	-0.933	0.114	-0.723	0.048	-0.966	0.051	-1.082	0.024	-0.614

Table 3.3. shows DFT calculation of charge- transfer complex and binding energy of TNT which is analyzed around the backbone of five PBI molecules where all configurations were found in optimum position among 214 configurations for each PBI molecule. The two symbols ΔQ and ΔE

denote the charge-transfer and binding energy between the backbone of each PBI's molecule and three analytes, respectively.

For all relaxed geometries, the substitutes in the bay-positions play an important role to determine the charge transfer and binding energy values. These substitutes twist the two naphthalene units of the backbone of PBIs, which makes the interaction between the bound state of the analyte and the localized state of backbone, different from one backbone to another. Also the geometry of the bay-position leads to the analytes binding in different locations and that causes the magnitude of the binding energy to change.

3.2.3 Molecular junction and the conductance

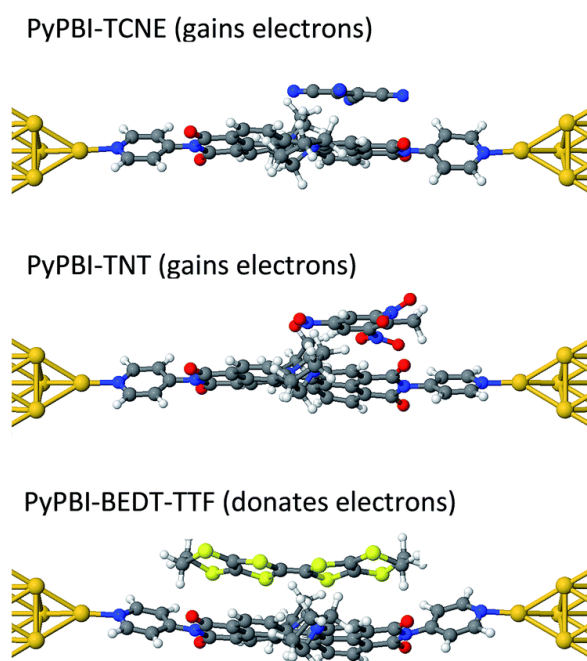


Figure 3.9. Optimized configuration Py-PBI with (TCNE, TNT, and BEDT-TTF).

Figure 3.9 shows the relaxed configurations contain of Py-PBI molecule bound to three analytes (TCNE, TNT, and BEDT-TTF) attached between two gold electrodes. Figures (3.10 – 3.12) show the configuration for all optimised PBI-adsorbate complexes attached to gold electrodes.

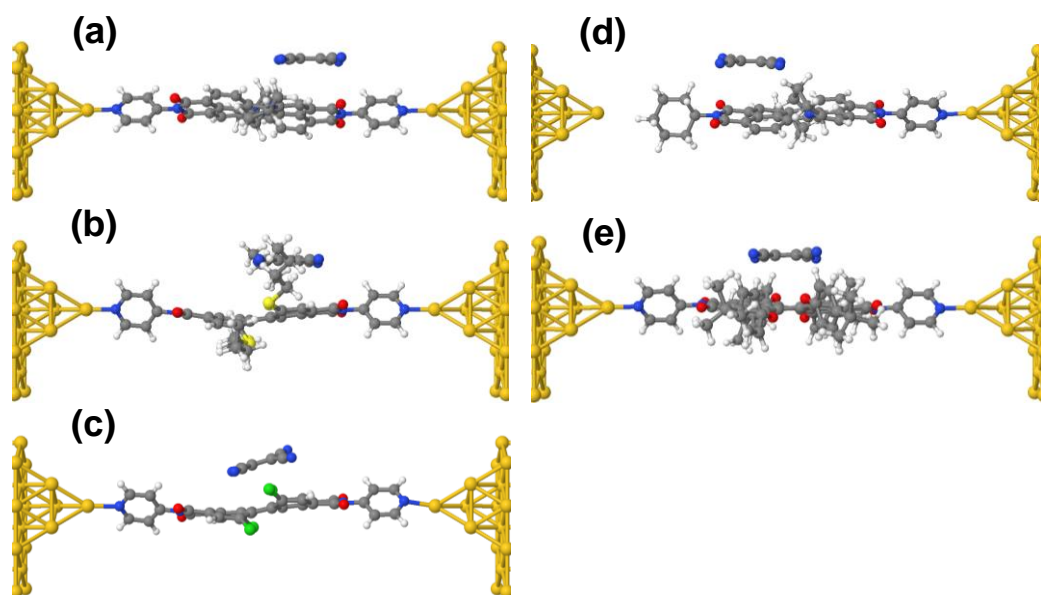


Figure 3.10. Optimized configurations of a single TCNE adsorbed on (a) Py-PBI, (b) aPy-PBI, (c) S-PBI, (d) P-PBI, and (e) Cl-PBI attached to two metallic leads.

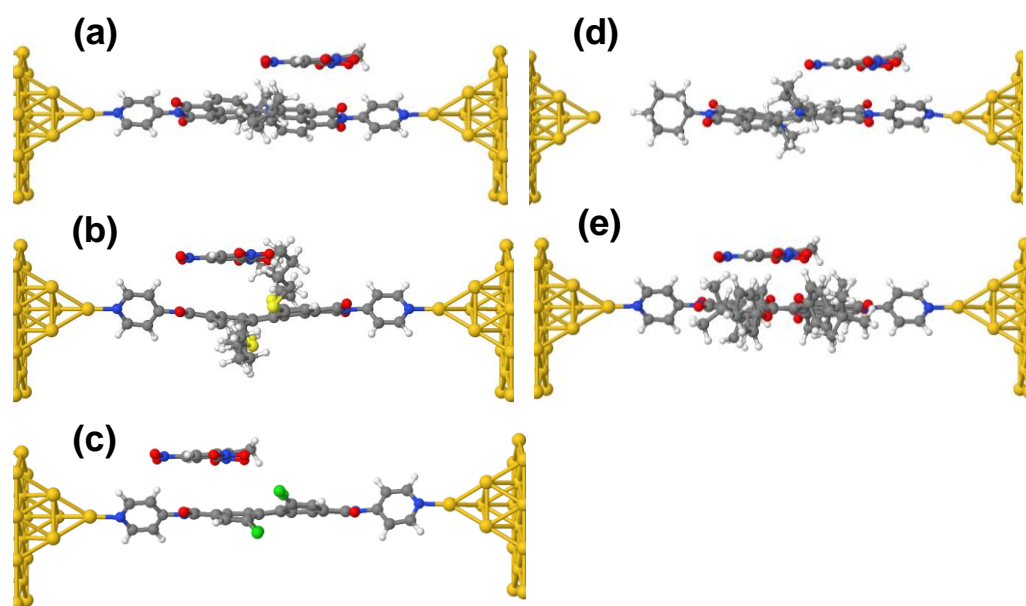


Figure 3.11. Optimized configurations of a single TNT adsorbed on (a) Py-PBI, (b) aPy-PBI, (c) S-PBI, (d) P-PBI, and (e) Cl-PBI attached to two metallic leads.

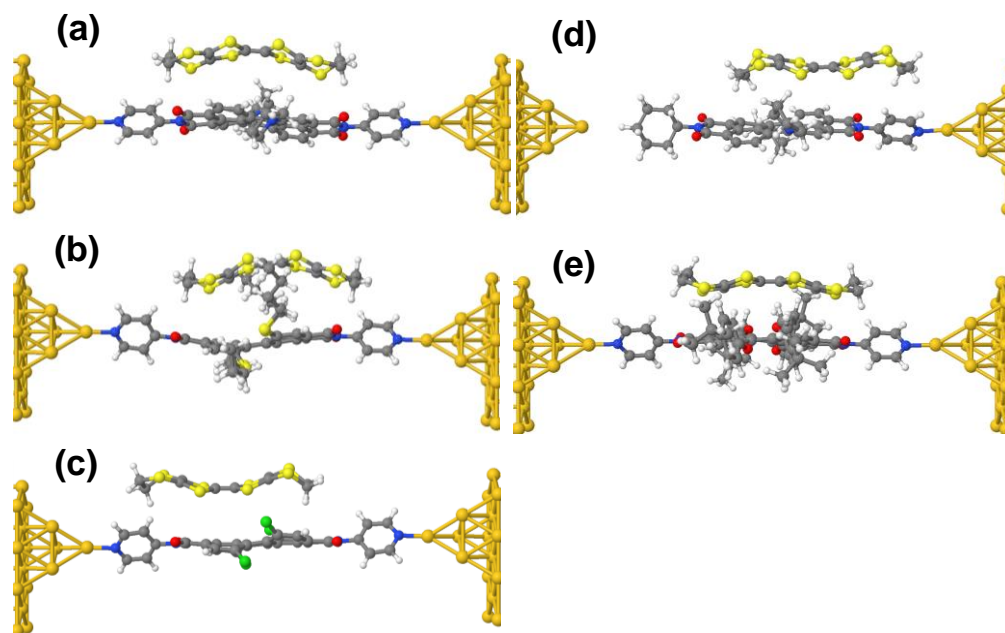


Figure 3.12. Optimized configurations of a single BEDT-TTF adsorbed on (a) Py-PBI, (b) aPy-PBI, (c) S-PBI, (d) P-PBI, and (e) Cl-PBI attached to two metallic leads.

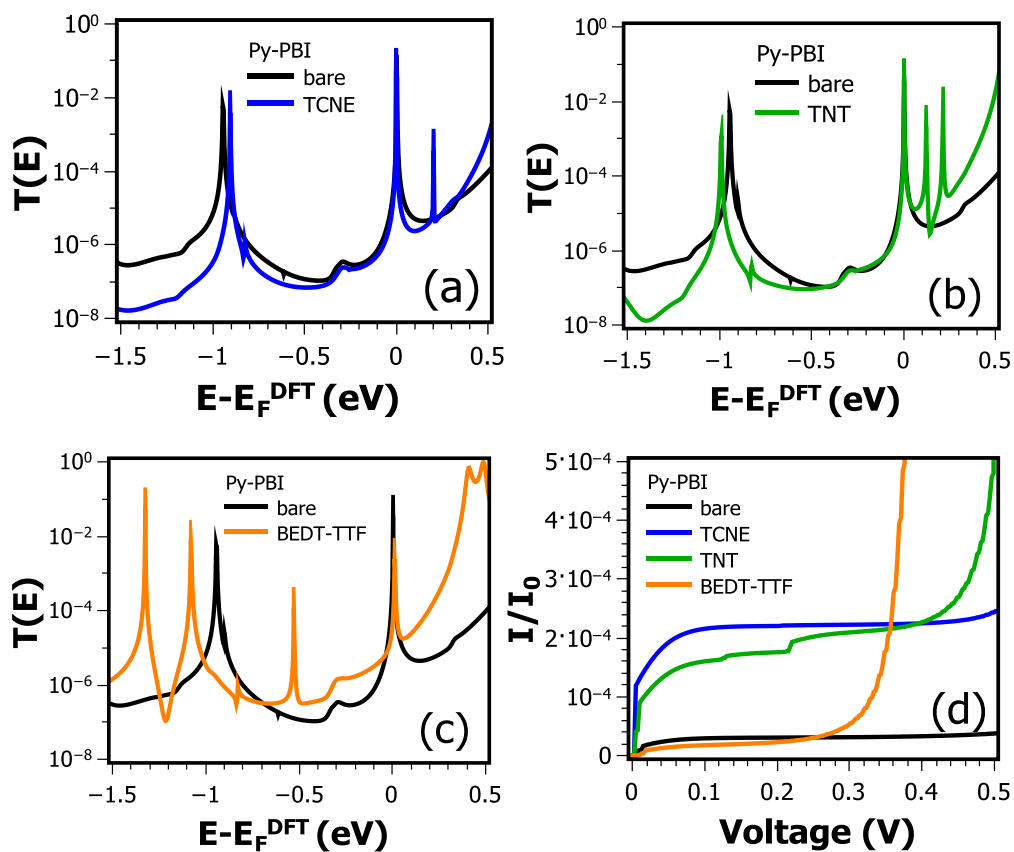


Figure 3.13. DFT calculations of the transmission coefficients as a function of energy at $T=0K$ for optimum configuration of **Py-PBI** with (a) TCNE, (b) TNT, and (c) BEDT-TTF. The fourth figure (d) shows the current as a function of voltage at $T=300K$ for the bare **Py-PBI** and in the presence of the three analyte molecules (TCNE, TNT, and BEDT-TTF).

Figures 3.13a-c show the transmission coefficients $T(E)$ due to the binding of each of the three analyte molecules on Py-PBI. For the two acceptor molecules TCNE and TNT, there is a shifting of the HOMO resonance and extra resonances appear close to the LUMO. For the donor BEDT-TTF a resonance also appears in the HOMO-LUMO gap, accompanied by additional resonances below the HOMO. Figure 3.13d shows the corresponding I-V characteristics of each of the complexes, demonstrating that for optimally-bound complexes, the distinct I-V curves can be used to discriminate between BEDT-TTF and the other analytes, although the difference between TCNE and TNT is smaller.

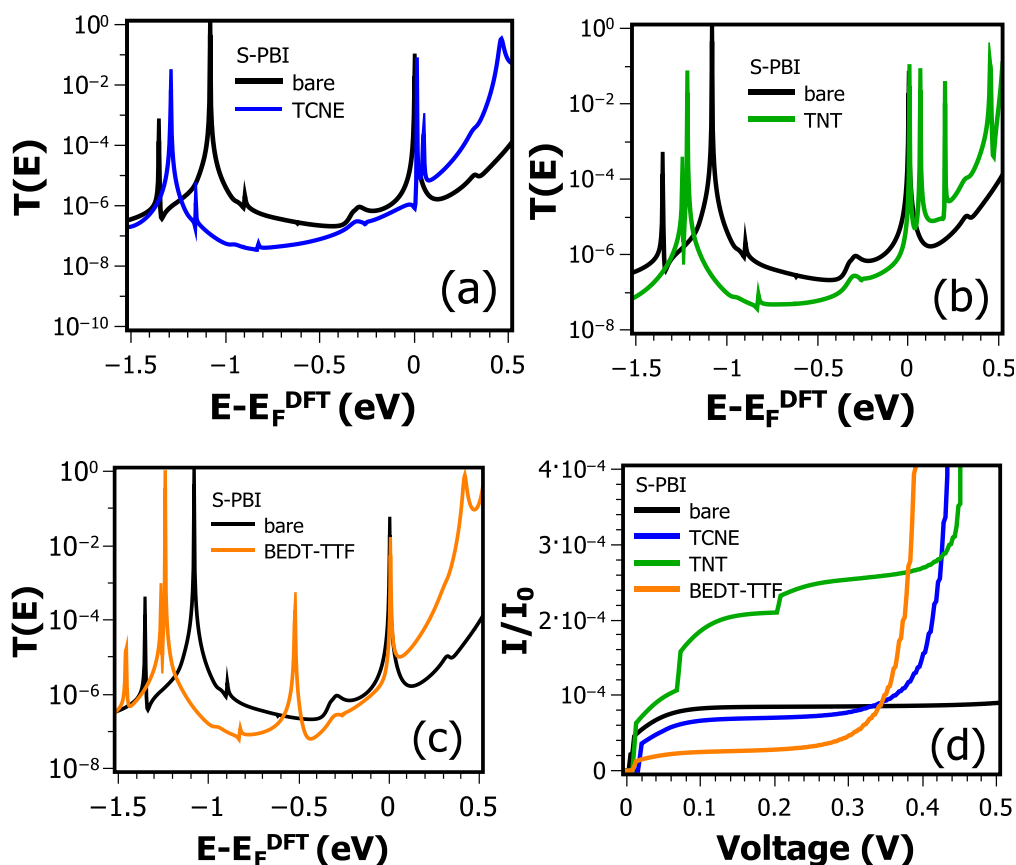


Figure 3.14. DFT calculations of the transmission coefficients as a function of energy at $T=0K$ for optimum configuration of **S-PBI** with (a) TCNE, (b) TNT, and (c) BEDT-TTF. The fourth figure (d) shows the current as a function of voltage at $T=300K$ for the bare **S-PBI** and in the presence of the three analyte molecules (TCNE, TNT, and BEDT-TTF).

For the S-PBI structures in Figures 3.10c, 3.11c and 3.12c, Figures 13.14a-c show the transmission coefficients $T(E)$ versus E for each the optimally-bound TCNE, TNT and BEDT-TTF complex to the backbone of S-PBI molecule. In the presence of TCNE and TNT, the HOMO resonances shift on the opposite direction to those obtained with Py-PBI, the extra resonances also appear close to the LUMO. For BEDT-TTF, similarly with Py-PBI the resonance also appears in the HOMO-LUMO gap. The corresponding I-V characteristics of each of the complexes was computed in figure 13.14d, also showing the discrimination between BEDT-TTF and TNT but here the difference between TCNE and BEDT-TTF is smaller. The different responses of the backbone of S-PBI are probably associated with the substitute groups in the bay position which lead to a twist of the backbone and this causes the analytes to bind in different locations.

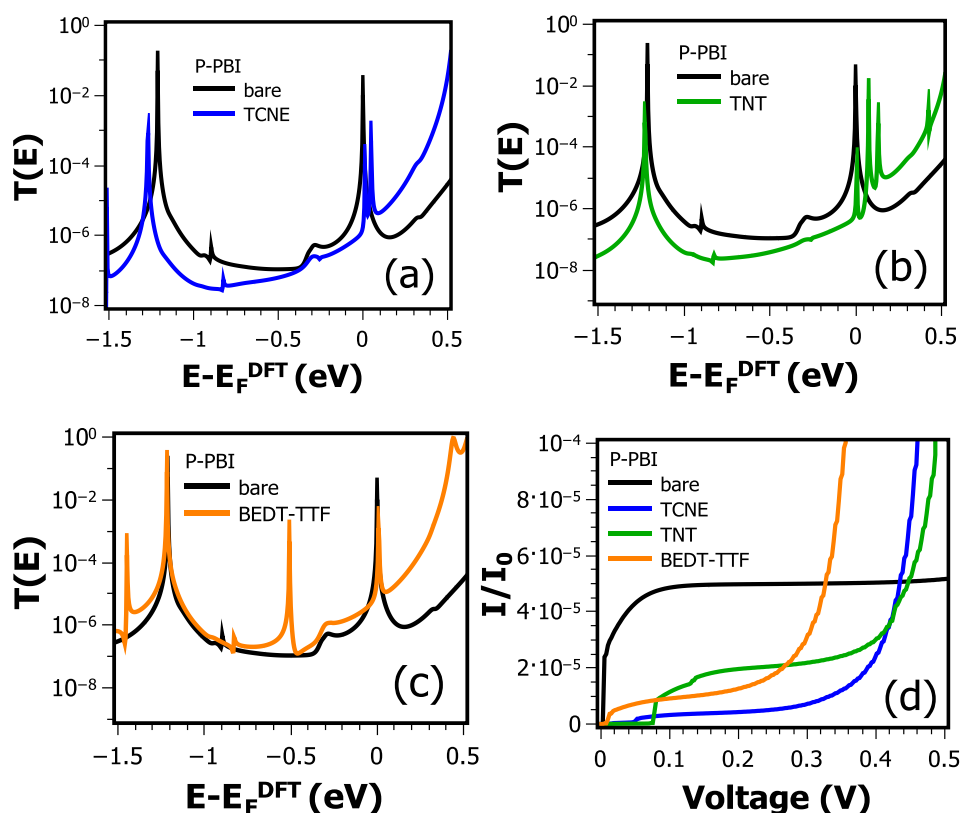


Figure 3.15. DFT calculations of the transmission coefficients as a function of energy at $T=0K$ for optimum configuration of **P-PBI** with (a) TCNE, (b) TNT, and (c) BEDT-TTF. The fourth figure (d) shows the current as a function of voltage at $T=300K$ for the bare **P-PBI** and in the presence of the three analyte molecules (TCNE, TNT, and BEDT-TTF).

Figures 13.15a-c show the transmission coefficients $T(E)$ as a function of energy E for the structures in Figures 3.10d, 3.11d and 3.12d, which show each of the three analyte molecules on P-PBI molecule. The calculation implies almost the same behaviour for transmission curves in the presence of three analytes which happened with S-PBI molecule. Figure 13.15d also shows the corresponding I-V characteristics which demonstrates well the discrimination between the three analytes.

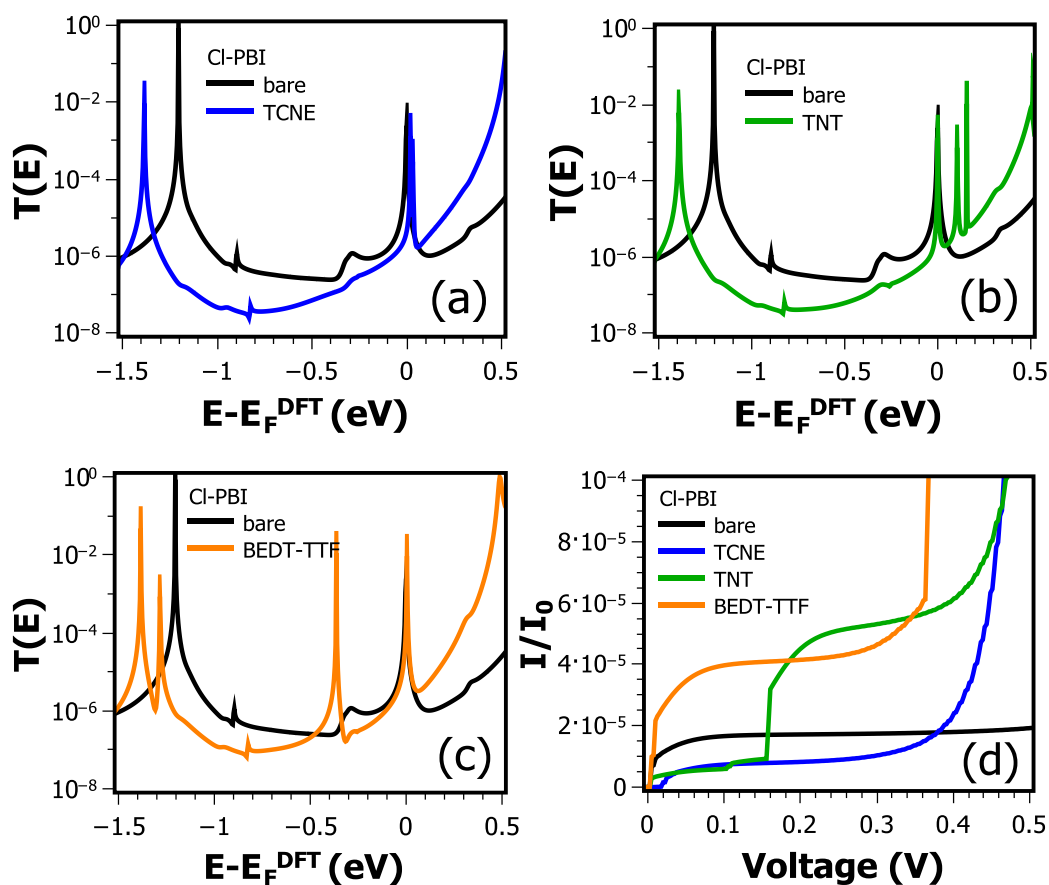


Figure 3.16. DFT calculations of the transmission coefficients as a function of energy at $T=0K$ for optimum configuration of **CI-PBI** with (a) TCNE, (b) TNT, and (c) BEDT-TTF. The fourth figure (d) shows the current as a function of voltage at $T=300K$ for the bare **CI-PBI** and in the presence of the three analyte molecules (TCNE, TNT, and BEDT-TTF).

Similarly, for the structures in Figures 3.10e, 3.11e and 3.12e, Figures 13.16a-c for the case of three analytes bound to CI-PBI backbone, the calculations show the same properties of

transmission curves except in the presence of TCNE, there is no extra resonance close to LUMO. Figure 13.16d shows the corresponding I-V characteristics which again demonstrates the discrimination between the three analytes.

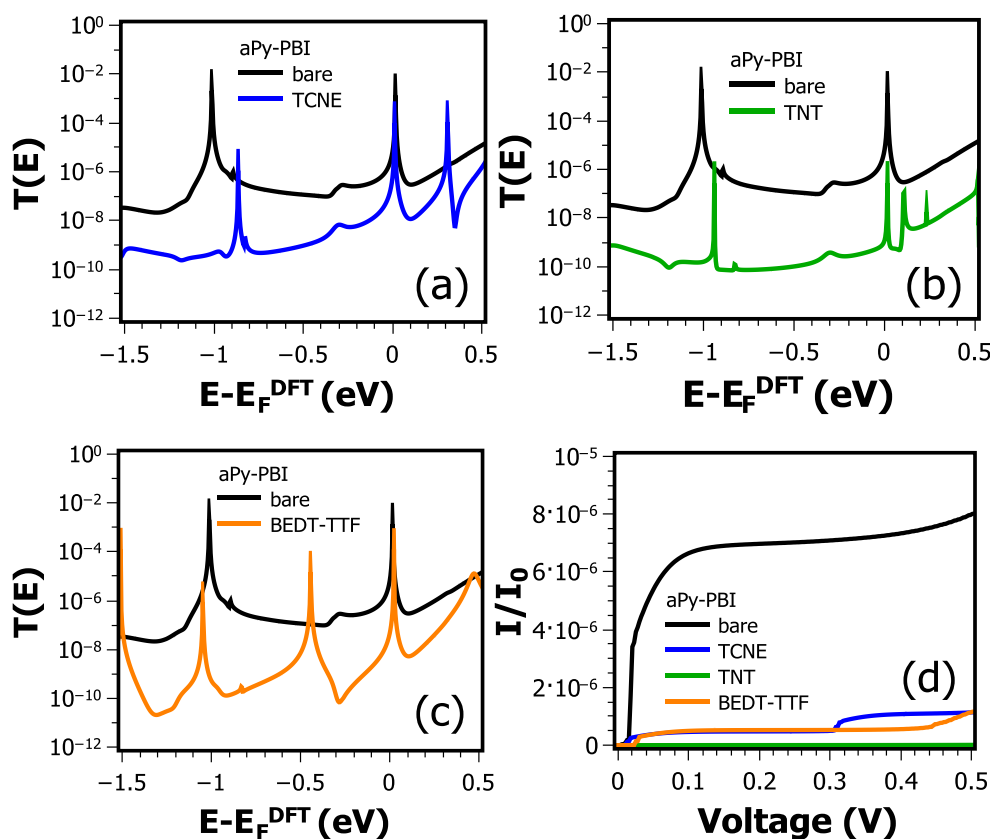


Figure 3.17. DFT calculations of the transmission coefficients as a function of energy at $T=0K$ for optimum configuration of **aPy-PBI** with (a) TCNE, (b) TNT, and (c) BEDT-TTF. The fourth figure (d) shows the current as a function of voltage at $T=300K$ for the bare **aPy-PBI** and in the presence of the three analyte molecules (TCNE, TNT, and BEDT-TTF).

Finally, for the structures in Figures 3.10f, 3.11f and 3.12f, Figures 13.17a-c show the transmission coefficients $T(E)$ versus E for each of three analytes bound to the backbone of the asymmetric molecule aPy-PBI. Here, for all cases the transmission curves around E_F decrease, in the presence of TCNE and TNT, there is also shifting of the HOMO resonance in the same direction that happened for Py-PBI and it is also accompanied by additional

resonances close to LUMO. For the donor BEDT-TTF a resonance also appears in the HOMO-LUMO gap.

3.2.4 Evaluating of error in the currents for a distribution of geometries

The error estimate associated with the statistical analysis of the 214 current curves is given by

$$\sigma_m = \sigma / \sqrt{214 - 1} \quad (3.2.2)$$

$$\sigma = \sqrt{\frac{1}{214} \sum_{i=1}^{214} (I_i - \langle I \rangle)^2} \quad (3.2.3)$$

where σ_m is standard deviation in the mean of current $\langle I \rangle$.

3.2.5 Fluctuation positions of the analytes above the PBIs backbone

The results of Figure 3.13 correspond only to optimally-bound analytes. At room temperature, the adsorbates are subject to thermal fluctuations and will sample many positions across the PBI backbones. To investigate the role of fluctuations, for each PBI molecule we repeated the above calculations for 214 configurations of each adsorbate. The results for the Py-PBI molecule are shown in figures (4.18a-c). For illustrative purposes, we only show 35 configurations (the results for all 214 transmission curves are shown in Figures (3.19)-(3.23)). In each case we see that fluctuations in the position of the analyte cause the transmission resonances to shift over a range of energies. In many cases, these possess a characteristic Fano line shape, associated with the interaction between localized states on the analytes and extended states on the PBI backbones [91, 97]. After computing the ensemble average of these curves, the resulting ensemble-averaged, room-temperature current as a function of voltage is shown in figure (3.18d), along with the standard deviation

in their means. This demonstrates that even in the presence of fluctuations, BEDT-TTF produces a distinctly different I-V curve from the other two analytes.

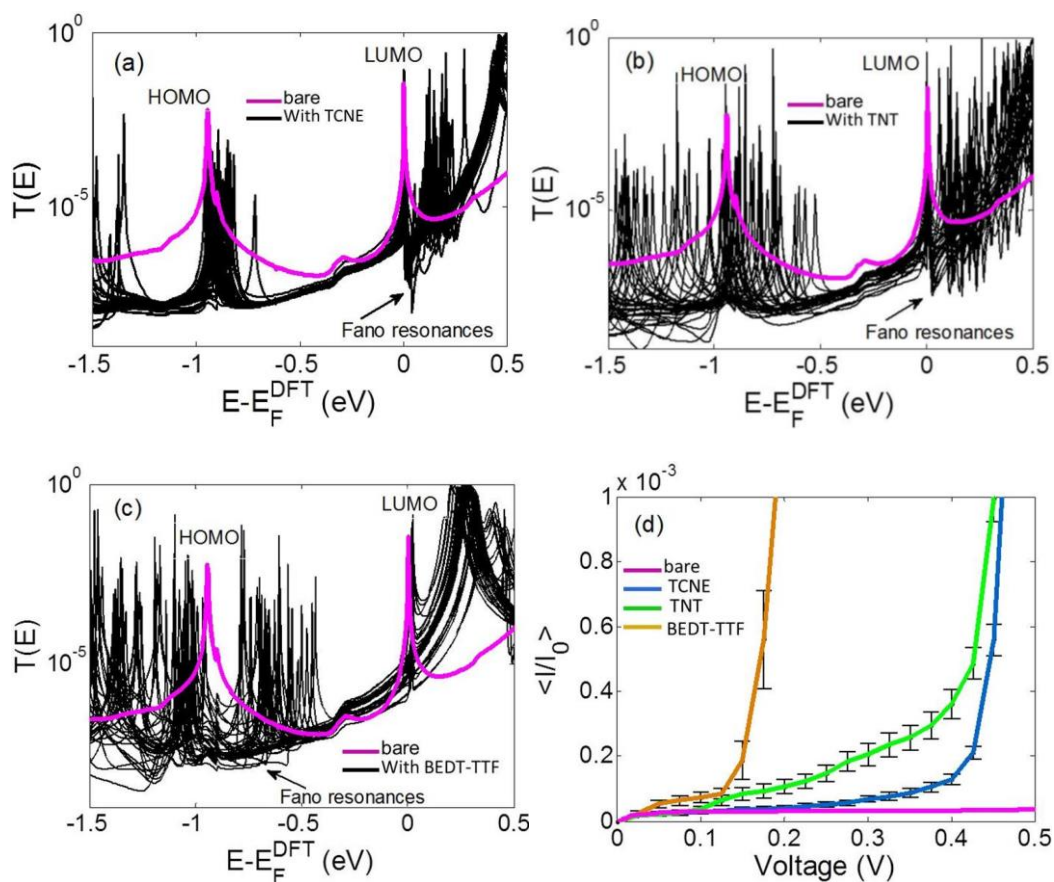


Figure 3.18. Illustrates the transmission curves of 35 fluctuation position in case Py-PBI to explain the effect of adsorption of analyte molecules (a) TCNE, (b) TNT, (c) BEDT-TTF, and (d) shows the ensemble-averaged of current as a function of voltage at $T=300K$ for bare Py-PBI and in the presence of the three analyte molecules (TCNE, TNT, and BEDT-TTF), where the error bars in Figure 3.18d shows the standard deviation in the means of the currents.

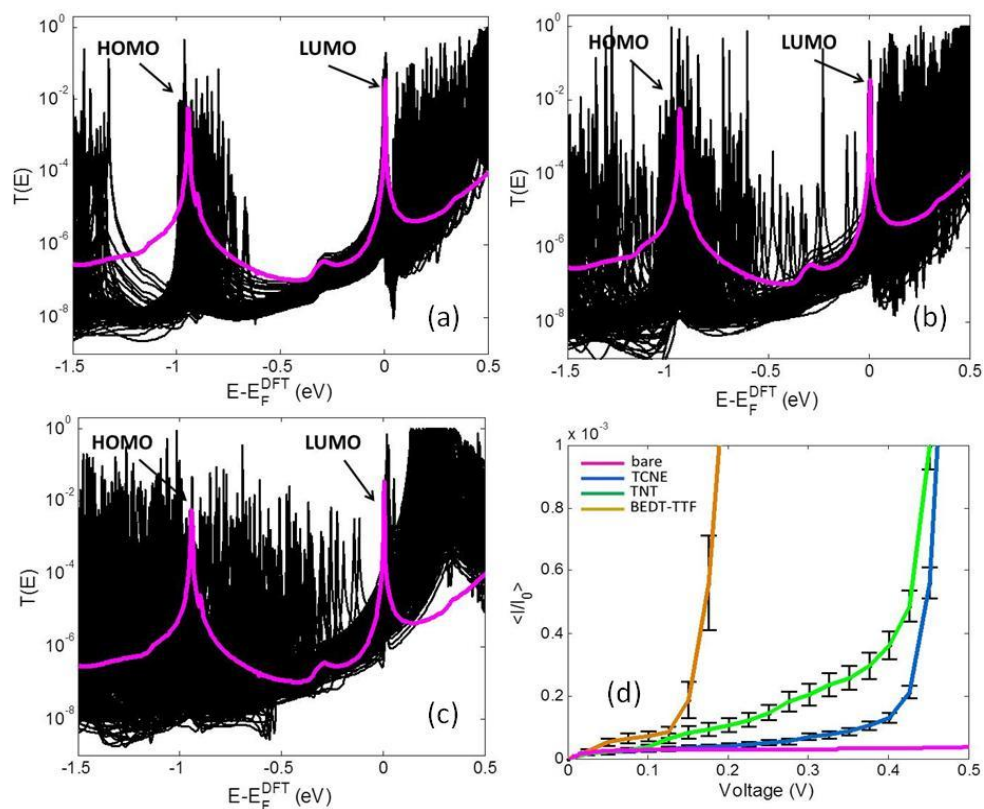


Figure 3.19. DFT calculations of the transmission coefficients as a function of energy for Py-PBI with different configurations of the single-molecules absorbrates (a) TCNE , (b) TNT, and (c) BEDT-TTF, and (the pink line) is bare case.. The fourth figure (d) shows the average of current as a function of voltage at $T=300K$ which pass across Py-PBI with three analytes molecules (TCNE, TNT, and BEDT-TTF), where the error bars in Figure 3.19d shows the standard deviation in the means of the currents.

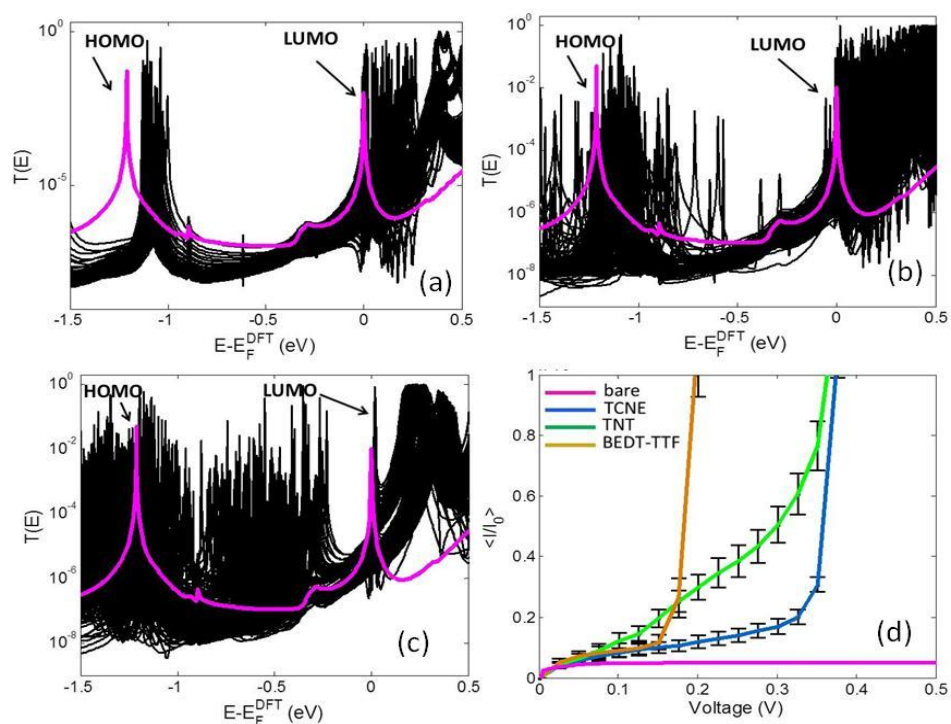


Figure 3.20. DFT calculations of the transmission coefficients as a function of energy for P-PBI with different configurations of the single-molecules absorbates (a) TCNE , (b) TNT, and (c) BEDT-TTF, and (the pink line) is bare case.. The fourth figure (d) shows the average of current as a function of voltage at $T=300K$ which pass across P-PBI with three analytes molecules (TCNE, TNT, and BEDT-TTF), where the error bars in figure 4.20d shows the standard deviation in the means of the currents.

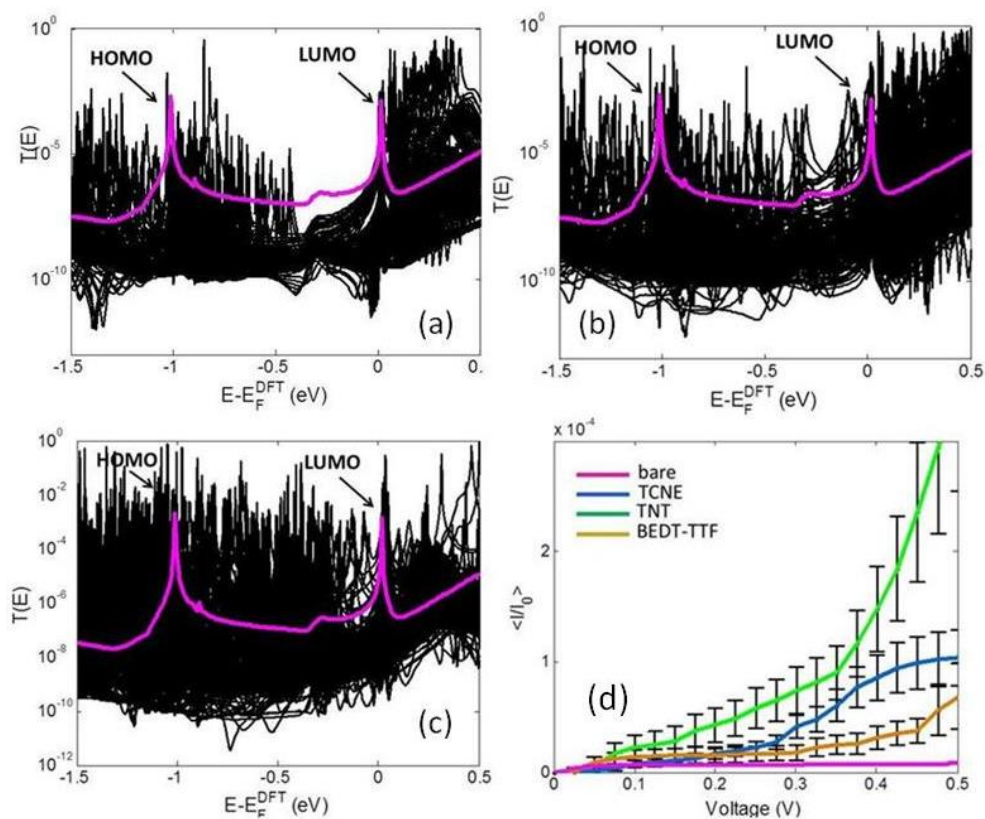


Figure 3.21. DFT calculations of the transmission coefficients as a function of energy for aPy-PBI with different configurations of the single-molecules absorbates (a) TCNE , (b) TNT, and (c) BEDT-TTF, and (the pink line) is bare case.. The fourth Figure (d) shows the average of current as a function of voltage at $T=300K$ which pass across aPy-PBI with three analytes molecules (TCNE, TNT, and BEDT-TTF), where the error bars in Figure 3.21d shows the standard deviation in the means of the currents.

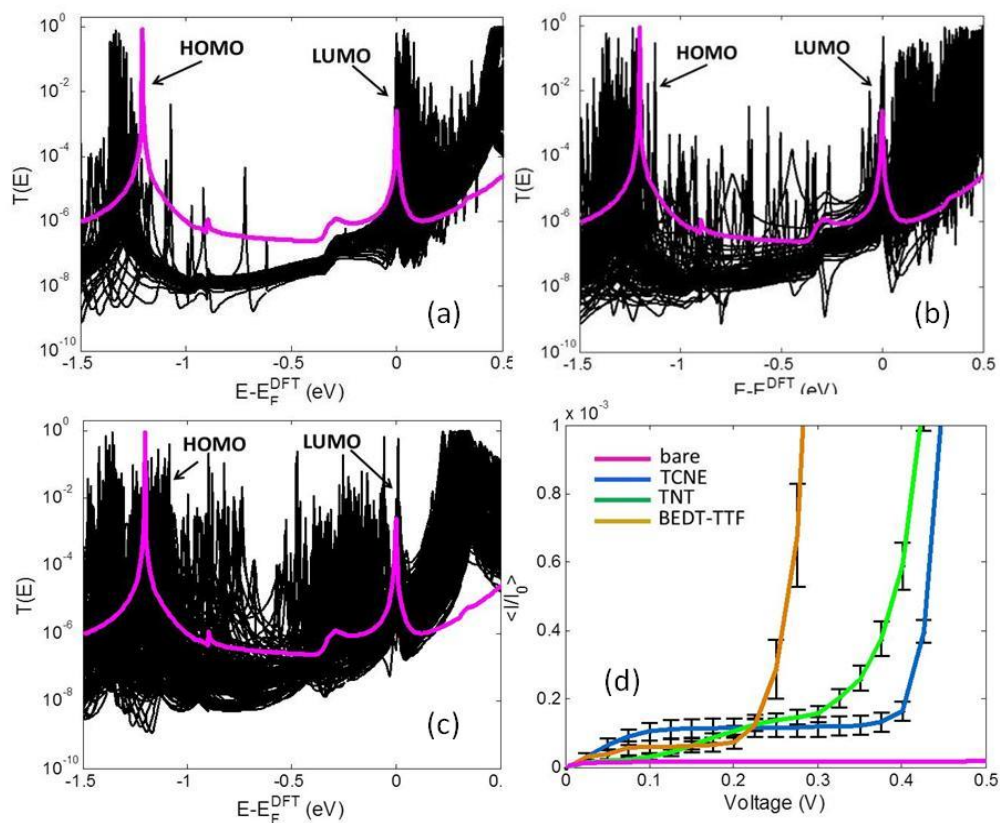


Figure 3.22. DFT calculations of the transmission coefficients as a function of energy for Cl-PBI with different configurations of the single-molecules absorbates (a) TCNE , (b) TNT, and (c) BEDT-TTF, and (the pink line) is bare case.. The fourth figure (d) shows the average of current as a function of voltage at $T=300\text{K}$ which pass across Cl-PBI with three analytes molecules (TCNE, TNT, and BEDT-TTF), where the error bars in figure 3.22d shows the standard deviation in the means of the currents.

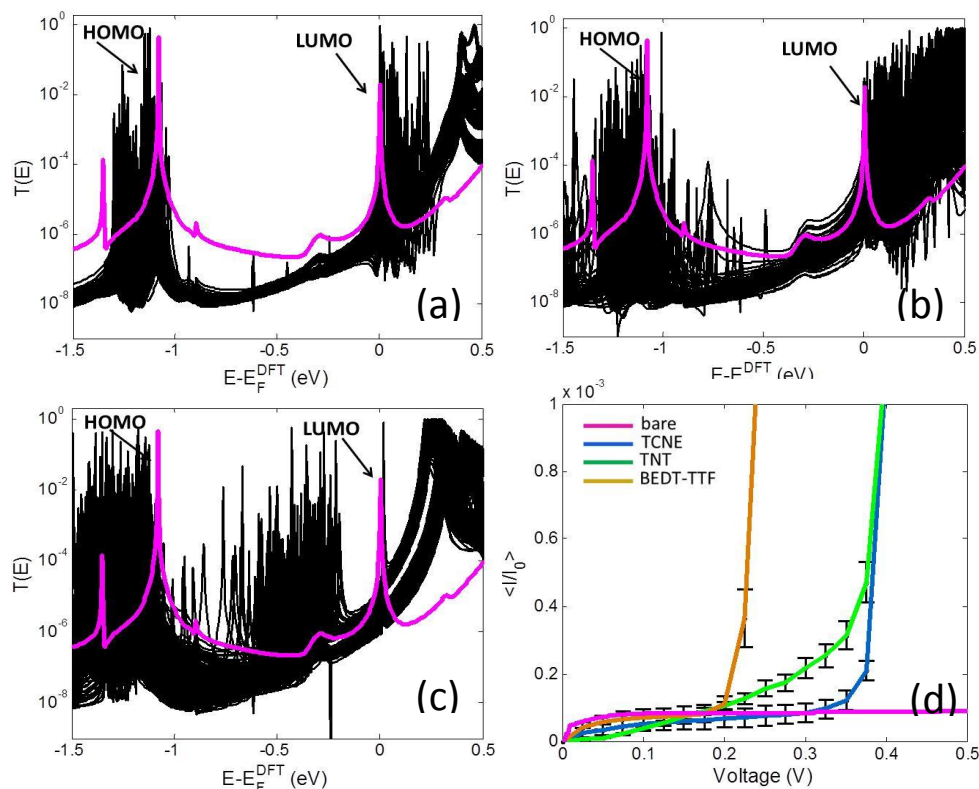


Figure 3.23. DFT calculations of the transmission coefficients as a function of energy for S-PBI with different configurations of the single-molecules absorbates (a) TCNE , (b) TNT, and (c) BEDT-TTF, and (the pink line) is bare case. The fourth Figure (d) shows the average of current as a function of voltage at $T=300\text{K}$ which pass across S-PBI with three analytes molecules (TCNE, TNT, and BEDT-TTF), where the error bars in Figure 3.23d shows the standard deviation in the means of the currents.

The corresponding room-temperature, ensemble-averaged zero-bias conductances for all analytes and backbone molecules are shown in Figure (3.24). This demonstrates that not only I-V curves, but also the conductance of each PBI backbone changes due to the adsorption of a single analyte molecule. For any one PBI derivative (e.g. P-PBI TNT compared with BEDT-TTF), the change in conductance upon binding may not discriminate between all analytes. However, the spectrum of five conductance changes forms a unique fingerprint, which can be used to discriminate between all three analytes.

For the five molecules: Py-PBI, P-PBI, aPy-PBI, Cl-PBI and S-PBI in the absence and presence of the three analytes for 214 positions, the transmission coefficients $T(E)$ versus

energy E were computed as shown in Figures 3.19-3.23 (a-c). The calculations show that with acceptors TCNE and TNT, there are shifting in the HOMO resonances and many extra resonances close to LUMO. Whereas in the presence of donor BEDT-TTF, there are also shifting in resonances HOMO below the HOMO of the bare case accompanied by additional resonances in the HOMO-LUMO gap. Figure 3.19d-3.23d shows the average of current as a function of voltage at $T=300\text{K}$ which pass across the all PBIs with three analytes molecules (TCNE, TNT, and BEDT-TTF), where the error bars shows the standard deviation in the means of the currents.

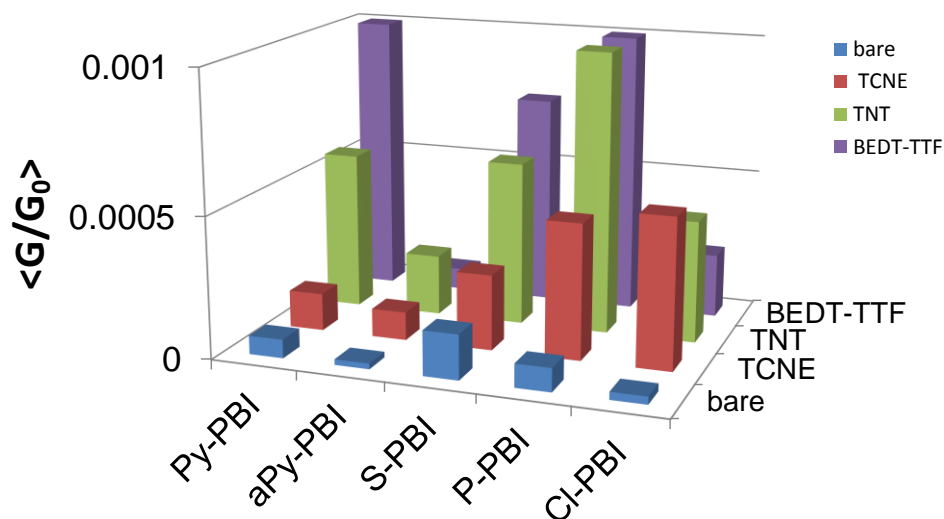


Figure 3.24. The room-temperature, ensemble-averaged conductance across the PBI family due to charge transfer complex formation (obtained from the average of the 214 configurations of the TCNE, BEDT-TTF and TNT) around the backbone of five PBIs.

It is interesting to note that the behaviour of the ensemble average is qualitatively different from the optimal binding configuration. Figures (3.17) and (3.21) show the transmission coefficient for the molecule aPy-PBI, in the absence and presence of the analytes. It is clear that the conductance in the presence of the analytes in their optimal binding configurations is lower than in the case of bare molecule. In contrast, figure (3.25 b) shows that the ensemble-averaged conductance, is higher in the presence of the analytes.

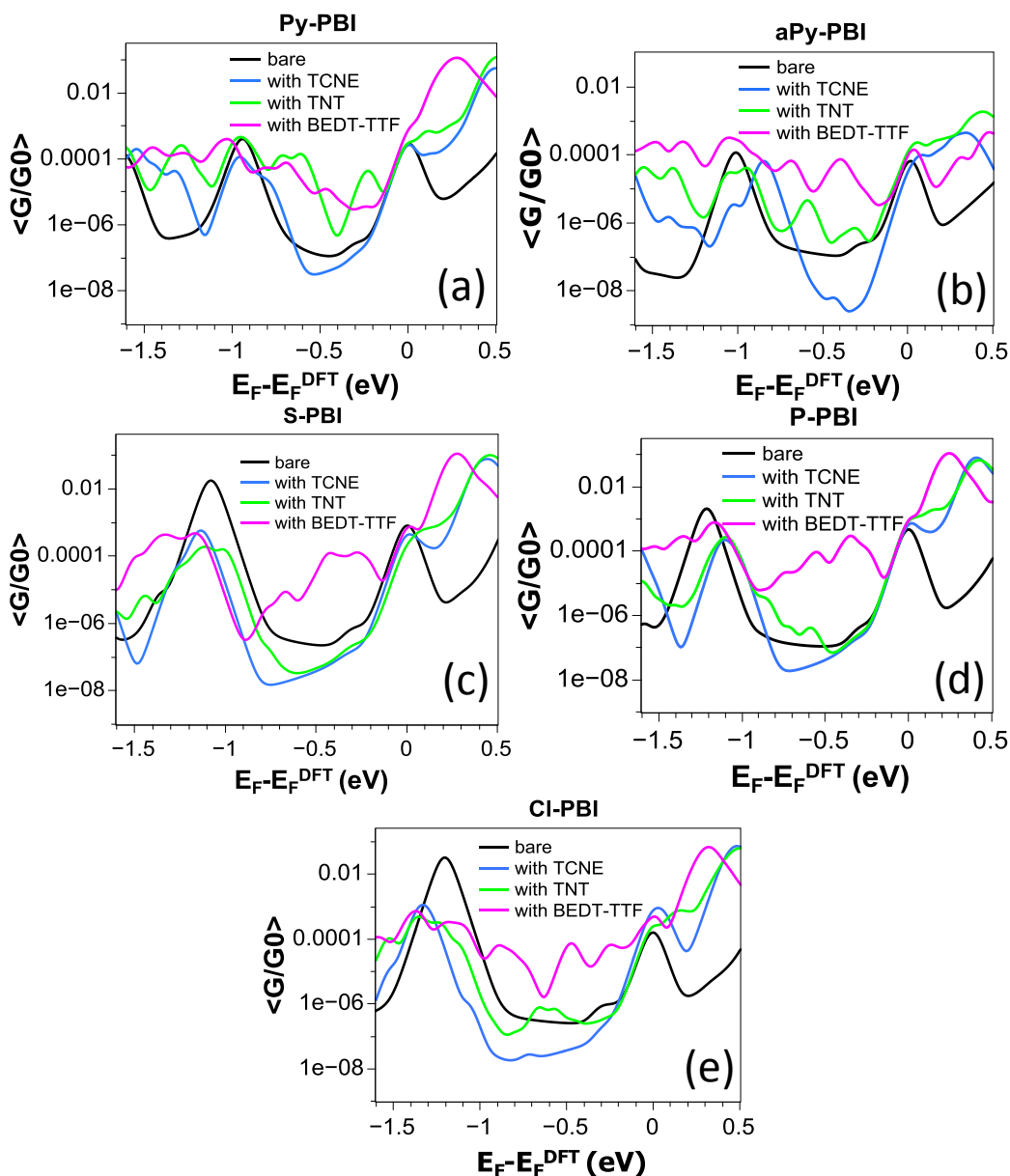


Figure 3.25. The room-temperature, configurationally-averaged as a function of Fermi energy for three analyte molecules (TCNE, TNT, and BEDT-TTF) absorbed on five PBI molecules.

3.2.6 Quantifying the sensitivity of the PBIs for discriminating sensing.

To quantify the potential of the five PBI derivatives (labeled $j=1, \dots, 5$) for the discriminating sensing of the three analytes TCNE, TNT and BEDT-TTF, (labeled $n=1,2,3$ and $m=1,2,3$) we calculated the ensemble-averaged, room-temperature currents I_{jn} as a function of voltage V and computed the following correlators of the currents

$$A_j^{nm} = \int_{-V/2}^{V/2} dV \left(I_{jn}(V) - I_{jm}(V) \right)^2 \quad (3.2.4)$$

These were then normalized by the squared currents of the bare backbones to yield the quantities:

$$X_j^{nm} = \frac{A_j^{nm}}{\int_{-V/2}^{V/2} dV \left(I_j(V_{bare}) \right)^2} \quad (3.2.5)$$

For $n \neq m$, table 1 shows the values of X_j^{nm} obtained for $V=1$ volt. Clearly, as defined, $X_j^{nm} = 0$ when $n = m$. In practice, a sensing event would involve measurement of a new set of curves ($I_{jm}(V)$ in Eq. (3.1.2)) and combining these with a ‘calibration set of curves ($I_{jn}(V)$ in Eq. (3.1.2)), in which case X_j^{nm} would be small but not zero when $n = m$.

Table 3.4. The values of X_j^{nm}

	PBIs	X_j^{12}	X_j^{13}	X_j^{23}
	aPy-PBI	0.3043	0.2776	0.0044
	Cl-PBI	0.0031	0.2457	0.2508
	P-PBI	0.0021	0.4101	0.4011
	Py-PBI	0.3641	0.4365	0.9161
	S-PBI	0.0309	0.1344	0.1748
SUM		0.7045	1.5043	1.7472

Table (3.4) and Figure (3.26) shows the value of X_j^{nm} when $n \neq m$. Ideally, to avoid false positives, these numbers should be as large as possible and since they are largest for Py-PBI, we conclude that Py-PBI is the best individual sensor. Nevertheless, for the most accurate discriminating sensing, the fingerprint of an analyte across all five backbones should be used.

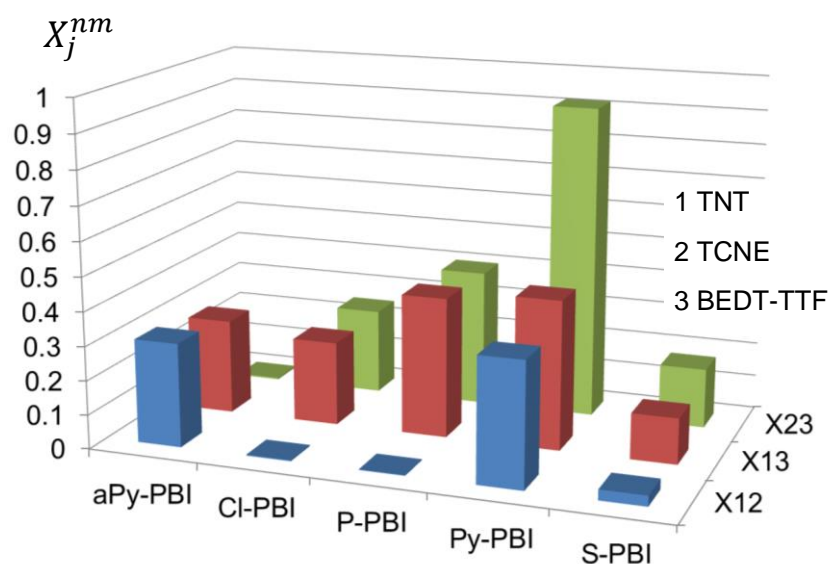


Figure 3.26. Comparison between the normalized correlators X_j^{nm} where n labels the three analytes (TNT, TCNE, and BEDT-TTF) and j labels the five PBIs. $V=1.0$ volts.

3.3 Summary

We demonstrated the potential of perylene bisimide (PBI) for label-free sensing of organic molecules by investigating the change in electronic properties of five symmetric and asymmetric PBI derivatives, which share a common backbone, but are functionalised with various bay-area substituents. Density functional theory was combined with a Greens function scattering approach to compute the electrical conductance of each molecule attached to two gold electrodes by pyridyl anchor groups. We studied the change in their conductance in response to the binding of three analytes, namely TNT, BEDT-TTF and TCNE, and found that the five different responses provided a unique fingerprint for the discriminating sensing of each analyte. This ability to sense and discriminate was a direct consequence of the extended π system of the PBI backbone, which strongly binds the analytes, combined with the different charge distribution of the five PBI derivatives, which leads to a unique electrical response to analyte binding.

Chapter 4

Three-State Single-Molecule Naphthalenediimide Switch:

Integration of a Pendant Redox Unit for Conductance Tuning

The following work was carried out in collaboration with the experimental group of Bern University. I will present my theoretical work on a single-molecule naphthalenediimide switch, alongside the Bern experimental results. The results presented here were published in the following paper [124]:

“Three States Single-Molecule Naphthalenediimide Switch: Integration of Pendant Redox Unit for Conductance Tuning”

Angewandte Chemie International Edition, 54.46 (2015): 13586-13589.

4.1 Introduction

Functional molecules with bi-/multi-stable states have been studied intensively [125-130] because they are potentially interesting building blocks for molecular-level electronics [131-136] and ultra-high density storage devices [137, 138]. Various switchable molecules were fabricated by incorporating photochromic or redox-active moieties within the molecular

charge transport pathway, *e.g.*, tetrathiafulvalene (TTF), [6, 139] benzodifuran (BDF), [140] anthraquinone (AQ), [7] and ferrocene (Fc) [141]. In these studies, a functional unit was involved in the charge transport pathway, which is expected to provide more significant tuning of single-molecule conductance. On the other hand, single-molecule devices with a pendant functional unit (Figure 4.2a), which is not directly involved in the charge transport pathway, are also of great interest because it offers much more flexibility for molecular design and synthesis, and therefore, finer tuning of the charge transport through the single molecule device.

Naphthalene diimide (NDI) molecules (Figure 4.1) have rapidly emerged as an interesting class of materials in organic electronics (See more details in chapter 1). Core substituted NDIs with electron-donor groups can be tuned to improve the optical/electrical properties [142]. More interestingly, substitution of the naphthalene core provides the opportunity to study charge transport through the naphthalene unit (marked as gray in Figure 4.2b) while diimide unit (marked as green in Figure 4.2b) served as a pendant functional unit with strong coupling to the naphthalene backbone in which improving the response to an external stimulus such as, an applied electrochemical gating. Varying the applied potential to the NDI molecules, a sequence of two sequential electron transfer reactions transforms the neutral species (NDI-N) into the corresponding radical-anion (NDI-R), and finally into the di-anion species (NDI-D). Therefore this core substituted NDI molecule can be considered as a prototypical molecular junction to evaluate the effect of pendant redox groups on the single-molecule conductance.

In this Chapter, I report an electrochemically controlled STM-based break junction study [7] of a NDI-BT molecule (which is shown in Figure 4.1) with pendant diimide redox unit strongly coupled to the molecular backbone. We demonstrate that these reversible redox-transitions in the pendant diimide unit indeed cause pronounced changes in the charge

transport through the single molecular NDI-BT junction. To get better understanding of the microscopic mechanism of the electrochemical gating, we employed density functional theory (DFT) to model the charge double layer in the molecular junction comprised of the ions in the supporting electrolyte and computed the electrical conductance with non-equilibrium Green's function (NEGF) method as a function of the NDI-BT redox-states.

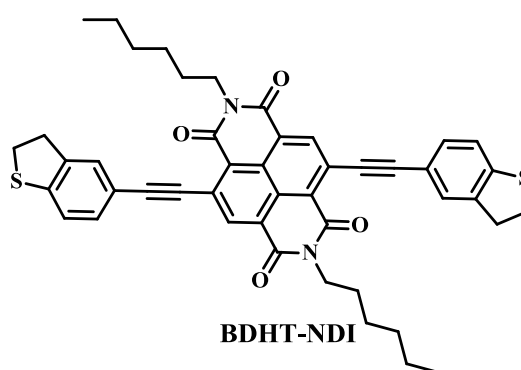


Figure 4.1. The chemical structure of NDI-BT and its synthetic approach.

4.2 Experimental work:

4.2.1 Single-molecule break junction experiments

The Bern Scanning Tunnelling Microscopy Break Junction (STMBJ) experiments were performed with a Molecular Imaging PicoSPM in an environmental chamber and equipped with a dual preamplifier. The current-distance measurements were performed with a lab-build analog ramp unit. The current was recorded at a fixed bias potential during repeated formation and breaking of the molecular junctions [2].

Au(111) was used as the substrate and the facet cleaned before the experiments using electrochemical polishing and butane flame annealing followed by cooling under Ar atmosphere. Then, the freshly prepared substrate was drop-casted with 30 μL of 0.5 mM NDI-BT in THF. For the electrochemically controlled STMBJ experiments, single Pt wires

were used as the counter and quasi-reference electrodes and the gold STM tips prepared with AC etching in a 1:1 (v/v) mixture of 30% HCl and ethanol solution, were coated with polyethylene to ensure that the electrochemical current on the tip is below 1~2 pA. Finally, the Kel-F cell was mounted on top of the substrate and the supporting electrolyte (ionic liquid HMImpF6) was added into the cell. The STM images and cyclic voltammograms were recorded frequently during the measurements. The latter were used to check the redox peak position and to ensure that there is no oxygen in the system and no drift of the reference electrode potential. After assembling the experiment, the tip was approached toward the substrate to fulfill the preset tunnelling parameters ($i_T = 100$ pA and a bias voltage $V_{\text{bias}} = 0.10$ V).

After positioning the tip in the tunnelling regime, the STM feedback is switched off and current-distance measurements were carried out. For the stretching cycle measurements, the controlling software approaches the STM tip to the drop-casted gold surface. The approach was stopped until a predefined upper current limit was reached to a value which corresponds to the formation of several gold-gold contact. After a few ms delay ensuring the formation of stable contacts, the tip was withdrawn until a low current limit of ~ 10 pA was reached. The approaching and withdrawing rates were both 87 nm/s. The whole current-distance traces were recorded with a digital oscilloscope in blocks of 186 individual traces. Up to 2000 traces were recorded for each set of experimental conditions to guarantee the statistical significance of the results.

The design of NDI-BT is based on the following considerations: i) NDI can be reversibly transformed into the respective radical anion and dianion with distinguishable energy gaps, ii) the presence of a dihydrobenzo[*b*]thiophene anchor group enables NDI-BT to be contacted to source-drain electrodes (Figure 4.2b) [143] and iii) the presence of triple carbon-carbon bonds introduces a certain rigidity into the NDI-BT. The NDI-BT assembly

was prepared on an Au(111) substrate by drop-casting 30 μL of a solution of 0.5 mM NDI-BT in THF. As the reduction of the NDI-BT to the dianion requires rather negative potentials, cyclic voltammetry (CV) and STMBJ measurements were carried out in HMImpF₆ (1-hexyl-3-methylimidazolium hexafluorophosphate) in an oxygen-free environment. Compared to the electrochemical response of the bare Au(111)/HMImpF₆ interface (grey curve in Figure 4.3a), two pairs of reversible redox-peaks appear in the voltammogram when the NDI-BT layer is present (black curve in Figure 4.3a).

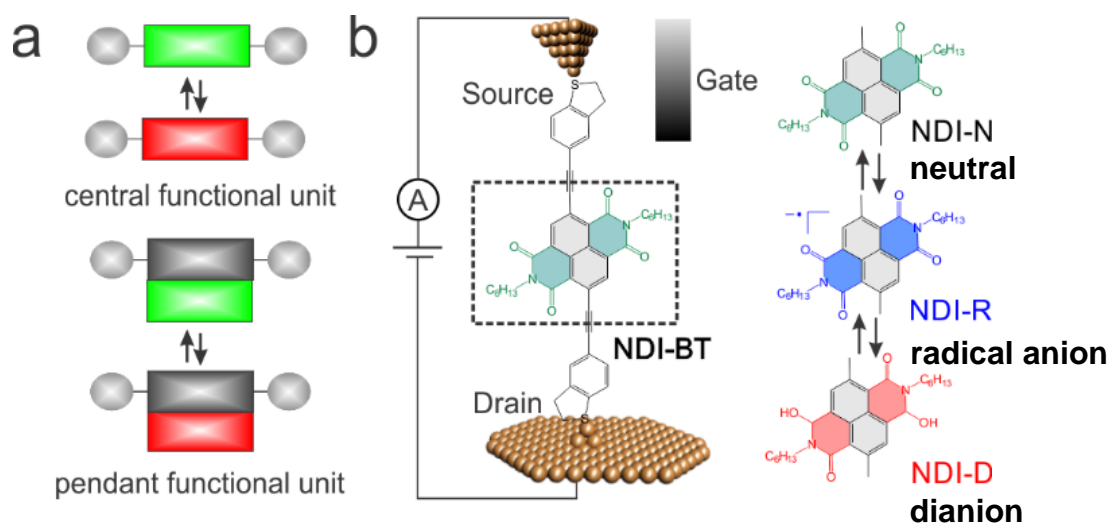


Figure 4.2. (a) Schematic illustration of single-molecule device with a central redox unit in the charge transport pathway and a pendant redox unit. (b) Schematic illustration of electrochemically gated break junction experiment and molecular structure of NDI-BT in neutral state (NDI-N), radical anion state (NDI-R) and dianion state (NDI-D).

The first redox peak is located around -0.85V versus Fc/Fc^+ and is attributed to the NDI-N/NDI-R redox process. The second redox peak is observed around -1.15V versus Fc/Fc^+ corresponds to the redox process of NDI-R to the NDI-D states.

The charge transport properties of the single NDI-BT molecule were studied by STM-BJ measurements at room temperature [2]. Figure 4.3b displays representative conductance (G) versus distance (Δz) traces measured at three different electrode potentials corresponding to

NDI-N (black), NDI-R(blue), and NDI-D(red). Most of the curves show an initial conductance feature at G_0 with $G_0 = 2e^2/h = 77.5 \mu\text{S}$, which corresponds to the single gold-gold atomic conductance [3]. Subsequently, the conductance decreases abruptly (“jump out of contact”)[144] by several orders of magnitude. The plateaus observed in the range from $\sim 10^{-3} G_0$ to $10^{-4} G_0$ are assigned to the conductance features of the single molecular NDI junctions, which strongly depend on the applied potential.

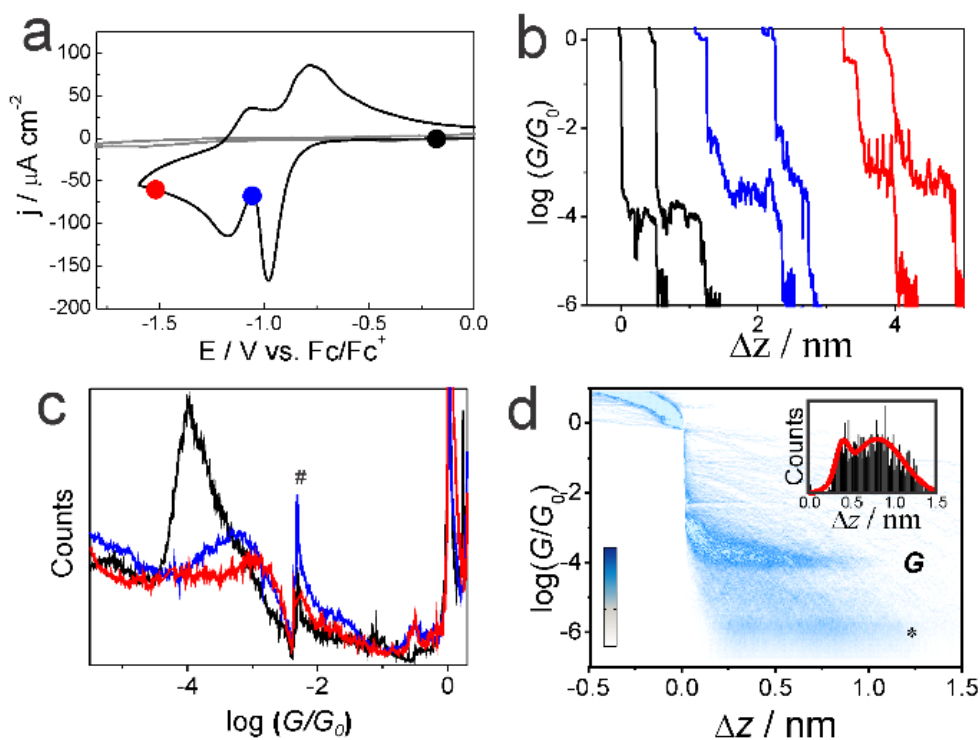


Figure 4.3. Figure 4.3 (a) CVs of NDI-BT immobilized on the Au(111) electrode (black curve) and bare Au(111) (gray curve) in HMImPF₆. The scan rate was 50 mV s⁻¹. (b) Typical conductance-distance traces at different potential black: NDI-N at -0.2 V, blue: NDI-R at -1.05 V, red: NDI-D -1.5 V versus Fc/Fc⁺ (c) conductance histogram constructed from 1000 individual traces sampled at different potential, # presents an artifact caused by the switching between different current measured range of the linear amplifier (d) 2D conductance-distance histogram of NDI-N, presents the current measurement noise level during the electrochemical-STM BJ measurement. The inset Figure d displays the characteristic displacement histograms of NDI-N.

The two-dimensional (2D) conductance histogram [145, 146] shown in Figure 4.3d provides direct access to the evolution of molecular junctions during the formation, stretching and

break-down steps. The high-density data cloud around $10^{-4.5} G_0 \leq G \leq 10^{-3.5} G_0$ represents the conductance range of the single NDI-N molecule bridging the gold electrodes. The inset Figure 4.3d displays the characteristic displacement histograms[147] of NDI-N and shows that two peaks corresponding to tunnelling and molecular junction in figure 4.3d led to a junction formation probability of about 80 %.

The reversibility of the switching process was also evaluated by continuous conductance switching between different charge states. As shown in Figure 4.4a, each conductance histogram is constructed from 1000 individual traces, and the applied potential changed per 1000 traces between -0.2 V (NDI-N), -1.05 V (NDI-R), and -1.5 V (NDI-D) versus Fc/Fc^+ , respectively. It was found that the NDI-BT can be switched forward and backward from NDI-N via NDI-R to the NDI-D state (1st-5000th traces), or switched between the NDI-N and NDI-R state (5000th to 7000th traces). These switching cycles suggest that the three charge states of the NDI molecule can be tuned reversibly by changing the applied potential even after more than 7000 stretching cycles (Figure 4.4b). The conductance peak became slightly broader during the switching as a result of desorption of NDI-BT from the electrodes at a negative potential [148].

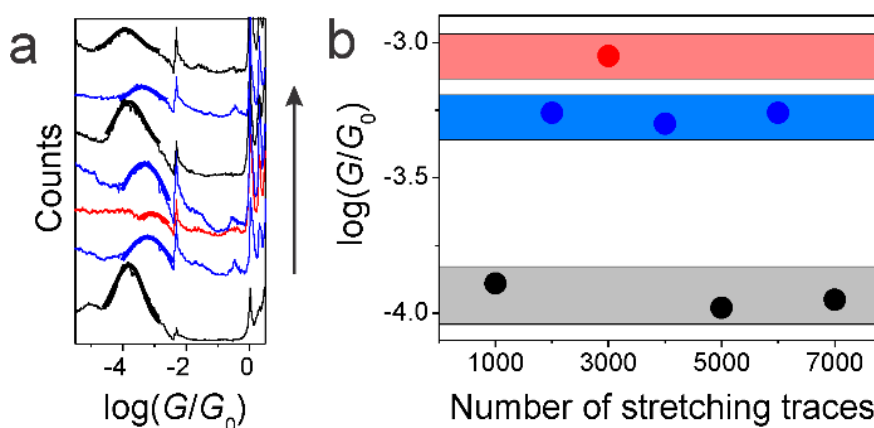


Figure 4.4. (a) Conductance histogram constructed from 1000 individual traces for each applied potential (b) Most-probable conductance value determined from conductance histograms shown in (a).

4.2.2 Further analysis of NDI-D conductance measurement

As shown in Figure 4.5a, it is found that many stretching curves show no molecular conductance plateau but only direct tunnelling, which is due to a desorption processes that happens close to the reduction potential of NDI-D. The desorption effect reduces the possibility for binding of the thiol anchor to gold electrodes. Thus the conductance peak in the conductance histogram of NDI-D is relatively small due to the low junction formation probability. For better statistics of the conductance peak of NDI-D, we also try to construct the conductance histogram excluding the traces that show no molecular plateau by fitting the conductance traces with stretching distance less than 1.0 nm (which is determined from the separation of stretching distance distribution shown in Figure 4.5b). As shown in Figure 4.5c, we observed a clear conductance peak located at $\sim 10^{-3} G_0$, which agrees well with the most probable conductance of NDI-D determined without data selection.

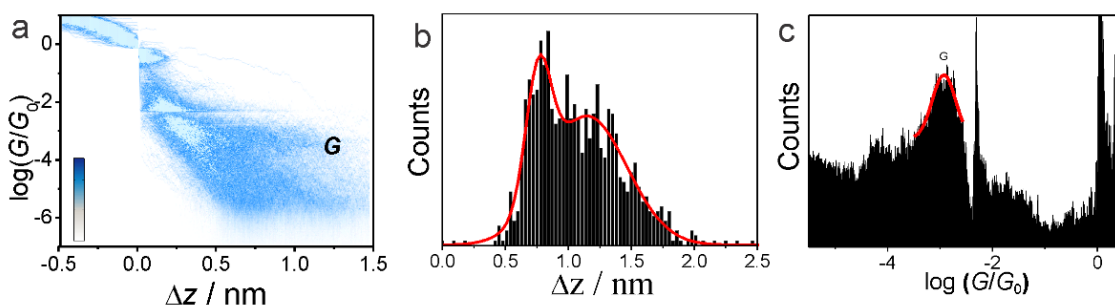


Figure 4.5. (a) 2D conductance-distance histogram of NDI-D (b) Characteristic displacement histograms of NDI-D determined from conductance region between $10^{-6} G_0$ and $0.7 G_0$. (c) Conductance histogram of NDI-D excluding the traces show no molecular plateau.

4.3 Theoretical Method

To understand the observed switching mechanism between the three states of electrochemical gating we theoretically investigated the effect of the charge double layer on the conductance. The primary role of the charge double layer in our calculations is to control

the number of electrons on the NDI-molecule. To perform conductance calculations we used the Gollum [111] quantum transport code and the optimal gold-molecule-gold junction geometries and the Hamiltonian matrix elements were obtained using SIESTA [107]. To accurately describe single occupied levels of the NDI all calculations were spin-polarized and the electron transmission coefficient function $T(E)$ calculated as the average of the spin up and spin down transmission coefficients.

4.3.1 The junction and Charge double layer geometries

To calculate electrical properties for NDI molecule which was shown in chapter 1, the following method was applied. To begin with, the relaxed geometry of each molecule was found using the density functional (DFT) code SIESTA [107] which employs Troullier-Martins pseudopotentials to represent the potentials of the atomic cores [108] and a local atomic-orbital basis set. In particular, we used the customized basis set definitions to investigate the effects on the Mulliken population count in SIESTA while using the generalized gradient approximation (GGA-PBE) for the exchange and correlation (GGA) [109]. The Hamiltonian and overlap matrix elements are calculated on a real-space grid defined by a plane-wave cutoff of 150 Ry. NDI molecule is relaxed into the optimum geometry until the forces on the atoms are smaller than 0.02 eV/Å. Tolerance of Density Matrix is 10^{-4} , and in case of the isolated molecules a sufficiently-large unit cell was used for steric and electrostatic reasons.

For the relaxed geometry of isolated NDI molecule, we have constructed the junction geometries by placing the optimized NDI molecules between two nanogap gold electrodes. An example for the junction geometry is shown in Figure 4.6. After the NDI molecule is placed between the gold electrodes the geometry was again optimized. The optimization was performed with the SIESTA code using DZP basis sets for all elements except gold, for

which DZ basis set was used, GGA-PBE exchange-correlation parameterization, 0.0001 density-matrix tolerance and 200Ry grid cutoff. The Mulliken charges are computed consistently with the same setup. The initial distance between S atom (DHBT anchor group) and the centre of the apex atom of each gold pyramid was initially 2.4 Å. After geometry optimization the distance changed to a final value of 2.63 Å.

The charge double layers are added to both sides of the planar backbone of the molecule in the optimized junction geometry as shown in Figures 4.7 and 4.8. The charge double layer is built from sodium and chloride ions with fixed 2.23 Å distance between the sodium and chloride ions. After the charge double layer was added to the optimized junction geometry we performed a self-consistent single energy calculation to obtain the optimal electronic structure and performed electron transport calculation with the obtained Hamiltonian and overlap matrices. The charge of the molecule is calculated from the Mulliken population computed by SIESTA. To modify the amount of charge on the molecule we varied the charge double layer-molecular plane distance, denoted y , while the distance between the ions within the double layer were kept fixed. The distance y is defined as distance between the plane of the molecule and the centre of the closest ion. Figure 4.10 shows the number of electrons (ΔN) transferred from the NDI molecule to the gold electrodes as a function of distance y (Å). To account for the effect of varying environment this calculation was repeated with randomly constructed double layers. The charge double layer is initially constructed as an 2×8 array of sodium ion chloride ion pairs and then four pairs were randomly removed from this array to obtain the randomly constructed double layer.”.

The electron and spin transport calculations were performed with the GOLLUM implementation of non-equilibrium Green’s function (NEGF) method [111] to compute the transmission coefficient $T(E)$ for electrons of energy E passing from the left gold electrode to the right electrode. GOLLUM is a next-generation code, born out of the SMEAGOL code

[112] and uses NEGF combined with density functional theory to compute transport properties of a wide variety of nanostructures. The precise methodology of computing a non-spin-polarized and spin-polarized electron transport over a junction geometry is described in ref [111]. The Hamiltonian and overlap matrices are calculated with SIESTA, with the same parameters that used in Figure 4.6. The Mulliken charges are computed consistently with the same setup.

Once the transmission coefficient $T^\sigma(E)$ for electrons of energy E , spin of $\sigma = [\uparrow, \downarrow]$ passing through the molecule from one electrode to the other is computed, we calculate the zero-bias electrical conductance G using the finite temperature Landauer formula [Eq. 4.1.2 in the Chapter 3].

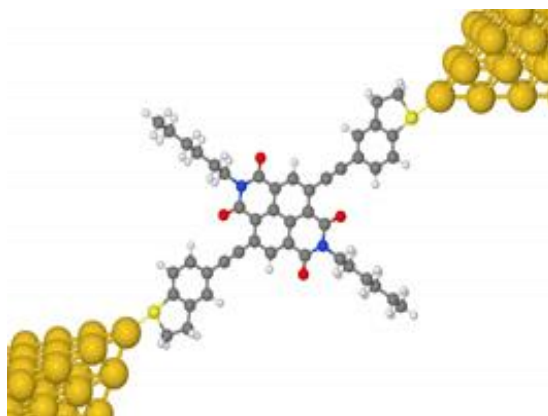


Figure 4.6. Optimized configuration of NDI molecule attached to gold electrodes.

In case of spin-polarized calculation $T(E)$ is the spin-averaged transmission coefficients. Figure 4.13 compares the zero and room temperature conductances calculated from the same transmission coefficients. Near the resonance peaks the conductance varies with temperature significantly.

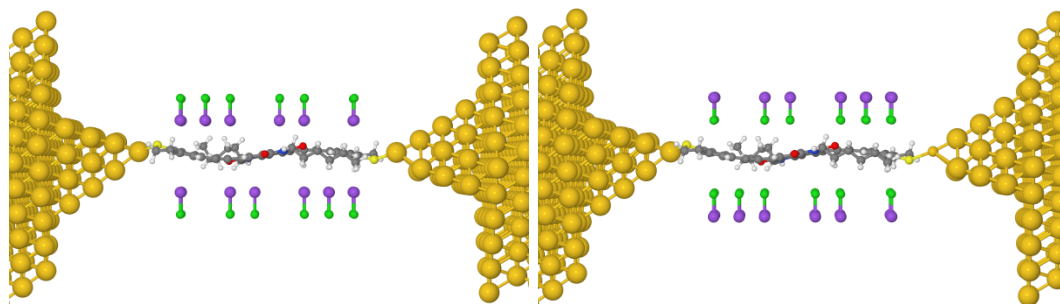


Figure 4.7. NDI molecule attached to gold electrodes in the presence of charge double layer above and below the molecule. The positive sodium ion is purple and the negative chloride ion is green.

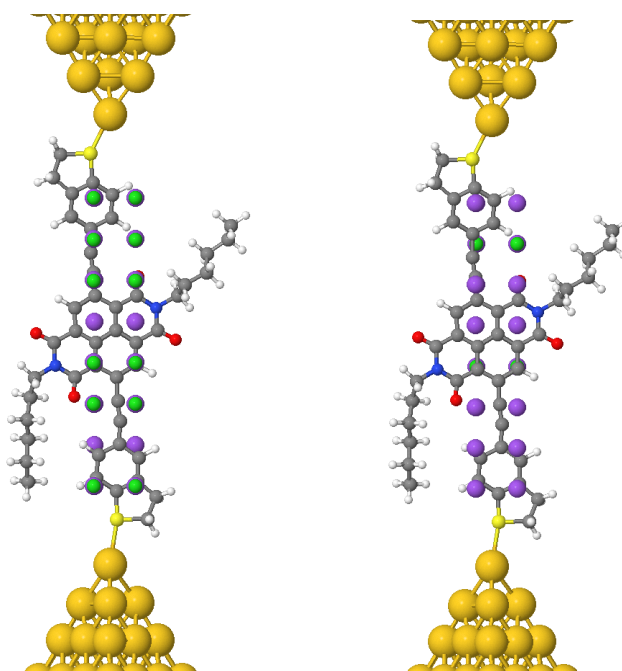


Figure 4.8. shows the geometries on Figure 4.7 from another orientation to illustrate the charge double layer around the backbone of the molecule.

4.4 Results and discussion

The three stages of gating are modelled with the three types of charge double layers (CDLs) shown in Figure 4.9. To model the effect of gating, the distance (y) between the double layers and the plane of the molecule was adjusted such that the number of extra electrons on the molecule was 0, 1 and 2 for the neutral, radical anion and dianion states, respectively. Figure 4.9a shows a negative charge double layer (the negative ions of the double layer lie closer to the plane of the NDI molecule) for which the NDI is neutral. Figures 4.9b, c show

positive charge double layers that attract electrons from the gold leads to the molecule, thereby creating the radical anion and dianion states.

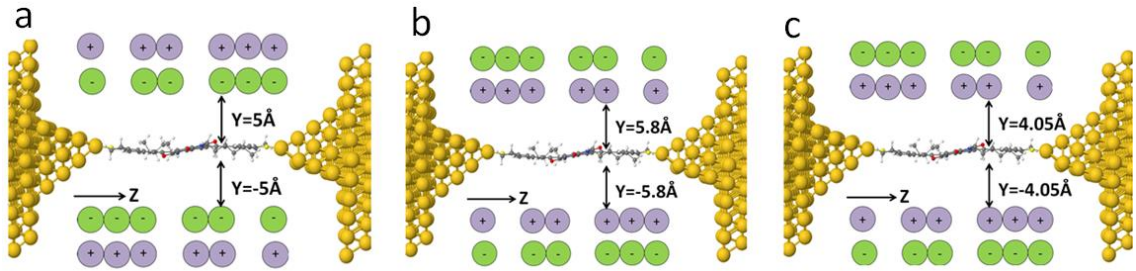


Figure 4.9. Junction geometries with charge double layers for the three states of electrochemical gating. (a) The neutral state with negative-positive CDL that adjusts the molecular charge to zero. (b) and (c) The radical anion and dianion states with positive-negative CDLs.

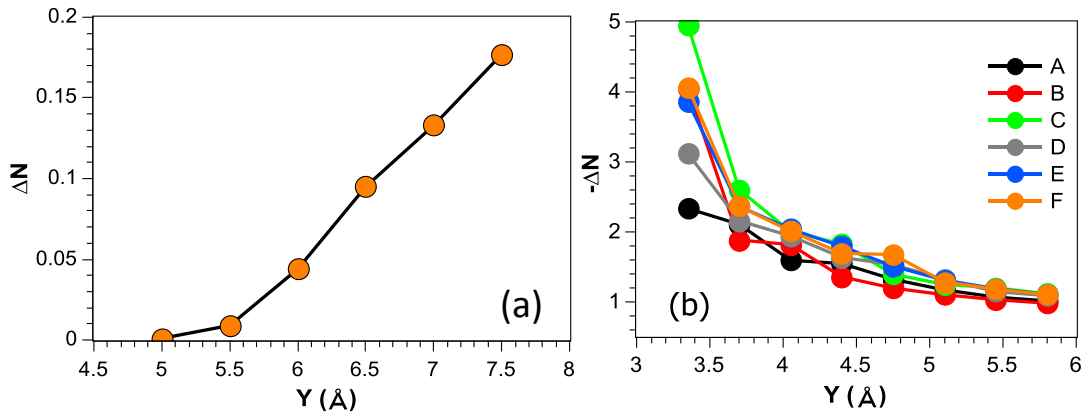


Figure 4.10. The number of electrons (ΔN) transferred from the NDI molecule to the gold electrodes as a function of distance Y (\AA) between the molecule and the double layer. (a) shows ΔN when the chloride points towards the NDI, and (b) shows $-\Delta N$ when the sodium points towards the NDI (the online color) A, B, C, D, E and F are different randomly-chosen charge double layers.

To account for fluctuations in the charge double layer, the transmission coefficient and conductance were computed for different charge double layer arrangements, in which the anions and cations were randomly arranged at a fixed distance y . These were then averaged to yield the theoretical conductance G and transmission coefficient $T(E)$ as shown in Figure (4.14a-d).

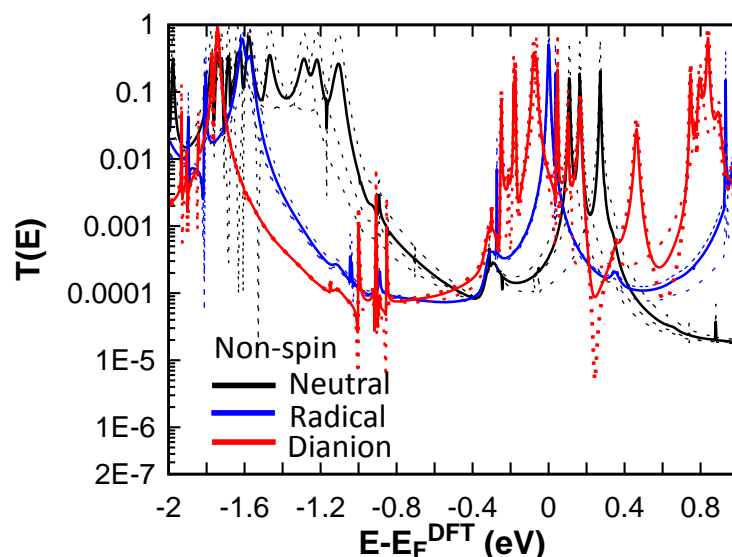


Figure 4.11. shows (the dotted lines) the transmission coefficient curves for randomized configurations of double layers with non-spin polarization, where the thick lines are the averaged transmission coefficient as a function of energy for NDI-molecule attached to the electrodes in the three cases: neutral (black) , radical (blue), and dianion (red).

The conductances, which were computed from the transmission coefficients at the Fermi energy using the room temperature Landauer formula, show an increasing trend upon moving from neutral state to the dianion state. In the radical anion state, the Fermi energy is trapped between two single electron resonances. This is apparent only in the spin-polarized calculation. In contrast, and as expected, the non-spin-polarized calculations give qualitatively different (and inaccurate) theoretical trends because single occupied orbitals are by definition located at the Fermi energy, and thereby result in an unphysical high conductance for the radical state (see Figure 4.11 and 4.12).

Figure 4.14d illustrates that the electrochemical gating experiment consistently increases the conductance as the molecular charge goes from the neutral state to the dianion state. This trend of theoretical charge double layer model agrees well with the experiment as Figure 4.14d illustrates. The theoretical conductance values are higher than the measured ones for all three states, which can be attributed to the neglect of environmental and thermal

effects.[20] DFT is also known to underestimate the HOMO-LUMO gap, which results in an overestimated conductance.[14, 16, 21].

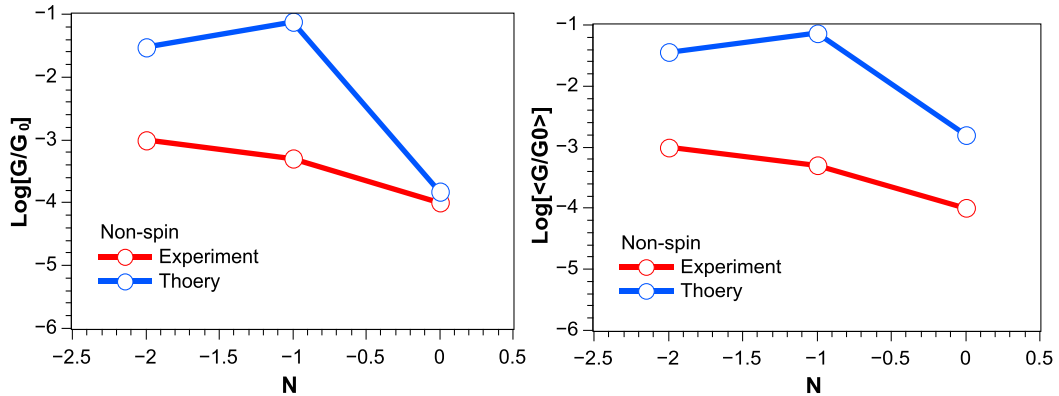


Figure 4.12. DFT Non-spin-polarized calculations to explain the comparison between the experimental and theoretical results, where left shows the logarithm scale of electrical conductance of particular configuration, and right shows the logarithm scale of ensemble averaged of electrical conductance of randomized configurations.

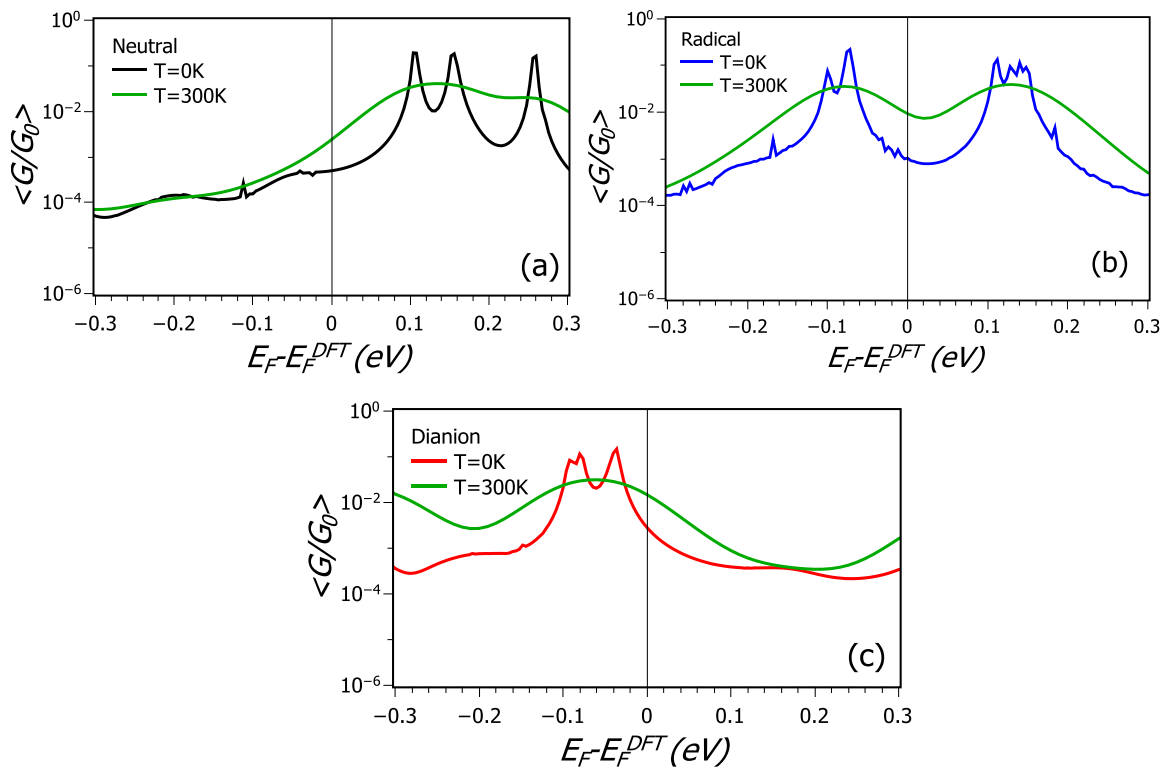


Figure 4.13. Shows the comparison between the room temperature and zero temperature conductances for a range of Fermi energies.

Figures 4.13a-c demonstrate the zero and room temperature conductance comparison in the three states, the calculation shows near the resonance peaks the conductances vary with temperature significantly.”

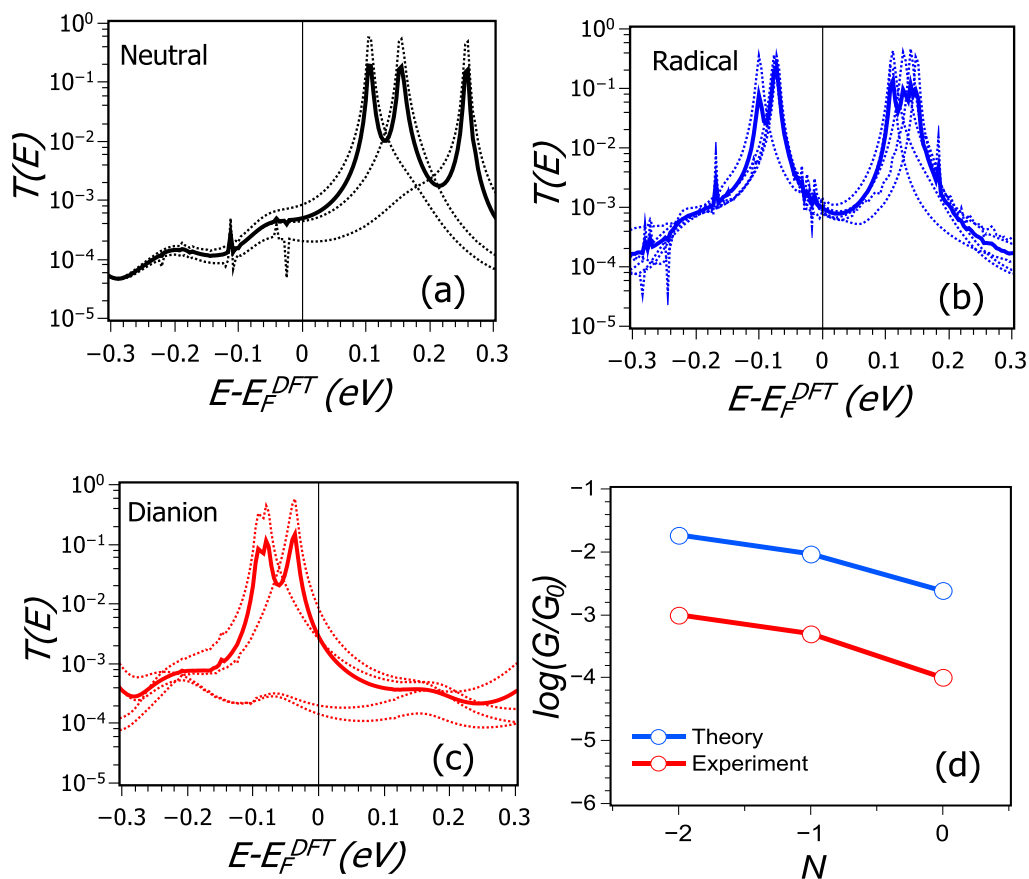


Figure 4.14. (a), (b) and (c) show the transmission curves for junction geometries with double layers located at distances $y=5\text{\AA}$, $y=5.8\text{\AA}$ and $y=4.05\text{\AA}$, respectively. Example junction geometries are shown in Figure 4.9 (a), (b) and (c). The continuous curves are the averaged transmission coefficients and the dotted curves show the transmission coefficients for different charge double layer arrangements. The colour code refers to the three different states, NDI-N (black), NDI-R (blue) and NDI-D (red). (d) shows the measured and computed averaged conductance values for the three states of the electrochemical gating experiment. The computed conductance values are calculated from the averaged transmission coefficient using the finite temperature Landauer formula (Eq. 4.1.2 in the Chapter 3) with the temperature 300K.

4.5 Summary

We studied charge transport phenomena through a core substituted naphthalenediimide (NDI) single-molecule junctions using the electrochemical STM-based break junction technique in combination with DFT calculations. The conductance switch among three well-defined states is acquired by electrochemically controlling the redox state of the pendant diimide unit of the molecule in ionic liquid, and the conductance difference is more than one order of magnitude between di-anion states and neutral state. The potential dependent charge transport characteristics of the NDI molecules are confirmed by DFT calculations accounting for electrochemical double-layer effects on the conductance of the NDI junctions. This work suggested that the integration of redox unit in the pendant position with strong coupling to molecular backbone can significantly tune the charge transport of the single-molecule device by controlling different redox states.

Chapter 5

Tuning the thermoelectric properties of metallo-porphyrins

In this chapter I will present my work published recently in *Nanoscale* [72] on thermoelectric properties of metallo-porphyrins. I demonstrate that by varying the transition metal-centre of the porphyrin molecule over a range of metallic atoms the molecular energy levels relative to the Fermi energy of the electrodes can be varied leading tuning of the thermoelectric properties of metallo-porphyrins.

5.1 Motivation

Porphyrin-based molecules are attractive as building blocks for molecular-scale devices, because they are conjugated, rigid, chemically stable and form metallo-porphyrins by coordinating with a variety of metallic ions. This combination of desirable properties has already been exploited in nature, where for example the metallo-porphyrin acts as a charge carriers in naturally occurring processes such as photosynthesis and in the respiratory chain. Recently a number of groups have investigated the electrical conductance of porphyrin-based molecules, [53, 57, 149]. Crucial to further development of such systems for future applications is an understanding of their thermoelectric properties at the nanoscale.

Thermoelectric devices can be used to convert waste heat into electricity and therefore have the potential to reduce the global demand for energy, particularly from information

technologies. The thermopower S of a material or nanoscale junction is defined as $S = -\Delta V/\Delta T$, where ΔV is the voltage difference generated between the two ends of the junction when a temperature difference ΔT is established between them. In this Chapter, I will explore the potential of porphyrin-based molecules for high-performance thermoelectricity. By varying the metal atom, I find that both the sign and the magnitude of the thermopower can be tuned. I identify Fe, Mn and Zn porphyrins as particularly attractive materials, due to their high thermopowers (-280, -260 and +230 $\mu\text{V}/\text{K}$ respectively), which as discussed in the conclusion, exceed the experimental values of all single-molecule thermopowers measured reported to date. Thermopower is an intrinsic property and therefore these values will be manifest in self-assembled monolayers of these molecules and therefore our results could lead to new families of thin-film thermoelectric devices.

The rewards for such improvement in thermoelectric performance cannot be overstated. Mankind wastes at least 20% of the 15 terawatts required annually for global power consumption as low level heat (<200 °C). Widespread availability of new low-cost organic thermoelectric devices would allow direct heat-to-electrical energy from (at least some) of this vast, essentially untapped, resource generating a new industrial sector based on local power generation from otherwise wasted energy sources amounting up to 50 billion £ yr^{-1} .

The results in this work will be of fundamental interest to the molecular electronics and nanoelectronics communities, chemists and physicist working on the fundamental aspects of electron and thermal transport, as well as engineers seeking to improve the performance of their thermoelectric devices.

5.2 Introduction

The ability to generate a voltage from a temperature gradient has been known since the early 19th century [150]. This Seebeck effect is exploited to generate electricity from sources of waste heat such as automobile exhausts and industrial manufacturing processes and the inverse process (i.e. the Peltier effect) is used in cascade coolers for on-chip cooling of electronic devices [151-154]. Nowadays, a great deal of effort is aimed at increasing the efficiency of these effects and identifying the parameters that control the thermoelectric performance of materials and devices [155-161]. Although most common thermoelectric materials are inorganic, there is growing interest in the development of organic thermoelectric materials [52-54, 155-159, 162, 163], partly because many widely-deployed inorganic thermoelectric materials are toxic, expensive to process and have limited global supplies. Since the thermoelectric performance of inorganic materials can be enhanced by taking advantage of nanostructuring [162-167] there is particular interest in exploiting the room-temperature properties of single-molecules attached to nanogap electrodes, which can be regarded as the ultimate nanostructured devices. In what follows our aim is to explore the potential for thermoelectricity of single-molecule metallo-porphyrin junctions. Porphyrins are attractive as building blocks for molecular-scale devices, because they are conjugated, rigid, chemically stable and form metalloporphyrins by coordinating a variety of metallic ions [52-60].

From the point of view of optimising thermoelectric properties, junctions formed from these molecules are of interest, because by varying the metal atom residing in the core of the organic porphyrin framework, it should be possible to tune the molecular energy levels relative to the Fermi energy E_F of the electrodes. If energy levels can be caused to sit close to E_F , then this is expected to lead to transport resonances, which enhance the thermopower.

Eq. (2.29) in Chapter 2 demonstrates that S is enhanced by increasing the slope of $\ln T(E)$ near $E=E_F$ and hence it is of interest to explore whether or not the ability to vary the metal centre in metallo-porphyrins can be used to move resonances close to E_F .

In what follows, we shall demonstrate that this is indeed the case and that large positive and negative thermopowers are achievable.

5.3 Methods

As shown in Figure 5.1, the porphyrin monomer of interest consists of four pyrrole cores (the inner ring π -system) with side groups comprising a phenyl ring connected via two oxygen atoms to electrically-inert alkyl groups ($-C_8H_{17}$). The core of porphyrin is connected via thiol anchor groups to gold electrodes. Our aim in this paper is to investigate the effect on thermoelectric performance of varying the metal atom χ over the series of $\chi =$ Co, Cu, Fe, Mn, Ni, and Zn.

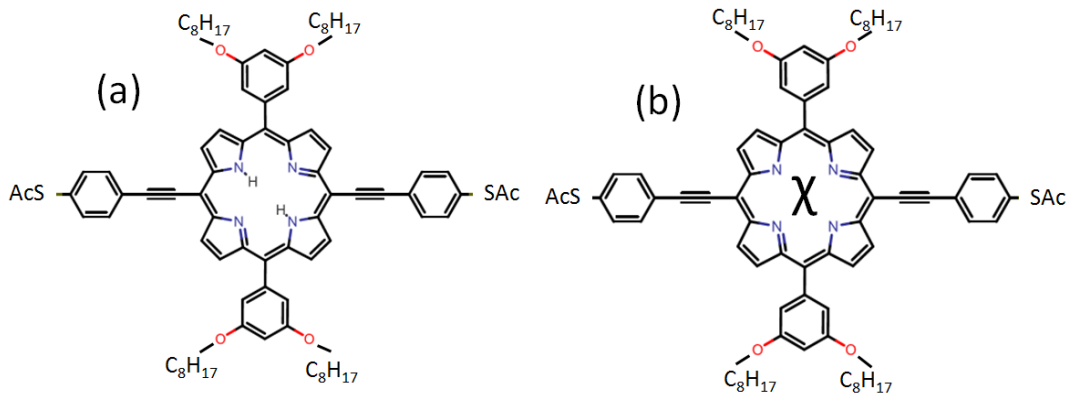


Figure 5.1. Porphyrin-based molecular structures (a) without metallic atom, (b) with different metallic atoms $\chi =$ Co, Cu, Fe, Mn, Ni, and Zn.

To calculate the electrical properties of each metallo-porphyrin, we used the spin density functional theory (DFT) code SIESTA [107] which employs Troullier-Martins

pseudopotentials to represent the potentials of the atomic cores [108], and a local atomic-orbital basis set. A double-zeta polarized basis set was used for all atoms and the generalized gradient approximation (GGA-PBE) for the exchange and correlation functionals [109, 110]. The Hamiltonian and overlap matrices are calculated on a real-space grid defined by a plane-wave cut-off of 150 Ry. Each molecule was relaxed to the optimum geometry until the forces on the atoms are smaller than 0.02 eV/\AA and in case of the isolated molecules, a sufficiently-large unit cell was used to avoid inter-cell interactions. All porphyrin molecules with metallic atoms χ were found to be slightly twisted after relaxation.

After obtaining the relaxed geometry of each isolated molecule, the molecules were placed between two gold electrodes, as shown in Figure 5.2. For structures such as those shown in Figure 5.2, the central region of the junction is composed of a single molecule attached to two gold (111) leads. The equilibrium distance between the sulfur atom of each anchor group and the centre of the apex atom of each gold pyramid was initially 2.5 \AA . After geometry optimization the distance changed slightly from the initial value to a final value of 2.63 \AA .

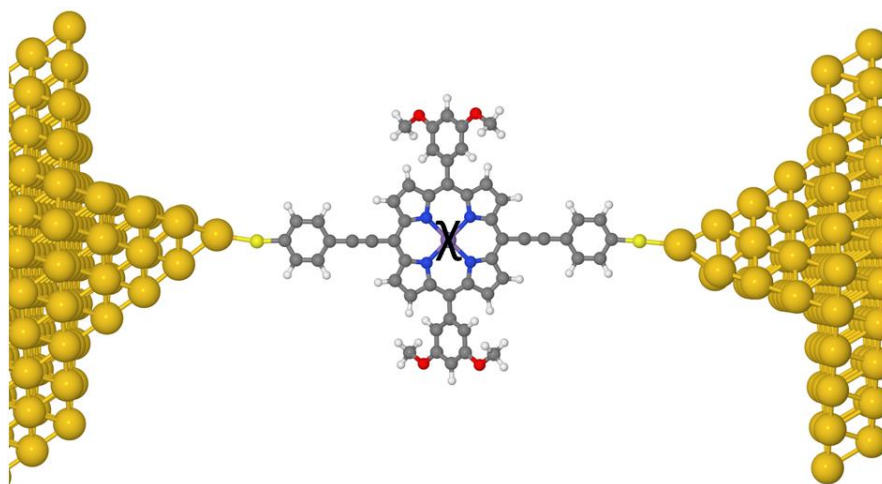


Figure 5.2. An example of an optimized junction configuration. To reduce the computational cost, we replace the electrically-inert alkyl group ($-\text{C}_8\text{H}_{17}$) with a methyl group ($-\text{CH}_3$).

To reduce the computational cost, we replace the electrically-inert alkyl group (-C₈H₁₇) with a methyl group (-CH₃). I used the Gollum method [111] to compute the spin-dependent transmission coefficients $T^\sigma(E)$ for electrons of energy E passing from the left gold electrode to the right electrode. Gollum is a next-generation code, born out of the SMEAGOL code [112] and uses the mean-field Hamiltonian and overlap matrices obtained from density functional theory to compute transport properties of a wide variety of nanostructures. After computing $T^\sigma(E)$, we evaluated the zero-bias thermoelectric coefficients over a wide range of Fermi energies and temperatures by using Eqs. (2.19) and (2.20) and also Eqs. (2.26)-(2.30) in chapter 2.

5.4 Results and Discussion

For each metallo-porphyrin P- χ in Figure 5.1b, the charge transfer between the metal atom and the porphyrin framework was calculated (as shown in Table 5.1). As expected, the calculations show that all metal atoms donate electrons to the porphyrin host. As examples, Figure 5.3 shows the frontier orbitals, spin-dependent and total transmission coefficients of the bare porphyrin (left) and Fe-porphyrin (right) relative to the DFT-predicted Fermi energy E_F^{DFT} . Results for other molecules are shown in Figures (5.8)-(5.14).

Atom	Spin up	Spin down	Total No. of electrons	ΔN
Co	4.70	3.41	8.12	0.88
Cu	5.37	4.85	10.2	0.77
Fe	4.64	2.02	6.66	1.34
<u>Mn</u>	5.23	0.67	5.90	1.1
Zn	4.58	4.58	9.16	0.84
Ni	4.62	4.62	9.25	0.75

Table 5.1. Spin-DFT-PBI calculation of the number of spin up and spin down electrons on each metal atom χ , along with the number ΔN of electrons lost by the metal atoms to the porphyrin host.

Figure 5.3(a) shows that for the bare porphyrin, the transmission $T(E)$ at the DFT-given Fermi level (E_F^{DFT} , indicated by the vertical black line) is closest to the HOMO resonance and the slope of the curve is negative. On the other hand for the Fe porphyrin, figure 5.3b shows that the Fermi level is nearest to the LUMO resonance and the slope is positive in both Figures 5.3b. Hence from Eq. (2.29), one expects the thermopower of the former (latter) to be positive (negative).

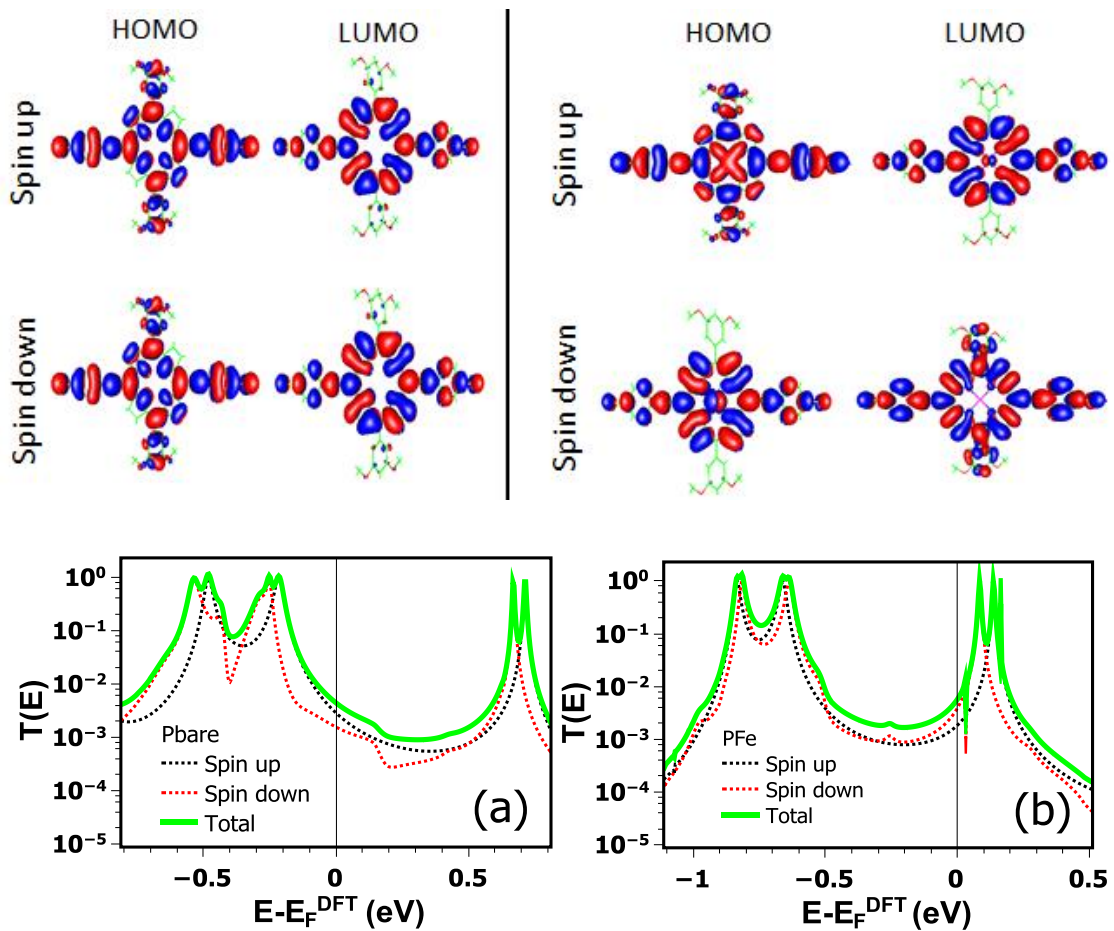


Figure 5.3. Top panels: Iso-surfaces of frontier molecular orbitals of the bare porphyrin (Porphyrin - bare) and the iron-porphyrin (Porphyrin-Fe(II)) obtained using spin-polarized DFT. Red corresponds to positive and blue to negative regions of the wave functions. Lower panels: The spin-dependent and total transmission coefficients as a function of energy for bare porphyrin (left) and porphyrin-Fe (right).

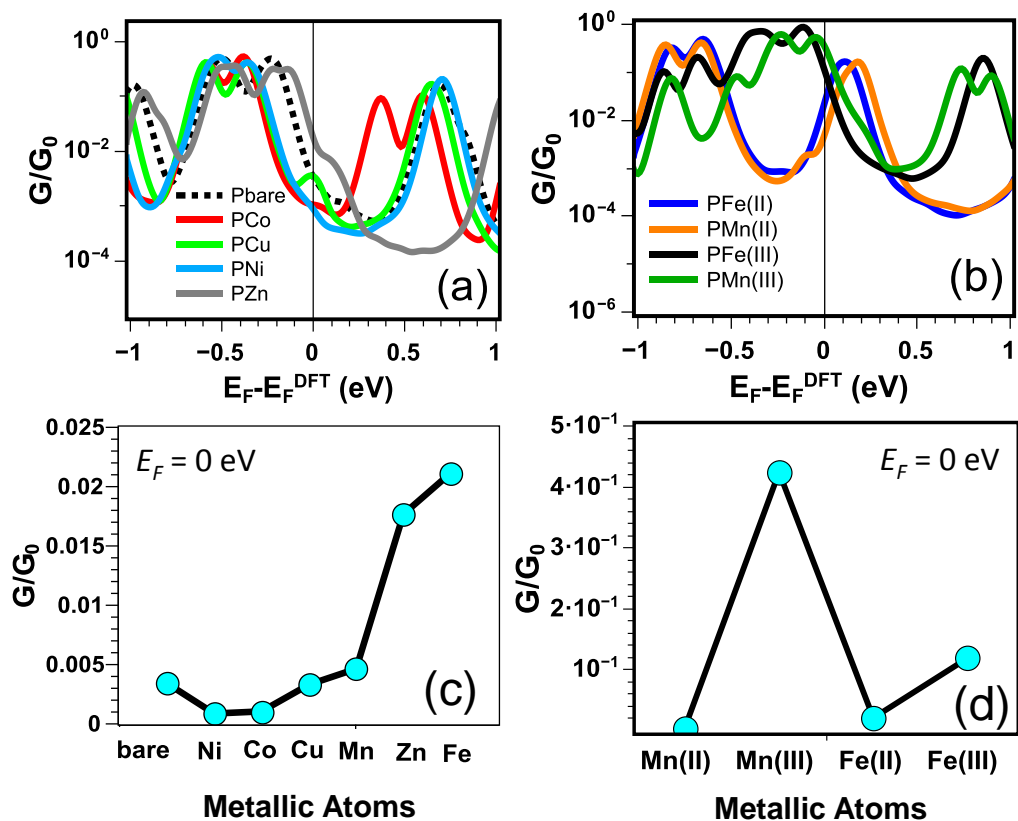


Figure 5.4. (colour online) DFT spin-dependent room-temperature electrical conductance (in units of $G_0 = 2e^2/h = 77 \mu\text{Siemens}$) over a range of Fermi energies for (a) the P-bare and P-Co, Cu, Ni and Zn and (b) the P-bare and P-Fe(II), P-Mn(II), PFe(III) and PMn(III). (c) Room-temperature values of G for P-bare, P-Co, P-Cu, P-Ni, P-Zn, P-Fe(II) and P-Mn(II) are 3.43×10^{-3} , 1.05×10^{-3} , 3.48×10^{-3} , 8.7×10^{-4} , 1.7×10^{-2} and 2.1×10^{-2} respectively. (d) Room-temperature values of G for the porphyrins Mn(II), Mn(III), Fe(II) and Fe(III). The lines in (c) and (d) are guides to the eye.

Figure 5.4 shows the total room temperature electrical conductance for each P- χ . Figure 5.4(a) shows that the bare (dotted line) and Co, Cu, Zn and Ni porphyrins (solid lines), exhibit HOMO-dominated conductance at the DFT Fermi energy,

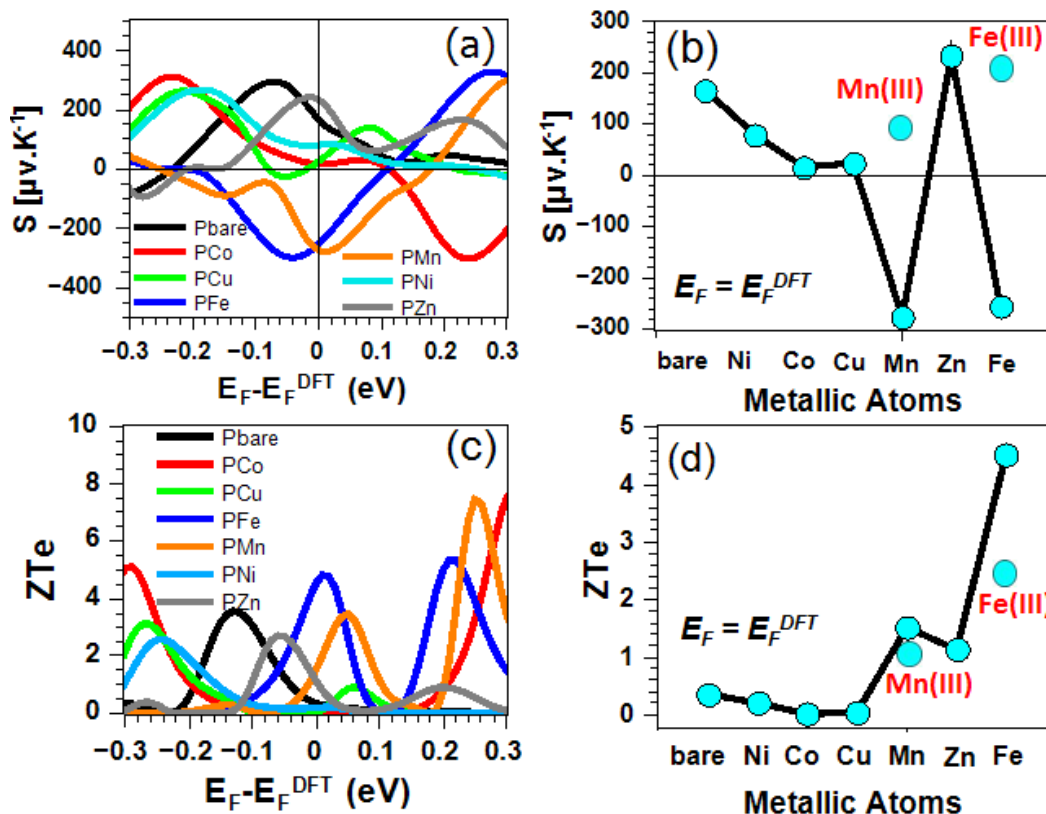


Figure 5.5. The room-temperature thermopower S and figure of merit ZT_e . (a) and (c) show plots of S and ZT_e over a range of Fermi energies E_F relative to the DFT-predicted Fermi energy E_F^{DFT} . The right column shows room-temperature values obtained using $E_F = E_F^{\text{DFT}}$ of S and ZT_e for each metallo-porphyrin.

whereas Figure 5.4b shows that for the Mn(II) and Fe(II) porphyrins, we obtain LUMO-dominated conductance. Figure 5.4c shows the room-temperature conductance at the DFT Fermi energy and shows that the pattern of increasing conductance is Ni < Co < Cu < Bare < Mn(II) < Zn < Fe(II). The conductance of porphyrin-Cu ($3.49 \times 10^{-3} G_0$) is slightly higher than of porphyrin-bare, ($3.43 \times 10^{-3} G_0$). This order is in agreement with previous measurements on similar molecules [57]. We are not aware of conductance measurements of the Mn, Zn and Fe porphyrins.

In the case of Mn and Fe, metalloporphyrins exist more commonly as P-M(III) in the presence of a counter anion. Since it is straightforward to oxidise/reduce between Fe(II)/(III) and Mn(II)/(III), we have also computed all thermoelectric properties for

Fe(III) and Mn(III) complexed with a Cl⁻ counter ion (See Figures (5.16)–(5.22)). The resulting room-temperature conductances are shown in Figure 5.4b reveals that in the presence of the counter anion, transport becomes LUMO dominated. Figure 5.4d compares the room-temperature conductances of Fe(II)/(III) and Mn(II)/(III) and shows that the presence of a counter anion increases the electric conductance.

Figures 5.5b and 5.5d show results for the Seebeck coefficient (thermopower) S and electronic contribution to the figure of merit ZT_e at room temperature. It is well-known that DFT can give an inaccurate value for the Fermi energy and therefore Figures 5.5a and 5.5c show corresponding results for a range of Fermi energies E_F relative to the DFT-predicted Fermi energy E_F^{DFT} , whereas Figures 5.5b and 5.5d show room-temperature values of S and ZT_e for each metallo-porphyrin, evaluated at the DFT Fermi energy. Figure 5.5b demonstrates that both the magnitude and sign of thermopower S are sensitive to the metal atoms at the centre of the porphyrin monomer, which determine the location of transport resonances relative to the Fermi energy. Furthermore, in the case of Fe and Mn, Figure 5.5b reveals that the sign of the thermopower can be switched from negative to positive upon complexation with Cl⁻, due to their switching from HOMO to LUMO dominated transport.

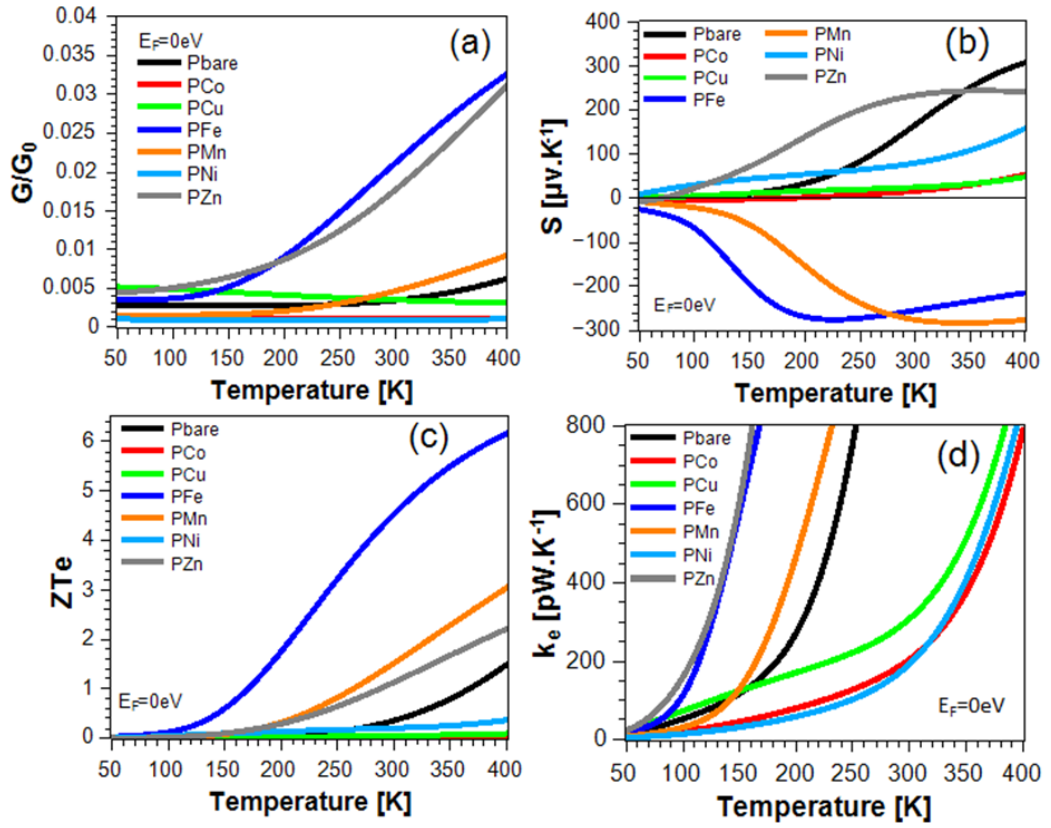


Figure 5.6. (a, b, c and d) represent the electrical conductance, Seebeck coefficients S (thermopower), electronic contribution to the figure of merit ZT_e and electronic contribution to the thermal conductance k_e over a range of temperatures, evaluated at $E_F = E_F^{DFT}$.

At the DFT-predicted Fermi energy, the highest values of the thermopower are obtained in the presence of Mn, Fe and Zn, for which S takes values -280 , -260 and $+230$ $\mu\text{V}/\text{K}$ respectively, all of which have a greater magnitude than the thermopower of the bare porphyrin (165 $\mu\text{V}/\text{K}$). The lowest values of all are obtained for Co, closely followed by Cu. For Fe(III)-P we obtain $S = +218$ $\mu\text{V}/\text{K}$ at room temperature and for Mn(III)-P we find $S = +95$ $\mu\text{V}/\text{K}$. Corresponding results for the electronic contribution to the figure of merit ZT_e are shown in Figure 5.5d. The highest values of ZT_e are obtained in the presence of Zn, Mn and Fe, reflecting the high values of their thermopowers and conductances.

Figure 5.6 shows the electrical conductance G , Seebeck coefficients S (thermopower), electronic contribution to the figure of merit ZT_e and electronic contribution to the thermal conductance k_e as a function of temperature, obtained using the DFT-predicted Fermi energy E_F^{DFT} . These results show that the magnitudes of all quantities increase with increasing temperature.

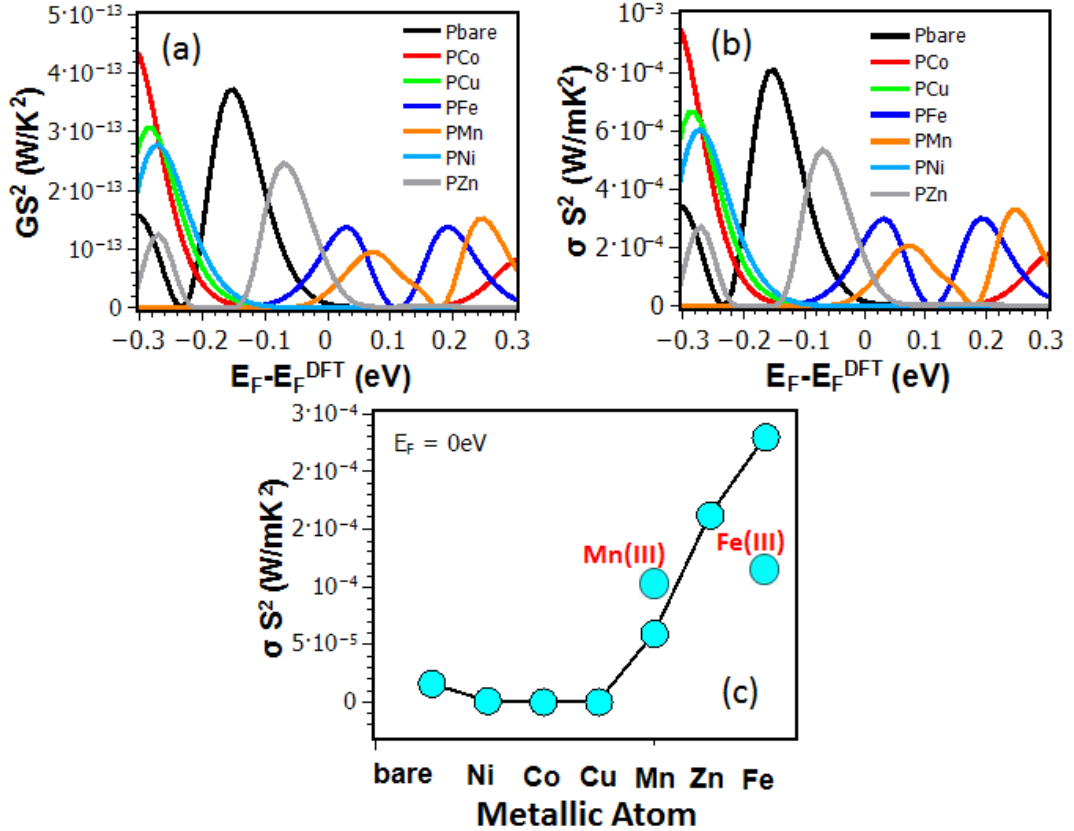


Figure 5.7. The upper figure (a) shows room-temperature values of the product GS^2 , while figure (b) shows the power factor $P = S^2GL/A$ evaluated at $E_F = E_F^{DFT}$. The lower figure (c) shows room-temperature values of power factor $P = S^2GL/A$ for each metallo-porphyrin.

A crucial quantity determining the efficiency of a thermoelectric material or device is the dimensionless figure of merit $ZT = S^2GT/\kappa$, whose denominator κ is the total thermal conductance due to both phonons and electrons. This differs from the electronic figure of merit $ZT_e = S^2GT/\kappa_e$ whose denominator contains only the thermal conductance due to electrons. For a bulk material, ZT is often written in the form $ZT = (P/\kappa)T$, where κ is the

total thermal conductivity and P is the power factor defined by as $P = S^2\sigma$, where σ is the electrical conductivity. In practice for a single molecule, ZT is difficult to measure experimentally, because the thermal conductance κ of a single molecule is not directly accessible. However the numerator of ZT (i.e. the power factor P) is accessible. The notion of conductivity is not applicable to transport through single molecules, but to compare with literature values for bulk materials, we define $\sigma = GL/A$, where L and A are equal to the length and the cross-sectional area of the molecule respectively. In what follows, the values $L = 4.0$ nm and $A = 1.8$ nm² are used. From the results of Figures 5.4 and 5.5, the quantity GS^2 and power factors $P = S^2GL/A$ for each of the studied molecules are shown in Figure 5.7.

These results show that Mn, Mn(III), Fe(III), Zn and Fe porphyrins have the highest power factors of 5.9×10^{-5} W/m.K², 5.4×10^{-4} W/m.K², 9.5×10^{-4} W/m.K², 1.6×10^{-4} W/m.K² and 2.3×10^{-4} W/m.K² respectively.

5.4.1 Plots of frontier orbitals and spin-dependent transmission coefficients.

The spin dependent transport calculations show similar behaviour for $T(E)$ for both up spin and down spin close to the Fermi energy (0 eV) in all P- χ molecules. However, at higher energies, there can be large differences between the two. For example, in the case of P-Fe (Figure 5.9), at an energy value of $E-E_F \sim 2$ eV the transmission resonances differ. The spin up transmission curve shows a clear antiresonance, and this resonance has the shape of a Fano resonance, while the down spin shows a normal Breit-Wigner resonance. This difference can be explained by the nature of the LUMO orbitals which for the spin down are

all delocalized along the molecular backbone but for the spin up, the LUMO+1 and LUMO+2 orbitals are clearly localized on the central unit of the molecule.

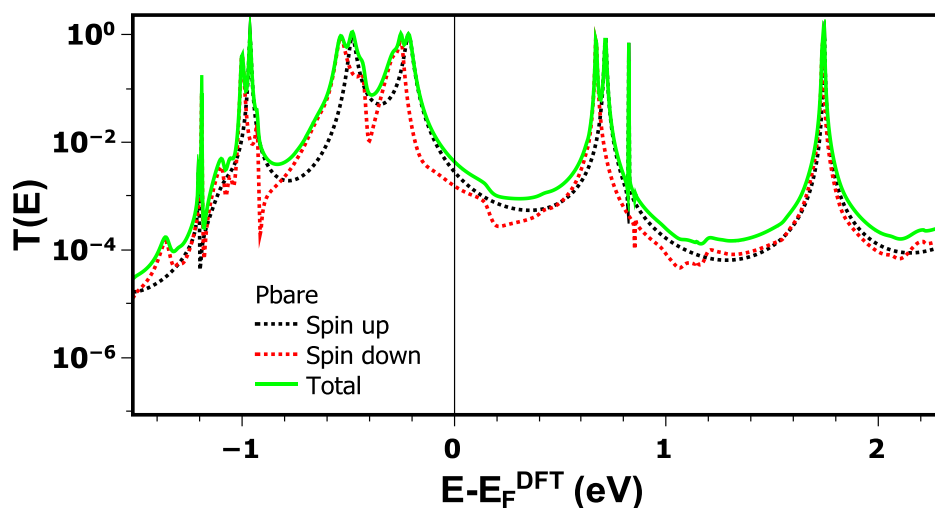
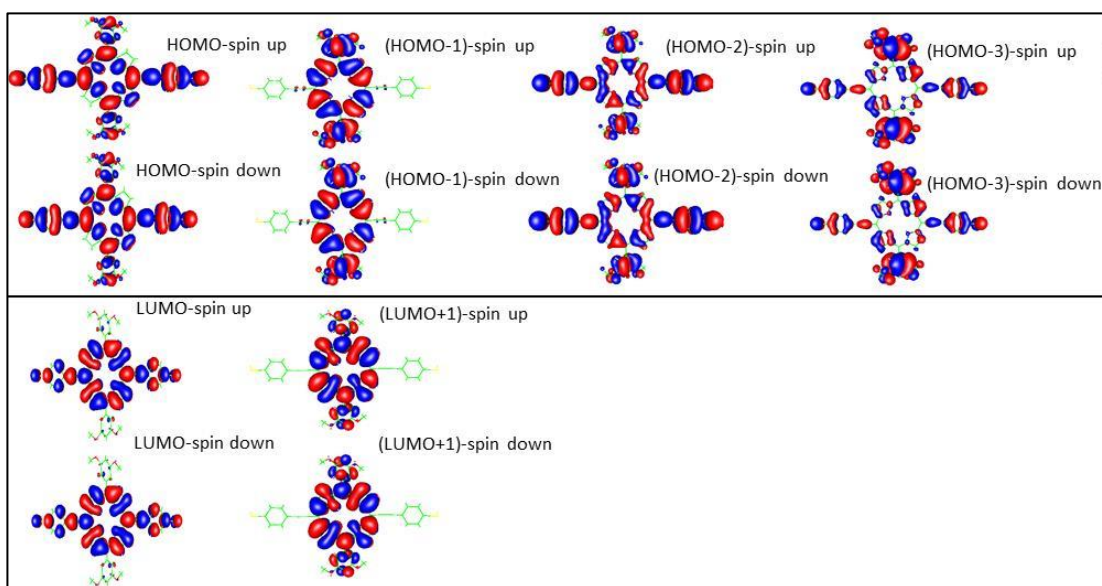


Figure 5.8. Frontier molecular orbitals of the P-bare obtained using the spin- dependent DFT. Red corresponds to positive and blue to negative regions of the wave functions. Below each plot of molecular orbitals, we present the spin-dependent and total transmission coefficients as a function of energy.

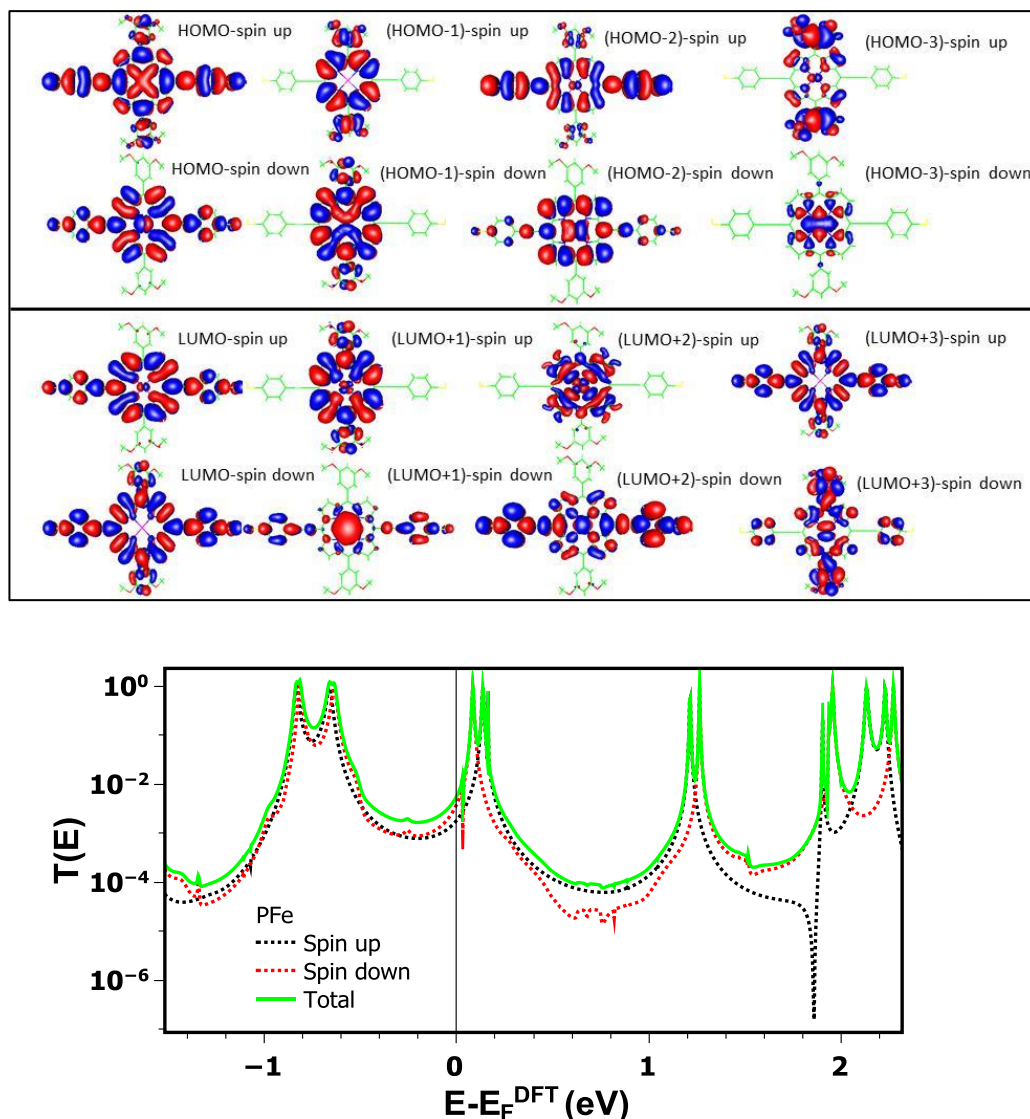


Figure 5.9. Frontier molecular orbitals of the PFe obtained using the spin- dependent DFT. Red corresponds to positive and blue to negative regions of the wave functions. Below each plot of molecular orbitals, we present the spin-dependent and total transmission coefficients as a function of energy.

Figure 5.8 shows that for bare-porphyrin, The spin dependent transport calculations show similar behaviour for both up spin and down spin for $T(E)$ close to the Fermi energy (0 eV) and a normal Breit-Wigner resonances appear at the HOMO and LUMO levels. That can be associated with the nature of the HOMO and LUMO orbitals which for both up spin and down spin are all delocalized along the molecular backbone.

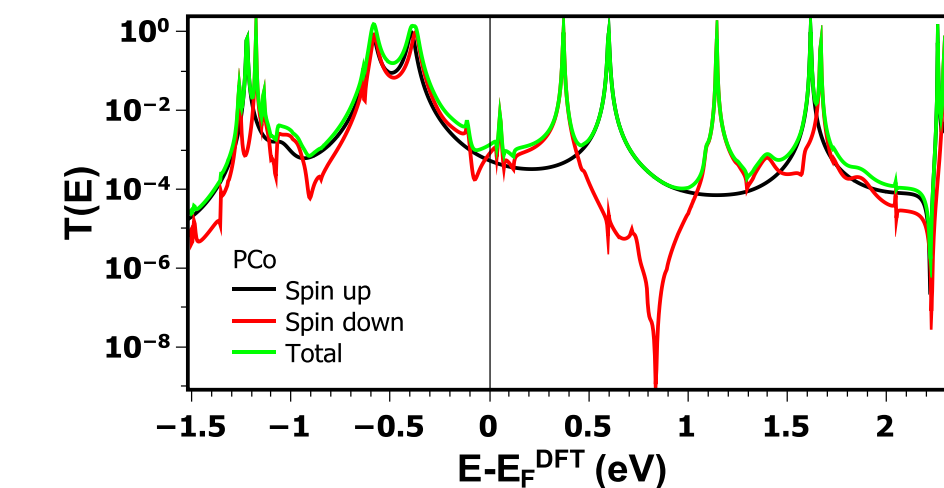
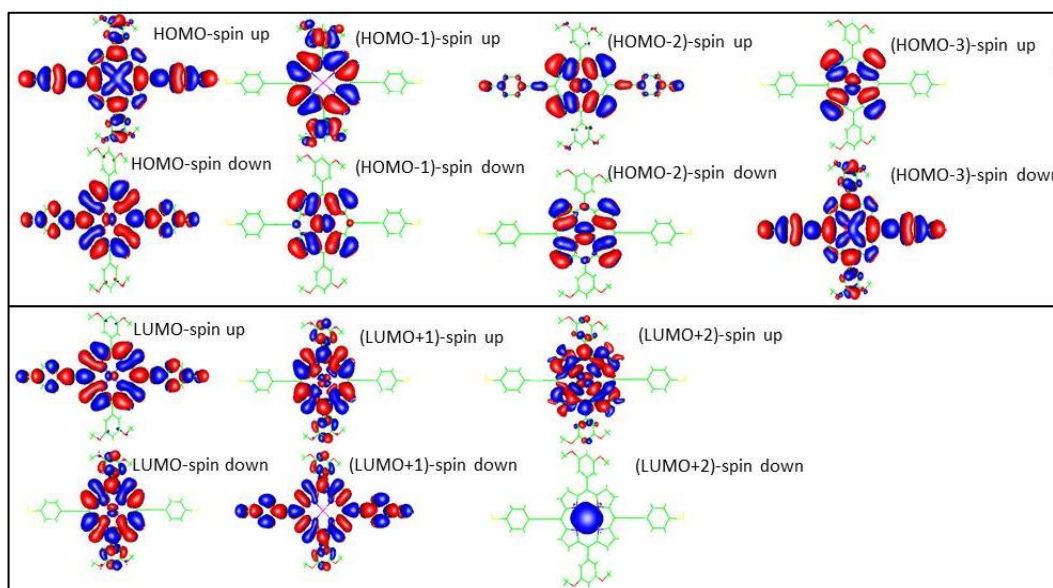


Figure 5.10. Frontier molecular orbitals of the PCo obtained using the spin-dependent DFT. Red corresponds to positive and blue to negative regions of the wave functions. Below each plot of molecular orbitals, we present the spin-dependent and total transmission coefficients as a function of energy.

Figure 5.10 shows that for the Co-porphyrin, at an energy of $E - E_F \sim 0.8$ eV, the spin down transmission shows anti-resonance. This explains that LUMO spin down orbital localized only on the metallic atom Co.

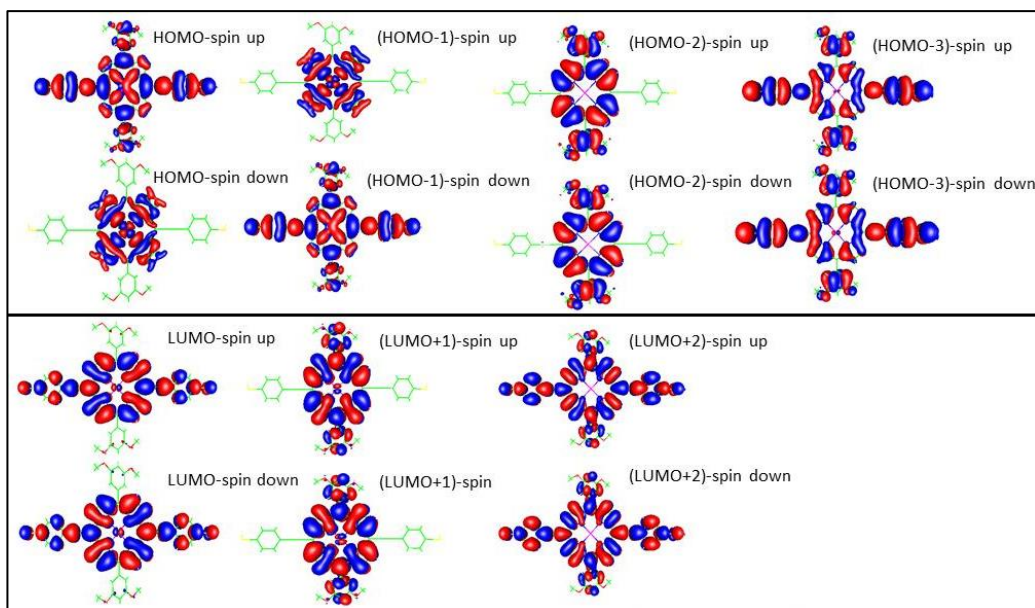


Figure 5.11. Frontier molecular orbitals of the PCu obtained using the spin- dependent DFT. Red corresponds to positive and blue to negative regions of the wave functions. Below each plot of molecular orbitals, we present the spin-dependent and total transmission coefficients as a function of energy.

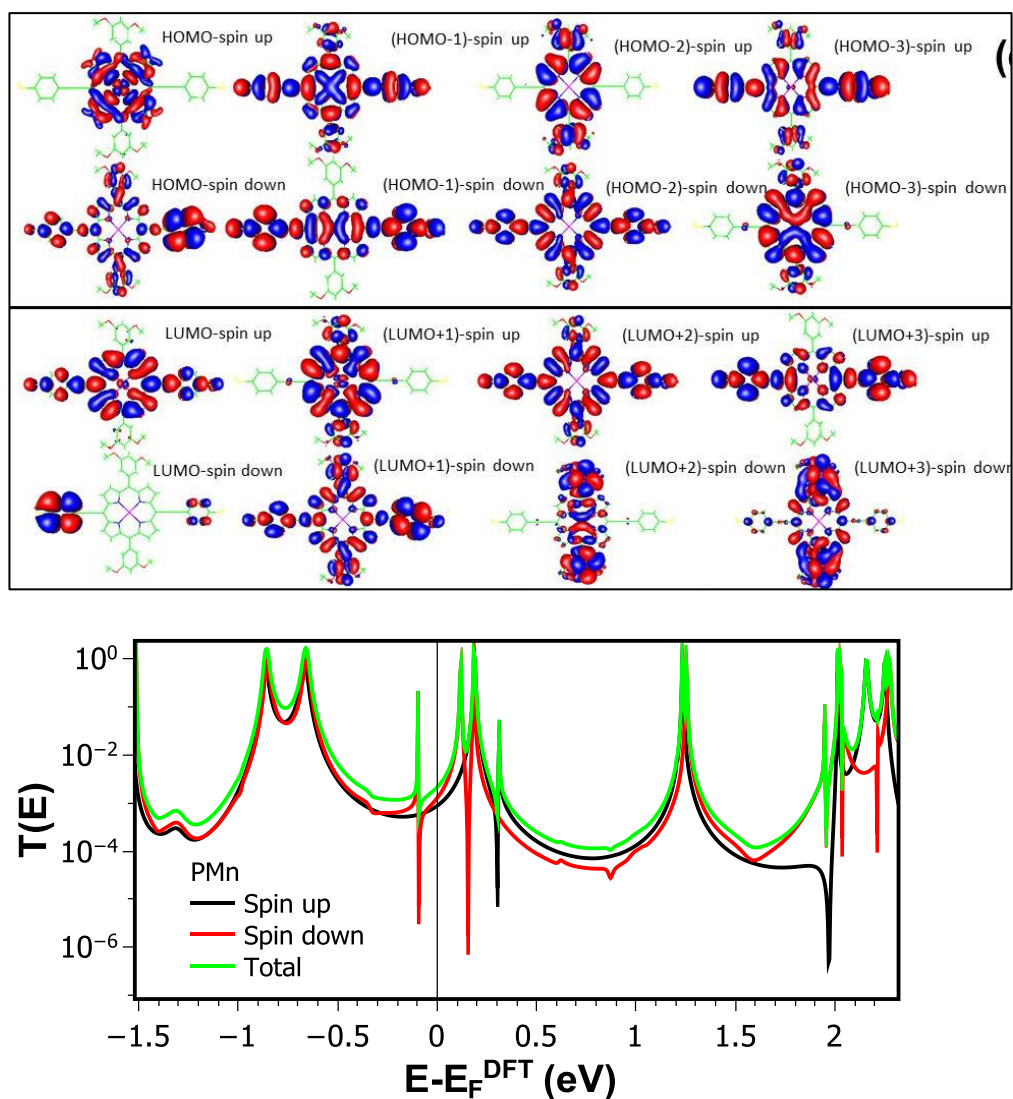


Figure 5.12. Frontier molecular orbitals of the PMn obtained using the spin- dependent DFT. Red corresponds to positive and blue to negative regions of the wave functions. Below each plot of molecular orbitals, we present the spin-dependent and total transmission coefficients as a function of energy.

For the Mn-porphyrin, the spin dependent-transmission calculation shows Fano-resonances around the DFT Fermi energy ($E_F=0\text{eV}$). This explains the different distribution of orbitals localized along the backbone.

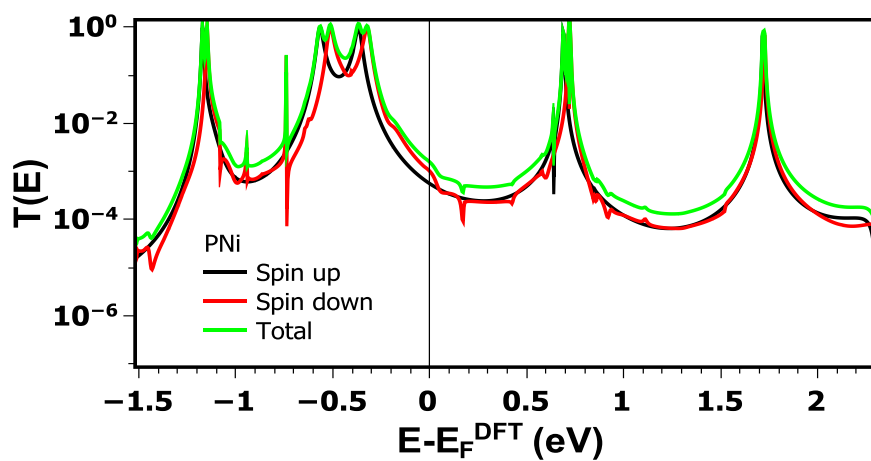
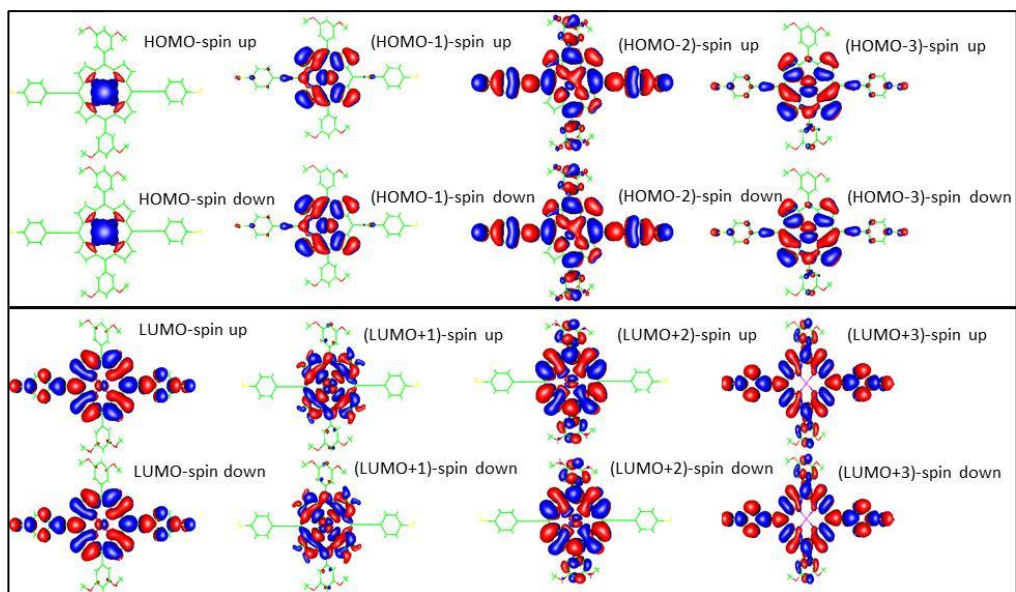


Figure 5.13. Frontier molecular orbitals of the PNi obtained using the spin- dependent DFT. Red corresponds to positive and blue to negative regions of the wave functions. Below each plot of molecular orbitals, we present the spin-dependent and total transmission coefficients as a function of energy.

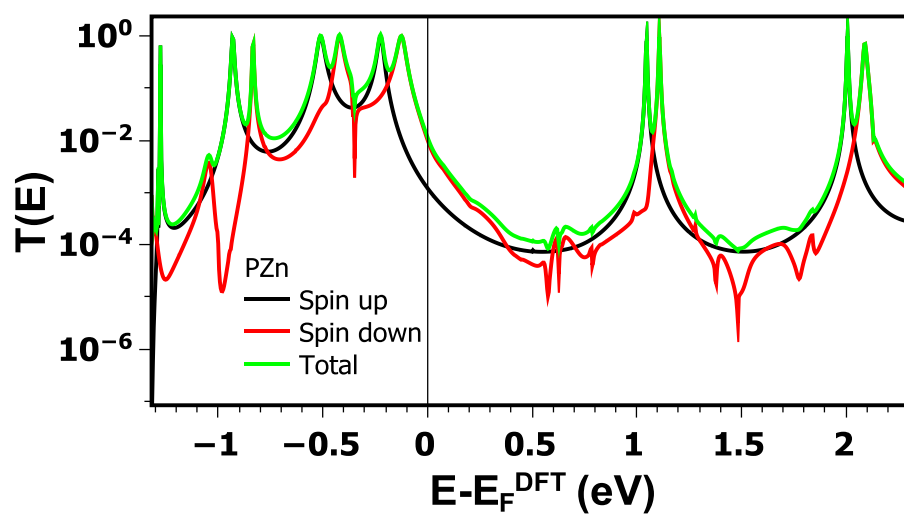
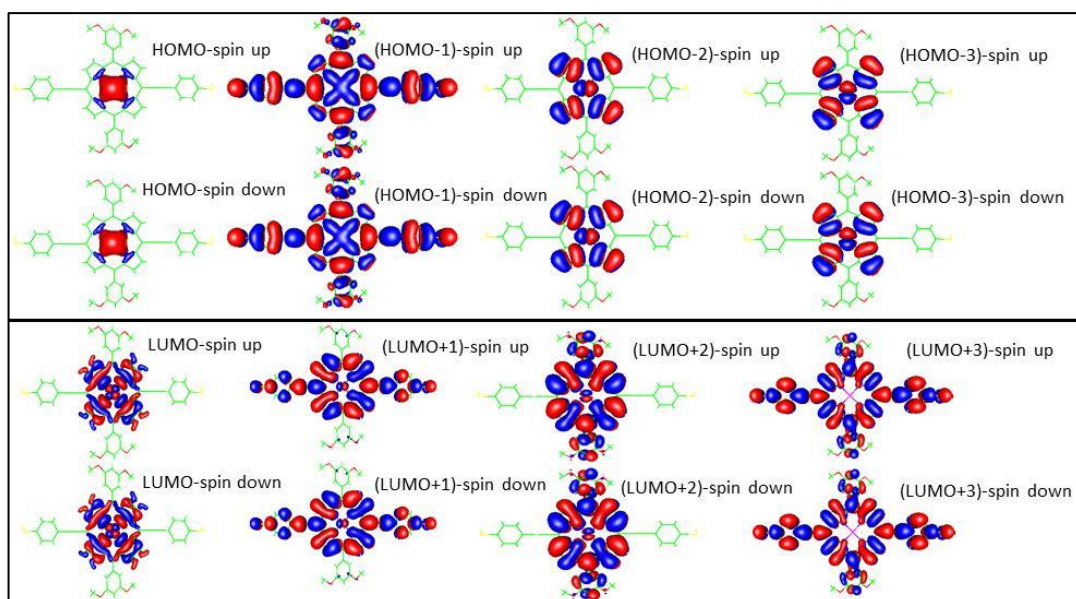


Figure 5.14. Frontier molecular orbitals of the PZn obtained using the spin-dependent DFT. Red corresponds to positive and blue to negative regions of the wave functions. Below each plot of molecular orbitals, we present the spin-dependent and total transmission coefficients as a function of energy.

5.4.2 Thermoelectric properties of Fe(III)-porphyrin in presence of a Cl counter anion.

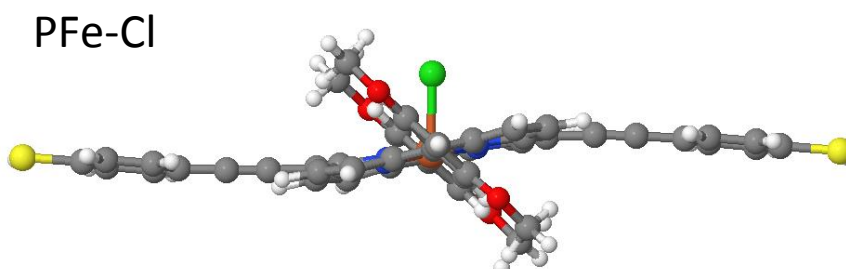


Figure 5.15. Optimized geometry of porphyrin with central Fe(III)-Cl complex.

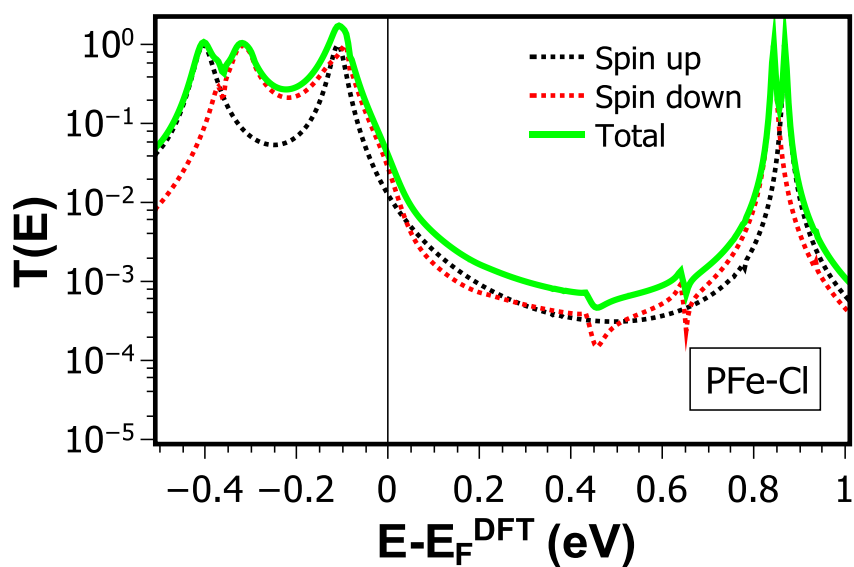


Figure 5.16. The spin-dependent and total transmission coefficients as a function of energy for Fe(III)-porphyrin in presence of a Cl counter anion, the structure of which is shown in figure 5.15.

Figure (5.16) shows spin-dependent and total transmission coefficients relative to the DFT-predicted Fermi energy E_F^{DFT} of the Fe(III)-porphyrin in the presence of a Cl⁻ counter ion. The green line shows that total transport through the Fe-Cl-porphyrin is HOMO-dominated,

whereas for the non-complexed Fe(II)-porphyrin (see Figure 5.3b) transport is LUMO dominated.

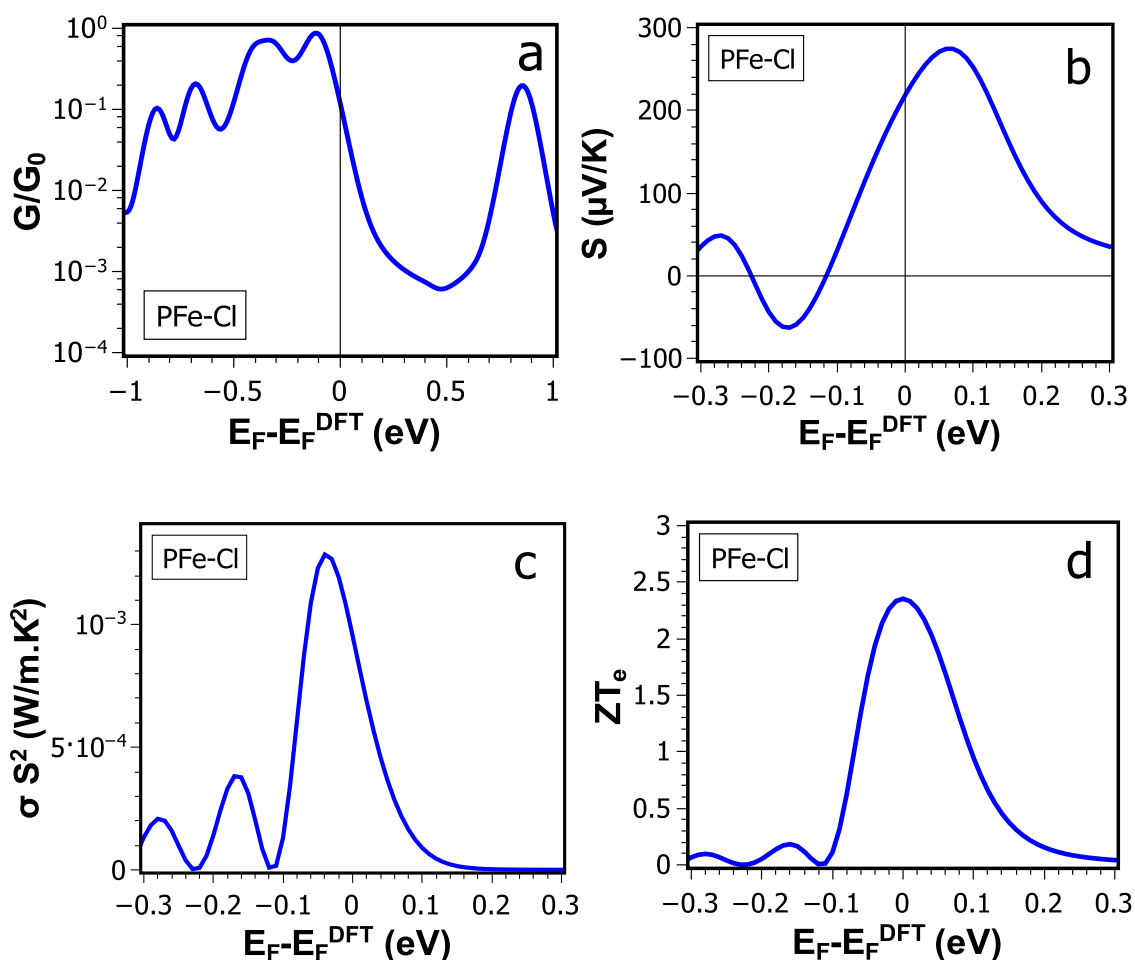


Figure 5.17. For the structure in figure 5.15, figures (a, b, c and d) show the room-temperature electrical conductance G , thermopower S , power factor $P = S^2\sigma$ and electronic figure of merit ZT_e over a range of Fermi energies E_F relative to the DFT-predicted Fermi energy E_F^{DFT} .

Figure 5.17a shows the room-temperature electrical conductance for Fe-porphyrin in presence of Cl⁻ shown in Figure (5.15). The HOMO-dominated conductance at the DFT Fermi energy leads to the positive Seebeck coefficient (thermopower) S shown in Figure 5.17b, the power factor $S^2\sigma$ (Figure 5.17c) and electronic contribution to the figure of merit ZT_e (Figure 5.17d), all at room temperature. These results are for a range of Fermi energies E_F relative to the DFT-predicted Fermi energy E_F^{DFT} .

Figure 5.17b demonstrates that in presence of Fe(III)-Cl at the centre of the porphyrin monomer, the magnitude of thermopower S is changed to $+218 \mu\text{V}/\text{K}$, compared with $-260 \mu\text{V}/\text{K}$ for Fe(II).

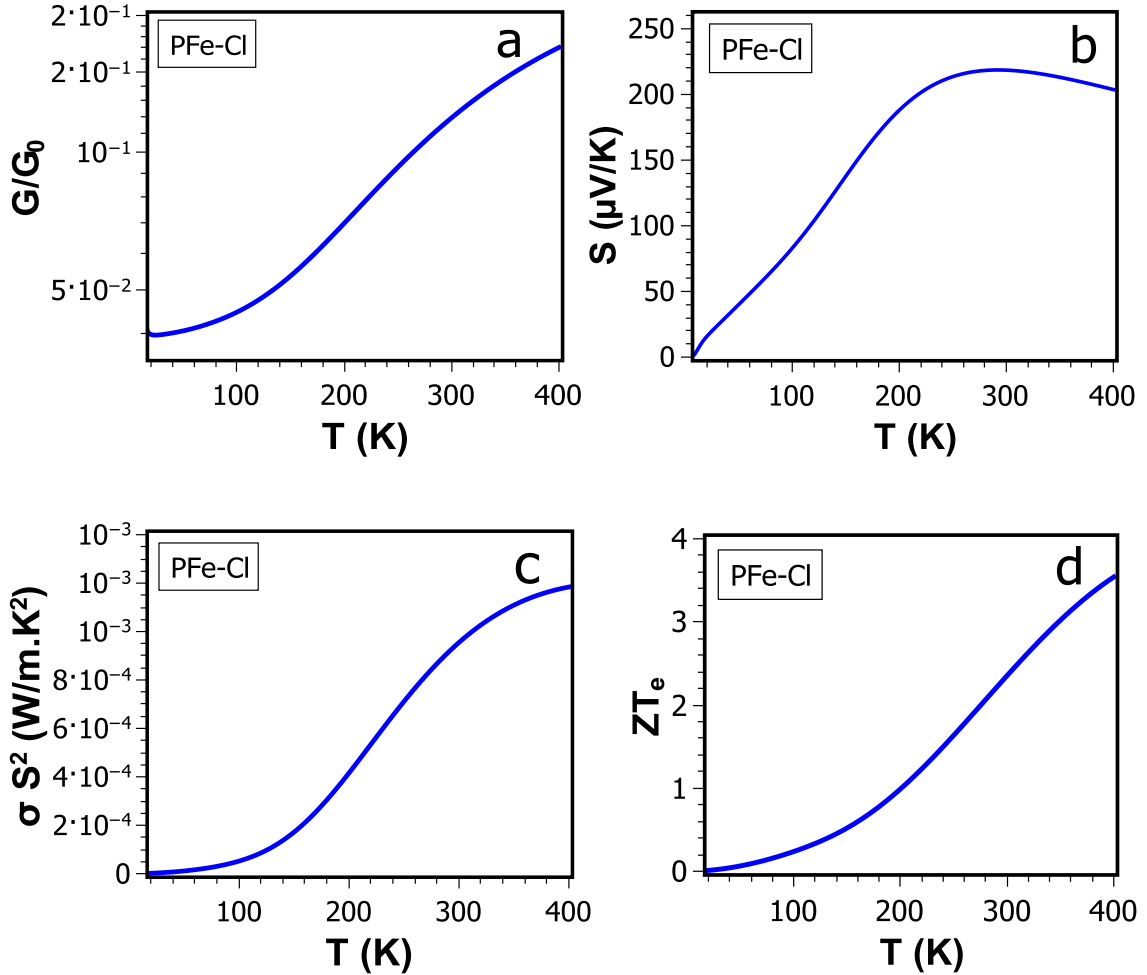


Figure 5.18. For the structure in figure 5.15, figures (a, b, c and d) show the electrical conductance, Seebeck coefficients S (thermopower), power factor $P = S^2\sigma$, electronic contribution to the figure of merit ZT_e as a function of temperature, evaluated at $E_F = E_F^{DFT}$.

Figure 5.18 shows the electrical conductance G , Seebeck coefficients S (thermopower), power factor $S^2\sigma$ and electronic figure of merit ZT_e as a function of temperature for the structure in figure 5.15, obtained using the DFT-predicted Fermi energy E_F^{DFT} .

5.4.3 The calculation of Mn-porphyrin in presence of (Cl).

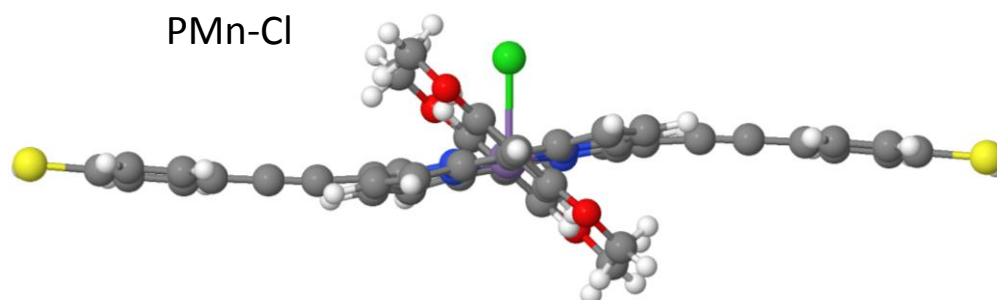


Figure 5.19. Optimized geometry of porphyrin with central Mn(III)-Cl complex.

For the structure in Figure 5.19, Figure 5.20 shows spin-dependent and total transmission coefficients relative to the DFT-predicted Fermi energy E_F^{DFT} . The green line shows that the total transmission through the Mn(III)-Cl porphyrin is HOMO-dominated, whereas Figure 5.4b shows that for Mn(II) porphyrin transport is LUMO dominated.

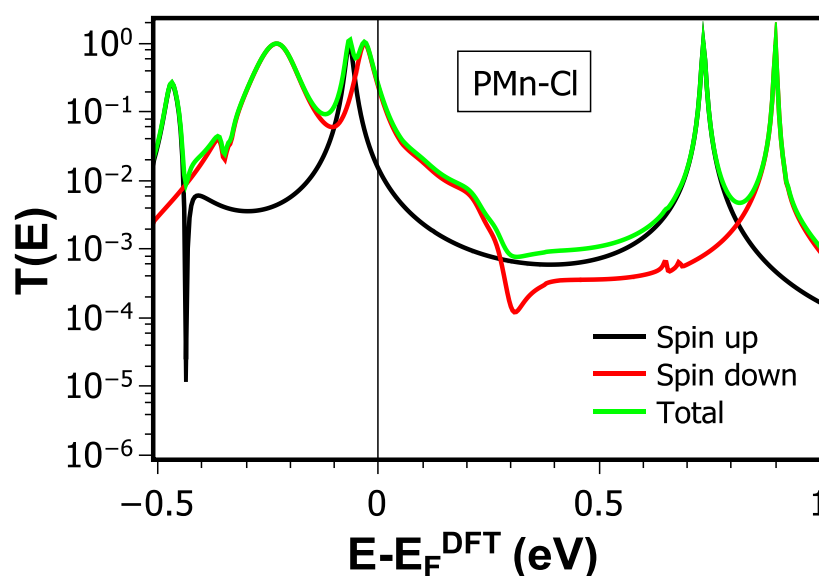


Figure 5.20. The spin-dependent and total transmission coefficients as a function of energy for Mn-porphyrin in presence of (Cl), which is shown in Figure 5.19.

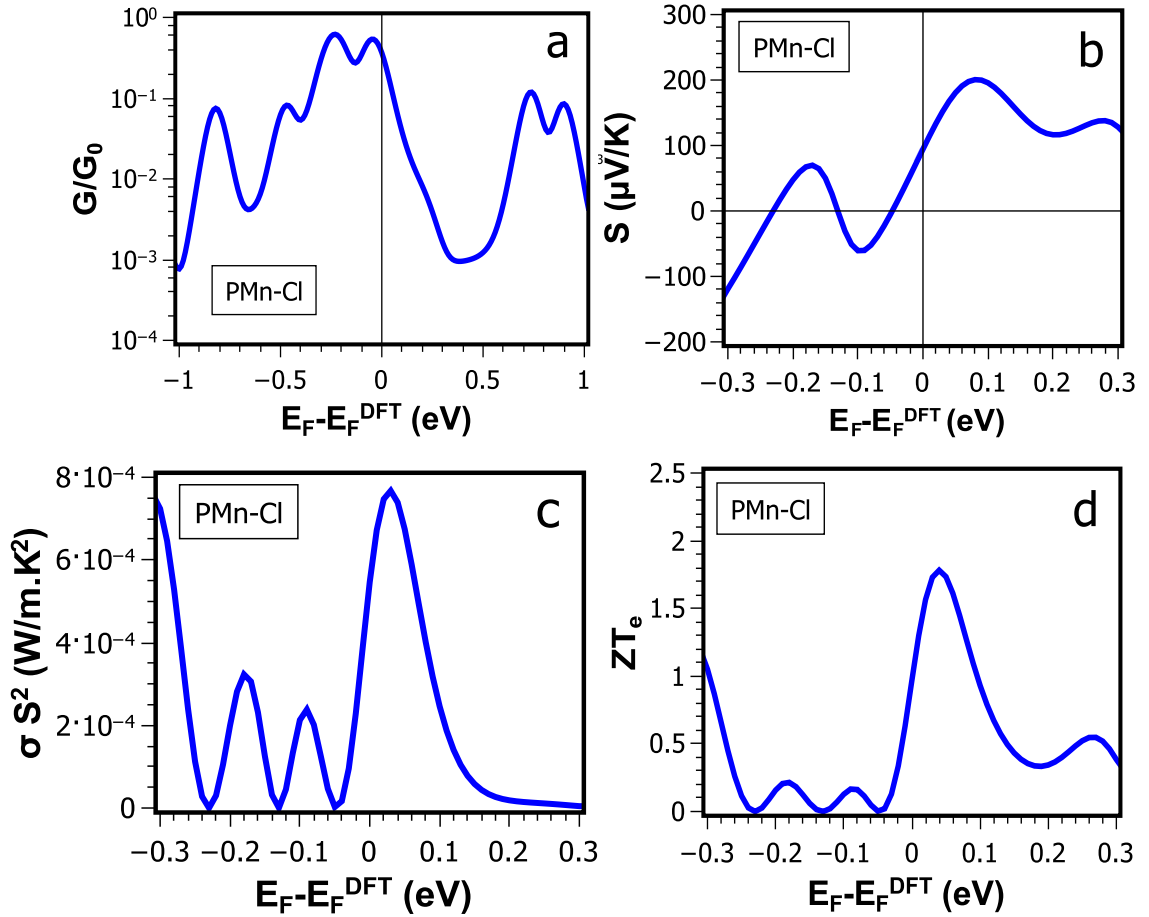


Figure 5.21. for the structure in figure 5.19, figures (a, b, c and d) show the room-temperature electrical conductance G , thermopower S , power factor $P = S^2\sigma$ and electronic figure of merit ZT_e over a range of Fermi energies E_F relative to the DFT-predicted Fermi energy E_F^{DFT} .

For the structure in figure 5.19, Figure 5.21 shows that the room-temperature electrical conductance for Mn-porphyrin in presence of (Cl) is HOMO-dominated conductance at the DFT Fermi energy. Figure 5.21b, 5.21c and 5.21d show results for the Seebeck coefficient (thermopower) S , power factor $S^2\sigma$, electronic contribution to the figure of merit ZT_e at room temperature. These results are for a range of Fermi energies E_F relative to the DFT-predicted Fermi energy E_F^{DFT} . Figure 5.21b demonstrates that in presence of Mn-Cl at the centre of the porphyrin monomer, the magnitude of thermopower S is changed to $+95 \mu V/K$.

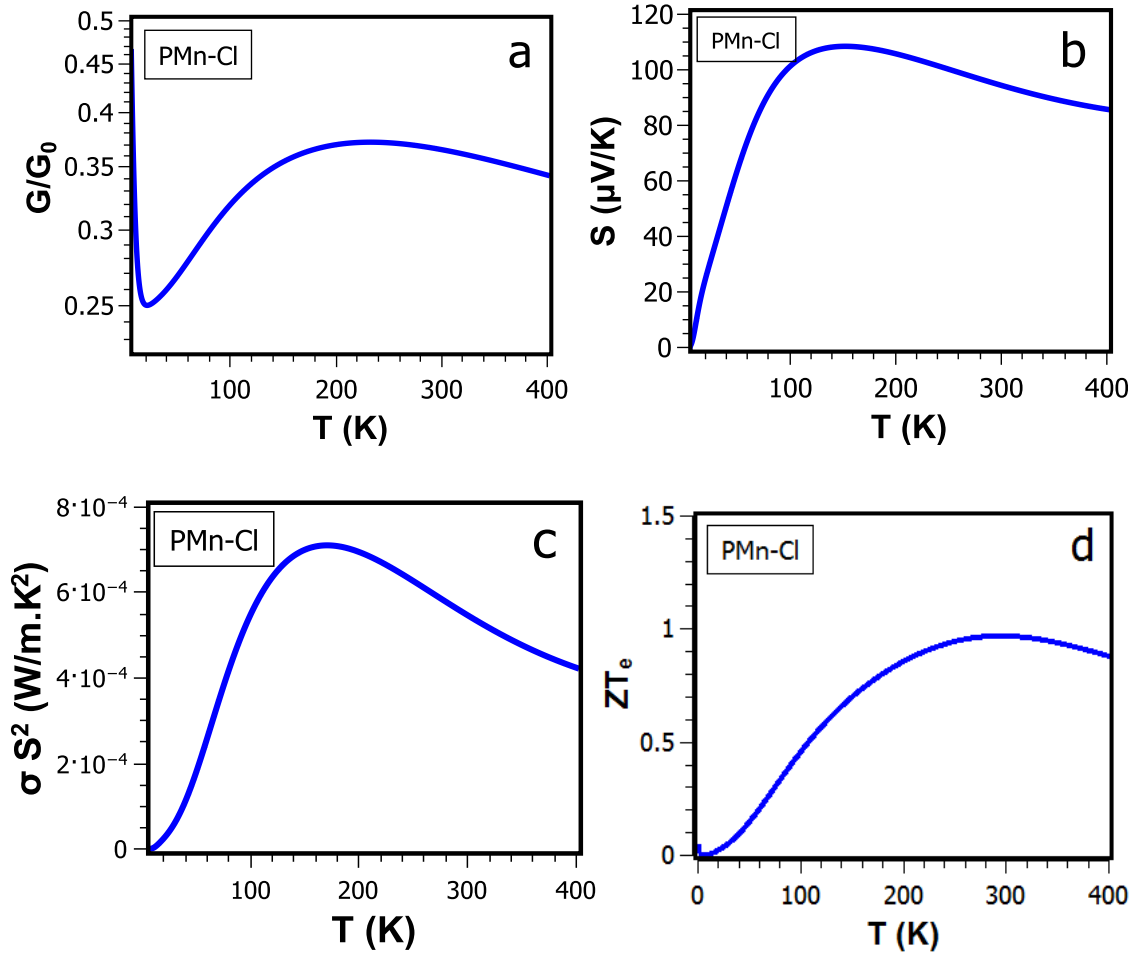


Figure 5.22: For the structure in figure 5.19, (a, b, c and d) represent the electrical conductance, Seebeck coefficients S (thermopower), power factor $P = S^2\sigma$, electronic contribution to the figure of merit ZT_e as a function of temperature, evaluated at $E_F = E_F^{DFT}$.

For the structure in figure 5.19, Figures 5.22(a, b, c and d) show the electrical conductance G , Seebeck coefficients S (thermopower), power factor $S^2\sigma$ and electronic figure of merit ZT_e as a function of temperature, obtained using the DFT-predicted Fermi energy E_F^{DFT} .

5.5 Summary

In this work we investigated the thermoelectric properties of metalloporphyrins connected by thiol anchor groups to gold electrodes. By varying the transition metal-centre over the family Mn, Co, Ni, Cu, Fe, and Zn we are able to tune the molecular energy levels relative to the Fermi energy of the electrodes. The resulting single-molecule room-temperature thermopowers range from almost zero for Co and Cu centres, to +80 $\mu\text{V/K}$ and +230 $\mu\text{V/K}$ for Ni and Zn respectively. In contrast, the thermopowers with Mn(II) or Fe(II) metal centres are negative and lie in the range -280 to -260 $\mu\text{V/K}$. Complexing these with a counter anion to form Fe(III) and Mn(III) changes both the sign and magnitude of their thermopowers to +218 and +95 respectively. The room-temperature power factors of Mn(II), Mn(III), Fe(III), Zn and Fe(II) porphyrins are predicted to be $5.9 \times 10^{-5} \text{ W/m.K}^2$, $5.4 \times 10^{-4} \text{ W/m.K}^2$, $9.5 \times 10^{-4} \text{ W/m.K}^2$, $1.6 \times 10^{-4} \text{ W/m.K}^2$ and $2.3 \times 10^{-4} \text{ W/m.K}^2$ respectively, which makes these attractive materials for molecular-scale thermoelectric devices.

Chapter 6

A New Approach to Materials Discovery for Electronic and Thermoelectric Properties of Single-Molecule Junctions

In the this Chapter, I will present a new approach to materials discovery for electronic and thermoelectric properties of single-molecule junctions. In this work, I have investigated a large set of symmetric and asymmetric molecules to demonstrate a general rule for molecular-scale quantum transport, which provides a new route to materials design and discovery. The rule states “the conductance of an asymmetric molecule is the geometric mean of the conductance of the two symmetric molecules derived from it and the thermopower of the asymmetric molecule is the algebraic mean of their thermopowers” This work has been in collaboration with University of Bern, Switzerland and Xiamen University, China. The results presented here were published in the ref [168].

6.1 Introduction

Nowadays there exist a variety of techniques for measuring the electrical conductance G and thermopower S of single molecules, such as scanning tunneling microscopy (STM) [26, 169],

current probe atomic force microscopy [170, 171], STM-break junction (STM-BJ) [172-174], crossed-wire geometry [175], nanoparticle junctions [176, 177], mechanically controlled break junctions (MCBJ) [178], electromigration setups [179, 180] and nanopores [14]. Schematically, the measured systems are of the form electrode-X-B-Y-electrode, where X and Y are anchor groups, which bind the molecule to the electrodes and B is the functional backbone of the molecule. A number of experimental and theoretical studies demonstrated that useful electronic and thermoelectric functionalities, such as switching, sensing, rectifying and heat-to-electricity converters can be optimised by modifying the backbone B of the molecules, as well as the anchors [8, 83, 181, 182]. For molecules of length less than approximately 3nm, charge transport has been shown to be dominated by phase coherent electron transport [183], and therefore the subparts X, B and Y cannot be assigned their own conductance or thermopower within the molecule. Nevertheless a recent experimental and theoretical study demonstrated that for molecules containing serially connected meta, para or ortho phenyl rings, their conductances obtained by changing the sequencing of the rings are related to each other [20], which implies that molecular subparts X, B and Y are individually characterizable by single numbers. These ‘circuit rules’ provide a theoretical basis for the systematic categorisation of trends in single-molecule measurement data. They provide guidance for the design and synthesis of molecular devices with optimal electronic and thermoelectric properties by treating molecular components as individual building blocks. In this chapter we show that this rule is much more widely applicable than initially suggested in ref. [20] and can be applied to a very wide range of symmetric and asymmetric molecules, with or without donor and/or acceptor groups. For the first time we also provide a circuit rule for the thermopower S (i.e. Seebeck coefficient) of single molecules. These circuit rules are of interest, because they provide rules for the discovery of new materials by predicting electronic and thermoelectric properties of molecules. This is particularly important, because theoretical

methods such as density functional theory and GW many body theory are do not usually provide quantitative predictions of such properties [184].

It is well known that the transmission coefficient of two serially-connected phase-coherent scatterers with individual transmission coefficients T_1 and T_2 , is of the form $T = \frac{T_1 T_2}{1 - 2\sqrt{R_1 R_2} \cos \varphi + R_1 R_2}$, where φ is a quantum phase arising from quantum interference (QI) between the scatterers [185]. Consequently the transmission coefficient T cannot normally be factorized to a product of terms associated with the individual scatterers alone. Nevertheless, the following argument leads us to a ‘circuit rule’ which describes how the transmission changes when the sequential order of the scatterers is changed. First we note that Dyson’s equation for the Green’s function of a structure comprising three serially-connected subsystems X, B, Y is of the form

$$\begin{bmatrix} E - H_X & -V_X & 0 \\ -V_X^\dagger & E - H_B & -V_Y \\ 0 & -V_Y^\dagger & E - H_Y \end{bmatrix} \begin{bmatrix} G_{XX} & G_{XB} & G_{XY} \\ G_{BX} & G_{BB} & G_{BY} \\ G_{YX} & G_{YB} & G_{YY} \end{bmatrix} = I, \quad (6.1)$$

where H_X (H_Y) is the Hamiltonian of the combined left electrode and anchor X (right electrode and anchor Y) and V_X (V_Y) is the coupling between the backbone of the molecule and the anchor X (Y). From this expression, the relevant sub-matrix of the Green’s function that describes electron propagation across the molecule from X to Y is

$$G_{YX} = g_Y V_Y^\dagger G_{BB} V_X^\dagger g_X, \quad (6.2)$$

where $G_{BB} = (E - H_B - \Sigma)^{-1}$ is the Green’s function of the coupled backbone and g_X (g_Y) is the Green’s function of the combined left electrode and anchor X (right electrode and anchor Y) and $\Sigma = V_X g_X V_X^\dagger + V_Y^\dagger g_Y V_Y$. If the electrodes are coupled to the anchors through a single site at both ends, the transmission coefficient through the molecule from one electrode to the other is $T_{XBY} = (\hbar v)^2 |[G_{YX}]_{ij}|^2$, where v is the group velocity of the electrodes, i and j

denote the anchor sites connected to electrodes [184-186]. For molecules such as those shown in Figure 6.1, the anchors are linked to only single sites k, l in the backbone, in which case the transmission coefficients takes the form

$$T_{XBY} = \hbar v \left| [g_Y V_Y^\dagger]_{ik} \right|^2 \left| [G_{BB}]_{kl} \right|^2 \hbar v \left| [V_X^\dagger g_X]_{lj} \right|^2 = A_X \times B_B \times A_Y, \quad (6.3)$$

where $A_X = \hbar v \left| [V_X^\dagger g_X]_{lj} \right|^2$, $A_Y = \hbar v \left| [g_Y V_Y^\dagger]_{ik} \right|^2$ and $B_B = \left| [G_{BB}]_{kl} \right|^2$. The factor B_B depends on X and Y via the self-energies $V_X g_X V_X^\dagger$ and $V_Y^\dagger g_Y V_Y$. However if the couplings are sufficiently weak and the Fermi energy does not coincide with the poles of g_X and g_Y , then Σ can be negligible and from Eq. (6.3) it follows that

$$T_{XBY}^2 = T_{XBX} T_{YBY} \quad (6.4)$$

The dependency of B_B of X and Y is the smallest when the Fermi energy is located far away from the poles of g_X and g_Y , which is the case for off-resonant electron transport in the co-tunneling regime. Based on the Landauer formula, and since Eq. (6.4) is valid for a range of energies larger than $kT = 25$ meV, the room temperature conductance also satisfies

$$G_{XBY}^2 = G_{XBX} G_{YBY}. \quad (6.5)$$

Since this approximate relation is true for a range of energies within the HOMO-LUMO gap, the rules for the derivatives of the logarithm of the transmission coefficients are expected to satisfy $\frac{d}{dE} \log T_{XBY}^2 = \frac{d}{dE} \log T_{XBX} + \frac{d}{dE} \log T_{YBY}$, which leads the circuit rule for the low-temperature thermopower [187]:

$$2S_{XBY} = S_{XBX} + S_{YBY} \quad (6.6)$$

Although density functional theory (DFT) is not a quantitative theory, it has been shown to correctly predict trends in transport properties. In order to demonstrate that the above rules are valid for a wide range of molecular junctions, we performed DFT-based electron transport

calculations for 193 molecules. The molecules are classified according to their backbone structures, and their attached anchors (as shown in Figure 6.1a-c). In Figure 6.1, X and Y indicate the location of the anchor groups. The anchor groups X and Y are chosen from the family CN, Py, BT, NH₂, S, several of which have been studied extensively in the literature [188-195]. In Figure 6.1a, shows 180 molecules formed from 12 backbones and five anchor groups. In the case of the 10 X-R-Y molecules shown Figure 6.1b, X and Y are chosen to be one of CN, PY, NH₂, S and in the case of 3 X-But-Y, shown in Figure 6.1c, X and Y are chosen to be either S or NH₂. Figures 6.1a,b illustrate the anchor as well as the aromatic rings, to which the anchor is attached.

6.2 Methods

In order to demonstrate computationally the circuit formulas, we performed DFT based electron transport calculations on systematically constructed gold-molecule-gold systems. All together 193 molecules were constructed with attached gold pyramids as electrodes, with anchors and backbones showed in Figures 6.1a-c.

To consistently attach the pyramids to the molecules with many different backbones and anchors, we first prepared a relaxed molecular geometry with their planar and extended conformations. The relaxation was performed with MOPAC2012 RHF method and PM7 parameter-set [196] with constraints that kept the molecular conformations planar. During the relaxation, the non-hydrogen atoms were allowed to move only in the molecular plane and only the hydrogen atoms were allowed to move away from the molecular plane.

The initial conformation for the relaxation was linear extended where the anchors are at the two far ends of the molecule modelling a possible conformation within a break-junction experiment (shown Figure 6.2a) when a typical conductance plateau is recorded [190, 197].

This is typically occurring when the gap between the electrodes is slightly less than the molecular length, illustrated in Figure 6.2a.

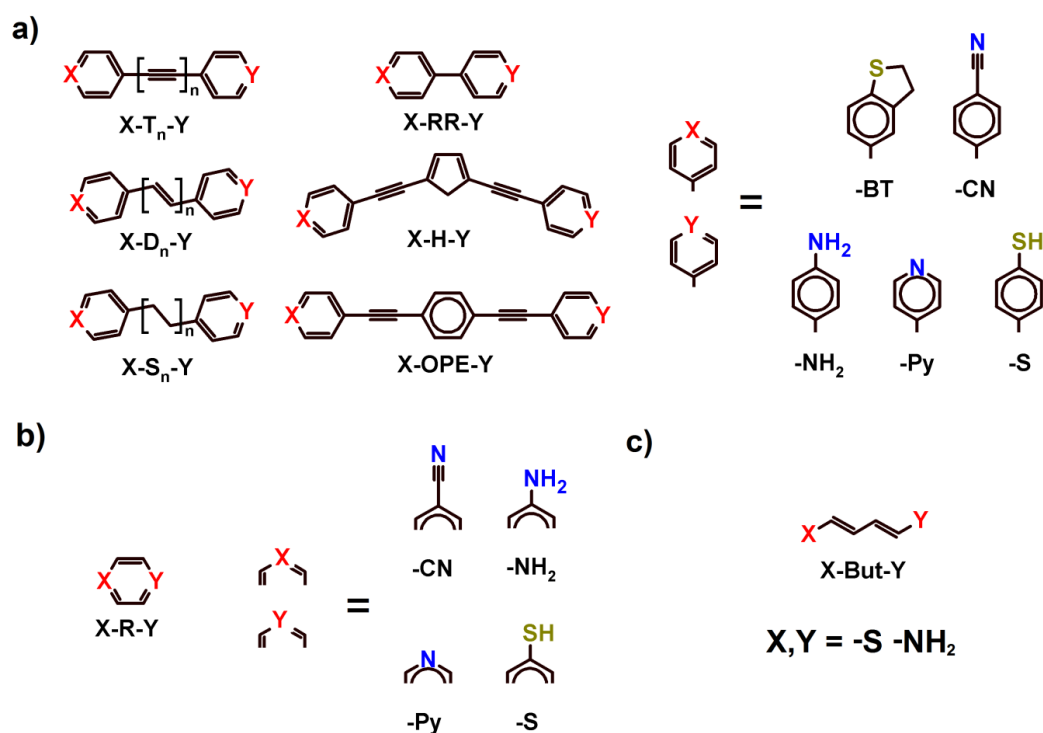


Figure 6.1. The 193 combinations of backbones and anchors used to obtain figure 6.4.1(a) The left column shows 3 alkanes, 3 alkenes and 3 alkynes (where $n=1, 2, 3$) and the second-from-left column shows 3 other backbones. (i.e. a total of 12 backbones). The right panel shows 5 anchors cyano (CN), pyridil (Py), dihidrbenzothiol (BT), amine (NH_2) and thiol(S). These combine to yield 12×5 symmetric molecules and $12 \times 5 \times 4 / 2 = 120$ asymmetric molecules (b) Molecules with a single ring as the backbone and four kinds of anchors: in total there are 4 symmetric and 6 asymmetric variants of these. c) shows a single Butadiene chain with two kinds of anchors: in total there is one symmetric and two asymmetric versions of this. All of the molecular geometries are shown in Figures (6.6)-(6.19).

In the case of thiol, the sulphur was capped with a hydrogen atom for the relaxation, then after the relaxation the hydrogen atom from the sulphur was removed. We performed relaxations with SIESTA [107] DFT code (force tolerance = 0.01, GGA, DZP) as well for a few molecules and found that planar conformations are usually stable, with significant exceptions of $X-RR-Y$ type molecules, where the aromatic rings are twisted away from each other.

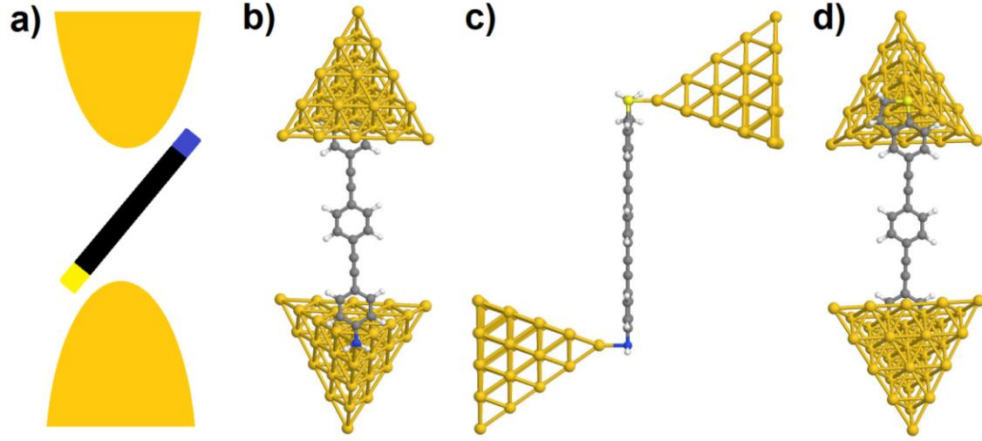


Figure 6.2 a) Molecule arrangement in break-junction experiment. b),c),d) Top, side and bottom views, respectively, of the model junction geometry of a particular case (BT-OPE-NH₂) for systematic comparisons.

Since our investigation focuses on the electronic structures, we consistently kept the all structures planar. For the planar molecular structures a 35-atom 111 directed gold pyramid was attached to the anchoring atoms (S and N) perpendicularly to the molecular plane. The apex gold atom-anchor atom distance was set 2.1Å for the Py, CN anchors, 2.3Å for the NH₂ and BT and 2.35Å for the thiol anchor. This setup allowed consistent systematic comparisons between molecules with different backbones and anchors. The electronic transport calculations were performed by first obtaining the Hamiltonian of the isolated Au-molecule-Au structure by SIESTA, DZP basis set and GGA-PBE exchange-correlation potential parameterization. Then the obtained Hamiltonian was used in GOLLUM [198], with wide-band approximation to calculate the transmission coefficients, the room temperature conductance and the room temperature thermopower with the DFT computed Fermi energy. The wide-band lead was attached to the two outer layers of the gold pyramid with $\Gamma = 4.0eV$ coupling [199]. The anchor and backbone parameters were determined by minimizing numerically the function $\sum_B^{backbones} \sum_X^{anchors} \sum_{Y \geq X}^{anchors} \left(a_X + b_B + a_Y - \log_{10} \frac{G_{XBY}}{G_0} \right)^2$ with respect to the various a_X, b_B parameters with the constraint $b_{RR} = 0$, using Broyden-

Fletcher–Goldfarb–Shanno (BFGS) method, where “backbones” and “anchors” are in Figure 6.1, G_{XBY} is the DFT-computed conductance value, and $Y \geq X$ denotes the exclusion of the double counting the same molecule.

6.3 Results and discussion

For transport calculations, the planar conformations of the molecules were considered, and the gold leads were attached perpendicularly to the plane of the molecules as shown in Figure 6.2. Examples of transmission curves for a selection of molecules are shown in Figure 6.3.

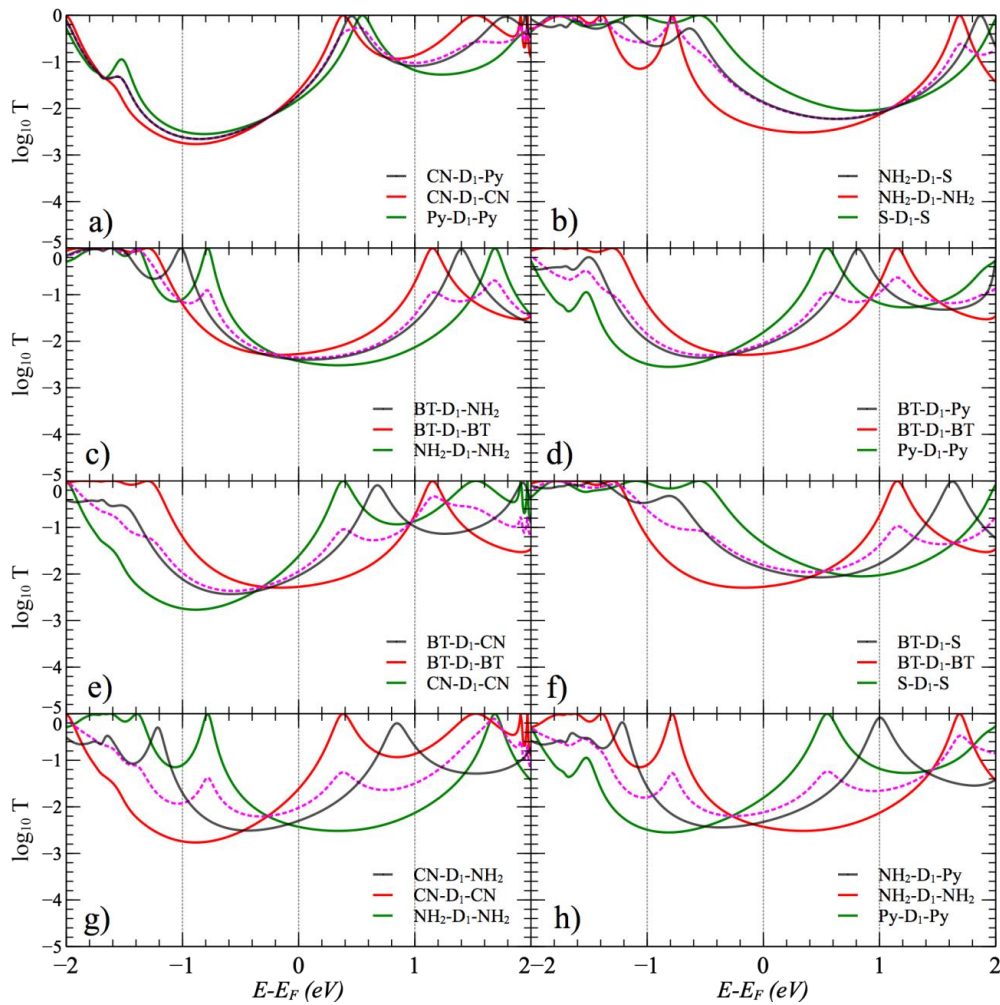


Figure 6.3. Transmission coefficients for symmetric and asymmetric molecules $X-D_1-X$, $Y-D_1-Y$ and $X-D_1-Y$. The dashed pink curves show the circuit rule predictions for $X-D_1-Y$. Additional transmission coefficient curves are shown in Figures (6.20)-(6.38).

The circuit formulae are first verified by calculating the room temperature conductance and thermopower, using the DFT predicted Fermi energies for all molecules. To demonstrate the circuit rule for conductance, we separately computed the electrical conductances (G_{XBY} , G_{XBX} , G_{YBY}) and Seebeck coefficients (S_{XBY} , S_{XBX} , S_{YBY}) of the individual molecules and then plotted the square root of the product $\sqrt{G_{XBX}G_{YBY}}$ versus G_{XBY} . In Figure 6.4a, the small scatter about a straight line demonstrates that in the majority of the cases the circuit rule gives an accurate prediction for the conductance. To demonstrate the circuit rule for thermopower, we separately computed the Seebeck coefficients (S_{XBY} , S_{XBX} , S_{YBY}) and then plotted the average $(S_{XBX} + S_{YBY})/2$ versus S_{XBY} , as shown in Figure 6.4b. This remarkable result means that from measurements of the conductances G_{XBX} , G_{YBY} it is possible to predict the conductance G_{XBY} and similarly for the Seebeck coefficients.

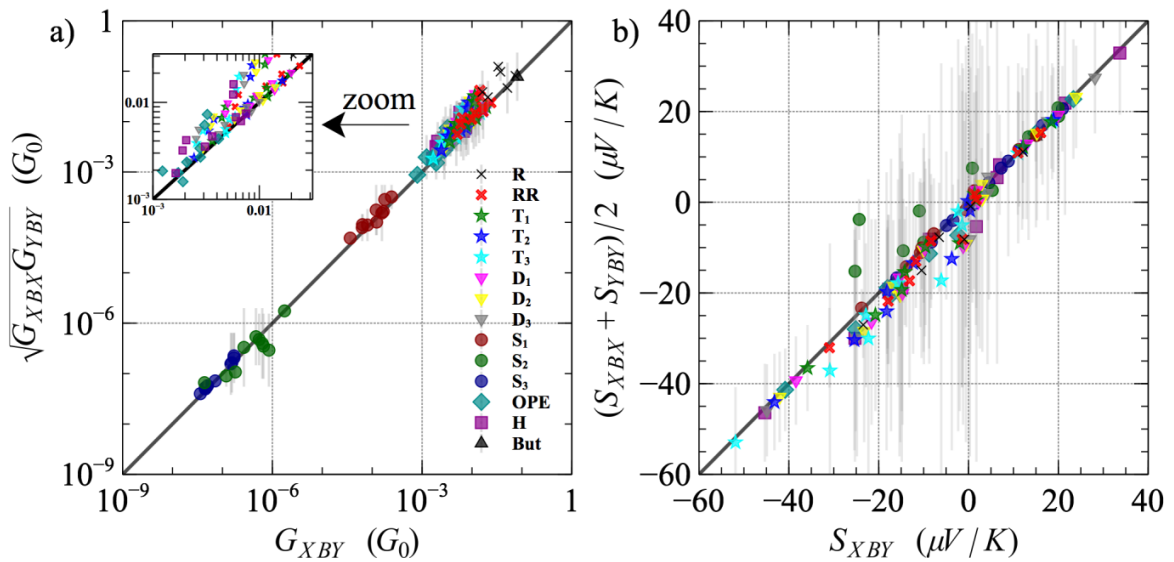


Figure 6.4. a) Comparison between the conductances G_{XBY} and the geometric means $(G_{XBX}G_{YBY})^{1/2}$. b) Comparison between the thermopowers S_{XBY} and the arithmetic means $(S_{XBX} + S_{YBY})/2$. The top and bottom ends of the vertical grey lines show the values for the symmetric molecules used in the circuit rules. The different colours and markers indicate the various molecular backbones. The notation in the legend is as follows the backbone labelling in Figure 6.1.

We now discuss the sources of deviations from the circuit rule predictions. The inset of Figure 6.4a, shows that in a number of cases a slight systematic deviation can be observed. The origin of these deviations is illustrated by Figure 6.3, which shows several different

transmission coefficient curves of the X-D₁-Y type molecules. These show that if the resonances of the two symmetric molecules are close to each other, then the circuit rule is accurate over almost the whole of HOMO-LUMO gap; for example in Figures 6.3a,b, the dashed purple curves compare well with the black curves. In these cases $V_X g_X V_X^\dagger \approx V_Y^\dagger g_Y V_Y$, therefore even if B_B depends strongly on the self-energy terms, the dependence is similar in all of the symmetric and asymmetric cases and both side of the Eq. (6.4) follow the same energy dependence. On the other hand, if the location of the resonances of X-B-X and Y-B-Y differ significantly (from Figure 6.3c to 6.3h), the error in circuit rule for the transmission coefficient is large. In particular cases, when transport through one anchor (such as X=NH₂) is HOMO dominated, whereas the other anchor (such as Y=Py) is LUMO dominated, but their HOMO-LUMO gaps are similar, then the two self energy terms $V_X g_X V_X^\dagger$ and $V_Y^\dagger g_Y V_Y$ are expected to be very different. Such examples can be seen in in Figures 6.3g,h.

We also note that the errors in circuit rule predictions for the thermopower are not necessarily correlated with those of the conductance. While the magnitude of transmission coefficients is inaccurate, the slope of the transmission curve of the X-D₁-Y in the log plot in Figure 6.3g,h (black curve) remains comparable with the slope of the ones obtained with the circuit rule (dashed purple). In general, Σ is the smallest and the circuit rule most accurate when the Fermi energy is furthest from both the HOMO and LUMO resonances. We note that the DFT calculations typically significantly underestimate the HOMO-LUMO gap [200-202], therefore for realistic electronic structures the circuit rule may applicable even more accurately than shown in Figure 6.3 and Figure 6.4. Other possibilities, that may hinder the accuracy of the circuit rules for realistic conductance, are thermal fluctuation of the molecular conformation and the experimental distributions of junction geometries [203].

To facilitate the utilisation of the above circuit rules for single-molecule-junction materials discovery, we note that they are a consequence of the fact that the transmission coefficients

T_{XBY} can be factorized into a product of the kind $A_X B_B A_Y$, where A_X and A_Y do not depend on B, but B_B may depend on X and Y. Nevertheless when the Fermi energy is located in the valley of the HOMO-LUMO gap it is possible that Σ is negligible and therefore B_B depends only on connectivity and is independent of the choice of the anchor groups. Typically if this is the case, the transmission coefficients can be factorized to independent factors of anchors and backbones, and these factors are transferable between different molecules. In other word, the logarithm of the conductance and the thermopower are sums of transferable factors. To verify this factorizability, we now assume that computed logarithmic conductance values and thermopower values can be written

$$\log_{10} \frac{G_{XBY}}{G_0} = a_X + b_B + a_Y \quad (6.7)$$

$$\frac{S_{XBY}}{k_B/e} = a'_X + b'_B + a'_Y \quad (6.8)$$

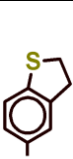
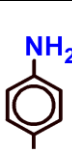
where the factors $a_X, b_B, a_Y, a'_X, b'_B, a'_Y$ are independent and transferable. To obtain these parameters, we minimize numerically the function

$$F = \sum_B^{\text{Backbones}} \sum_X^{\text{Anchors}} \sum_{Y \geq X}^{\text{Anchors}} \left(a_X + b_B + a_Y - \log_{10} \frac{G_{XBY}}{G_0} \right)^2, \quad (6.9)$$

where the G_{XBY} values are the DFT-computed conductance values (see Methods section). We note that the separation between the anchor and backbone terms is arbitrary, therefore we set the backbone term of X-RR-Y type molecules to zero, i.e. we choose $b_{RR} = 0$, and in this calculation we choose the molecules in Figure 6.1a only. With this choice the a_X terms parametrize the anchoring structures shown in Figure 6.1a and Table 6.1, that is the anchor plus the aromatic ring. Consequently the b_B terms parametrize the backbone, that is the inner part of the molecules between the aromatic rings in Figure 1a. From $n_A=5$ different anchors and $n_B=12$ different backbones, this procedure yields 5 a_X parameters and 12 b_B parameters, from which we can reproduce the logarithmic conductance of $n_A(n_A+1)n_B/2=180$ molecules.

Similarly, the same minimizing procedure is used to obtain the thermopower parameters a'_X and b'_B . Table 6.1 shows the anchor and backbone parameters obtained using the above minimizing procedure. To demonstrate that they can be used to predict conductances and thermopowers, Figure 6.5a shows a comparison between the sum $a_X + b_B + a_Y$, and the conductance G_{XBY} while Figure 6.5b compares $a'_X + b'_B + a'_Y$ with S_{XBY} .

Table 6.1. Anchor and backbone parameters obtained by fitting Eqs. (6.7) and (6.8) to the DFT-computed room temperature conductances ($\log_{10}(G/G_0)$) and thermopowers (Se/k_B) respectively

Anchor X with rings						
		-BT	-CN	-NH ₂	-Py	-S
a_X		-1.12	-0.89	-1.20	-0.87	-0.68
a'_X		-0.02	-0.24	0.06	-0.17	0.19
Backbones B	RR	T ₁	T ₂	T ₃	OPE	H
b_B	0.00	-0.12	-0.25	-0.38	-0.73	-0.46
b'_B	0.00	-0.01	-0.05	-0.09	-0.02	-0.01
Backbones B	D ₁	D ₂	D ₃	S ₁	S ₂	S ₃
b_B	-0.09	-0.22	-0.35	-2.04	-4.57	-5.19
b'_B	-0.01	-0.01	-0.01	0.03	0.06	0.10

In Figure 6.5a, for each molecule, for the DFT computed conductance value G_{XBY} on the horizontal axis, we plotted the corresponding $10^{a_X+b_B+a_Y}G_0$ value marked by a red cross. The fact that the majority of the red crosses are close to the diagonal black line shows that the 5 a_X parameters and 12 b_B parameters in Table 6.1 can reproduce the logarithmic conductance of the 180 molecules in Figure 6.1a accurately. In essence, by minimizing the function F with respect to the 5 a_X parameters and 12 b_B parameters, we obtain their optimal value which holds the information of the conductance values of the 180 molecules. This is possible only

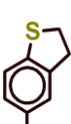
because the conductance can be factorized with good accuracy according to eq. (6.4) and therefore the 180 molecular conductances are not independent. Similarly, in Figure 6.5b, for each molecule, for the DFT computed thermopower value S_{XBY} on the horizontal axis, we plotted the corresponding $(a'_X + b'_B + a'_Y)S_0$ value marked by a red x. It is interesting to note that for the conductance, the values of anchor parameter a_X in Table 6.1 vary less than the values of the backbone parameters b_B . This is in contrast with the thermopower, for which the magnitudes of the anchor parameters a'_X vary more than the magnitudes of the backbone parameters b'_B , which suggests that the anchor may play a more dominant role in controlling the thermopower than the conductance.

Having demonstrated the validity of the circuit rules, within a consistent set of DFT-based calculation, we now discuss how they can be used experimentally for real-world discovery of single-molecule junction properties. Although DFT is widely used for analysing electron transport in single molecule junctions, it is at best a qualitative theory and therefore for accurate utilisation of the rules, the parameters a_X, b_B, a_Y and a'_X, b'_B, a'_Y should be determined experimentally. In a typical break junction experiment, the measured value of G_{XBY} varies markedly from measurement to measurement, because of variability in the atomic arrangement of the electrodes and in the electrode-anchor group binding geometry. Consequently many (often thousands) of conductance measurements are made and histograms of the logarithmic conductance $g_{\text{XBY}} = \log_{10} G_{\text{XBY}}/G_0$ are constructed. If \bar{g}_{XBY} is the most probable value of such a histogram, then the experimentally-quoted value is $\bar{G}_{\text{XBY}}/G_0 = 10^{\bar{g}_{\text{XBY}}}$. This variability is reflected in the anchor parameters a_X, a_Y . Therefore when applying the circuit rule to such experiments, it should be applied in a statistical sense. If the most probable values of a_X, a_Y are \bar{a}_X, \bar{a}_Y , then the most probable value of $\log_{10} \frac{G_{\text{XBY}}}{G_0}$ is $\bar{g}_{\text{XBY}} = \bar{a}_X + b_B + \bar{a}_Y$. Conversely, when the fitting procedure of equation (6.9) in ‘Methods’ is carried out using experimentally-quoted values, the resulting parameters are $\bar{a}_X, b_B, \bar{a}_Y$,

rather than a_X, b_B, a_Y . This is another reason why it is unsafe to use DFT values to make quantitative predictions, because it is usually much too expensive to simulate conductance histograms and therefore typically conductances of only a few anchoring configurations are reported.

At present we are aware of only one set of measurements on both asymmetric (X-B-Y) and symmetric (X-B-X and Y-B-Y) molecules with the same backbone. In ref [204] the measured conductance values of molecules S-R-S, NH₂-R-NH₂ are found to be 0.012G₀, 0.005G₀ respectively and for the asymmetric NH₂-R-S molecule two conductance values 0.006G₀ and 0.009G₀ were reported. The circuit rule gives $G/G_0 = 0.008$, which compares well with both of the measured values, thereby providing a direct experimental verification of the circuit rule. To illustrate how the circuit rules can be used to predict experimental conductances for future molecules from measured values of molecules available in the literature, we make use of the above factorisation procedure. To perform the fitting, we collected measured conductances for 19 different molecules from the literature [20, 194, 205-207] and used these to characterize 5 anchors and 6 backbones.

Table 6.2. Anchor and backbone parameters obtained by fitting Eq. (6.7) to the experimental room temperature conductance ($\log_{10}(G/G_0)$). For the $n_A=5$ anchor and $n_B=6$ backbone, the parameters give the conductance of $n_A(n_A+1)n_B/2=90$ molecules in the form of $G_{XBY} = 10^{a_X+b_B+a_Y} G_0$.

Anchor X with rings		 -BT	 -CN	 -NH ₂	 -Py	 -S
a_X (from experiments)	-	-1.12	-2.15	-1.44	-1.58	-1.22
Backbones B	RR	T ₁	T ₂	T ₄	OPE	OPE(meta)
b_B (from experiments)	0.00	-0.31	-0.63	-1.20	-1.37	-2.75

In Table 6.2 the anchor and backbone parameters are listed characterized with the experimental conductances. The parameters obtained from the experimental values are smaller than the theoretical values, as expected, due to the DFT's systematic errors with underestimating the HOMO-LUMO gap [202, 208], and the neglect of environmental and thermal effects in the calculations [203] Figure 6.5a and Table 6.3 show that the characterisation can reproduce the conductance of the 19 different molecules with good accuracy (marked with green triangles). The selection covers the typical experimental range of conductances from $10^{-2}G_0$ to $10^{-6}G_0$. Usually the short molecules with higher conductance, due to the snap back effect in the break-junction methods, are difficult to measure reliably. The long molecules with lower conductances (below $10^{-6} G_0$), due to the instrumental sensitivity, are also difficult to measure. The X-T_n-X type molecules are from ref [207], where X = Py, NH₂, S, BT and CN, and n=1,2 and 4, but varies for different X because not all molecules could be synthesized. The conductances for the Py-OPE-Py and Py-OPE(Meta)-Py type molecules are from ref [20] (Py-OPE(Meta)-Py denotes pmp), for the molecule NH₂-OPE-NH₂ is from ref [206] and S-OPE-S molecule is from ref[189]. From ref [192] we obtained the conductance of NH₂-RR-NH₂ and from ref [194] Py-RR-Py. The precise conductance values used in the calculations are quoted in Table 6.3.

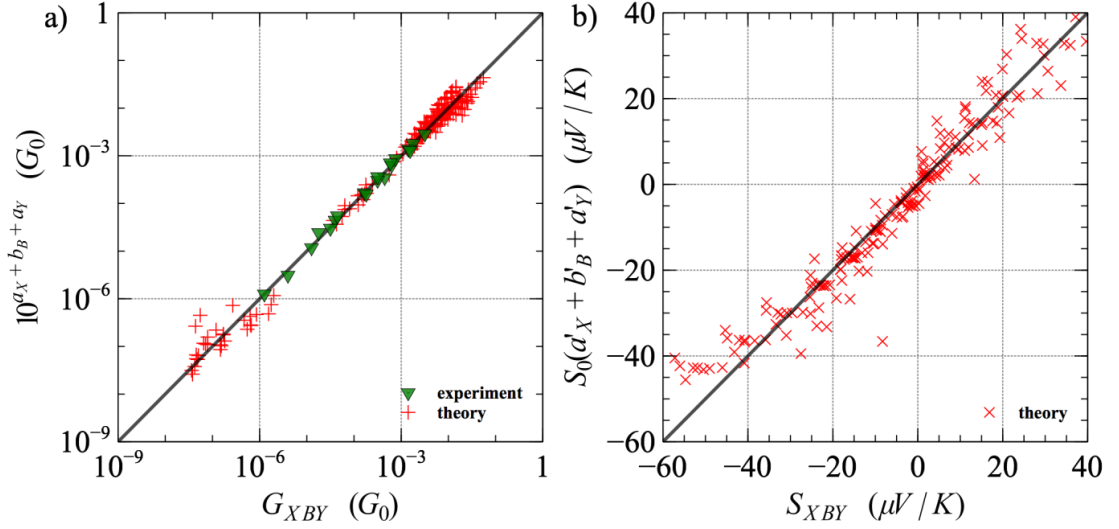


Figure 6.5. Factorized conductance and thermopower approximation are plotted against the DFT computed values (red markers) and experimental values (green triangle). In panel a), for each DFT-computed conductance G_{XBY} , a red cross marks the corresponding $10^{a_X + b_B + a_Y} G_0$ values. In panel b), for each DFT-computed thermopower S_{XBY} , a red cross marks the corresponding $(a'_X + b'_B + a'_Y) S_0$ values. In both cases the a_X and a'_X parameters and b_B and b'_B parameters are taken from Table 6.1. The green triangles in panel a) show the factorization of a selection of experimental conductance from the literature, quoted in Table 6.3. For each experimental conductance G_{XBY} the green triangle marks the corresponding $10^{a_X + b_B + a_Y} G_0$ value, where the a_X parameters and b_B parameters are taken from Table 6.2. $G_0 = 2e^2/h$, $S_0 = k_B/e$.

Finally we note that in Figure 6.5a, the green triangles, and Table 6.2, 6.3 and 6.4 are based on experimental conductance values, which naturally includes the effect of fluctuations. The fact that the green triangles are close to the diagonal demonstrates that the circuit rule indeed applies to 19 different experimentally-quoted most-probable conductances.

Table 6.3. Comparison between experimental conductances and the computed conductances from Eq. (6.7), using the fitted anchor and backbone parameters shown in Table 6.2. ^(a) Experimental values are taken from ref [143] by averaging STM-BJ and MCBJ values, ^(b) from ref [144], ^(c) from ref [20], ^(d) from ref [189], ^(e) from ref [206] and ^(f) from ref [139].

Molecule X B Y	Experimental $\log_{10} \frac{G}{G_0}$	$a_X + b_B + a_Y$	Molecule X B Y	Experimental $\log_{10} \frac{G}{G_0}$	$a_X + b_B + a_Y$
Py T ₁ Py	-3.35 ^(a)	-3.47	CN T ₁ CN	-4.75 ^(a)	-4.61
Py T ₂ Py	-3.78 ^(a)	-3.79	CN T ₂ CN	-4.9 ^(a)	-4.93
Py T ₄ Py	-4.4 ^(a)	-4.36	CN T ₄ CN	-5.4 ^(a)	-5.5
NH ₂ T ₁ NH ₂	-3.205 ^(a)	-3.19	S T ₁ S	-2.75 ^(a)	-2.75
NH ₂ T ₂ NH ₂	-3.5 ^(a)	-3.51	S T ₂ S	-3.12 ^(a)	-3.07
BT T ₁ BT	-2.5 ^(a)	-2.55	Py OPE Py	-4.5 ^(c)	-4.53
BT T ₂ BT	-2.845 ^(a)	-2.87	S OPE S	-3.74 ^(d)	-3.81
BT T ₄ BT	-3.5 ^(a)	-3.44	NH ₂ OPE NH ₂	-4.35 ^(e)	-4.25
Py RR Py	-3.23 ^(b)	-3.15	Py Meta Py (pmp) ^(c)	-5.9 ^(c)	-5.91
NH ₂ RR NH ₂	-2.81 ^(f)	-2.89			

Table 6.4. Conductance predictions for a few new molecules based on Table 6.2^(a). Predictions from Table 6.2^(a) for all combinations of backbones and anchors are presented in Table 6.5.

Molecule X B	$a_X + b_B + a_Y$ ($\log_{10}(G/G_0)$)	Molecule X B	$a_X + b_B + a_Y$ ($\log_{10}(G/G_0)$)
Py-T ₁ -CN	-4.04	Py-OPE-NH ₂	-4.39
Py-T ₁ -NH ₂	-3.33	Py-OPE-BT	-4.07
Py-T ₁ -BT	-3.01	Py-OPE-S	-4.17
Py-T ₁ -S	-3.11	CN-OPE-CN	-5.67
CN-T ₁ -NH ₂	-3.9	CN-OPE-NH ₂	-4.96
CN-T ₁ -BT	-3.58	CN-OPE-BT	-4.64
CN-T ₁ -S	-3.68	CN-OPE-S	-4.74
NH ₂ -T ₁ -BT	-2.87	NH ₂ -OPE-BT	-3.9
NH ₂ -T ₁ -S	-2.97	NH ₂ -OPE-S	-4.03
BT-T ₁ -S	-2.65	BT-OPE-BT	-3.61
Py-OPE-CN	-5.1	BT-OPE-S	-3.71

6.4 Associated Content

These Figures contain all of the molecular geometries and all computed transmission coefficient functions. Theoretical predictions for the conductance of all anchor group/backbone combinations are included in Table 6.5.

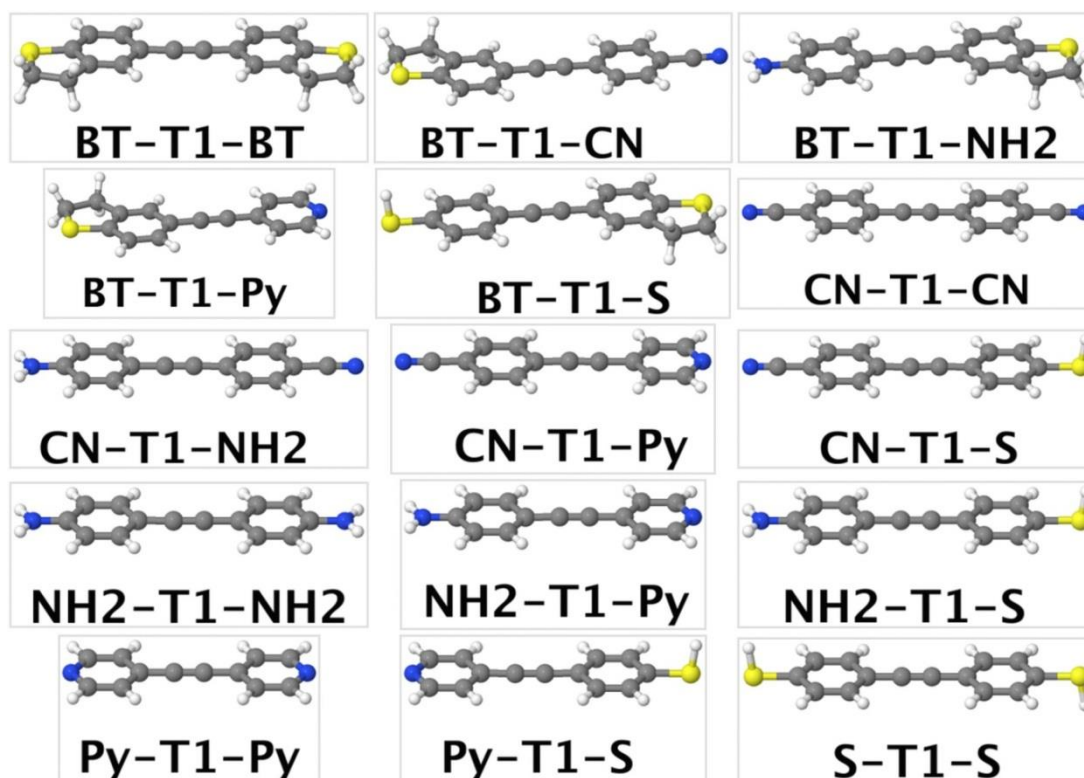


Figure 6.6. Molecules with T1 backbone.

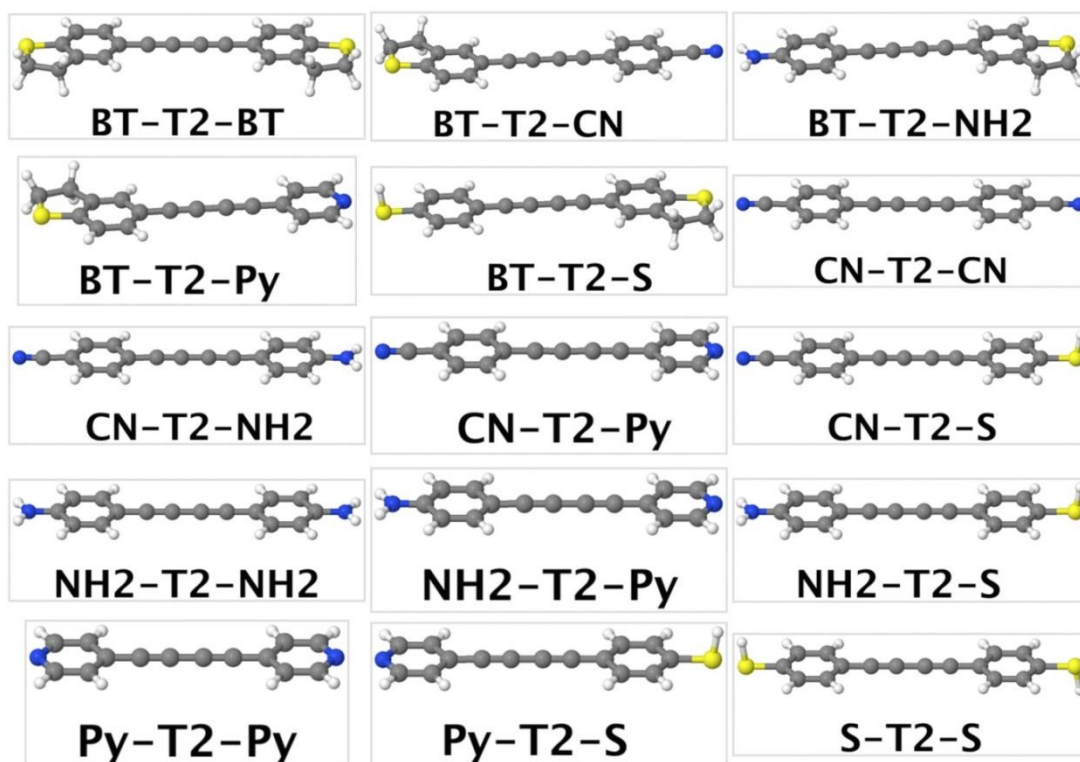


Figure 6.7. Molecules with T2 backbone.

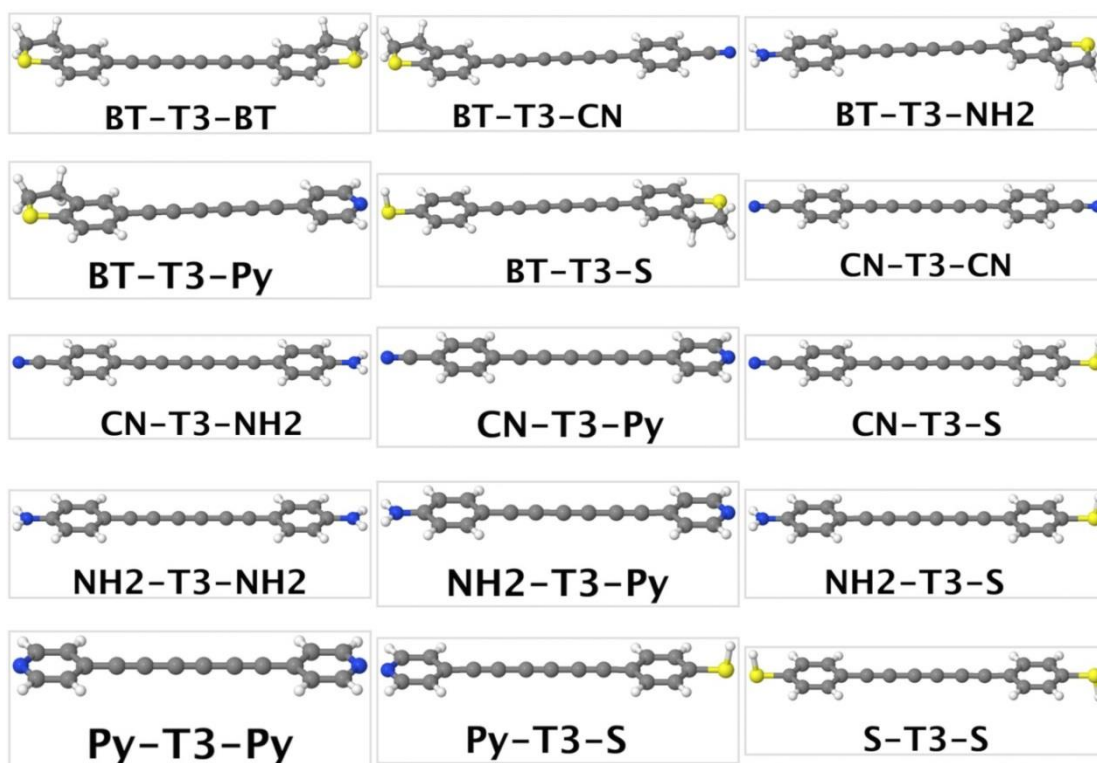


Figure 6.8. Molecules with T3 backbone.

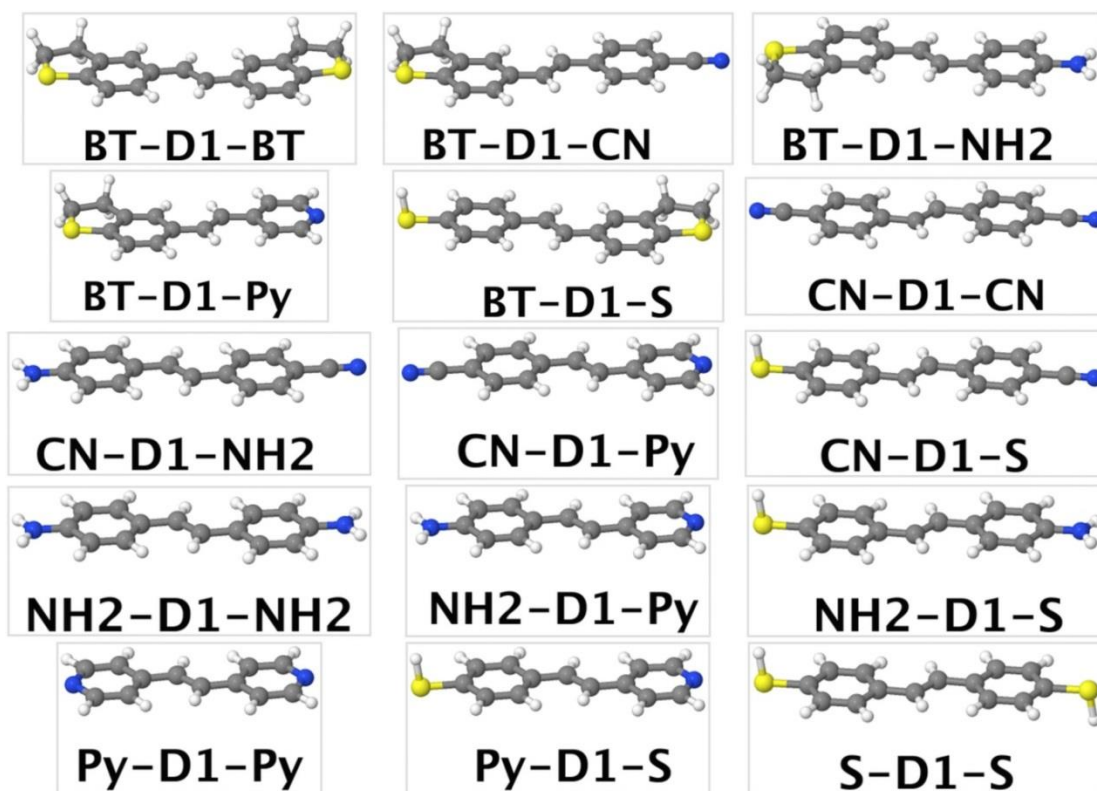


Figure 6.9. Molecules with D1 backbone.

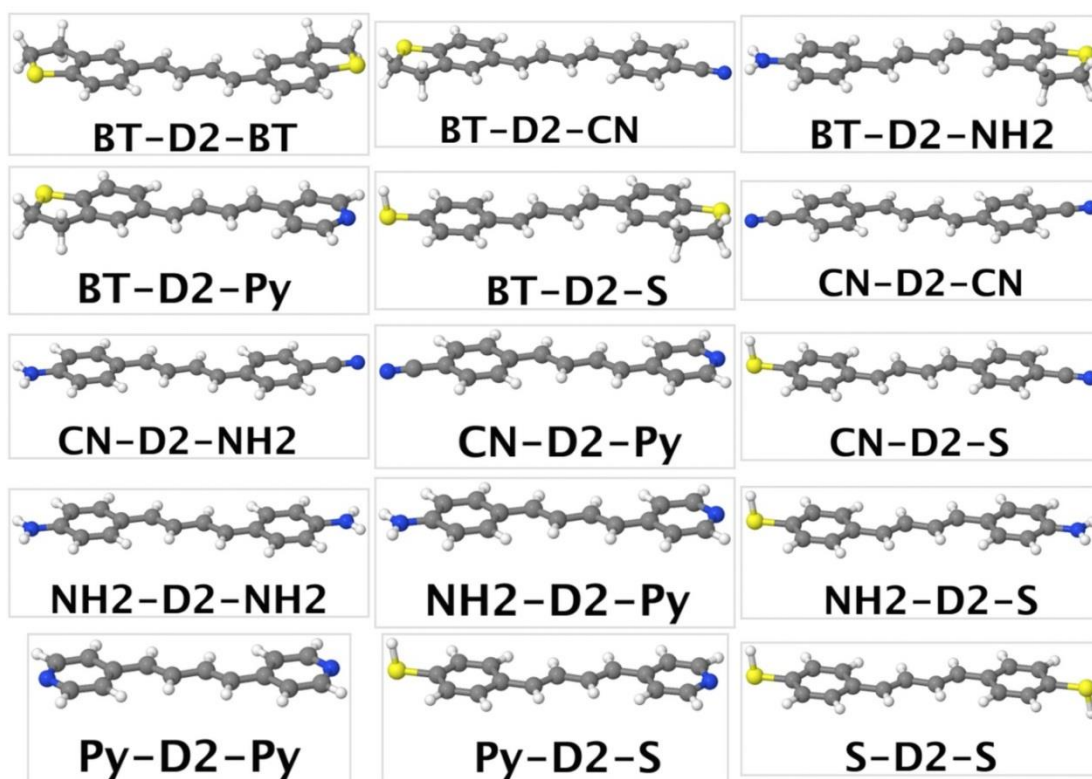


Figure 6.10. Molecules with D2 backbone.

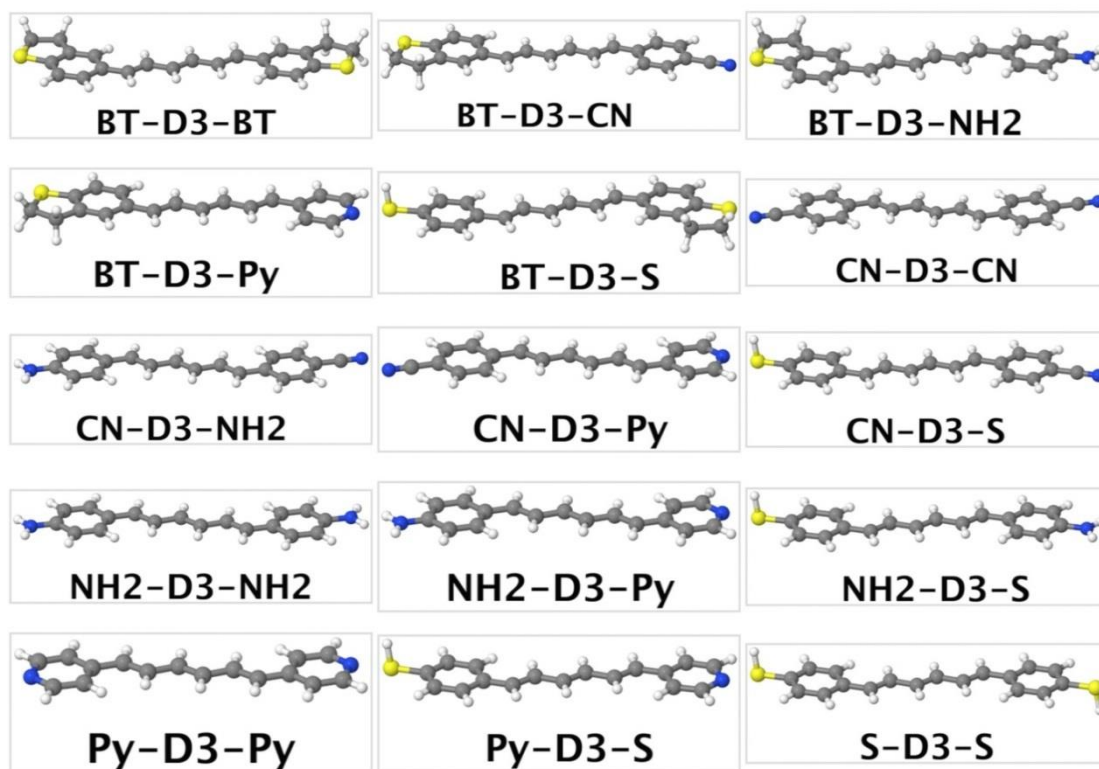


Figure 6.11. Molecules with D3 backbone.

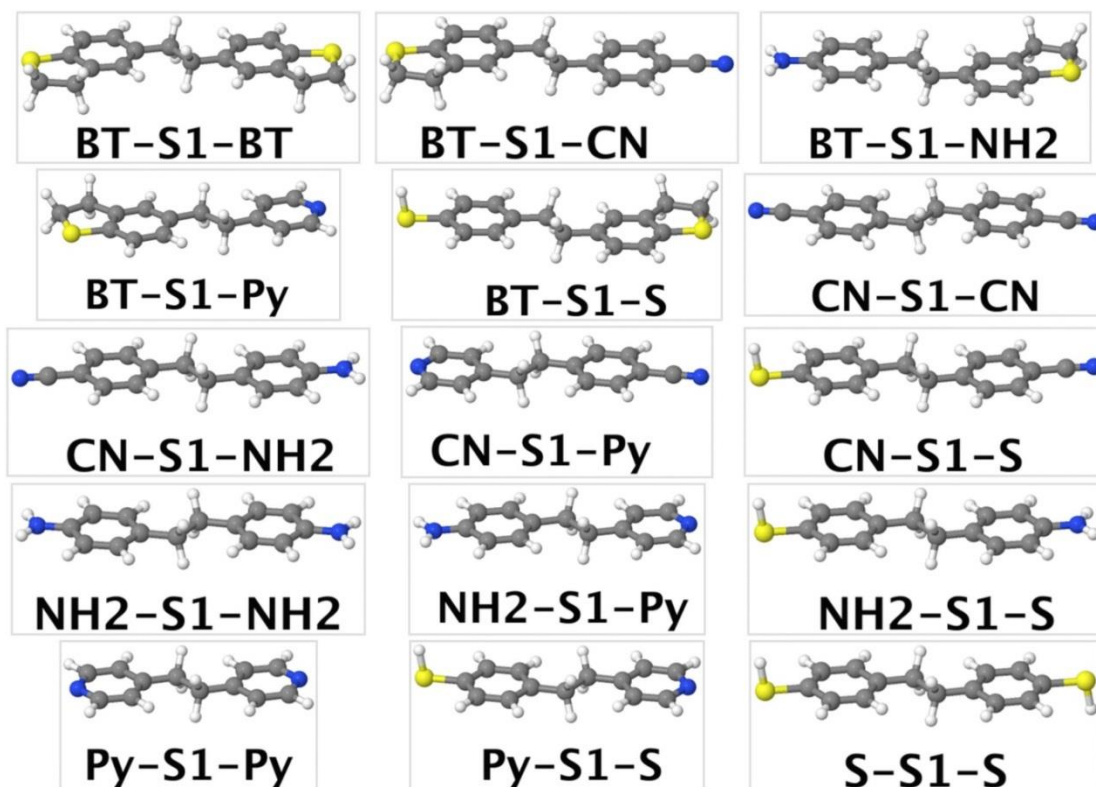


Figure 6.12. Molecules with S1 backbone.

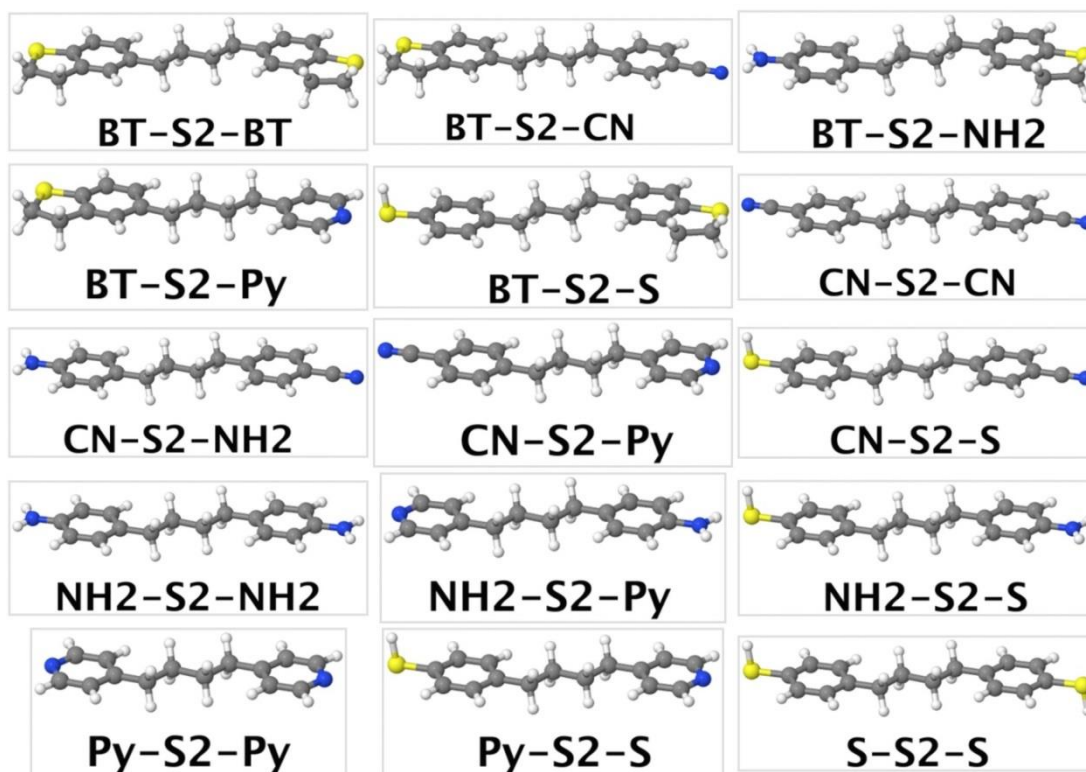


Figure 6.13. Molecules with S2 backbone.

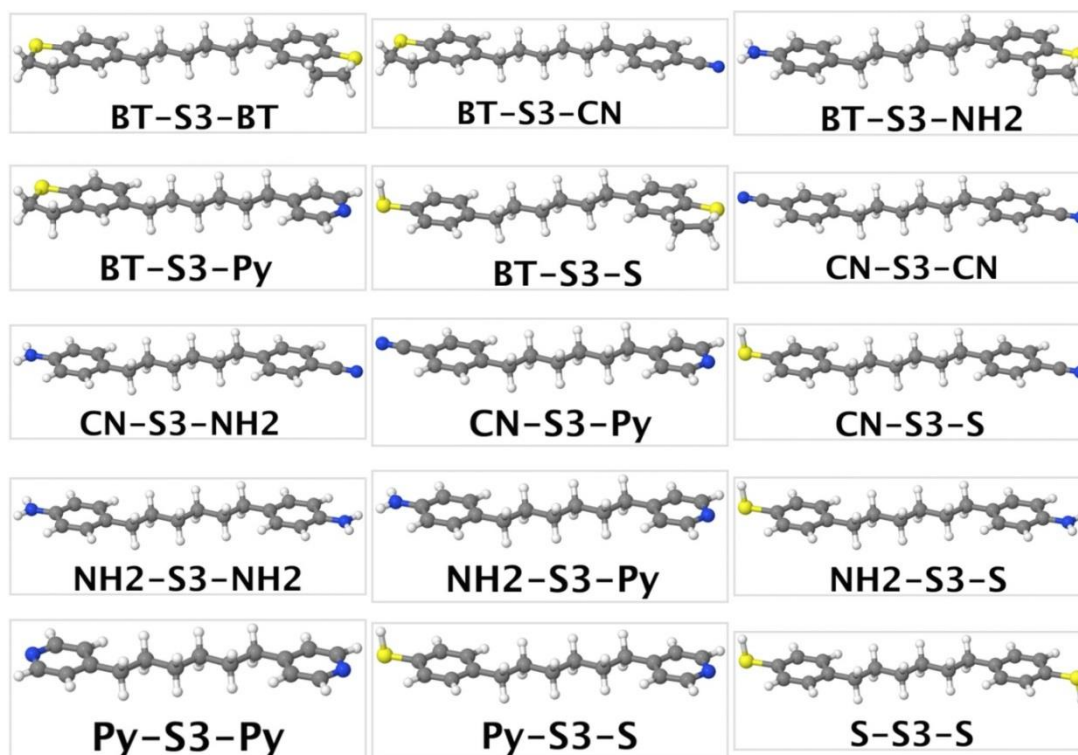


Figure 6.14. Molecules with S3 backbone.

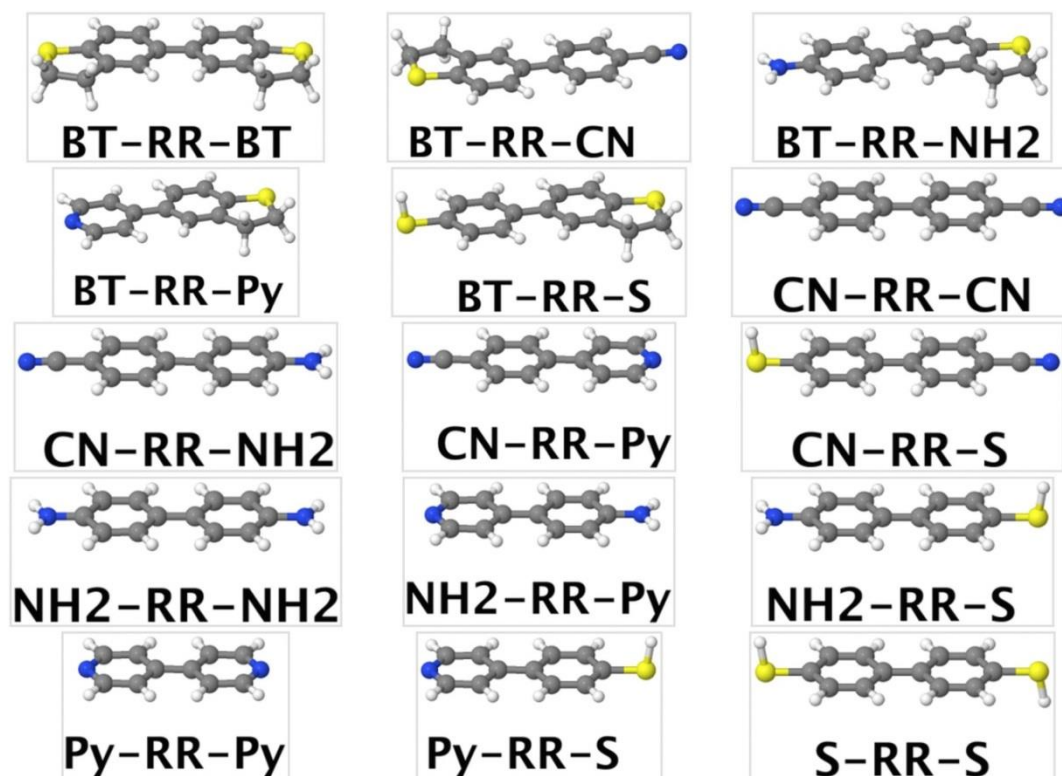


Figure 6.15. Molecules with RR backbone.

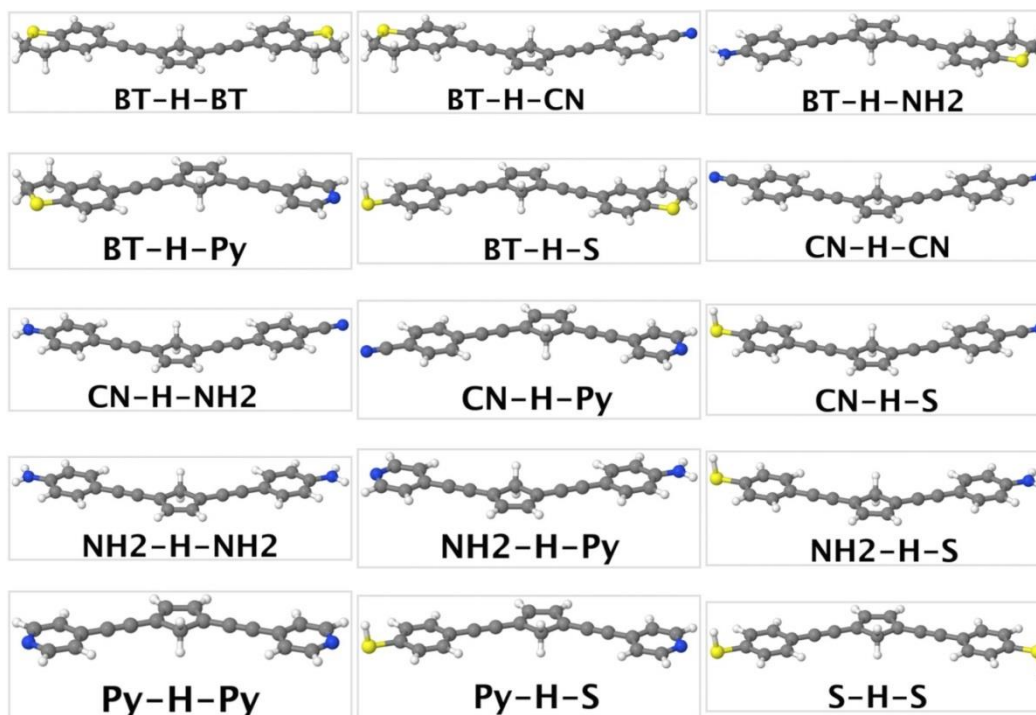


Figure 6.16. Molecules with H backbone.

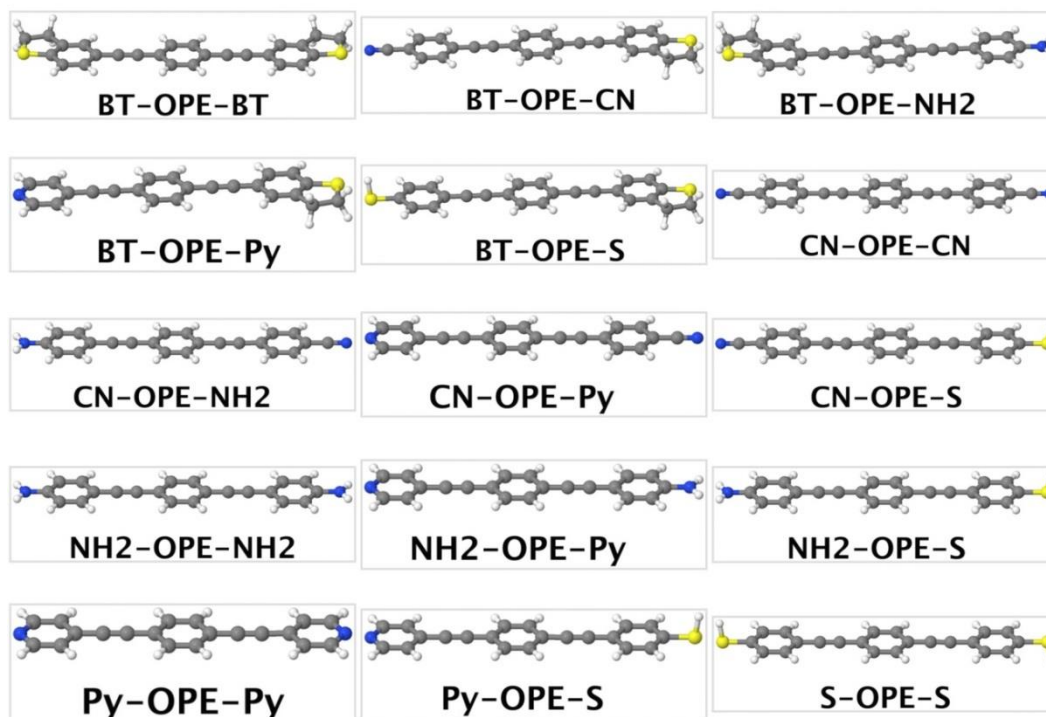


Figure 6.17. Molecules with OPE backbone.

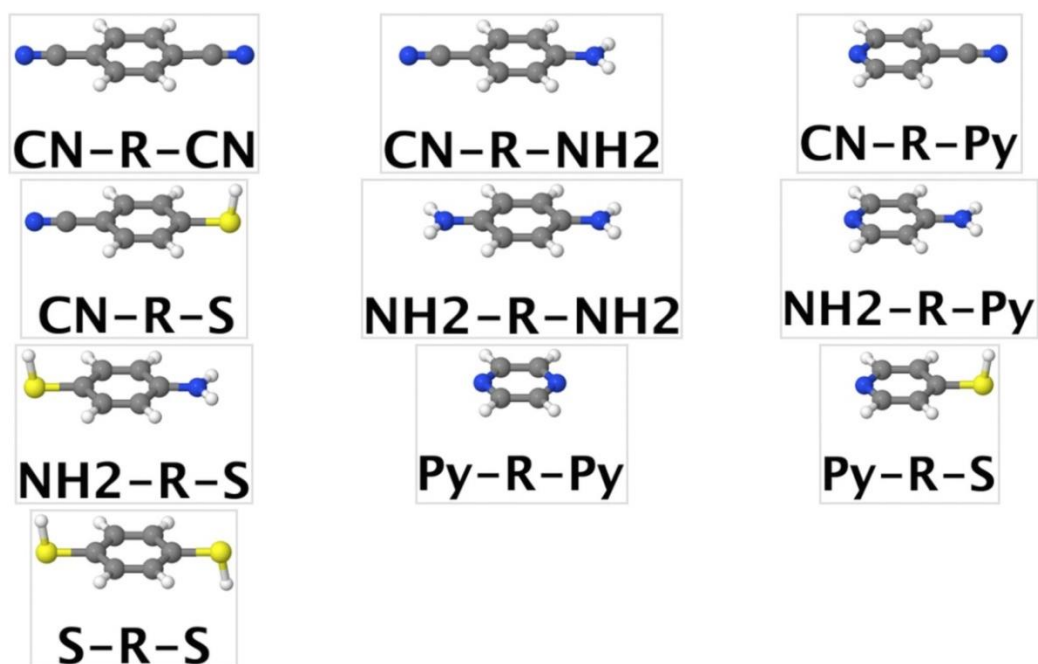


Figure 6.18. Molecules with R backbone.

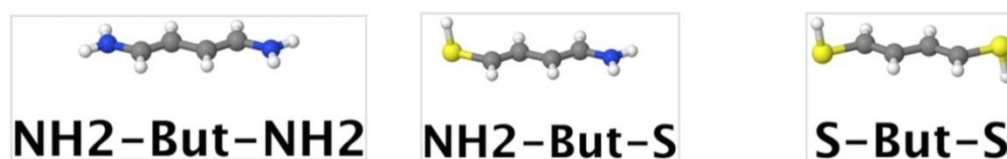


Figure 6.19. Molecules with But backbone.

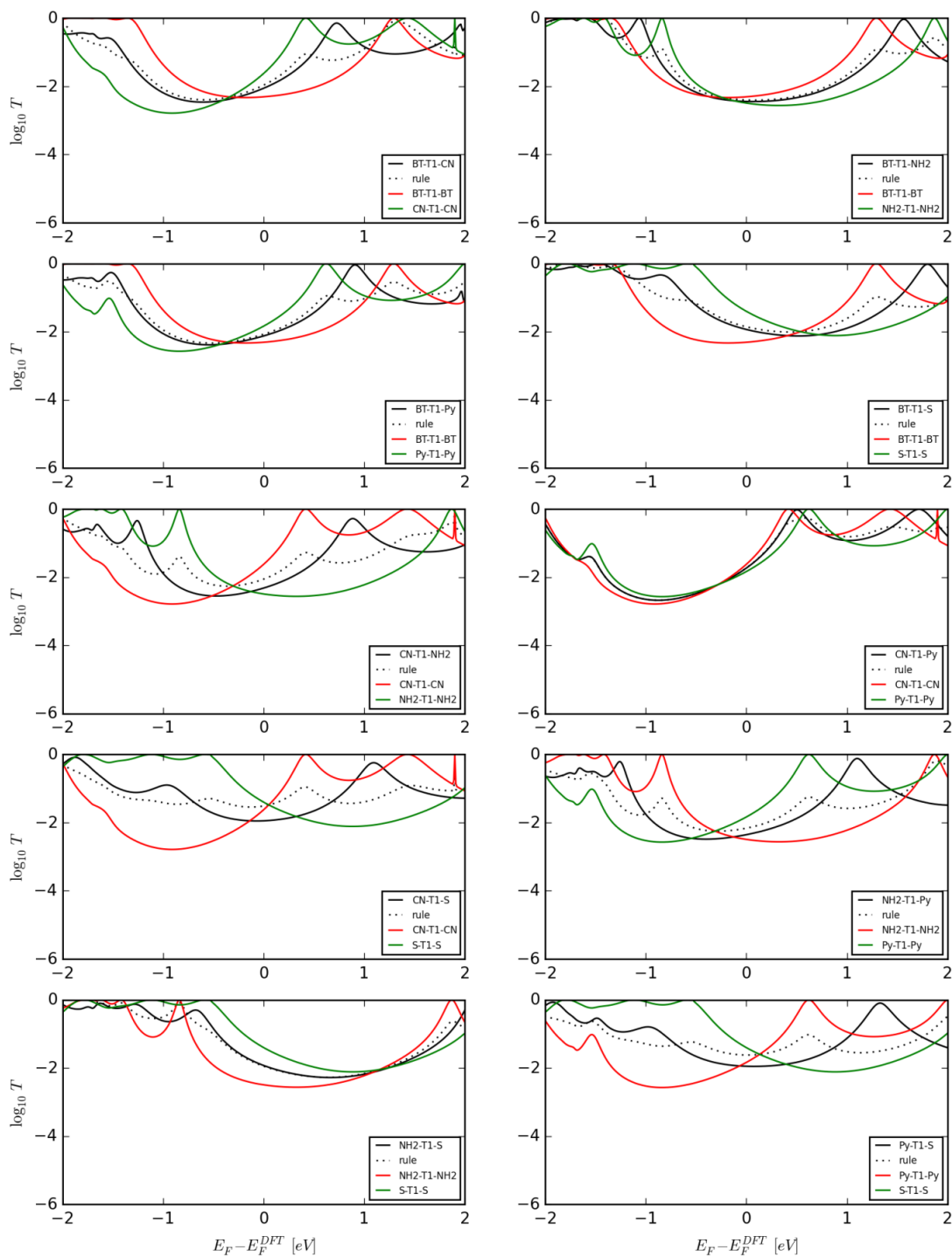


Figure 6.20. Transmission coefficient function for molecules with backbone T1 and the circuit rule check (dotted curves).

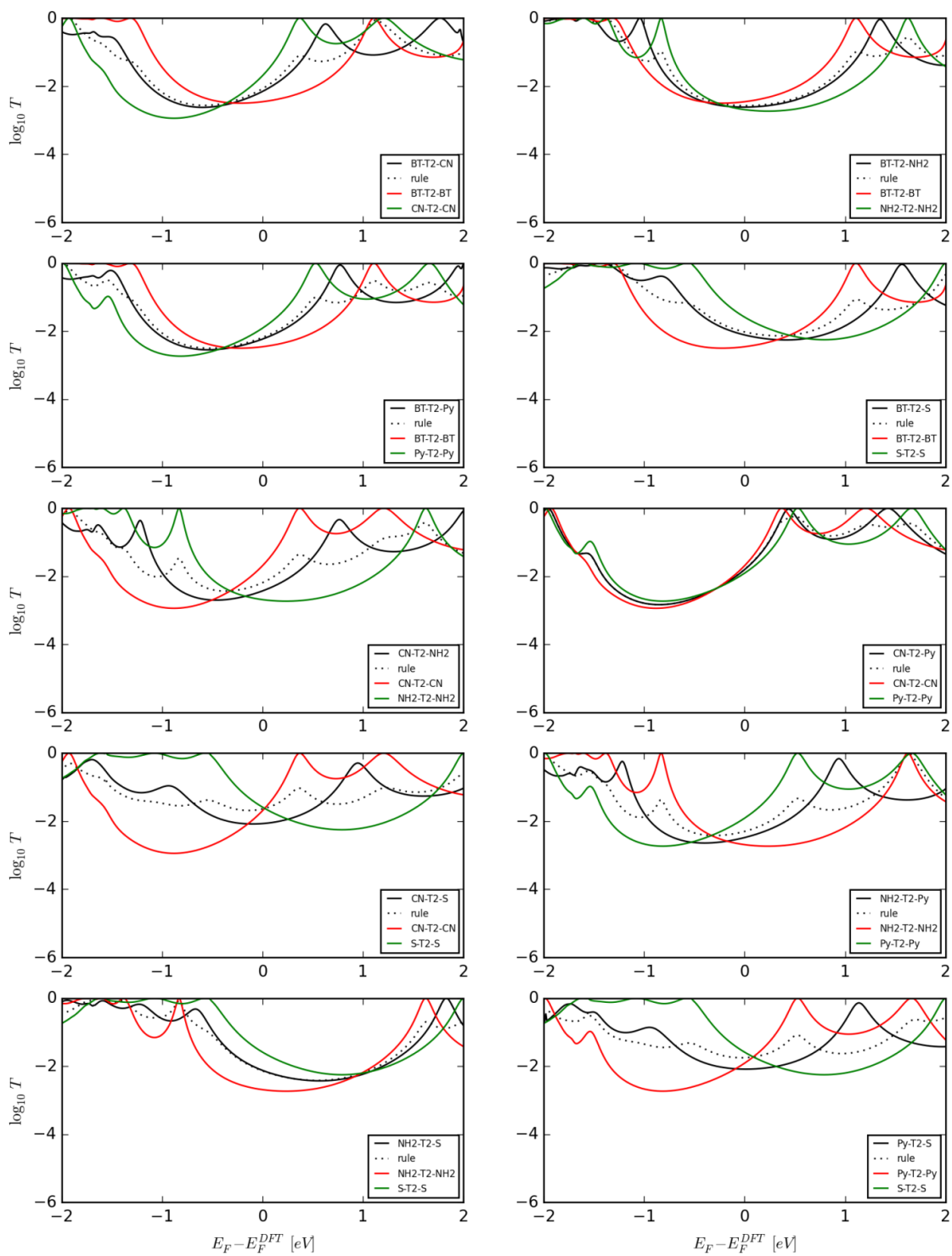


Figure 6.21. Transmission coefficient function for molecules with backbone T2 and the circuit rule check (dotted curves).

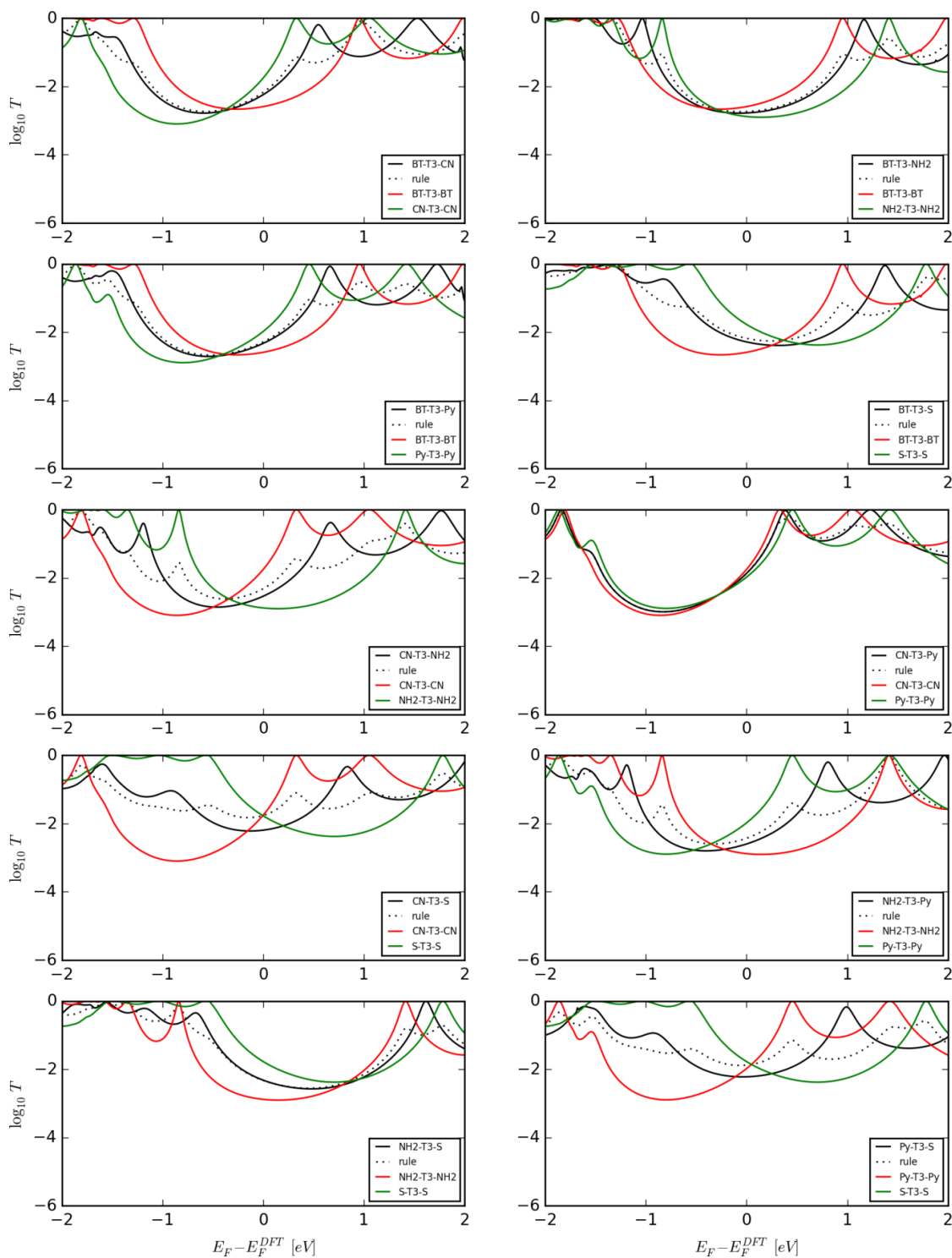


Figure 6.22. Transmission coefficient function for molecules with backbone T3 and the circuit rule check (dotted curves).

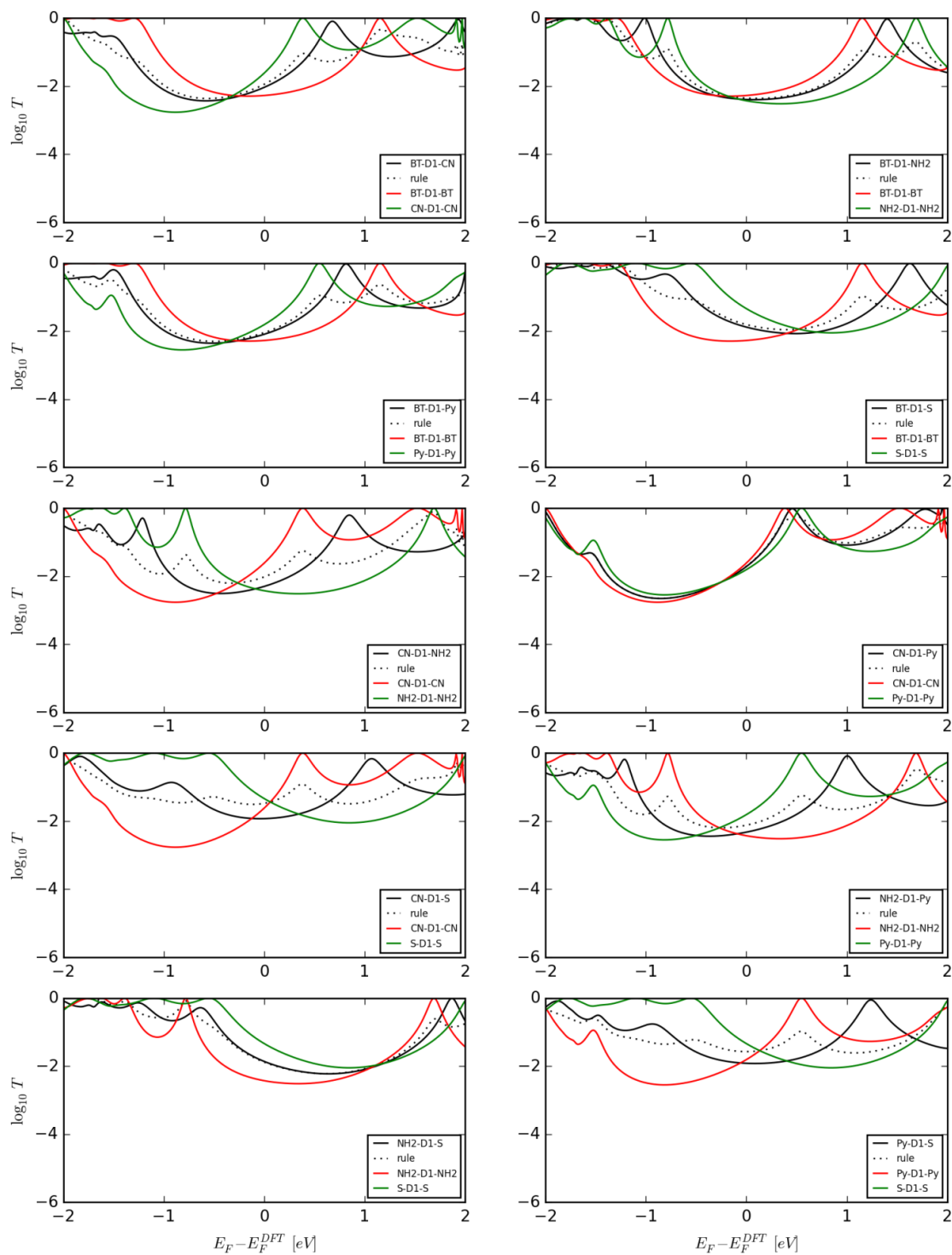


Figure 6.23. Transmission coefficient function for molecules with backbone D1 and the circuit rule check (dotted curves).

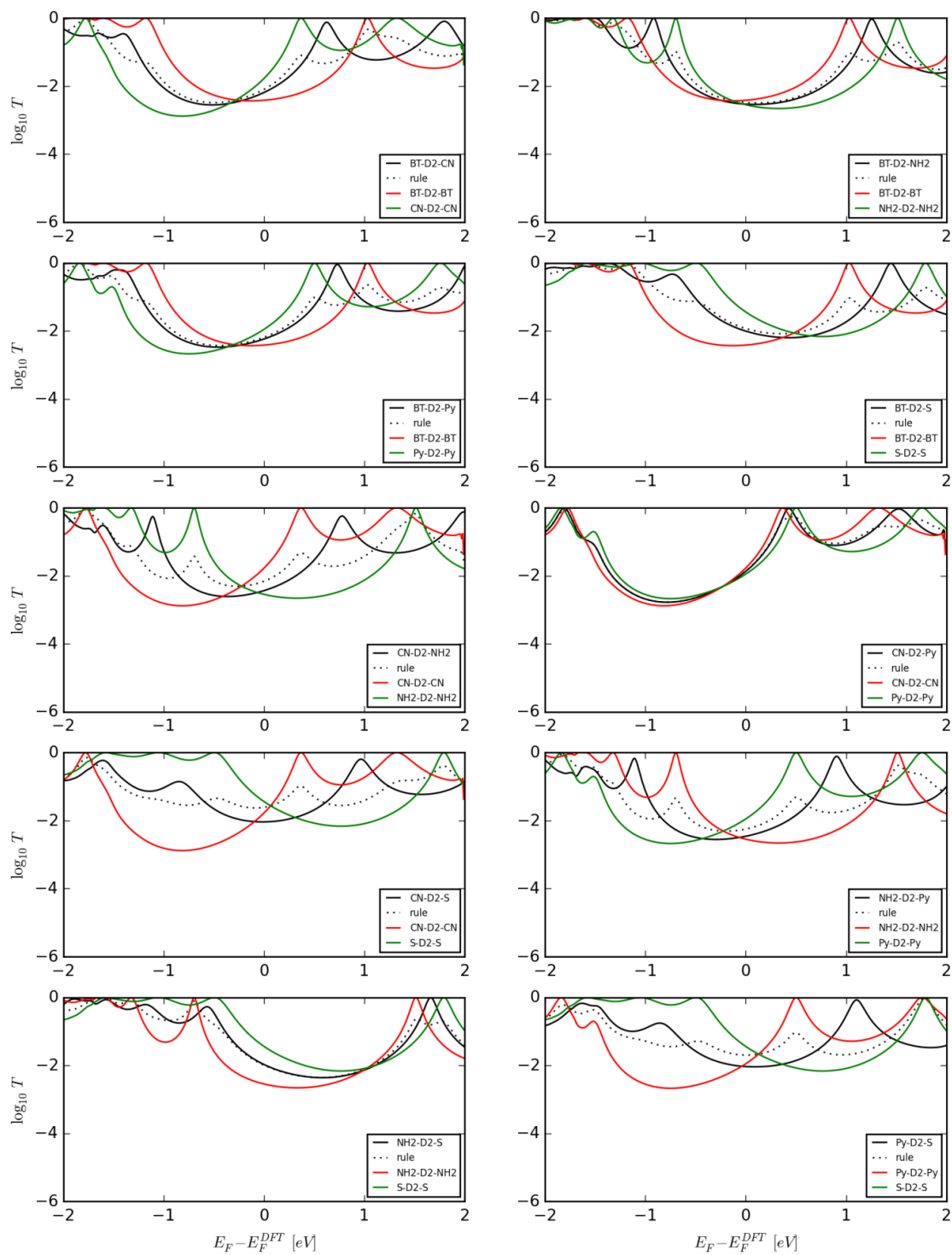


Figure 6.24. Transmission coefficient function for molecules with backbone D2 and the circuit rule check (dotted curves).

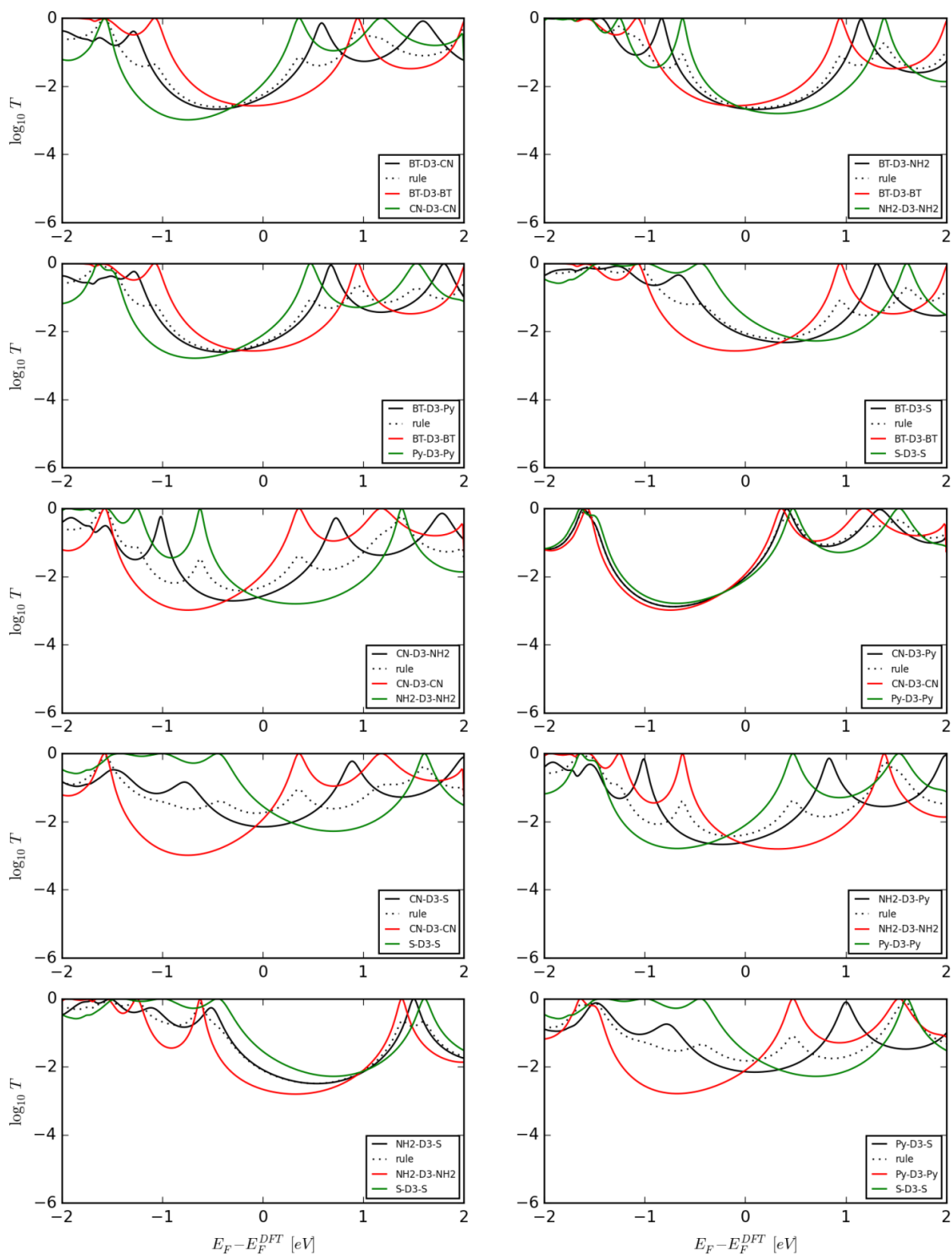


Figure 6.30. Transmission coefficient function for molecules with backbone D3 and the circuit rule check (dotted curves).

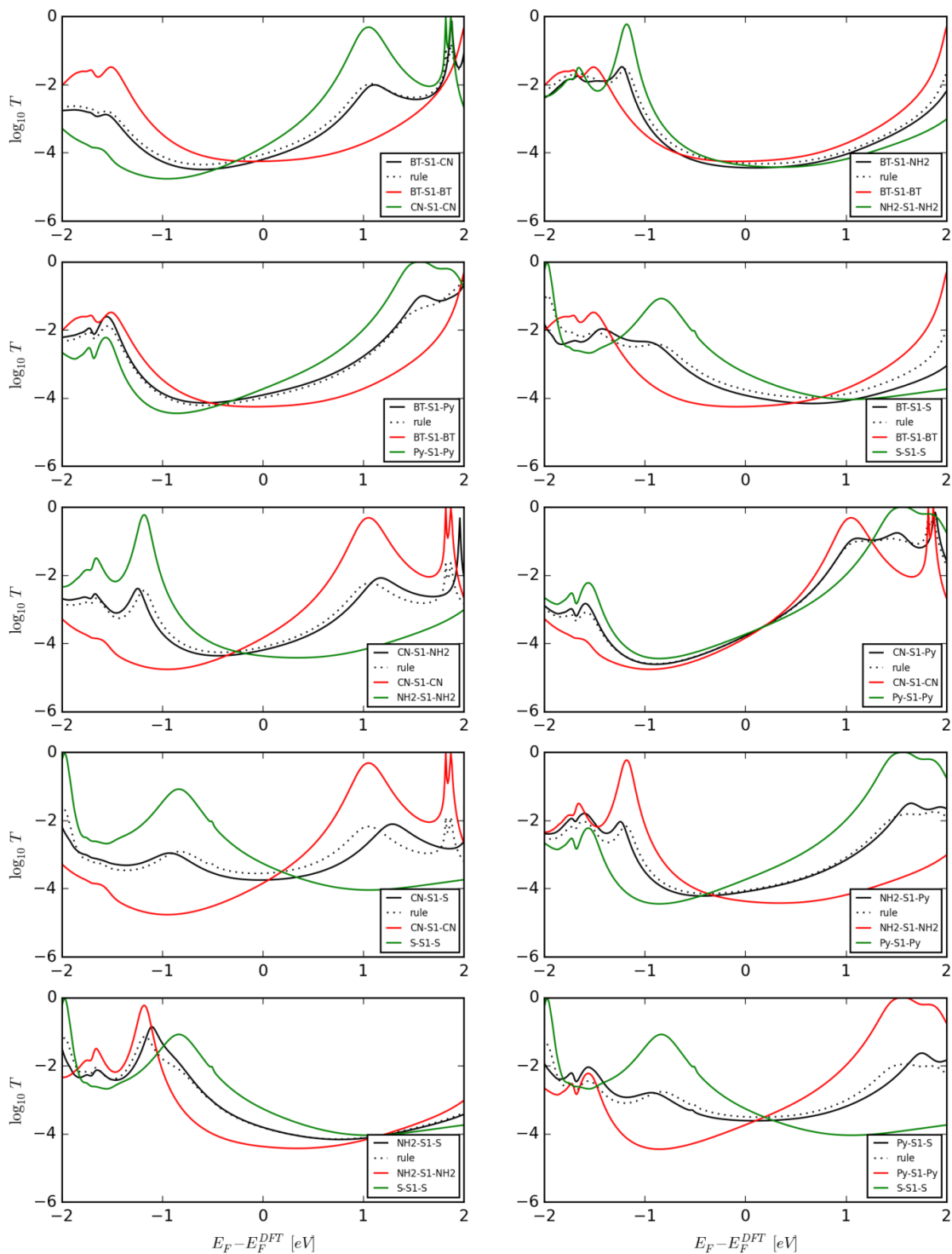


Figure 6.31. Transmission coefficient function for molecules with backbone S1 and the circuit rule check (dotted curves).

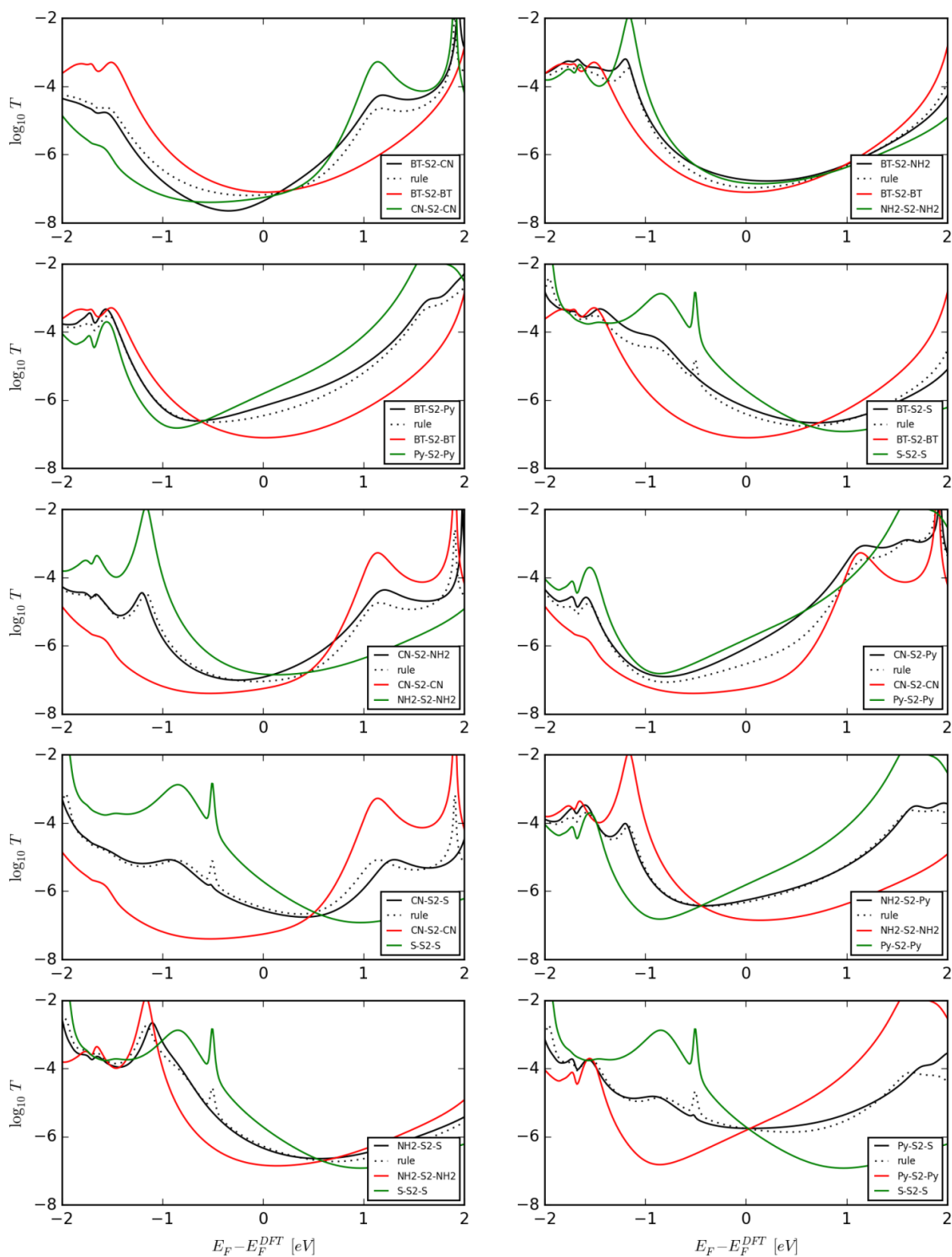


Figure 6.32. Transmission coefficient function for molecules with backbone S2 and the circuit rule check (dotted curves).

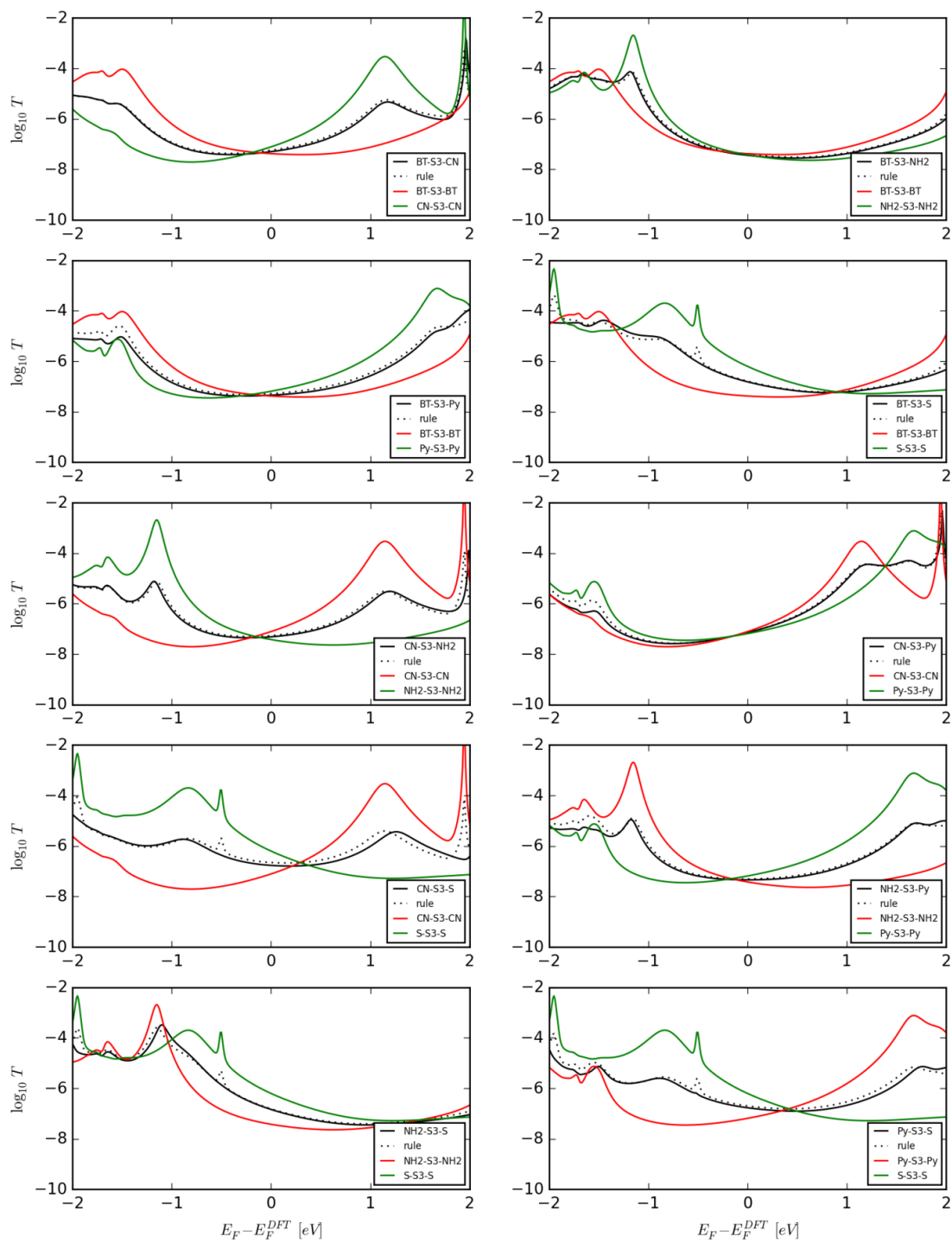


Figure 6.33. Transmission coefficient function for molecules with backbone S3 and the circuit rule check (dotted curves).

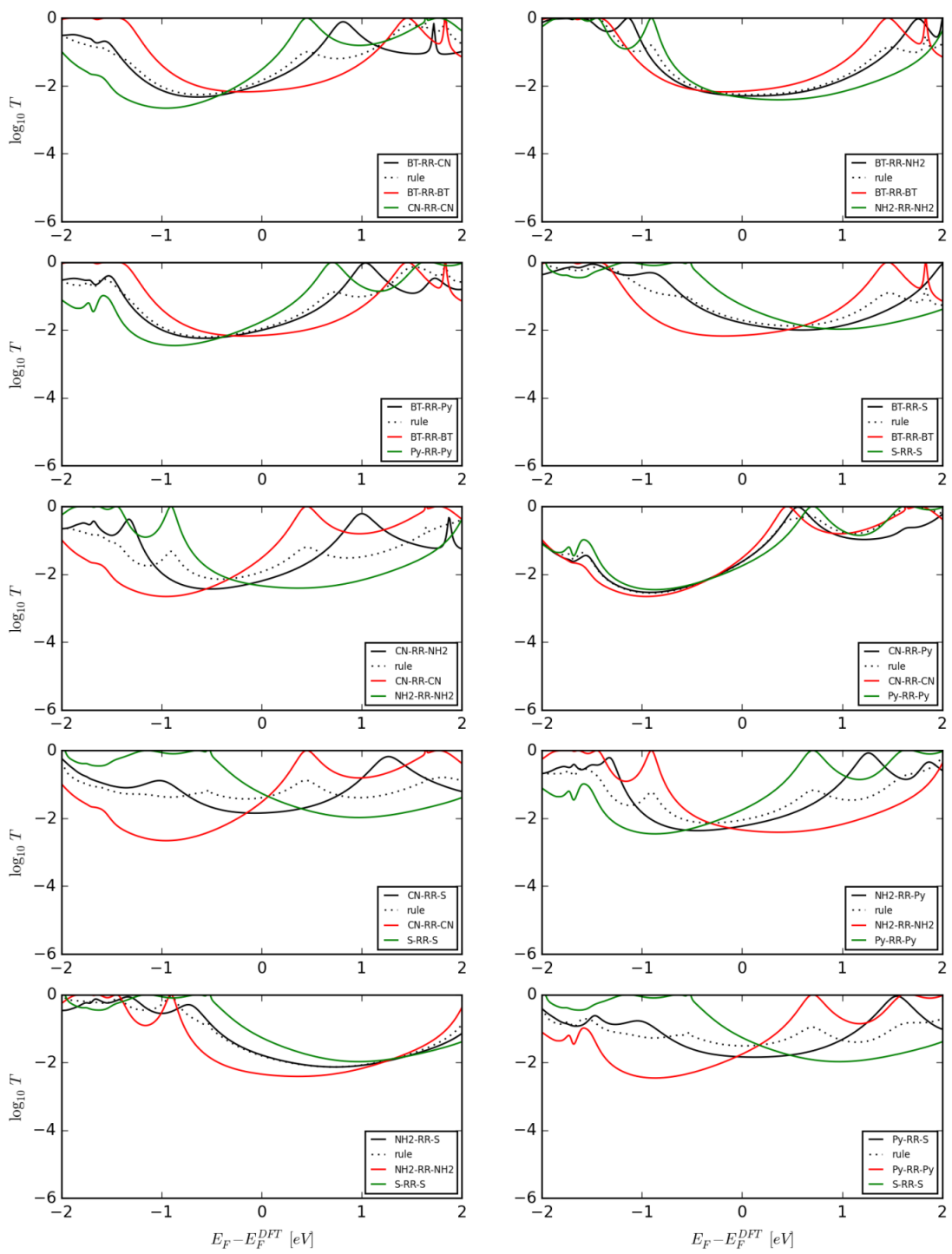


Figure 6.34. Transmission coefficient function for molecules with backbone RR and the circuit rule check (dotted curves).

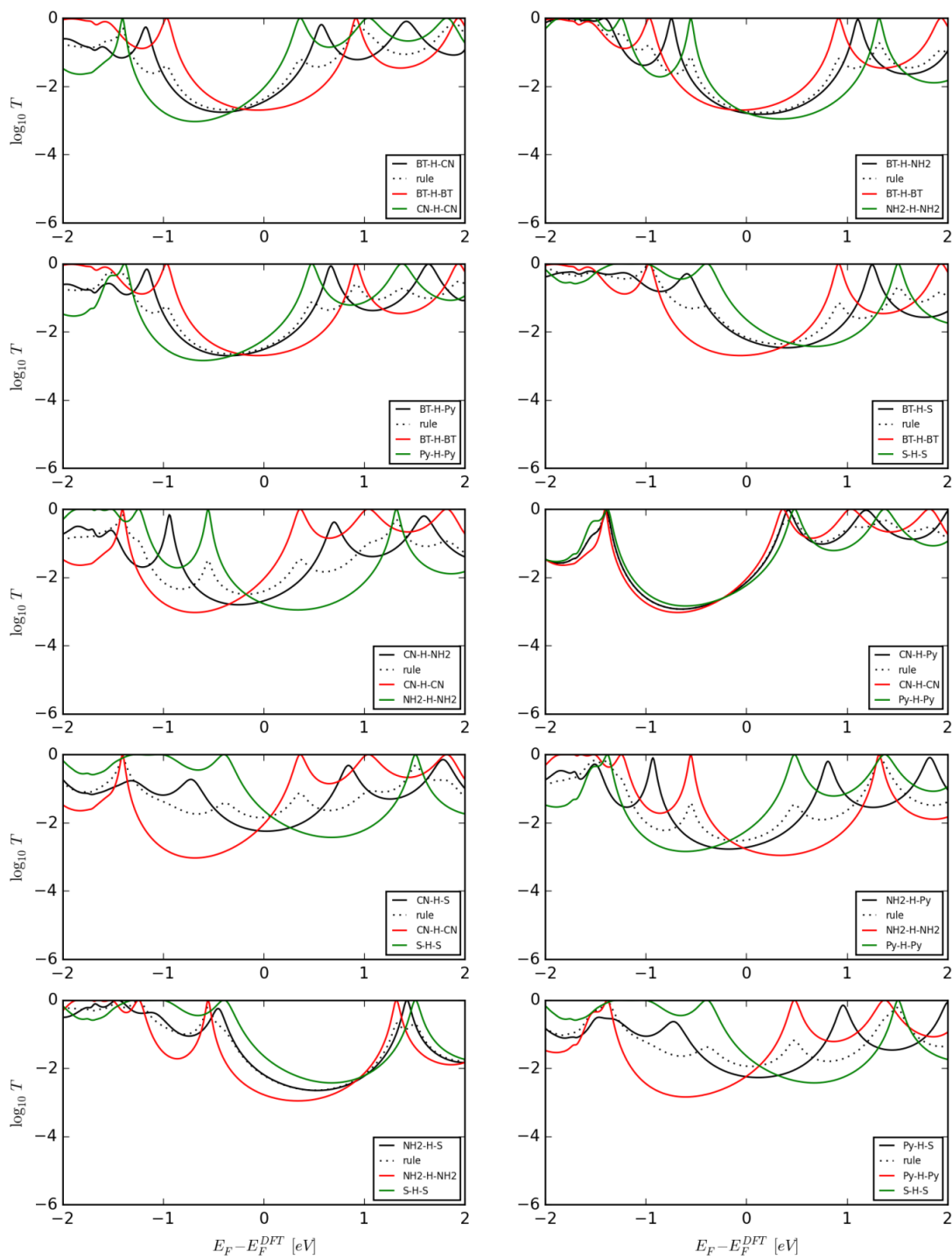


Figure 6.35. Transmission coefficient function for molecules with backbone H and the circuit rule check (dotted curves).

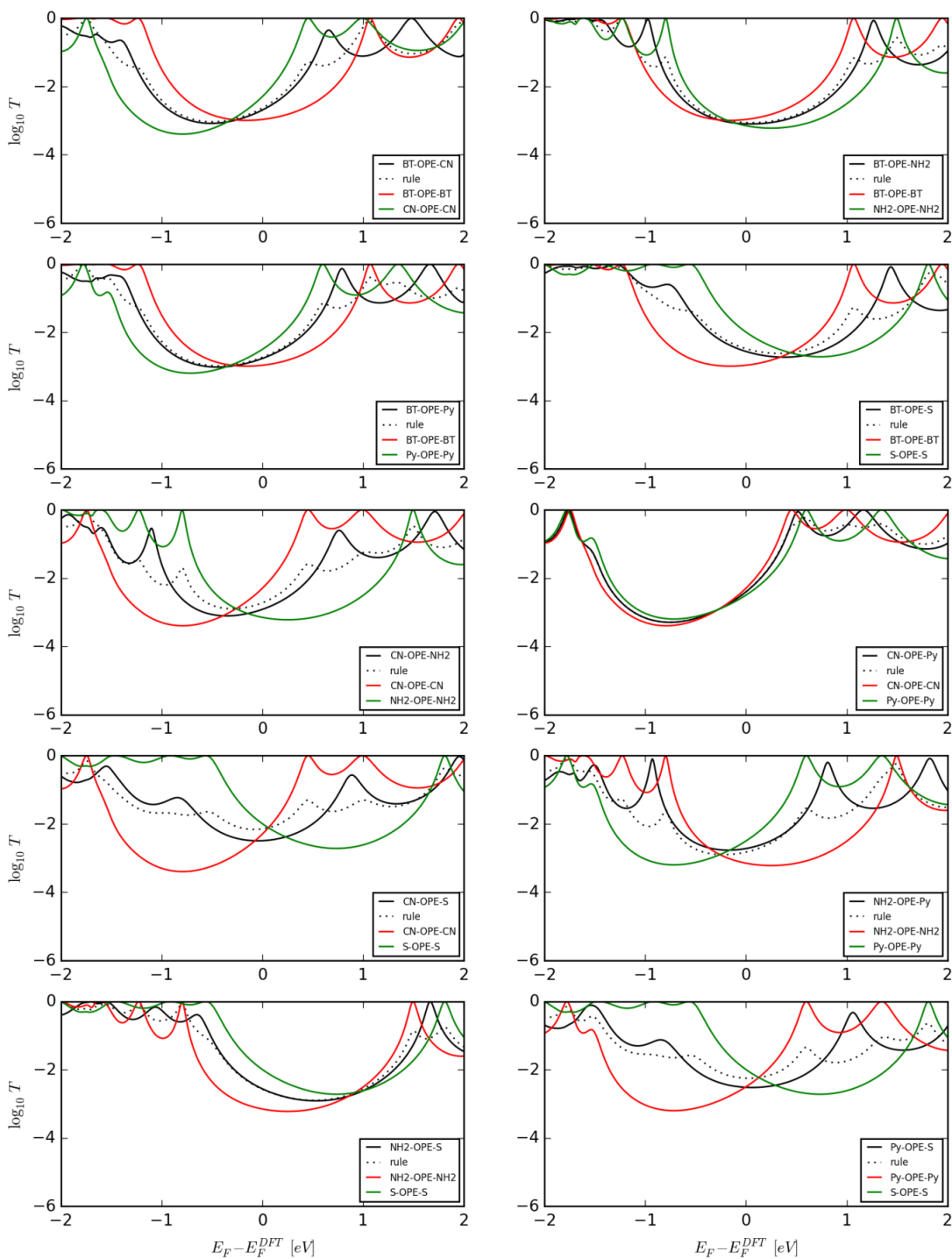


Figure 6.36. Transmission coefficient function for molecules with backbone OPE and the circuit rule check (dotted curves).

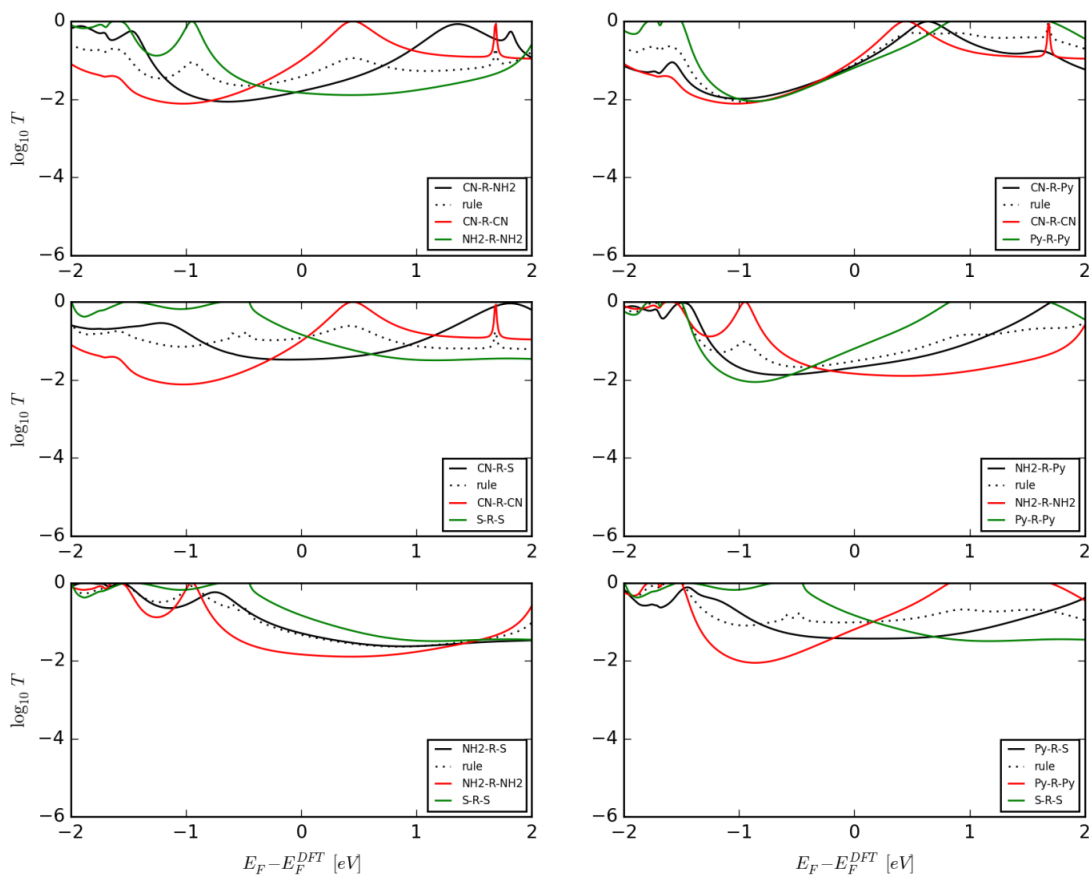


Figure 6.37. Transmission coefficient function for molecules with backbone R and the circuit rule check (dotted curves).

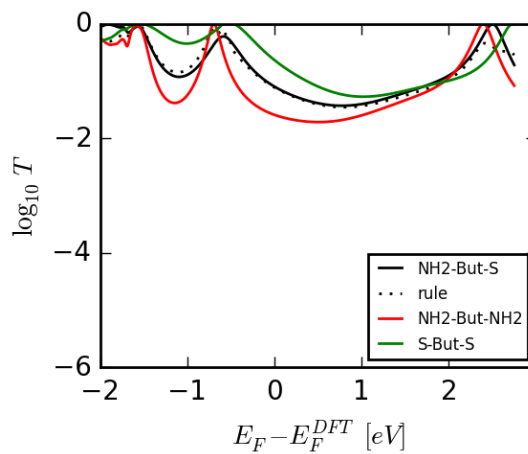


Figure 6.38. Transmission coefficient function for molecules with backbone But and the circuit rule check (dotted curves).

Table 6.5 Conductance predictions based on experimental values which are in parenthesis if it has been used for the predictions.

Molecule	Conductance Prediction ($\log_{10} G/G_0$)	Molecule	Conductance Prediction ($\log_{10} G/G_0$)	Molecule	Conductance Prediction ($\log_{10} G/G_0$)
Py-T1-Py	-3.47 (-3.35)	Py-T4-Py	-4.36 (-4.4)	Py-Meta-Py	-5.91(-5.9)
Py-T1-CN	-4.04	Py-T4-CN	-4.93	Py-Meta-CN	-6.48
Py-T1-NH2	-3.33	Py-T4-NH2	-4.22	Py-Meta-NH2	-5.77
Py-T1-BT	-3.01	Py-T4-BT	-3.9	Py-Meta-BT	-5.45
Py-T1-S	-3.11	Py-T4-S	-4.0	Py-Meta-S	-5.55
CN-T1-CN	-4.61 (-4.75)	CN-T4-CN	-5.5 (-5.4)	CN-Meta-CN	-7.05
CN-T1-NH2	-3.9	CN-T4-NH2	-4.79	CN-Meta-NH2	-6.34
CN-T1-BT	-3.58	CN-T4-BT	-4.47	CN-Meta-BT	-6.02
CN-T1-S	-3.68	CN-T4-S	-4.57	CN-Meta-S	-6.12
NH2-T1-NH2	-3.19 (3.205)	NH2-T4-NH2	-4.08	NH2-Meta-NH2	-5.63
NH2-T1-BT	-2.87	NH2-T4-BT	-3.76	NH2-Meta-BT	-5.31
NH2-T1-S	-2.97	NH2-T4-S	-3.86	NH2-Meta-S	-5.41
BT-T1-BT	-2.55 (-2.5)	BT-T4-BT	-3.44(-3.5)	BT-Meta-BT	-4.99
BT-T1-S	-2.65	BT-T4-S	-3.54	BT-Meta-S	-5.09
S-T1-S	-2.75 (-2.75)	S-T4-S	-3.64	S-Meta-S	-5.19
Py-T2-Py	-3.79 (-3.78)	Py-OPE-Py	-4.53(-4.5)	Py-RR-Py	-3.16(-3.23)
Py-T2-CN	-4.36	Py-OPE-CN	-5.1	Py-RR-CN	-3.73
Py-T2-NH2	-3.65	Py-OPE-NH2	-4.39	Py-RR-NH2	-3.02
Py-T2-BT	-3.33	Py-OPE-BT	-4.07	Py-RR-BT	-2.7
Py-T2-S	-3.43	Py-OPE-S	-4.17	Py-RR-S	-2.8
CN-T2-CN	-4.93 (-4.9)	CN-OPE-CN	-5.67	CN-RR-CN	-4.3
CN-T2-NH2	-4.22	CN-OPE-NH2	-4.96	CN-RR-NH2	-3.59
CN-T2-BT	-3.9	CN-OPE-BT	-4.64	CN-RR-BT	-3.27
CN-T2-S	-4.0	CN-OPE-S	-4.74	CN-RR-S	-3.37
NH2-T2-NH2	-3.51 (-3.5)	NH2-OPE-NH2	-4.25(-4.35)	NH2-RR-NH2	-2.88(-2.81)
NH2-T2-BT	-3.19	NH2-OPE-BT	-3.93	NH2-RR-BT	-2.56
NH2-T2-S	-3.29	NH2-OPE-S	-4.03	NH2-RR-S	-2.66
BT-T2-BT	-2.87(-2.845)	BT-OPE-BT	-3.61	BT-RR-BT	-2.24
BT-T2-S	-2.97	BT-OPE-S	-3.71	BT-RR-S	-2.34
S-T2-S	-3.07(-3.12)	S-OPE-S	-3.81(-3.74)	S-RR-S	-2.44

6.5 Summary

We have investigated a large set of symmetric and asymmetric molecules to demonstrate a general rule for molecular-scale quantum transport, which provides a new route to materials design and discovery. The rule states “the conductance G_{XBY} of an asymmetric molecule is the geometric mean of the conductance of the two symmetric molecules derived from it and the thermopower S_{XBY} of the asymmetric molecule is the algebraic mean of their thermopowers”. The studied molecules have a structure X-B-Y, where B is the backbone of the molecule, while X and Y are anchor groups, which bind the molecule to metallic electrodes. When applied to experimentally-measured histograms of conductance and thermopower, the rules apply to the statistically most probable values. We investigated molecules with anchors chosen from the following family: cyano, pyridyl, dihydrobenzothiol, amine and thiol. For the backbones B, we tested 14 different structures. We found that the formulae $(G_{XBY})^2 = G_{XBX} * G_{YBY}$ and $S_{XBY} = (S_{XBX} + S_{YBY}) / 2$ were satisfied in the large majority of the cases, provided the Fermi energy is located within the HOMO-LUMO gap of the molecules. The circuit rules imply that if measurements are performed on molecules with n_A different anchors and n_B different backbones, then properties of $n_A(n_A+1)n_B/2$ molecules can be predicted. So for example, in the case of 20 backbones and 10 anchors, 30 measurements (or reliable calculations) can provide a near quantitative estimate for 1070 measurements of other molecules, no extra cost.

Chapter 7

Conclusion

In conclusion, this thesis has presented a series of studies into electronic and thermoelectric properties of single organic molecules: perylene Bisimide (PBIs), *naphthalenediimide* (NDI), metallo-porphyrins and large set of symmetric and asymmetric molecules. In chapter 3, I presented a study of the electron transport properties of five PBI derivatives with various bay-area substituents: pyrrolidinyl (aPy-PBI, Py-PBI), tert-butyl-phenoxy (P-PBI), thiobutyl (S-PBI), and chlorine (Cl-PBI). Recent experimental papers measuring the electrical conductance of backbone molecules in different solvents have shown that the conductance can be changed by the solvent, even when the solvent does not form a complex with the backbone [209]. In our case, the analytes bind to the backbones with up to 1 eV of binding energy and the conductance changes are much larger. Our results compare well with recent experimental values for the electrical conductance of these molecules in the absence of adsorbates. I analyzed the change in conductance of these molecules when single molecules of three analytes (TCNE, TNT, and BEDT-TTF) were adsorbed onto the PBI backbones and found that the resulting changes in the ensemble-averaged room-temperature conductances produced a unique fingerprint for each analyte, which allows their discriminating sensing at the single molecule level. These conductance changes arose from a combination of charge redistribution associated with charge-transfer-complex formation,

and the formation of a Fano resonance associated with the interaction of a bound state on the adsorbate and extended orbitals of the PBI backbones.

Chapter 4 presented our collaboration with the group of Bern University. We studied charge transport through an NDI single-molecule junction using an electrochemical STM-BJ technique and through ab initio simulations based on DFT. Benefiting from the wide potential window of the ionic liquid, we are able to access the three charge states of the NDI molecule, which showed well-separated conductance features with an on/off ratio of around one order of magnitude between the most conductive NDI-R and the least conductive NDI-N state. The switching can be manipulated reversibly through the applied potential. Agreement between theory and experiment has been demonstrated by introducing a newly developed charge double layer model. The tristable charge states of the NDI molecule provide a unique opportunity beyond bistable on/off molecular switches, and lead to interesting logic gate and memory devices. More importantly, the comparable conductance changes between NDI molecules with pendent diimide units and with redox units integrated in molecular backbones suggests that the pendent redox unit can provide significant fine-tuning of single molecule conductance triggered by external stimuli, in this case, an electrochemical gate. This offers great flexibility for the molecular design and synthesis of future molecular devices.

In chapter 5, I have used spin-dependent density functional theory to study the thermoelectric properties of metallo-porphyrin monomers with central metal atoms chosen from the series Co, Cu, Fe, Mn, Ni, and Zn. We found that the energies of transport resonances can be tuned through the choice of central metal atom, leading to large negative thermopowers in the range -280 to -260 $\mu\text{V/K}$ for Mn(II)- and Fe(II)-porphyrins and a large positive thermopower of +230 $\mu\text{V/K}$ in the case of Zn-porphyrin. These Seebeck coefficients are almost independent of temperature at room temperature and are significantly

larger than recently-measured values of S at room temperature. For example, measured values include 8.7, 12.9 and 14.2 $\mu V/K$ for 1,4-benzenedithiol (BDT), 4,4' - dibenzenedithiol, and 4,4' ' -tribenzenedithiol respectively [210], -1.3 to 8.3 $\mu V/K$ for the benzene-based series of benzene-dithiol (BDT), 2,5-dimethyl-1,4-benzenedithiol (BDT2Me), 2,3,5,6-tetrachloro-1,4-benzenedithiol (BDT4Cl), 2,3,5,6-tetrafluoro-1,4-benzenedithiol (BDT4F) and BDCN [211, 212], 7.7 to 15.9 $\mu V/K$ for the series BDT, DBDT, TBDT and DMTBDT [213], -12.3 to 13.0 $\mu V/K$ for a series of amine-Au and pyridine-Au linked molecules [172] and -8.9 to -33.1 $\mu V/K$ for fullerene-based single-molecule junctions [158, 211, 214]. Furthermore Zn-porphyrins have a large electronic figure of merit. At room temperature, we obtain power factors of 5.9×10^{-5} W/m.K² for Mn-porphyrin, 5.4×10^{-4} W/m.K² For Mn(III)-porphyrin, 9.5×10^{-4} W/m.K² for Fe(III)-porphyrin, 1.6×10^{-4} W/m.K² for Zn-porphyrin and 2.3×10^{-4} W/m.K² for Fe(II)-porphyrin. These compare favourably with power factors of other organic materials, whose reported values range from 0.016 $\mu W/m.K^2$ and 0.045 $\mu W/m.K^2$ for Polyaniline and Polypyrrole respectively [215], to 12 $\mu W/m.K^2$ for PEDOT:PSS [216] and 12 $\mu W/m.K^2$ for C₆₀/Cs₂Co₃ Dph-BDT [217]. This ability to tune the thermoelectric properties of single molecules, combined with the fact that the Seebeck coefficient is an intrinsic property, which does not scale with the number of molecules conducting in parallel, suggests that self-assembled monolayers or few-layers of metallo-porphyrins have potential for high-performance conversion of heat into electricity and efficient Peltier cooling. The technical step of translating single-molecule properties into thin films is a significant challenge and a major programme of fundamental research will be needed to fully address this issue. Nevertheless, the recent theoretical study of the thermal conductance of single alkane and alkyne molecules compares favourably with experiments on thin films of such molecules [218] and gives us confidence single-molecule thermal properties do survive in molecular films.

Furthermore many of the barriers to be overcome are already clear. For example, to take advantage of the quantum effects described in this chapter, the film thickness should be less than the electronic phase-breaking length, which at room temperature is of order 3nm [53, 219, 220]. If molecules are first deposited onto a bottom electrode, then the top electrode should be added without destroying the integrity of the molecular film. One solution to the “top-contact problem” would be to use a two-dimensional electrode material such as graphene as the top electrode. Success would depend on alignment or misalignment of the two contacts and the presence of step edges and other defects in the transferred two-dimensional material. In the case of hexagonal materials such as graphene, such defects would include non-hexagonal rings [221], which would alter the binding energy and electronic coupling to molecular anchor groups. It is well established that both molecules and electrodes should be treated in an holistic manner when designing single-molecule junctions [222] and the same will be true of thin films. For the purpose of increasing ZT and reducing the thermal conductance, one strategy will involve choosing electrode materials which maximise phonon scattering at the molecule-electrode interface and taking advantage of phonon filtering by the electrodes, as described in [218]. In addition, intermolecular interactions may be utilised to optimise thin-film properties beyond those accessible to single molecules.

Chapter 6 in this thesis documented our study of a large set of symmetric and asymmetric molecules to demonstrate a general rule for molecular-scale quantum transport. We have demonstrated that for a large variety of molecules of the type X-B-Y with different backbones B and anchors X,Y, the molecular conductance and thermopower of asymmetric molecules can be obtained as geometric and algebraic averages of the zero-bias conductances and thermopowers of their symmetric counterparts respectively. At a fundamental level, a requirement for the validity of this ‘circuit rule’ is that the parts X, B

and Y should be weakly coupled, so that multiple scattering effects contained in the self-energy Σ in Eq.(6.2) can be neglected. This also requires that the Fermi energy should be located within the HOMO-LUMO gap of the molecules and therefore transport should be ‘off-resonance’ and take place via coherent tunnelling. The validity of this circuit rule is demonstrated through DFT calculations on 193 molecules, which confirms that the rule applies to molecules exhibiting off-resonance transport. In our experience of comparing theory with measurements of single-molecule electron transport, we have found that in almost all cases, unless an electrostatic or electrochemical gate is applied, transport does not take place near resonances and therefore the rule can be expected to have wide applicability. The derivation of the rule assumes that transport takes place via coherent tunnelling and that inelastic effects are negligible. Experiment demonstrates that the length scale for the onset of significant inelastic scattering at room temperature can be of order 3 nm [183, 223]. All the molecules in our study were shorter than this length. Furthermore comparison with 19 experimental molecular conductance values from the literature, originating from different laboratories shows that the circuit rules can be applied successfully at room temperature. Finally we note that as demonstrated in refs [224, 225] the backbone contribution B_B (see eq. (6.3)) depends on the points of contact k, l of the anchors to the backbone and therefore the circuit rule should be applied only to families of molecules containing backbones with the same connectivity to the anchors or equivalently, backbones with different connectivities should be treated as distinct entities, which means for example that a meta-connected backbone is distinct from a para-connected backbone as values of b_B of OPE and OPE(meta) show in Table 6.2.

For a workable thermoelectric device one needs to increase both the Seebeck coefficient S and the electrical conductance G and simultaneously minimise the thermal conductance. The proposed circuit rule addresses the first two challenges by predicting S and G of hitherto

unsynthesized molecules, thereby avoiding unnecessary synthetic effort. The rule also provides new insight and chemical intuition by organising a large body of information. The utility of the rule for ‘materials discovery’ derives from the potential translation of single-molecule functionality into thin molecular films, formed from a monolayer of molecules is sandwiched between a planar bottom electrode and a planar top electrode, in which the current/heat flows through the molecules from the bottom to the top electrode. The question of how single-molecule properties translate into thin films is non-trivial and beyond the scope of this work. However knowledge of transport properties at the single molecule level will surely inform our understanding of such thin-film materials.

For other properties, the rules can be used to obtain inequalities. For example, they imply that if S_{XX} and S_{YY} have the same sign then the power factor $P_{XY} = G_{XY}S_{XY}^2$ is bounded by the power factors of the symmetric molecules, that is $P_{YY} \leq P_{XY} \leq P_{XX}$ and if S_{XX} and S_{YY} have opposite sign, the powerfactor will be diminished significantly. To aid utilisation of the rules for the discovery of new junction properties, we also demonstrated that conductances and thermopowers can be characterized by transferable anchor and backbone parameters. Such characterization can be used to identify optimally functioning molecular devices for future synthesis. The accuracy of this characterization was demonstrated using experimental conductances of 19 different molecules from the literature.

Bibliography

- [1] G.E. Moore, Cramming more components onto integrated circuits. *Electronics*, 38(8) (1965).
- [2] C. Li, I. Pobelov, T. Wandlowski, A. Bagrets, A. Arnold, F. Evers, Charge transport in single Au| alkanedithiol| Au junctions: coordination geometries and conformational degrees of freedom, *Journal of the American Chemical Society* 130 (2008) 318-326.
- [3] B. Xu, N.J. Tao, Measurement of single-molecule resistance by repeated formation of molecular junctions, *Science* 301 (2003) 1221-1223.
- [4] R. Huber, M.T. González, S. Wu, M. Langer, S. Grunder, V. Horhoiu, M. Mayor, M.R. Bryce, C. Wang, R. Jitchati, Electrical conductance of conjugated oligomers at the single molecule level, *Journal of the American Chemical Society* 130 (2008) 1080-1084.
- [5] W. Hong, H. Valkenier, G. Mészáros, D.Z. Manrique, A. Mishchenko, A. Putz, P.M. García, C.J. Lambert, J.C. Hummelen, T. Wandlowski, An MCBJ case study: The influence of π -conjugation on the single-molecule conductance at a solid/liquid interface, *Beilstein journal of nanotechnology* 2 (2011) 699-713.
- [6] N.J. Kay, S.J. Higgins, J.O. Jeppesen, E. Leary, J. Lycoops, J. Ulstrup, R.J. Nichols, Single-molecule electrochemical gating in ionic liquids, *Journal of the American Chemical Society* 134 (2012) 16817-16826.
- [7] M. Baghernejad, X. Zhao, K. Baruël Ørnsø, M. Füg, P. Moreno-García, A.V. Rudnev, V. Kaliginedi, S. Vesztergom, C. Huang, W. Hong, *Electrochemical Control*

of Single-Molecule Conductance by Fermi-Level Tuning and Conjugation Switching, *Journal of the American Chemical Society* 136 (2014) 17922-17925.

[8] A. Aviram, M.A. Ratner, Molecular rectifiers, *Chemical Physics Letters* 29 (1974) 277-283.

[9] B.L. Feringa, *Molecular switches* (Wiley Online Library, 2001).

[10] B. Valeur, I. Leray, Design principles of fluorescent molecular sensors for cation recognition, *Coordination Chemistry Reviews* 205 (2000) 3-40.

[11] J.T. Robinson, F.K. Perkins, E.S. Snow, Z. Wei, P.E. Sheehan, Reduced graphene oxide molecular sensors, *Nano letters* 8 (2008) 3137-3140.

[12] R.L. Carroll, C.B. Gorman, The genesis of molecular electronics, *Angewandte Chemie International Edition* 41 (2002) 4378-4400.

[13] C. Joachim, J. Gimzewski, A. Aviram, Electronics using hybrid-molecular and mono-molecular devices, *Nature* 408 (2000) 541-548.

[14] J. Chen, M. Reed, A. Rawlett, J. Tour, Large on-off ratios and negative differential resistance in a molecular electronic device, *Science* 286 (1999) 1550-1552.

[15] C. Collier, E. Wong, M. Belohradský, F. Raymo, J. Stoddart, P. Kuekes, R. Williams, J. Heath, Electronically configurable molecular-based logic gates, *Science* 285 (1999) 391-394.

[16] S. Datta, W. Tian, S. Hong, R. Reifenberger, J.I. Henderson, C.P. Kubiak, Current-voltage characteristics of self-assembled monolayers by scanning tunneling microscopy, *Physical Review Letters* 79 (1997) 2530.

[17] R.M. Metzger, Unimolecular electrical rectifiers, *Chemical reviews* 103 (2003) 3803-3834.

- [18] B. Capozzi, Q. Chen, P. Darancet, M. Kotiuga, M. Buzzeo, J.B. Neaton, C. Nuckolls, L. Venkataraman, Tunable charge transport in single-molecule junctions via electrolytic gating, *Nano letters* 14 (2014) 1400-1404.
- [19] L.A. Algharagholi, Q. Al-Galiby, H.A. Marhoon, H. Sadeghi, H.M. Abduljalil, C.J. Lambert, Tuning thermoelectric properties of graphene/boron nitride heterostructures, *Nanotechnology* 26 (2015) 475401.
- [20] D.Z. Manrique, C. Huang, M. Baghernejad, X. Zhao, O.A. Al-Owaedi, H. Sadeghi, V. Kaliginedi, W. Hong, M. Gulcur, T. Wandlowski, A quantum circuit rule for interference effects in single-molecule electrical junctions, *Nat. Commun.* 6 (2015).
- [21] J.R. Heath, M.A. Ratner, *Molecular electronics*, (2003).
- [22] G. Cuniberti, G. Fagas, K. Richter, *Introducing molecular electronics: A brief overview* (Springer, 2005).
- [23] C. Li, H. Wonneberger, Perylene imides for organic photovoltaics: yesterday, today, and tomorrow, *Advanced Materials* 24 (2012) 613-636.
- [24] Z. Chen, M.G. Debije, T. Debaerdemaeker, P. Osswald, F. Würthner, Tetrachloro-substituted Perylene Bisimide Dyes as Promising n-Type Organic Semiconductors: Studies on Structural, Electrochemical and Charge Transport Properties, *ChemPhysChem* 5 (2004) 137-140.
- [25] Y. Wen, Y. Liu, C.a. Di, Y. Wang, X. Sun, Y. Guo, J. Zheng, W. Wu, S. Ye, G. Yu, Improvements in Stability and Performance of N, N'-Dialkyl Perylene Diimide-Based n-Type Thin-Film Transistors, *Advanced Materials* 21 (2009) 1631-1635.
- [26] Z. Donhauser, B. Mantooth, K. Kelly, L. Bumm, J. Monnell, J. Stapleton, D. Price, A. Rawlett, D. Allara, J. Tour, Conductance switching in single molecules through conformational changes, *Science* 292 (2001) 2303-2307.

- [27] B. Xu, X. Xiao, X. Yang, L. Zang, N. Tao, Large gate modulation in the current of a room temperature single molecule transistor, *Journal of the American Chemical Society* 127 (2005) 2386-2387.
- [28] I. Díez-Pérez, Z. Li, S. Guo, C. Madden, H. Huang, Y. Che, X. Yang, L. Zang, N. Tao, Ambipolar transport in an electrochemically gated single-molecule field-effect transistor, *ACS nano* 6 (2012) 7044-7052.
- [29] X. Li, J. Hihath, F. Chen, T. Masuda, L. Zang, N. Tao, Thermally activated electron transport in single redox molecules, *Journal of the American Chemical Society* 129 (2007) 11535-11542.
- [30] C. Li, A. Mishchenko, Z. Li, I. Pobelov, T. Wandlowski, X. Li, A. Bagrets, F. Evers, Electrochemical gate-controlled electron transport of redox-active single perylene bisimide molecular junctions, *Journal of Physics: Condensed Matter* 20 (2008) 374122.
- [31] M.C.R. Delgado, E.-G. Kim, D.t.A.d.S. Filho, J.-L. Bredas, Tuning the charge-transport parameters of perylene diimide single crystals via end and/or core functionalization: a density functional theory investigation, *Journal of the American Chemical Society* 132 (2010) 3375-3387.
- [32] C.W. Tang, Two-layer organic photovoltaic cell, *Applied Physics Letters* 48 (1986) 183-185.
- [33] X. Zhan, Z.a. Tan, B. Domercq, Z. An, X. Zhang, S. Barlow, Y. Li, D. Zhu, B. Kippelen, S.R. Marder, A high-mobility electron-transport polymer with broad absorption and its use in field-effect transistors and all-polymer solar cells, *Journal of the American Chemical Society* 129 (2007) 7246-7247.
- [34] S.K. Lee, Y. Zu, A. Herrmann, Y. Geerts, K. Müllen, A.J. Bard, Electrochemistry, spectroscopy and electrogenerated chemiluminescence of perylene,

terrylene, and quaterrylene diimides in aprotic solution, *Journal of the American Chemical Society* 121 (1999) 3513-3520.

[35] G. Seybold, G. Wagenblast, New perylene and violanthrone dyestuffs for fluorescent collectors, *Dyes and Pigments* 11 (1989) 303-317.

[36] M. Thelakkat, P. Pösch, H.-W. Schmidt, Synthesis and characterization of highly fluorescent main-chain copolyimides containing perylene and quinoxaline units, *Macromolecules* 34 (2001) 7441-7447.

[37] H. Tian, P.-H. Liu, F.-S. Meng, E. Gao, S. Cai, Wide spectral photosensitization for SnO₂ nanoporous electrode with soluble perylene derivatives and cyanine dyes, *Synthetic Metals* 121 (2001) 1557-1558.

[38] P. Ranke, I. Bleyl, J. Simmerer, D. Haarer, A. Bacher, H. Schmidt, Electroluminescence and electron transport in a perylene dye, *Applied Physics Letters* 71 (1997) 1332-1334.

[39] J.J. Dittmer, E.A. Marseglia, R.H. Friend, Electron trapping in dye/polymer blend photovoltaic cells, *Advanced Materials* 12 (2000) 1270-1274.

[40] B.R. Baker, R.Y. Lai, M.S. Wood, E.H. Doctor, A.J. Heeger, K.W. Plaxco, An electronic, aptamer-based small-molecule sensor for the rapid, label-free detection of cocaine in adulterated samples and biological fluids, *Journal of the American Chemical Society* 128 (2006) 3138-3139.

[41] Z. Liu, H.-L. Wang, M. Cotlet, Energy Transfer from a Cationic Conjugated Polyelectrolyte to a DNA Photonic Wire: Toward Label-Free, Sequence-Specific DNA Sensing, *Chemistry of Materials* 26 (2014) 2900-2906.

[42] B. Davis, J. Richens, P. O'Shea, Label-Free Critical Micelle Concentration Determination of Bacterial Quorum Sensing Molecules, *Biophysical journal* 101 (2011) 245-254.

- [43] P.D. Garimella, T. Meldrum, L.S. Witus, M. Smith, V.S. Bajaj, D.E. Wemmer, M.B. Francis, A. Pines, Hyperpolarized xenon-based molecular sensors for label-free detection of analytes, *Journal of the American Chemical Society* 136 (2013) 164-168.
- [44] H. Im, H. Shao, Y.I. Park, V.M. Peterson, C.M. Castro, R. Weissleder, H. Lee, Label-free detection and molecular profiling of exosomes with a nano-plasmonic sensor, *Nature Biotechnology* 32 (2014) 490-495.
- [45] M. Li, J. Lu, J. Qi, F. Zhao, J. Zeng, J.C.-C. Yu, W.-C. Shih, Stamping surface-enhanced Raman spectroscopy for label-free, multiplexed, molecular sensing and imaging, *Journal of biomedical optics* 19 (2014) 050501-050501.
- [46] J. Ren, X.-L. Zhao, Q.-C. Wang, C.-F. Ku, D.-H. Qu, C.-P. Chang, H. Tian, New fluoride fluorescent chemosensors based on perylene derivatives linked by urea, *Dyes and pigments* 64 (2005) 193-200.
- [47] T.H. Rehm, M.R. Stojković, S. Rehm, M. Škugor, I. Piantanida, F. Würthner, Interaction of spermine-alanine functionalized perylene bisimide dye aggregates with ds-DNA/RNA secondary structure, *Chemical Science* 3 (2012) 3393-3397.
- [48] F. Würthner, M. Stolte, Naphthalene and perylene diimides for organic transistors, *Chemical Communications* 47 (2011) 5109-5115.
- [49] X. Zhan, A. Facchetti, S. Barlow, T.J. Marks, M.A. Ratner, M.R. Wasielewski, S.R. Marder, Rylene and related diimides for organic electronics, *Advanced Materials* 23 (2011) 268-284.
- [50] Z. Liu, G. Zhang, Z. Cai, X. Chen, H. Luo, Y. Li, J. Wang, D. Zhang, New Organic Semiconductors with Imide/Amide-Containing Molecular Systems, *Advanced Materials* 26 (2014) 6965-6977.
- [51] A.J. Avestro, D.M. Gardner, N.A. Vermeulen, E.A. Wilson, S.T. Schneebeli, A.C. Whalley, M.E. Belowich, R. Carmieli, M.R. Wasielewski, J.F. Stoddart, Gated

Electron Sharing Within Dynamic Naphthalene Diimide-Based Oligorotaxanes, *Angewandte Chemie* 126 (2014) 4531-4538.

[52] G. Dorough, J. Miller, F.M. Huennekens, Spectra of the Metallo-derivatives of α , β , γ , δ -Tetraphenylporphine, *Journal of the American Chemical Society* 73 (1951) 4315-4320.

[53] G. Sedghi, V.M. García-Suárez, L.J. Esdaile, H.L. Anderson, C.J. Lambert, S. Martín, D. Bethell, S.J. Higgins, M. Elliott, N. Bennett, Long-range electron tunnelling in oligo-porphyrin molecular wires, *Nature nanotechnology* 6 (2011) 517-523.

[54] D. Gust, J.D. Roberts, Nitrogen-15 nuclear magnetic resonance studies of porphyrins, *Journal of the American Chemical Society* 99 (1977) 3637-3640.

[55] Z. Li, M. Smeu, M.A. Ratner, E. Borguet, Effect of anchoring groups on single molecule charge transport through porphyrins, *The Journal of Physical Chemistry C* 117 (2013) 14890-14898.

[56] Z. Li, E. Borguet, Determining charge transport pathways through single porphyrin molecules using scanning tunneling microscopy break junctions, *Journal of the American Chemical Society* 134 (2011) 63-66.

[57] Z.-F. Liu, S. Wei, H. Yoon, O. Adak, I. Ponce, Y. Jiang, W.-D. Jang, L.M. Campos, L. Venkataraman, J.B. Neaton, Control of Single-Molecule Junction Conductance of Porphyrins via a Transition-Metal Center, *Nano Letters* 14 (2014) 5365-5370.

[58] Y. Li, J. Yao, S. Zhong, Z. Zou, Theoretical investigations on the orientational dependence of electron transport through porphyrin molecular wire, *Current Applied Physics* 11 (2011) 1349-1353.

- [59] R. Ferradás, V.M. García-Suárez, J. Ferrer, Symmetry-induced interference effects in metalloporphyrin wires, arXiv preprint arXiv:1208.3157 (2012).
- [60] I. Beletskaya, V.S. Tyurin, A.Y. Tsivadze, R. Guillard, C. Stern, Supramolecular chemistry of metalloporphyrins, *Chemical reviews* 109 (2009) 1659-1713.
- [61] R. Landauer, Spatial variation of currents and fields due to localized scatterers in metallic conduction, *IBM Journal of Research and Development* 1 (1957) 223-231.
- [62] M. Büttiker, Y. Imry, R. Landauer, S. Pinhas, Generalized many-channel conductance formula with application to small rings, *Physical Review b* 31 (1985) 6207.
- [63] S. Datta, *Electronic transport in mesoscopic systems* (Cambridge university press, 1995).
- [64] P. Brouwer, Scattering approach to parametric pumping, *Physical Review B* 58 (1998) R10135.
- [65] V.V. Maslyuk, S. Achilles, I. Mertig, Spin-polarized transport and thermopower of organometallic nanocontacts, *Solid State Communications* 150 (2010) 505-509.
- [66] V.M. García-Suárez, R. Ferradás, J. Ferrer, Impact of Fano and Breit-Wigner resonances in the thermoelectric properties of nanoscale junctions, *Physical review b* 88 (2013) 235417.
- [67] S. Datta, *Electronic transport in mesoscopic systems* (Cambridge university press, 1997).
- [68] N. Claughton, C. Lambert, Thermoelectric properties of mesoscopic superconductors, *Physical review b* 53 (1996) 6605.
- [69] U. Sivan, Y. Imry, Multichannel Landauer formula for thermoelectric transport with application to thermopower near the mobility edge, *Physical review b* 33 (1986) 551.

- [70] L. Hicks, M. Dresselhaus, Thermoelectric figure of merit of a one-dimensional conductor, *Physical review b* 47 (1993) 16631.
- [71] H.J. Goldsmid, *Thermoelectric refrigeration* (Plenum Press New York, 1964).
- [72] Q.H. Al-Galiby, H. Sadeghi, L.A. Algharagholy, I. Grace, C. Lambert, Tuning the thermoelectric properties of metallo-porphyrins, *Nanoscale* 8 (2016) 2428-2433.
- [73] V.M. García-Suárez, C.J. Lambert, D.Z. Manrique, T. Wandlowski, Redox control of thermopower and figure of merit in phase-coherent molecular wires, *Nanotechnology* 25 (2014) 205402.
- [74] E.N. Economou, *Green's functions in quantum physics* (Springer, 1984).
- [75] P.A. Mello, N.K. Kumar, N. Kumar, *Quantum transport in mesoscopic systems: complexity and statistical fluctuations, a maximum-entropy viewpoint* (Oxford University Press, 2004).
- [76] D.S. Fisher, P.A. Lee, Relation between conductivity and transmission matrix, *Physical review b* 23 (1981) 6851.
- [77] D. Visontai, *Quantum and Classical Dynamics of Molecule Size Systems*, PhD thesis, Lancaster University (2011).
- [78] S. Sanvito, *Giant Magnetoresistance and Quantum Transport in Magnetic Hybrid Nanostructures*, PhD thesis, Lancaster University (1999).
- [79] C.M. Finch, *An understanding of electrical characteristics of organic molecular devices*, PhD thesis, Lancaster University (2008).
- [80] J.G. MacKinnon, H. White, Some heteroskedasticity-consistent covariance matrix estimators with improved finite sample properties, *Journal of econometrics* 29 (1985) 305-325.
- [81] D. Ryndyk, R. Gutiérrez, B. Song, G. Cuniberti, in: *Energy Transfer Dynamics in Biomaterial Systems*, (Springer, 2009).

- [82] C. Lambert, V. Hui, S. Robinson, Multi-probe conductance formulae for mesoscopic superconductors, *Journal of Physics: Condensed Matter* 5 (1993) 4187.
- [83] C.M. Finch, S. Sirichantaropass, S.W. Bailey, I.M. Grace, V.M. García-Suárez, C.J. Lambert, Conformation dependence of molecular conductance: chemistry versus geometry, *Journal of Physics: Condensed Matter* 20 (2008) 022203.
- [84] S.W.B. I. M. Grace, C. J. Lambert, and J. H. Jefferson, *Molecular nanowires and other quantum objects* (NATO ASI Series, 2004).
- [85] S. Athanasopoulos, *Electronic Properties of Hybrid Carbon Nanotubes* (PhD thesis, Lancaster University, PhD thesis, Lancaster University, 2005).
- [86] M. Leadbeater, C. Lambert, Superconductivity-induced phase-periodic transport in nanoscale structures, *Physical Review B* 56 (1997) 826.
- [87] P. Polinák, C. Lambert, J. Koltai, J. Cserti, Andreev drag effect via magnetic quasiparticle focusing in normal-superconductor nanojunctions, *Physical Review B* 74 (2006) 132508.
- [88] A.R. Rocha, V. Garcia-Suarez, S. Bailey, C. Lambert, J. Ferrer, S. Sanvito, Spin and molecular electronics in atomically generated orbital landscapes, *PHYSICAL REVIEW-SERIES B*- 73 (2006) 085414.
- [89] G. Breit, E. Wigner, Capture of slow neutrons, *Physical Review* 49 (1936) 519.
- [90] U. Fano, Effects of configuration interaction on intensities and phase shifts, *Physical Review* 124 (1961) 1866.
- [91] T. Papadopoulos, I. Grace, C. Lambert, Control of electron transport through Fano resonances in molecular wires, *Physical review b* 74 (2006) 193306.
- [92] S.-H. Ke, W. Yang, H.U. Baranger, Quantum-interference-controlled molecular electronics, *Nano letters* 8 (2008) 3257-3261.

- [93] R. Stadler, Quantum interference effects in electron transport through nitrobenzene with pyridil anchor groups, *Physical Review B* 80 (2009) 125401.
- [94] V. Petkov, M. Zworski, Breit–Wigner Approximation and the Distribution of Resonances, *Communications in Mathematical Physics* 204 (1999) 329-351.
- [95] K. Kobayashi, H. Aikawa, S. Katsumoto, Y. Iye, Tuning of the Fano effect through a quantum dot in an Aharonov-Bohm interferometer, *Physical Review Letters* 88 (2002) 256806.
- [96] C.M. Finch, An understanding of electrical characteristics of organic molecular devices, PhD thesis, Lancaster University (2008).
- [97] C. Finch, V. Garcia-Suarez, C. Lambert, Giant thermopower and figure of merit in single-molecule devices, *Physical review b* 79 (2009) 033405.
- [98] J.M. Soler, E. Artacho, J.D. Gale, A. García, J. Junquera, P. Ordejón, D. Sánchez-Portal, The SIESTA method for ab initio order-N materials simulation, *Journal of Physics: Condensed Matter* 14 (2002) 2745.
- [99] I.E. Gas, P. Hohenberg, W. Kohn, S.-C.E.I. Exchange, L. Sham, Nobel Focus: Chemistry by Computer, *Phys. Rev* 136 (1964) B864.
- [100] W. Kohn, L.J. Sham, Self-consistent equations including exchange and correlation effects, *Physical Review* 140 (1965) A1133.
- [101] R.M. Martin, *Electronic structure: basic theory and practical methods* (Cambridge university press, 2004).
- [102] R.G. Parr, W. Yang, *Density-functional theory of atoms and molecules* (Oxford university press, 1989).
- [103] E.K. Gross, E. Runge, *Many-particle theory*, (1986).
- [104] E.K. Gross, R.M. Dreizler, *Density functional theory* (Springer Science & Business Media, 2013).

- [105] C. Li, V. Stepanenko, M.J. Lin, W. Hong, F. Würthner, T. Wandlowski, Charge transport through perylene bisimide molecular junctions: An electrochemical approach, *physica status solidi (b)* 250 (2013) 2458-2467.
- [106] Q. Al-Galiby, I. Grace, H. Sadeghi, C.J. Lambert, Exploiting the extended π -system of perylene bisimide for label-free single-molecule sensing, *Journal of Materials Chemistry C* 3 (2015) 2101-2106.
- [107] J.M. Soler, E. Artacho, J.D. Gale, A. García, J. Junquera, P. Ordejón, D. Sánchez-Portal, The SIESTA method for ab initio order-N materials simulation, *Journal of Physics: Condensed Matter* 14 (2002) 2745.
- [108] N. Troullier, J.L. Martins, Efficient pseudopotentials for plane-wave calculations, *Physical Review B* 43 (1991) 1993.
- [109] J.P. Perdew, K. Burke, M. Ernzerhof, Generalized gradient approximation made simple, *Physical Review Letters* 77 (1996) 3865.
- [110] B. Hammer, L.B. Hansen, J.K. Nørskov, Improved adsorption energetics within density-functional theory using revised Perdew-Burke-Ernzerhof functionals, *Physical Review B* 59 (1999) 7413.
- [111] J. Ferrer, C.J. Lambert, V.M. García-Suárez, D.Z. Manrique, D. Visontai, L. Oroszlany, R. Rodríguez-Ferradás, I. Grace, S. Bailey, K. Gillemot, GOLLUM: a next-generation simulation tool for electron, thermal and spin transport, *New Journal of Physics* 16 (2014) 093029.
- [112] A.R. Rocha, V.M. Garcia-Suarez, S.W. Bailey, C.J. Lambert, J. Ferrer, S. Sanvito, Towards molecular spintronics, *Nature materials* 4 (2005) 335-339.
- [113] S. Chowdhury, P. Kebarle, Electron affinities of di- and tetracyanoethylene and cyanobenzenes based on measurements of gas-phase electron-transfer equilibria, *Journal of the American Chemical Society* 108 (1986) 5453-5459.

- [114] E. Kosower, (Academic Press, New York, 1969. xii, 472 pp., illus. \$22.50. Organic Chemistry, 1970).
- [115] V. Khodorkovsky, J. Becker, J. Farges, Organic Conductors: Fundamentals and Applications, Matcel Dekker, New York (1994) 75-88.
- [116] W.K. Maser, Organic superconductors (including fullerenes): Synthesis, structure, properties, and theory. By, JM Williams, JR Ferraro, RJ Thorn, KD Carlson, U. Geiser, HH Wang, AM Kini, and M.-H. Whangbo, Prentice Hall, Englewood Cliffs, NJ 1992, 400 pp., hardcover, \$91.00, ISBN 0-13-640566-5, Advanced Materials 6 (1994) 87-87.
- [117] J.M. Williams, H.H. Wang, T.J. Emge, U. Geiser, M.A. Beno, P.C. Leung, K. Douglas Carlson, R.J. Thorn, A.J. Schultz, M.H. Whangbo, Rational design of synthetic metal superconductors, Progress in Inorganic Chemistry, Volume 35 (1987) 51-218.
- [118] Y.-I. Kim, Bis (ethylenedithio) tetrathiafulvalene (BEDT-TTF) Charge Transfer Compounds with Copper (II) Halides:(BEDT-TTF)_{1-x}5CuX₂ (X= Cl, Br), BULLETIN-KOREAN CHEMICAL SOCIETY 24 (2003) 1389-1392.
- [119] F. Würthner, Perylene bisimide dyes as versatile building blocks for functional supramolecular architectures, Chemical Communications (2004) 1564-1579.
- [120] D.M. Ceperley, B. Alder, Ground state of the electron gas by a stochastic method, Physical Review Letters 45 (1980) 566.
- [121] J. Klimeš, D.R. Bowler, A. Michaelides, Van der Waals density functionals applied to solids, Physical review b 83 (2011) 195131.
- [122] H. Jansen, P. Ros, Non-empirical molecular orbital calculations on the protonation of carbon monoxide, Chemical Physics Letters 3 (1969) 140-143.

- [123] S.F. Boys, F.d. Bernardi, The calculation of small molecular interactions by the differences of separate total energies. Some procedures with reduced errors, *Molecular Physics* 19 (1970) 553-566.
- [124] Y. Li, M. Baghernejad, A.G. Qusiy, D. Zsolt Manrique, G. Zhang, J. Hamill, Y. Fu, P. Broekmann, W. Hong, T. Wandlowski, Three-State Single-Molecule Naphthalenediimide Switch: Integration of a Pendant Redox Unit for Conductance Tuning, *Angewandte Chemie International Edition* 54 (2015) 13586-13589.
- [125] A.C. Fahrenbach, C.J. Bruns, H. Li, A. Trabolsi, A. Coskun, J.F. Stoddart, Ground-State Kinetics of Bistable Redox-Active Donor–Acceptor Mechanically Interlocked Molecules, *Accounts of Chemical Research* 47 (2013) 482-493.
- [126] M. Irie, T. Fukaminato, K. Matsuda, S. Kobatake, Photochromism of diarylethene molecules and crystals: memories, switches, and actuators, *Chemical Reviews* 114 (2014) 12174-12277.
- [127] B.L. Feringa, R.A. van Delden, N. Koumura, E.M. Geertsema, Chiroptical molecular switches, *Chemical Reviews* 100 (2000) 1789-1816.
- [128] P. Ceroni, A. Credi, M. Venturi, *Electrochemistry of functional supramolecular systems* (John Wiley & Sons, 2010).
- [129] E. Laviron, General expression of the linear potential sweep voltammogram in the case of diffusionless electrochemical systems, *Journal of Electroanalytical Chemistry and Interfacial Electrochemistry* 101 (1979) 19-28.
- [130] C.P. Andrieux, C. Blocman, J.M. Dumas-Bouchiat, J.M. Saveant, Heterogeneous and homogeneous electron transfers to aromatic halides. An electrochemical redox catalysis study in the halobenzene and halopyridine series, *Journal of the American Chemical Society* 101 (1979) 3431-3441.

- [131] C.R. Arroyo, S. Tarkuc, R. Frisenda, J.S. Seldenthuis, C.H. Woerde, R. Eelkema, F.C. Grozema, H.S. van der Zant, Signatures of quantum interference effects on charge transport through a single benzene ring, *Angewandte Chemie* 125 (2013) 3234-3237.
- [132] Z. Li, M. Smeu, S. Afsari, Y. Xing, M.A. Ratner, E. Borguet, Single-Molecule Sensing of Environmental pH—an STM Break Junction and NEGF-DFT Approach, *Angewandte Chemie* 126 (2014) 1116-1120.
- [133] C. Huang, A.V. Rudnev, W. Hong, T. Wandlowski, Break junction under electrochemical gating: testbed for single-molecule electronics, *Chemical Society Reviews* 44 (2015) 889-901.
- [134] C. Jia, J. Wang, C. Yao, Y. Cao, Y. Zhong, Z. Liu, Z. Liu, X. Guo, Conductance Switching and Mechanisms in Single-Molecule Junctions, *Angewandte Chemie International Edition* 52 (2013) 8666-8670.
- [135] C. Jia, B. Ma, N. Xin, X. Guo, Carbon Electrode–Molecule Junctions: A Reliable Platform for Molecular Electronics, *Accounts of Chemical Research* 48 (2015) 2565-2575.
- [136] C. Jia, X. Guo, Molecule–electrode interfaces in molecular electronic devices, *Chemical Society Reviews* 42 (2013) 5642-5660.
- [137] H. Tian, Data processing on a unimolecular platform, *Angewandte Chemie International Edition* 49 (2010) 4710-4712.
- [138] J.E. Green, J.W. Choi, A. Boukai, Y. Bunimovich, E. Johnston-Halperin, E. DeIonno, Y. Luo, B.A. Sheriff, K. Xu, Y.S. Shin, A 160-kilobit molecular electronic memory patterned at 1011 bits per square centimetre, *Nature* 445 (2007) 414-417.
- [139] E. Leary, S.J. Higgins, H. van Zalinge, W. Haiss, R.J. Nichols, S. Nygaard, J.O. Jeppesen, J. Ulstrup, Structure– Property Relationships in Redox-Gated Single

Molecule Junctions— A Comparison of Pyrrolo-Tetrathiafulvalene and Viologen Redox Groups, *Journal of the American Chemical Society* 130 (2008) 12204-12205.

[140] Z. Li, H. Li, S. Chen, T. Froehlich, C. Yi, C. Schönenberger, M. Calame, S. Decurtins, S.-X. Liu, E. Borguet, Regulating a benzodifuran single molecule redox switch via electrochemical gating and optimization of molecule/electrode coupling, *Journal of the American Chemical Society* 136 (2014) 8867-8870.

[141] X.-S. Zhou, L. Liu, P. Fortgang, A.-S. Lefevre, A. Serra-Muns, N. Raouafi, C. Amatore, B.-W. Mao, E. Maisonhaute, B. Schöllhorn, Do molecular conductances correlate with electrochemical rate constants? Experimental insights, *Journal of the American Chemical Society* 133 (2011) 7509-7516.

[142] F. Würthner, S. Ahmed, C. Thalacker, T. Debaerdemaeker, Core-Substituted Naphthalene Bisimides: New Fluorophors with Tunable Emission Wavelength for FRET Studies, *Chemistry-A European Journal* 8 (2002) 4742-4750.

[143] P. Moreno-García, M. Gulcur, D.Z. Manrique, T. Pope, W. Hong, V. Kaliginedi, C. Huang, A.S. Batsanov, M.R. Bryce, C. Lambert, Single-molecule conductance of functionalized oligoynes: Length dependence and junction evolution, *Journal of the American Chemical Society* 135 (2013) 12228-12240.

[144] S.Y. Quek, M. Kamenetska, M.L. Steigerwald, H.J. Choi, S.G. Louie, M.S. Hybertsen, J. Neaton, L. Venkataraman, Mechanically controlled binary conductance switching of a single-molecule junction, *Nature nanotechnology* 4 (2009) 230-234.

[145] C.A. Martin, D. Ding, J.K. Sørensen, T. Bjørnholm, J.M. van Ruitenbeek, H.S. van der Zant, Fullerene-based anchoring groups for molecular electronics, *Journal of the American Chemical Society* 130 (2008) 13198-13199.

[146] A. Mishchenko, L.A. Zotti, D. Vonlanthen, M. Bürkle, F. Pauly, J.C. Cuevas, M. Mayor, T. Wandlowski, Single-molecule junctions based on nitrile-terminated

biphenyls: a promising new anchoring group, *Journal of the American Chemical Society* 133 (2010) 184-187.

[147] W. Hong, D.Z. Manrique, P. Moreno-García, M. Gulcur, A. Mishchenko, C.J. Lambert, M.R. Bryce, T. Wandlowski, Single molecular conductance of tolanes: experimental and theoretical study on the junction evolution dependent on the anchoring group, *Journal of the American Chemical Society* 134 (2012) 2292-2304.

[148] J.D.C. Jacob, T.R. Lee, S. Baldelli, In Situ Vibrational Study of the Reductive Desorption of Alkanethiol Monolayers on Gold by Sum Frequency Generation Spectroscopy, *The Journal of Physical Chemistry C* 118 (2014) 29126-29134.

[149] A.C. Aragonés, N. Darwish, W.J. Saletra, L. Perez-Garcia, F. Sanz, J. Puigmartí-Luis, D.B. Amabilino, I. Díez-Pérez, Highly Conductive Single-Molecule Wires with Controlled Orientation by Coordination of Metalloporphyrins, *Nano Letters* 14 (2014) 4751-4756.

[150] T.J. Seebeck, Ueber die magnetische Polarisation der Metalle und Erze durch Temperaturdifferenz, *Annalen der Physik* 82 (1826) 253-286.

[151] X. Chen, L. Chen, J. Guo, J. Chen, An available method exploiting the waste heat in a proton exchange membrane fuel cell system, *International Journal of Hydrogen Energy* 36 (2011) 6099-6104.

[152] S. Kumar, S.D. Heister, X. Xu, J.R. Salvador, G.P. Meisner, Thermoelectric generators for automotive waste heat recovery systems part I: numerical modeling and baseline model analysis, *Journal of Electronic Materials* 42 (2013) 665-674.

[153] B.I. Ismail, W.H. Ahmed, Thermoelectric power generation using waste-heat energy as an alternative green technology, *Recent Patents on Electrical & Electronic Engineering (Formerly Recent Patents on Electrical Engineering)* 2 (2009) 27-39.

- [154] D. Voneshen, K. Refson, E. Borissenko, M. Krisch, A. Bosak, A. Piovano, E. Cemal, M. Enderle, M. Gutmann, M. Hoesch, Suppression of thermal conductivity by rattling modes in thermoelectric sodium cobaltate, *Nature materials* 12 (2013) 1028-1032.
- [155] M. Bürkle, L.A. Zotti, J.K. Viljas, D. Vonlanthen, A. Mishchenko, T. Wandlowski, M. Mayor, G. Schön, F. Pauly, Ab initio study of the thermopower of biphenyl-based single-molecule junctions, *Physical review b* 86 (2012) 115304.
- [156] P. Chaikin, J. Kwak, Apparatus for thermopower measurements on organic conductors, *Review of Scientific Instruments* 46 (1975) 218-220.
- [157] S.-H. Ke, W. Yang, S. Curtarolo, H.U. Baranger, Thermopower of molecular junctions: An ab initio study, *Nano Letters* 9 (2009) 1011-1014.
- [158] C. Evangelii, K. Gillemot, E. Leary, M. Gonzalez, R-Bollinger, G.; Lambert, C.; Agrait, N, *Nano Lett* 13 (2013) 2141-2145.
- [159] A.A. Balandin, Thermal properties of graphene and nanostructured carbon materials, *Nature materials* 10 (2011) 569-581.
- [160] H. Sadeghi, S. Sangtarash, C.J. Lambert, Enhanced thermoelectric efficiency of porous silicene nanoribbons, *Scientific reports* 5 (2015).
- [161] H. Sadeghi, S. Sangtarash, C.J. Lambert, Enhancing the thermoelectric figure of merit in engineered graphene nanoribbons, *Beilstein journal of nanotechnology* 6 (2015) 1176-1182.
- [162] A. Kambili, G. Fagas, V.I. Fal'ko, C. Lambert, Phonon-mediated thermal conductance of mesoscopic wires with rough edges, *Physical review b* 60 (1999) 15593.

- [163] G. Fagas, A. Kozorezov, C. Lambert, J. Wigmore, A. Peacock, A. Poelaert, R. Den Hartog, Lattice dynamics of a disordered solid-solid interface, *Physical review b* 60 (1999) 6459.
- [164] R. Venkatasubramanian, E. Siivola, T. Colpitts, B. O'quinn, Thin-film thermoelectric devices with high room-temperature figures of merit, *Nature* 413 (2001) 597-602.
- [165] T. Harman, P. Taylor, M. Walsh, B. LaForge, Quantum dot superlattice thermoelectric materials and devices, *Science* 297 (2002) 2229-2232.
- [166] B. Poudel, Q. Hao, Y. Ma, Y. Lan, A. Minnich, B. Yu, X. Yan, D. Wang, A. Muto, D. Vashaee, High-thermoelectric performance of nanostructured bismuth antimony telluride bulk alloys, *Science* 320 (2008) 634-638.
- [167] K. Yanagi, S. Kanda, Y. Oshima, Y. Kitamura, H. Kawai, T. Yamamoto, T. Takenobu, Y. Nakai, Y. Maniwa, Tuning of the Thermoelectric Properties of One-Dimensional Material Networks by Electric Double Layer Techniques Using Ionic Liquids, *Nano Letters* 14 (2014) 6437-6442.
- [168] D.Z. Manrique, Q.H. Al-Galiby, W. Hong, C.J. Lambert, A new approach to materials discovery for electronic and thermoelectric properties of single-molecule junctions, *Nano Letters* (2016).
- [169] J. Repp, G. Meyer, S. Paavilainen, F.E. Olsson, M. Persson, Imaging bond formation between a gold atom and pentacene on an insulating surface, *Science* 312 (2006) 1196-1199.
- [170] D.J. Wold, R. Haag, M.A. Rampi, C.D. Frisbie, Distance dependence of electron tunneling through self-assembled monolayers measured by conducting probe atomic force microscopy: Unsaturated versus saturated molecular junctions, *Journal of Physical Chemistry B* 106 (2002) 2813-2816.

- [171] F.-R.F. Fan, J. Yang, L. Cai, D.W. Price, S.M. Dirk, D.V. Kosynkin, Y. Yao, A.M. Rawlett, J.M. Tour, A.J. Bard, Charge transport through self-assembled monolayers of compounds of interest in molecular electronics, *Journal of the American Chemical Society* 124 (2002) 5550-5560.
- [172] J.R. Widawsky, P. Darancet, J.B. Neaton, L. Venkataraman, Simultaneous determination of conductance and thermopower of single molecule junctions, *Nano letters* 12 (2011) 354-358.
- [173] L. Venkataraman, J.E. Klare, C. Nuckolls, M.S. Hybertsen, M.L. Steigerwald, Dependence of single-molecule junction conductance on molecular conformation, *Nat.* 442 (2006) 904-907.
- [174] W. Hong, H. Valkenier, G. Mészáros, D.Z. Manrique, A. Mishchenko, A. Putz, P.M. García, C.J. Lambert, J.C. Hummelen, T. Wandlowski, An MCBJ case study: The influence of π -conjugation on the single-molecule conductance at a solid/liquid interface, *Beilstein J. Nanotechnol.* 2 (2011) 699-713.
- [175] D.S. Seferos, S.A. Trammell, G.C. Bazan, J.G. Kushmerick, Probing π -coupling in molecular junctions, *P. NATL. ACAD. SCI. USA* 102 (2005) 8821-8825.
- [176] T. Dadoosh, Y. Gordin, R. Krahne, I. Khivrich, D. Mahalu, V. Frydman, J. Sperling, A. Yacoby, I. Bar-Joseph, Erratum: Measurement of the conductance of single conjugated molecules, *Nature* 436 (2005) 1200-1200.
- [177] J. Liao, L. Bernard, M. Langer, C. Schonenberger, M. Calame, Reversible formation of molecular junctions in 2D nanoparticle arrays, *Advanced Materials* 18 (2006) 2803-2804.
- [178] M.A. Reed, C. Zhou, C. Muller, T. Burgin, J. Tour, Conductance of a molecular junction, *Science* 278 (1997) 252-254.

- [179] J. Park, A.N. Pasupathy, J.I. Goldsmith, C. Chang, Y. Yaish, J.R. Petta, M. Rinkoski, J.P. Sethna, H.D. Abruña, P.L. McEuen, Coulomb blockade and the Kondo effect in single-atom transistors, *Nat.* 417 (2002) 722-725.
- [180] E. Osorio, T. Bjørnholm, J. Lehn, M. Ruben, H. Van der Zant, Single-molecule transport in three-terminal devices, *Journal of Physics: Condensed Matter* 20 (2008) 374121.
- [181] C.G. Péterfalvi, I. Grace, D.Z. Manrique, C.J. Lambert, Thermoelectric performance of various benzo-difuran wires, *J. Chem. Phys* 140 (2014) 174711.
- [182] C. Evangeli, K. Gillemot, E. Leary, M.T. González, G. Rubio-Bollinger, C.J. Lambert, N.s. Agrait, Engineering the thermopower of C60 molecular junctions, *Nano Letters* 13 (2013) 2141-2145.
- [183] X. Zhao, C. Huang, M. Gulcur, A.S. Batsanov, M. Baghernejad, W. Hong, M.R. Bryce, T. Wandlowski, Oligo (aryleneethynylene) s with terminal pyridyl groups: synthesis and length dependence of the tunneling-to-hopping transition of single-molecule conductances, *Chemistry of Materials* 25 (2013) 4340-4347.
- [184] C. Lambert, Basic concepts of quantum interference and electron transport in single-molecule electronics, *Chemical Society Reviews* 44 (2015) 875-888.
- [185] E. Scheer, *Molecular electronics: an introduction to theory and experiment* (World Sci., 2010).
- [186] R. Sparks, V.M. García-Suárez, D.Z. Manrique, C.J. Lambert, Quantum interference in single molecule electronic systems, *Physical Review B: Condensed Matter* 83 (2011) 075437.
- [187] C. Finch, V. Garcia-Suarez, C. Lambert, Giant thermopower and figure of merit in single-molecule devices, *Phys. Rev. b* 79 (2009) 033405.

- [188] W. Hong, D.Z. Manrique, P. Moreno-García, M. Gulcur, A. Mishchenko, C.J. Lambert, M.R. Bryce, T. Wandlowski, Single molecular conductance of tolanes: experimental and theoretical study on the junction evolution dependent on the anchoring group, *Journal of the American Chemical Society* 134 (2012) 2292-2304.
- [189] V. Kaliginedi, P. Moreno-García, H. Valkenier, W. Hong, V.M. García-Suárez, P. Buitter, J.L. Otten, J.C. Hummelen, C.J. Lambert, T. Wandlowski, Correlations between molecular structure and single-junction conductance: a case study with oligo (phenylene-ethynylene)-type wires, *Journal of the American Chemical Society* 134 (2012) 5262-5275.
- [190] K. Yoshida, I.V. Pobelov, D.Z. Manrique, T. Pope, G. Mészáros, M. Gulcur, M.R. Bryce, C.J. Lambert, T. Wandlowski, Correlation of breaking forces, conductances and geometries of molecular junctions, *Sci. Rep.* 5 (2015).
- [191] A. Mishchenko, L.A. Zotti, D. Vonlanthen, M. Bürkle, F. Pauly, J.C. Cuevas, M. Mayor, T. Wandlowski, Single-molecule junctions based on nitrile-terminated biphenyls: a promising new anchoring group, *Journal of the American Chemical Society* 133 (2010) 184-187.
- [192] M.S. Hybertsen, L. Venkataraman, J.E. Klare, A.C. Whalley, M.L. Steigerwald, C. Nuckolls, Amine-linked single-molecule circuits: systematic trends across molecular families, *Journal of Physics: Condensed Matter* 20 (2008) 374115.
- [193] S.Y. Quek, L. Venkataraman, H.J. Choi, S.G. Louie, M.S. Hybertsen, J. Neaton, Amine-gold linked single-molecule circuits: Experiment and theory, *Nano Letters* 7 (2007) 3477-3482.
- [194] S.Y. Quek, M. Kamenetska, M.L. Steigerwald, H.J. Choi, S.G. Louie, M.S. Hybertsen, J. Neaton, L. Venkataraman, Mechanically controlled binary conductance switching of a single-molecule junction, *Nat. Nanotechnol.* 4 (2009) 230-234.

- [195] K. Kanthasamy, H. Pfnür, Conductance through single biphenyl molecules: symmetric and asymmetric coupling to electrodes, *Beilstein J. Nanotechnol.* 6 (2015) 1690-1697.
- [196] J.J. Stewart, Optimization of parameters for semiempirical methods VI: more modifications to the NDDO approximations and re-optimization of parameters, *Journal of Molecular Modeling* 19 (2013) 1-32.
- [197] C. Huang, A.V. Rudnev, W. Hong, T. Wandlowski, Break junction under electrochemical gating: testbed for single-molecule electronics, *Chemical Society Reviews* 44 (2015) 889-901.
- [198] J. Ferrer, C.J. Lambert, V.M. García-Suárez, D.Z. Manrique, D. Visontai, L. Oroszlany, R. Rodríguez-Ferradás, I. Grace, S. Bailey, K. Gillemot, GOLLUM: a next-generation simulation tool for electron, thermal and spin transport, *New J. Phys.* 16 (2014) 093029.
- [199] C. Verzijl, J. Seldenthuis, J. Thijssen, Applicability of the wide-band limit in DFT-based molecular transport calculations, *Journal of Chemical Physics* 138 (2013) 094102.
- [200] D.A. Egger, Z.-F. Liu, J.B. Neaton, L. Kronik, Reliable Energy Level Alignment at Physisorbed Molecule–Metal Interfaces from Density Functional Theory, *Nano Letters* 15 (2015) 2448-2455.
- [201] C. Jin, M. Strange, T. Markussen, G.C. Solomon, K.S. Thygesen, Energy level alignment and quantum conductance of functionalized metal-molecule junctions: Density functional theory versus GW calculations, *J. Chem. Phys* 139 (2013) 184307.
- [202] S.Y. Quek, K.H. Khoo, Predictive DFT-based approaches to charge and spin transport in single-molecule junctions and two-dimensional materials: Successes and challenges, *Accounts of Chemical Research* 47 (2014) 3250-3257.

- [203] M. Berritta, D.Z. Manrique, C.J. Lambert, Interplay between quantum interference and conformational fluctuations in single-molecule break junctions, *Nanoscale* 7 (2015) 1096-1101.
- [204] K. Wang, J. Zhou, J.M. Hamill, B. Xu, Measurement and understanding of single-molecule break junction rectification caused by asymmetric contacts, *J. Chem. Phys* 141 (2014) 054712.
- [205] M. Baghernejad, D.Z. Manrique, C. Li, T. Pope, U. Zhumaev, I. Pobelov, P. Moreno-García, V. Kaliginedi, C. Huang, W. Hong, Highly-effective gating of single-molecule junctions: an electrochemical approach, *Chemical Communications* 50 (2014) 15975-15978.
- [206] M.T. González, X. Zhao, D.Z. Manrique, D. Miguel, E. Leary, M. Gulcur, A.S. Batsanov, G. Rubio-Bollinger, C.J. Lambert, M.R. Bryce, Structural versus electrical functionalization of oligo (phenylene ethynylene) diamine molecular junctions, *J. Phys. Chem. C* 118 (2014) 21655-21662.
- [207] P. Moreno-García, M. Gulcur, D.Z. Manrique, T. Pope, W. Hong, V. Kaliginedi, C. Huang, A.S. Batsanov, M.R. Bryce, C. Lambert, Single-molecule conductance of functionalized oligoynes: Length dependence and junction evolution, *Journal of the American Chemical Society* 135 (2013) 12228-12240.
- [208] T. Kim, P. Darancet, J.R. Widawsky, M. Kotiuga, S.Y. Quek, J.B. Neaton, L. Venkataraman, Determination of Energy Level Alignment and Coupling Strength in 4, 4'-Bipyridine Single-Molecule Junctions, *Nano Letters* 14 (2014) 794-798.
- [209] V. Fatemi, M. Kamenetska, J. Neaton, L. Venkataraman, Environmental control of single-molecule junction transport, *Nano Letters* 11 (2011) 1988-1992.
- [210] P. Reddy, S.-Y. Jang, R.A. Segalman, A. Majumdar, Thermoelectricity in molecular junctions, *Science* 315 (2007) 1568-1571.

- [211] J.A. Malen, S.K. Yee, A. Majumdar, R.A. Segalman, Fundamentals of energy transport, energy conversion, and thermal properties in organic–inorganic heterojunctions, *Chemical Physics Letters* 491 (2010) 109-122.
- [212] K. Baheti, J.A. Malen, P. Doak, P. Reddy, S.-Y. Jang, T.D. Tilley, A. Majumdar, R.A. Segalman, Probing the chemistry of molecular heterojunctions using thermoelectricity, *Nano Letters* 8 (2008) 715-719.
- [213] J.A. Malen, P. Doak, K. Baheti, T.D. Tilley, A. Majumdar, R.A. Segalman, The nature of transport variations in molecular heterojunction electronics, *Nano Letters* 9 (2009) 3406-3412.
- [214] S.K. Yee, J.A. Malen, A. Majumdar, R.A. Segalman, Thermoelectricity in fullerene–metal heterojunctions, *Nano Letters* 11 (2011) 4089-4094.
- [215] A. Shakouri, S. Li, in: *Thermoelectrics, 1999. Eighteenth International Conference on*, (IEEE, 1999).
- [216] H. Shi, C. Liu, J. Xu, H. Song, Q. Jiang, B. Lu, W. Zhou, F. Jiang, Electrochemical fabrication and thermoelectric performance of the PEDOT: PSS electrode based bilayered organic nanofilms, *Int. J. Electrochem. Sci* 9 (2014) 7629-7643.
- [217] M. Sumino, K. Harada, M. Ikeda, S. Tanaka, K. Miyazaki, C. Adachi, Thermoelectric properties of n-type C60 thin films and their application in organic thermovoltaic devices, *Applied Physics Letters* 99 (2011) 093308.
- [218] H. Sadeghi, S. Sangtarash, C.J. Lambert, Oligoynes molecular junctions for efficient room temperature thermoelectric power generation, *Nano Letters* 15 (2015) 7467-7472.

- [219] H. Sadeghi, J.A. Mol, C.S. Lau, G.A.D. Briggs, J. Warner, C.J. Lambert, Conductance enlargement in picoscale electroburnt graphene nanojunctions, *Proceedings of the National Academy of Sciences* 112 (2015) 2658-2663.
- [220] X. Zhao, C. Huang, M. Gulcur, A.S. Batsanov, M. Baghernejad, W. Hong, M.R. Bryce, T. Wandlowski, Oligo (aryleneethynylene) s with terminal pyridyl groups: synthesis and length dependence of the tunneling-to-hopping transition of single-molecule conductances, *Chemistry of Materials* 25 (2013) 4340-4347.
- [221] C. Lambert, D. Weaire, Theory of the arrangement of cells in a network, *Metallography* 14 (1981) 307-318.
- [222] W. Haiss, C. Wang, R. Jitchati, I. Grace, S. Martín, A.S. Batsanov, S.J. Higgins, M.R. Bryce, C.J. Lambert, P.S. Jensen, Variable contact gap single-molecule conductance determination for a series of conjugated molecular bridges, *Journal of Physics: Condensed Matter* 20 (2008) 374119.
- [223] G. Sedghi, V.M. García-Suárez, L.J. Esdaile, H.L. Anderson, C.J. Lambert, S. Martín, D. Bethell, S.J. Higgins, M. Elliott, N. Bennett, Long-range electron tunnelling in oligo-porphyrin molecular wires, *Nat. Nanotechnol.* 6 (2011) 517-523.
- [224] Sangtarash, Sara, et al. "Searching the hearts of graphene-like molecules for simplicity, sensitivity, and logic." *Journal of the American Chemical Society* 137.35 (2015): 11425-11431.
- [225] Geng, Y., Sangtarash, S., Huang, C., Sadeghi, H., Fu, Y., Hong, W., ... & Liu, S. X. (2015). Magic ratios for connectivity-driven electrical conductance of graphene-like molecules. *Journal of the American Chemical Society*, 137(13), 4469-4476.